

Nonlinear viscoelastic materials: bioinspired applications and new characterization measures

by

Randy H. Ewoldt

B.S., Mechanical Engineering, Iowa State University (2004)

M.S., Mechanical Engineering, M.I.T. (2006)

Submitted to the Department of Mechanical Engineering
in partial fulfillment of the requirements for the degree of

Doctor of Philosophy in Mechanical Engineering

at the

MASSACHUSETTS INSTITUTE OF TECHNOLOGY

June 2009

© Massachusetts Institute of Technology 2009. All rights reserved.

Author
Department of Mechanical Engineering
May 1, 2009

Certified by
Gareth H. McKinley
Professor, Mechanical Engineering
Thesis Supervisor

Certified by
Anette E. Hosoi
Associate Professor, Mechanical Engineering
Thesis Supervisor

Accepted by
David E. Hardt
Chairman, Department Committee on Graduate Students

Nonlinear viscoelastic materials: bioinspired applications and new characterization measures

by

Randy H. Ewoldt

Submitted to the Department of Mechanical Engineering
on May 1, 2009, in partial fulfillment of the
requirements for the degree of
Doctor of Philosophy in Mechanical Engineering

Abstract

Viscoelastic materials, such as biomaterials and non-Newtonian fluids, typically experience mechanical loading which evokes a nonlinear rheological response. Rheologically complex materials can provide novel functionality in biological and engineered systems. However, it is found that standard characterization techniques are insufficient to appropriately describe nonlinear viscoelasticity. The goal of this thesis is to transcend the limitations of current characterization methods as well as demonstrate applications of nonlinear viscoelastic materials, including reversible adhesion and snail-like wall climbing.

PART ONE of this thesis introduces a complete language and framework (or *ontology*) for characterizing nonlinear viscoelasticity using large amplitude oscillatory shear (LAOS) deformation. The LAOS protocol spans the 2D parameter space of deformation amplitude and frequency, known as a Pipkin space. Physically meaningful material measures are proposed, corresponding to clearly defined language such as strain-stiffening/softening and shear-thickening/thinning. The new ontology is general enough to be applied to any viscoelastic material, mapping behaviors from purely elastic to purely viscous, and any complex response in-between. The framework has been packaged into a distributable data analysis program (MITlaos) to widen its use in both academic and industrial settings.

PART TWO examines the nonlinear rheological response of various soft materials and constitutive models. The new framework is illustrated by examining prototypical nonlinear constitutive models (Giesekus, pseudoplastic Carreau, and elastoplastic Bingham). Various soft materials are tested experimentally, including pedal mucus gel from terrestrial gastropods, a wormlike micelle solution, ultrasoft hagfish slime, and an oilfield drilling fluid.

PART THREE describes the use of nonlinear rheological behavior to enable unique functionality, specifically for bioinspired snail-like wall climbing and tunable adhesion using magnetorheological fluids. Yield stress fluids are examined here to enable the bioinspired adhesive locomotion of a self-contained mechanical device (Robosnail, developed by Brian Chan, Ph.D. '09). Field-responsive magnetorheological fluids are

analyzed in the context of providing fast-switching reversible adhesion for use with adhesive locomotion devices and shape-changing soft robots.

In conclusion, interest in soft materials is increasing across many disciplines. The contributions presented here provide the means to a better understanding of biological and engineered systems which involve complex viscoelastic materials.

Thesis Supervisor: Gareth H. McKinley
Title: Professor, Mechanical Engineering

Thesis Supervisor: Anette E. Hosoi
Title: Associate Professor, Mechanical Engineering

Biography

Randy H. Ewoldt was born in 1981 and spent his childhood on a farm in Eldridge, Iowa. After finding equal success in music and the sciences at North Scott Senior High School, he chose to pursue a Bachelor of Science in Mechanical Engineering at Iowa State University. There he was recognized as the Top Graduate in the College of Engineering in 2004. He left Iowa for New England and the Massachusetts Institute of Technology, receiving a Master of Science in Mechanical Engineering in 2006, and continuing into the Ph.D. program. Randy is passionate about teaching, and has facilitated student learning in physics, math, and engineering at Iowa State and M.I.T. His honors include a National Science Foundation Graduate Research Fellowship, Best Student Poster at the 2005 Society of Rheology Conference, Department of Mechanical Engineering Outstanding Thesis Award for his M.S. thesis, and a Luis de Florez Innovation Award from the Department of Mechanical Engineering at M.I.T. for work contained in this Ph.D. thesis. Randy's industry experience has helped him to gain perspective on his research and teaching, most notably from the Boeing Co. where he supported the Space Shuttle program in 2002, and for InkTec Zone as a design engineer consultant between 2007 and 2008. Randy currently lives in Cambridge, MA with his wife, Erin, and their 20 month old son, Isaac.

Acknowledgments

I never imagined that life could be so rewarding and enjoyable while pursuing a Ph.D at M.I.T. This was made possible by the support of family and friends, and the fortune to have two of the best advisors in the department, Anette (Peko) Hosoi and Gareth McKinley. Their genuine enthusiasm and passion for research is contagious and incredibly motivating. I am grateful for their confidence in me, their advocacy for me, and their understanding that life is to be fully enjoyed by pursuing interests both inside and outside of the laboratory.

I thank my numerous lab mates, colleagues, and friends for their support and assistance. It is humbling to realize how many people have impacted me during my time at MIT, and I would like to mention a few of them here. Brian Chan created Robosnail and the opportunity to work on the rheology of snail slime, which was a gateway project into all of my thesis work. Peter Winter masterfully gave the MITlaos software a graphical user interface. Piotr Tourkine assisted with the adhesion research in Chapter 9, which is still ongoing. Suraj Deshmukh and Murat Ocalan taught me about magnetorheological fluids. Douglas Fudge let me play with hagfish slime. Both he and Tim Winegard taught me an appreciation for hagfish husbandry, a task which I will continue to defer to them whenever possible. Trevor Ng and Ryan Larson provided excellent discussions and feedback regarding the new measures for large amplitude oscillatory shear. Manfred Wilhelm and Kyu Hyun kindly hosted my visit to Germany to learn about the state-of-the-art in Fourier-transform rheology. I would like to thank the National Science Foundation Graduate Research Fellowship Program for funding, which provided the freedom to initially pursue this research. The DARPA Chemical Robots Program funded the research during my final three semesters.

On a more personal level, I am grateful to all members of “Team Peko” and the “Non-Newtonian Fluids Group” that have shared time with me in the lab. Amos Winter was a source of constant encouragement, Red Sox experiences, and rich conversation on both a technical and personal level. Trevor Ng, Chris Pipe, and Giorgia

Bettin made the lab a social and entertaining environment. Trush Majmudar always made time to answer my questions about research, writing, and life in general. Nahn Ju Kim conquered her fear of slimy animals to help me collect slugs after rainstorms in Cambridge. Tony Yu and Sungyon Lee have been friends ever since we all met as prospective graduate students (first at a different university, and then again at MIT). I had the fortune to learn and play squash with Amos Winter, Jerome Crest, Matthieu Varagnat, Brenden Epps, and others. Lunchtime was made more enjoyable by Jeremy Gordon, Philipp Erni, Michael Radavonovic, Ghassan Fayad, and Chris MacMinn, to name a few.

Gratitude to my family has continued through the course of this Ph.D. My parents, Bob and Rose Ewoldt, have supported my decisions and encouraged my independence, contributing to my confidence and motivation to complete this degree. Mark and Julie Bader have provided a great deal of support, encouragement, and enthusiasm, not to mention numerous opportunities to take a break and enjoy life more fully. My son Isaac has given me a greater perspective on life, and has been an outlet for creativity with music, song, and humor by responding with laughter and occasional applause, all without passing judgement (thus far).

I am especially thankful to my wife Erin. My choice to pursue a Ph.D. did not come without sacrifice, and I am grateful for all of the sacrifices she has made to support this endeavor. Furthermore, she has always been interested to know about my research and given me opportunities to explain my work to a non-specialist. Erin has also assisted with my Ph.D. work, including road trips with hagfish and graphical design advice for communicating my research. Erin has kept me balanced and provided a firm foothold in the real world outside of research, making life more fulfilling. She is an abundant source of encouragement and support, and without her I would not be the person I am today.

A.M.D.G.

R.H.E.

Contents

1	Introduction and background	35
1.1	Scope of thesis	37
1.2	Rheological characterization techniques	38
1.2.1	Non-oscillatory techniques	40
1.2.2	Oscillatory shear deformation	41
1.2.3	Inertio-elastic ringing (“free oscillation”)	46
2	New measures for characterizing nonlinear viscoelasticity with large amplitude oscillatory shear (LAOS)	59
2.1	Introduction	59
2.2	Interpretation of higher harmonics using the Chebyshev polynomial representation	65
2.3	Meaningful viscoelastic moduli in the nonlinear regime	70
2.3.1	Elastic modulus	71
2.3.2	Dynamic viscosity	75
2.3.3	Dimensionless index of nonlinearity	76
3	Data analysis software: MITlaos	79
3.1	Introduction	82
3.2	Installation	83
3.3	Running the program	83
3.3.1	Structure of Input Data File	83
3.3.2	Starting the Program	83

3.4	Main Window Overview	84
3.5	Data Input Panel	85
3.6	Input Variables Panel	87
3.7	Stress Filtering Panel	93
3.8	Save Panel	95
3.9	Main Buttons	99
3.10	Additional function: Plot3D	100
4	LAOS ontology applied	103
4.1	Constitutive model examples	103
4.1.1	Purely elastic strain-stiffening solid	103
4.1.2	Purely viscous shear-thinning fluid	105
4.1.3	Nonlinear viscoelastic Giesekus model	107
4.2	Experimental examples	112
4.2.1	Materials and Methods	112
4.2.2	Gastropod pedal mucus (a biopolymer hydrogel)	116
4.2.3	Wormlike micellar fluid	119
5	Nonstandard Large Amplitude Oscillations	127
5.1	Even-harmonics	127
5.2	Stress-controlled LAOS	133
6	Hagfish slime - an ultrasoft material	137
6.1	Background	137
6.2	Materials and methods	139
6.3	Results	141
7	LAOS of pseudoplastic and elastoviscoplastic materials	153
7.1	Introduction	154
7.2	Materials and Methods	156
7.2.1	Materials	156
7.2.2	LAOS protocol	157

7.2.3	Data processing	158
7.3	Response of model fluids with yield stress characteristics	159
7.3.1	Purely viscous Carreau model	160
7.3.2	Elastic Bingham model - homogeneous strain	163
7.3.3	Elastic Bingham model - torsional plate-plate response	166
7.4	Quantitative indicators of plastic behavior in LAOS	168
7.4.1	Harmonic analysis and Chebyshev coefficients	169
7.4.2	Viscoelastic moduli	170
7.4.3	Perfect plastic dissipation ratio	172
7.5	Experimental results	175
7.5.1	Xanthan gum LAOS response	177
7.5.2	Drilling fluid LAOS response	181
7.5.3	Rutgers-Delaware rule	187
7.6	Conclusions	189
8	Snail-like wall climbing with bioinspired slime simulants	191
8.1	Experimental	193
8.2	Results and discussion	195
8.2.1	Requirements of slime simulants	195
8.2.2	Rheological material functions	199
8.3	Demonstration of feasibility	212
8.4	Conclusions	213
9	Tunable and reversible adhesion using field-activated “smart” fluids	217
9.1	Experimental setup and materials	218
9.1.1	Instrumentation	219
9.1.2	Materials	220
9.1.3	Magnetic field configuration for pull-off tests	224
9.2	Background: fluid adhesion	226
9.3	Theory: magnetorheological fluid adhesion with an inhomogeneous field	228
9.4	Results: Passive Fluids	232

9.4.1	Newtonian oil viscous adhesion	232
9.4.2	Passive yield stress fluid adhesion	234
9.5	Results: Field-responsive magnetorheological fluid	236
9.5.1	Failure modes and pattern formation with magnetorheological fluid adhesion	241
9.6	Conclusions	243
10	Conclusions and outlook	247
A	Chebyshev polynomials	251
B	MATLAB source code	253
B.1	JoR_laos_batch_analyze_v2p0.m	253
B.2	JoR_laos_analyze_v3p3.m	254
B.3	cycletrim.m	267
B.4	FTtrig.m	268
B.5	legendre_decompose.m	269
B.6	legendre_compose.m	270
B.7	chebyshev_decompose.m	270
B.8	chebyshev_compose.m	272
C	Yield stress LAOS - supplementary figures	275
D	Details of Slime Simulant Survey	283
E	Supplemental information for normal adhesion tests	289
E.1	Newtonian silicone oil rheology	289
E.2	Magnetic field FEA	290

List of Figures

1-1	Several examples in which nonlinear viscoelastic material behavior is relevant, ranging from biological to engineered systems. (a) the adhesive locomotion of snails (see Chapter 8), (b) biomaterials and biofluids such as artery walls, blood, and cells (photo from N.I.H. Medical Encyclopedia), (c) bread dough processing (photo of Dr. Shen Kuan (Trevor) Ng by Donna Coveney), (d) personal care products such as hand lotions, (e) magnetorheological fluids (see Chapter 9).	36
1-2	Simple shear characterization of (a) purely elastic material response, and (b) purely viscous material response.	39
1-3	Schematic map of the input parameters for oscillatory shear rheometry, known as a Pipkin diagram (adapted from A. C. Pipkin[1]). For viscoelastic fluids, the limit of low frequency corresponds to approximately viscous behavior, whereas high frequency corresponds to approximately elastic behavior. Linear viscoelastic responses are expected at sufficiently small values of strain amplitude γ_0 . A. C. Pipkin drew a question mark in the region of intermediate frequency and large amplitude, the deformation regime in which many materials are processed and used.	42

1-4	The transient creep response of a viscous Newtonian fluid and a viscoelastic polymeric gel with equivalent instrument inertia and geometry. The viscoelastic fluid exhibits underdamped oscillations but little flow at long times as shown in (a). The short time creep response, shown in (b), is identical for the two fluids and is completely determined by instrument inertia and geometry. A short time asymptotic solution proportional to t^2 is also shown by the broken line. Creep ringing is caused by the coupling of instrument inertia with the elasticity of the viscoelastic sample (Rhamsan gum (courtesy of CPKelco, San Diego, CA) at 0.75 wt% 250mM NaCl, AR-G2, $D = 6$ cm 2° cone, $T = 25^\circ\text{C}$, $\sigma_0 = 1$ Pa for each).	47
1-5	Typical data (simulated) for inertial creep responses compared to ideal non-inertial responses: a) Newtonian; b) Kelvin-Voigt viscoelastic solid, under-damped; c) Jeffreys viscoelastic fluid, under-damped; d) an enlargement of the response near the origin shows that all models have the same quadratic response at short times, which is determined purely by the instrument inertia and geometry factor.	53
1-6	Creep test of native pedal mucus from the terrestrial gastropod <i>Helix aspera</i> ; inertio-elastic ringing fit to both a Kelvin-Voigt and Jeffreys model (AR-G2, $D=0.8$ cm plate with sandpaper, $1000\mu\text{m}$ gap, $T=22^\circ\text{C}$, $\sigma_0 = 5$ Pa $\ll \sigma_y$).	54
2-1	Oscillatory strain sweeps of pedal mucus from <i>Limax maximus</i> at a frequency $\omega = 3$ rad.s $^{-1}$. (a) Typical rheometer output of the fluid viscoelasticity as parameterized by the first-harmonic Fourier moduli; (b) Plotting the raw data from every-other point as $\sigma(t)$ vs. $\gamma(t)$ reveals additional nonlinear characteristics that are obscured by G'_1, G''_1	62
2-2	Applying the geometrical interpretation to the largest strain amplitude data point from Figure 2-1, ($\omega = 3$ rad.s $^{-1}$, $\gamma_0 = 2.8$); (a) total stress and elastic stress σ' , (b) total stress and viscous stress σ''	65

2-3	Diagram summarizing the interpretation of the third-harmonic phase angle δ_3 , as revealed by the third-order Chebyshev coefficients.	69
2-4	Definitions of new measures for reporting viscoelastic moduli: (a),(b) elastic moduli and dynamic viscosities, respectively, for a model linear viscoelastic response with $G' = 0.8$, $G'' = 0.6$ at ($\omega = 1 \text{ rad.s}^{-1}$, $\gamma_0 = 1$); (c),(d) elastic moduli and dynamic viscosities, respectively, for a nonlinear viscoelastic response (experimental data shown is same as Figure 2-2). The first harmonic moduli are shown for comparison. In the linear regime (a,b) all measures are equivalent to the linear viscoelastic moduli. A nonlinear material response (c,d) will result in different values for each material measure.	72
2-5	Different elliptical approximations to a nonlinear viscoelastic signal, using the newly proposed alternative measures of elastic modulus. . .	74
3-1	Flow chart of the processing sequence for the “MITlaos” data analysis software.	80
3-2	MITlaos Output: Overview plot example, shown here for pedal mucus from <i>Limax maximus</i> , $\omega = 3 \text{ rad.s}^{-1}$, $\gamma_0 = 2.8$, c.f. Figure 4-3.	81
3-3	MITlaos Output: Filter performance, shown here for pedal mucus from <i>Limax maximus</i> , $\omega = 3 \text{ rad.s}^{-1}$, $\gamma_0 = 2.8$, c.f. Figure 4-3.	82
3-4	The MITlaos main window (arrows added to show the standard order of completion).	84
3-5	Data Input Panel.	85
3-6	Choose Data Window.	85
3-7	Import Wizard (only used to preview data).	86
3-8	Input Variables panel.	87
3-9	Input Variables panel, with ‘Convert Displacement’ and ‘Convert Torque’ options selected, and the ‘Time’ column input turned on.	89
3-10	ProcessPartDataGUI window.	90
3-11	Data Set with Incorrectly Specified Columns.	92

3-12 Data Set with a Stepwise Increase in Amplitude.	93
3-13 Stress Filtering panel.	93
3-14 FTharmonicGUI window.	95
3-15 Save panel.	96
3-16 datasaveGUI window.	97
3-17 figuresaveGUI window.	99
3-18 Main Program Buttons.	99
3-19 Plot3D user interface.	101
4-1 Pipkin diagram plots of resulting viscoelastic parameters for a simulated nonlinear viscoelastic fluid (Giesekus model, $\lambda_1 = 1$ s, $\eta_s = 0.01$ Pa.s, $\eta_p = 10$ Pa.s, and $\alpha = 0.3$); (a) first order elastic modulus G'_1 , contours shown at increments of 2 Pa (b) first order dynamic viscosity η'_1 , contours shown at increments of 2 Pa (c) normalized third-order elastic Chebyshev coefficient e_3/e_1 , contours as labeled, (d) scaled third-order viscous Chebyshev coefficient v_3/v_1 , contours shown at ± 0.001 , ± 0.025 , ± 0.05 , ± 0.1 , $+0.15$, and (e) normalized intensity of the third harmonic I_3/I_1 , contours shown at 0.001, and increments of 0.01.	109

4-2	<p>Oscillatory shear test of pedal mucus from Figure 2-1, $\omega = 3 \text{ rad.s}^{-1}$, analyzed within the new framework; (a) Elastic moduli: minimum-strain and large-strain elastic moduli compared to first harmonic elastic modulus (b) Dynamic viscosities: minimum-rate and large-rate dynamic viscosities compared to first harmonic dynamic viscosity, (c) Intra-cycle elastic nonlinearity measures: scaled 3rd order elastic Chebyshev coefficient e_3/e_1 and strain-stiffening ratio S, both indicate intra-cycle strain-stiffening; (d) Intra-cycle measures of viscous nonlinearity: 3rd order viscous Chebyshev coefficient v_3/v_1 and shear-thickening ratio T, both indicate intra-cycle shear-thinning. Error bars are determined from the noise in the Fourier spectrum and are shown for representative points. The data point size exceeds the error margins at larger amplitudes. For e_3/e_1 and v_3/v_1 (star symbols) the data point size exceeds the error for all amplitudes.</p>	117
4-3	<p>Reconstruction of (a) elastic and (b) viscous stresses using the Chebyshev spectrum of each signal (c,d). The nonlinearity of each signal is predominantly described by including only the third-order contribution; contributions higher than $n = 3$ are comparably insignificant ($e_5, e_1, v_5/v_1 < 0.005$) (same experimental data as Figure 2-2).</p>	118
4-4	<p>Raw LAOS data for the micellar solution, shown as elastic Lissajous-Bowditch curves generated from experimental oscillatory tests. Each trajectory is positioned in a Pipkin space according to the imposed values (ω, γ_0). Solid lines are total stress $\sigma(t)/\sigma_{\max}$ vs. $\gamma(t)/\gamma_0$. The maximum stress, σ_{\max}, is indicated above each curve.</p>	120
4-5	<p>Elastic Lissajous-Bowditch curves generated from experimental oscillatory tests of the micellar solution, displayed in a Pipkin space. Each trajectory is positioned according to the imposed values (ω, γ_0). Solid lines are total stress (filtered) $\sigma(t)/\sigma_{\max}$ vs. $\gamma(t)/\gamma_0$, dashed lines are elastic stress $\sigma'(t)/\sigma_{\max}$ vs. $\gamma(t)/\gamma_0$. The maximum stress, σ_{\max}, is indicated above each curve.</p>	121

4-6	Viscous Lissajous-Bowditch curves generated from experimental oscillatory tests of the micellar solution, displayed in a Pipkin space. Each trajectory is positioned according to the imposed values (ω, γ_0) . Solid lines are total stress (filtered) $\sigma(t)/\sigma_{\max}$ vs. $\dot{\gamma}(t)/\dot{\gamma}_0$, dashed lines are viscous stress $\sigma''(t)/\sigma_{\max}$ vs. $\dot{\gamma}(t)/\dot{\gamma}_0$. The maximum stress, σ_{\max} , is indicated above each curve.	122
4-7	“Rheological Fingerprints” of the elastic properties of the micellar solution in large amplitude oscillatory shear. Each parameter is plotted in a Pipkin diagram as a function of the imposed frequency and strain amplitude. (a,b,c) Elastic moduli G'_M , G'_L , and G'_1 respectively; unlabeled contours shown at increments of 2 Pa (d) Intra-cycle elastic nonlinearity as indicated by the normalized third-order elastic Chebyshev term, e_3/e_1 ; contours shown at -0.05, ± 0.01 , and increments of 0.2.	123
4-8	Viscous properties of the micellar solution in large amplitude oscillatory shear, each parameter plotted in a Pipkin space; (a,b,c) Dynamic viscosities η'_M , η'_L , and η'_1 respectively; contours shown at increments of 2 Pa.s. Inter-cycle nonlinearities are indicated by gradients of these measures. Inter-cycle thinning is shown for sufficiently large and increasing values of the shear rate amplitude $\dot{\gamma}_0 = \gamma_0\omega$. (d) Intra-cycle viscous nonlinearity as indicated by the normalized third-order viscous Chebyshev term, v_3/v_1 ; contours shown at increments of 0.05. Intra-cycle thickening is indicated by $v_3/v_1 > 0$, whereas intra-cycle thinning is shown by $v_3/v_1 < 0$	124
5-1	A purely elastic oscillatory response for $G''_2 = -G''_0 = -0.1$, $G'_1 = 1$, and all other terms equal to zero. (a) elastic Lissajous curve of stress vs. strain, (b) p viscous Lissajous curve of stress vs. strain-rate. . . .	130
5-2	Oscillatory response of arbitrary construction which includes even harmonics.	131

5-3	Oscillatory response of arbitrary construction which includes even harmonics.	132
6-1	Photos of Atlantic hagfish used for this research. (a) top-down view of three hagfish in a large glass beaker, (b) collection of fresh slime exudate.	138
6-2	Microscope images of stabilized hagfish slime. The primary constituents of whole slime exudate are mucin vesicles and wound-up threads. Each egg-shaped thread winding is composed of a continuous filament of diameter $1-3\mu\text{m}$, with length up to 15 cm when fully unraveled.	138
6-3	Hagfish slime networks can sustain large stretch ratios while maintaining a cohesive mass. This photo shows Tim Winegard (hagfish wrangler, University of Guelph) raising the rheometer test geometry after experiments.	140
6-4	Results of a creep test conducted with “fresh” hagfish slime reconstituted from exudate mixed with seawater in the lab. At short times the strain oscillates due to inertio-elastic ringing, in which the sample elasticity couples with the finite instrument rotational inertia to “ring” at a resonant frequency, just like a mass at the end of a spring (see Section 1.2.3). At longer times the strain is approximately constant, γ_{ss} , and this is representative of a primarily elastic material response.	142
6-5	Frequency sweep results with hagfish slime reconstituted from fresh exudate. The strain amplitude was prescribed ($\gamma_0 = 10\%$). The mechanical resistance is so low ($G' < 0.03 \text{ Pa}$) that inertial effects from the rheometer spindle easily appear in the data, with a sharp jump in raw phase angle from $\delta = 14.7^\circ$ to $\delta = 134.9^\circ$ at $\omega = 1 \text{ rad.s}^{-2}$, corresponding to the resonant frequency of the material-instrument system $\omega^* = 0.99 \text{ rad.s}^{-1}$ (Fig. 6-4).	143
6-6	Large amplitude oscillatory shear test with hagfish slime reconstituted from fresh exudate. The strain amplitude was prescribed as indicated on the abscissa ($\omega = 0.15 \text{ rad.s}^{-1}$).	144

6-7	Creep tests conducted with hagfish slime reconstituted from stabilized exudate mixed with seawater in the lab. Various stress amplitudes are imposed to examine the nonlinear rheological response. (a) time dependent creep response curves at each imposed stress, (b) elastic analysis of each curve including the differential modulus K' (Eq. 6.12) and initial secant modulus G_0 (Eq. 6.11.	145
6-8	Photos of successive extensional flow tests performed on a single sample of hagfish slime, made from fresh slime exudate. The shape of the filament at the end of each run changes slightly; note that after Run 3 the shape is convex near the center of the filament due to the gel-like nature of the slime mass.	149
6-9	Extensional flow results for hagfish slime, corresponding to the tests shown in Figure 6-8. (a) Successive tests on the same sample show repeatable results. (b) The plate separation imposes a constant extensional deformation rate, $\dot{\epsilon} = 0.2 \text{ s}^{-1}$, if homogeneous deformation is assumed.	150
6-10	Analysis of the extensional flow measurements shown in Figure 6-9 (Run 1), with standard assumptions for kinematics of radial deformation, $R(t) = R_0 \exp(-\dot{\epsilon}t/2)$. (a) apparent stress difference, and (b) apparent extensional viscosity.	151
7-1	Validation of the MITlaos software (Chapter 3), using a strain sweep for xanthan gum solution (0.2 wt%) at $\omega = 3.75 \text{ rad.s}^{-1}$. MITlaos software is used to analyze the raw stress and strain waveforms resulting from Arbitrary Waveshape tests (squares). A duplicate test was performed with the typical oscillation test mode of the ARES rheometer software (circles), which provides viscoelastic parameters but no raw data or assessment of higher harmonic content. The superposition of results indicates the validity of the Arbitrary Waveshape test and the MITlaos software for analyzing both linear and nonlinear LAOS results.	158

7-2 Lissajous-Bowditch curves of the Carreau pseudoplastic model (Eq. 7.2) for various values of the Carreau number $Cu = \lambda\gamma_0\omega$ and power law index n . Here $n = 1.0$ is Newtonian (dotted lines), $n = 0.5$ is shear-thinning (dashed lines), and $n = 0.0$ is the limiting case of viscoplastic yield stress behavior (solid lines). (a) 3D trajectories of the stress response $\sigma(t)/\sigma_{\max}$ as a function of the normalized LAOS inputs $\{x(t), y(t)\}$, shown for $\lambda\gamma_0\omega = 10$. Note that the maximum stress σ_{\max} is different for each value of n , as shown in (b), which depicts 2D Lissajous curves projected onto the planes of stress vs. strain ($\tilde{\sigma}(t)$ vs. $x(t)$) and stress vs. strain-rate ($\tilde{\sigma}(t)$ vs. $y(t)$). In (b) the stress is scaled by the Newtonian stress $\eta_0\dot{\gamma}_0$, rather than the maximum stress, at each value of the Carreau number $Cu = \lambda\gamma_0\omega$ 160

7-3 Lissajous-Bowditch curves for the elastic Bingham model in terms of the variables $\Gamma_0 = \gamma_0/\gamma_Y$, $N = \mu_p\dot{\gamma}_0/\sigma_Y$ defined by Yoshimura and Prudhomme[2]. (a) Homogeneous strain (e.g. cone-plate) response showing individual limit cycles of the oscillatory stress vs. strain (elastic curves) and stress vs. strain-rate (viscous curves). Maximum normalized stress $(\sigma/\sigma_Y)_{\max}$ is shown above each curve. (b) Steady oscillatory response of plate-plate deformation (inhomogeneous strain), curves of torque vs. displacement (elastic curves) and torque vs. displacement-rate (viscous curves). The maximum normalized torque shown above each curve, $(2M/\pi R^3\sigma_Y)_{\max}$ 164

7-4 The energy dissipated by a single LAOS response is represented by the area enclosed in a Lissajous curve of stress vs. strain. For a given strain amplitude γ_0 and maximum stress σ_{\max} , the maximum possible dissipated energy is the circumscribing rectangle of the perfect plastic model response, with strain amplitude γ_0 and yield stress $\sigma_Y = \sigma_{\max}$. The example shown here is the measured steady LAOS response of the drilling fluid at $\omega = 15 \text{ rad.s}^{-1}$, with $\gamma_0 = 3.16$, $\sigma_{\max} = 113 \text{ Pa}$, and $\phi = 0.829$ 173

7-5	Carreau model response, characterized by the perfect plastic dissipation ratio, ϕ (Eq. 7.12). (a) Behavior of ϕ with respect to normalized shear-rate amplitude. (b) Behavior of ϕ as a function of n , shown for various values of the Carreau number $Cu = \lambda\gamma_0\omega$: ϕ_{\max} , $\phi(\lambda\gamma_0\omega = 10)$, $\phi(\lambda\gamma_0\omega = 1)$	174
7-6	Viscosity flow curves for the 0.2wt% xanthan gum solution (squares, step shear rate for each data point) and the invert emulsion drilling fluid (circles, thixotropic loop test). Fits to the Carreau model are shown for each fluid (lines).	175
7-7	Steady-state Lissajous curves for the xanthan gum solution (0.2wt% aqueous). (a) Un-normalized 3D Lissajous curves at $\omega = 3.75 \text{ rad.s}^{-1}$. (b,c) Normalized curves arranged in a Pipkin space at the corresponding input parameters of frequency and strain-amplitude, $\{\omega, \gamma_0\}$. (b) individual plots of normalized stress (solid lines) and elastic stress (dashed lines) vs. strain; (c) individual plots of normalized stress (solid lines) and viscous stress (dotted lines) vs. strain-rate. The maximum stress σ_{\max} in each test is shown above each limit cycle.	178
7-8	Yield stress indicators for the xanthan gum solution (0.2wt% aqueous), shown as a function of the LAOS input parameters $\{\omega, \gamma_0\}$. (a,b) Stiffening index and Thickening index, respectively, lines shown at ± 0.01 . (c) perfect plastic dissipation ratio ϕ . $\phi > \pi/4$ indicates a region in which the xanthan gum solution is shear-thinning. The maximum observed value, $\phi_{\max} = 0.97$ at $\{\omega = 3.75 \text{ rad.s}^{-1}, \gamma_0 = 10\}$, does not indicate an idealized yield stress response, which would appear as $\phi_{PP} = 1$	179

7-9 Steady-state Lissajous curves for the drilling fluid, shown for a selected range of strains and frequencies. (a) Un-normalized 3D curves for fixed $\omega = 4.75 \text{ rad.s}^{-1}$ and strain-amplitudes $\gamma_0 = 0.562, 1, 1.78, 3.16, 5.62, 10$. (b,c) Normalized 2D projections of σ/σ_{\max} arranged in a Pipkin space at the corresponding input parameters $\{\omega, \gamma_0\}$ which generated each response curve. The maximum stress is shown above each curve. (b) individual plots of normalized stress (solid black lines) and elastic stress (dashed red lines) vs. strain; (c) individual plots of normalized stress (solid black lines) and viscous stress (dotted blue lines) vs. strain-rate. 182

7-10 Quantitative LAOS analysis of the drilling fluid. (a,b) Stiffening index and Thickening index, respectively, lines shown at ± 0.01 . (c) Perfect plastic dissipation ratio, ϕ , shown as contours in a Pipkin space. At small strain amplitude ϕ takes very small values indicated a predominantly elastic response, which at larger strain amplitude gives way to a predominantly viscous response and eventually a maximum dissipation ratio, $\phi_{\max} = 0.93$, nearing the behavior of an idealized perfect plastic response. 183

7-11 First-harmonic dynamic viscosity $v_1(\dot{\gamma}_0) = \eta'_1(\dot{\gamma}_0)$ from LAOS tests (closed symbols) compared to the apparent shear viscosity $\eta(\dot{\gamma})$ from the thixotropic loop test (open circles). Good correspondence is found between the tests at sufficiently large strain amplitudes $\gamma_0 \geq 3$, consistent with the Rutgers-Delaware rule. The viscosity at low shear-rates gives a lower bound for the Carreau model fitting parameter η_0 . The Carreau fit for $\eta_0 = 10^3 \text{ Pa.s}$, $\lambda = 53.5 \text{ s}$, $n = 0.099$, and $\eta_{\text{inf}} = 0.377 \text{ Pa.s}$ is given by the solid line. 186

7-12	Dynamic viscosity from LAOS tests (crossed symbols) compared to the apparent shear viscosity $\eta(\dot{\gamma})$ from the thixotropic loop test (open circles). (a) Large-rate dynamic viscosity η'_L , which shows excellent correspondence in the yielded regime, $\gamma_0 > 3$. (b) Magnitude of the first-harmonic complex viscosity, which slightly over-predicts the flow viscosity in the yielded regime, but suffers from less under-prediction in the unyielded regime.	187
8-1	Bottom view of a crawling terrestrial slug <i>Limax maximus</i> , 1 cm scale bar; a) muscular contractions compress the foot parallel to the substrate, creating an area of high shear stress which ruptures the mucus network structure; b) an interwave of low stress allows the network structure to reform into a solid-like material which holds the organism to the substrate. Compression waves move toward the head (top of picture) during locomotion.	192
8-2	Simple model of an adhesive locomotion system - the crawler consists of N discrete pads and rests on a fluid with thickness h . An internal controlled force iteratively moves one pad forward with respect to the rest.	195
8-3	Material selection space comparing yield stress fluids; Stars: native mucus gels, Triangles: polymeric solutions and gels, Hexagons: Particulate suspensions and gels, Circles: soft glassy materials. A suitable simulant will meet a minimum yield stress requirement and have a low post-yield viscosity. See Appendix D for material preparation and reference details.	198

8-4	Steady shear viscosity of simulants compared to native pedal mucus from <i>Helix aspera</i> ; native slime collected from two snails, tested with plate-plate fixtures $D = 0.8$ mm with sandpaper, $h = 100\mu\text{m}$; a) Carbopol-based simulant, plate-plate with sandpaper, solvent trap, $h = 1000\mu\text{m}$, $D = 4$ cm for 0.5%-2%, $D = 2$ cm for 3%-4%; b) Laponite-based simulant, solvent trap, $D = 6$ cm 1° cone-plate for 1%-2%, $D = 4$ cm 2° cone-plate for 2.5%, $D = 4$ cm plate-plate, $h = 1000\mu\text{m}$ with sandpaper for 3%-7%.	200
8-5	Linear viscoelastic moduli of simulants compared with native pedal mucus from <i>Limax maximus</i> ; pedal mucus tested with $D = 2$ cm plate with sandpaper, solvent trap, $h = 200\mu\text{m}$, $\sigma_0 = 5$ Pa; simulants tested with $D = 4$ cm plate with sandpaper, $h = 1000\mu\text{m}$, solvent trap; a) Carbopol-based simulant, $\sigma_0 = 5$ Pa; b) Laponite-based simulant, $\sigma_0 = 20$ Pa.	203
8-6	Large amplitude oscillatory shear (LAOS) of simulants compared with native pedal mucus from <i>Limax maximus</i> , same geometries as Figure 8-5, all samples tested at $\omega = 1$ rad.s ⁻¹ ; a) Carbopol-based simulant; b) Laponite-based simulant.	205
8-7	Lissajous curves resulting from the large amplitude oscillatory shear tests shown in Figure 8-6 for the polymer gel simulant(a) and the particulate gel simulant(b).	207
8-8	Lissajous curves resulting from the large amplitude oscillatory shear tests shown in Figure 8-6 for native pedal mucus from <i>Limax maximus</i>	208
8-9	Time-dependent stress overshoot of simulants, $D = 5$ cm 1° cone-plate; a) Carbopol 2%, error bars shown at one standard deviation; b) Laponite 3%.	210

8-10	(a) The common garden snail <i>helix aspera</i> (and other terrestrial gastropods) use the nonlinear viscoelastic properties of excreted trail mucus for transitory attachment, allowing locomotion on inclined surfaces. (b) Bioinspired embodiment of a mechanical crawler that successfully uses adhesive locomotion to traverse inclined and inverted surfaces, as in (c), using appropriately designed complex fluids described in this thesis.	212
9-1	(a) Sketch of the experimental setup for adhesive pull-off tests of a field-responsive magnetorheological fluid. Instrument materials are non-magnetic. The adhesive fluid layer (diameter D , gap height h) resides between rigid surfaces. The lower plate allows for a permanent magnet (diameter D_m) to be introduced to “activate” the adhesive with an inhomogeneous field. The top of the magnet is separated from the bottom of the fluid by a distance δ . (b) Free body diagrams for yield stress fluid adhesion. For the top plate only forces in the z -direction are shown. The fluid is modeled locally as a perfect plastic with radially dependent yield stress. Small gaps are assumed ($h/D \ll 1$), so that material deformation consists primarily of shear.	218
9-2	Rheological characterization of the passive yield stress fluid, Carbopol 2wt%, pH 7.	221
9-3	Steady flow characterization of the magnetorheological fluid, which behaves as a nearly perfect viscoplastic with constant stress as a function of shear rate (a). Another method of showing viscoplastic yield stress behavior is shown in (b), which depicts steady flow viscosity as a function of the imposed shear stress. The viscosity and stress values have been corrected for the parallel plate geometry.	223

9-4	Shear yield stress for the magnetorheological fluid as a function of the external magnetic field strength (field lines perpendicular to shearing direction). Yield stress values extracted from Fig. 9-3 (circles). The dashed line is a power law fit to the data (ignoring the data point at $B = 0.462$ T), resulting in $\alpha = 137737$ Pa.T ⁻²	224
9-5	Idealization of B-field which activates the magnetorheological fluid. The field is constant above the magnet ($R/R_m < 1$), then decays by the power-law r^{-3}	229
9-6	Newtonian oil adhesive performance, measured force as a function of apparent gap height. The Stefan adhesion model (dashed lines) is predictive for sufficiently small loads when system compliance is negligible, and sufficiently small values of $h(t)/R(t)$ such that the lubrication approximation holds. Here $D_0 = 49$ mm and $\eta = 9.281$ Pa.s for all tests. \dot{h} is given in the key. (a) $h_0 = 1.0$ mm, (b) $h_0 = 0.5$ mm.	233
9-7	Adhesive performance of the passive yield stress fluid, Carbopol 2wt%.	235
9-8	Experimentally measured adhesive performance of the “off state” MR fluid. Various separation speeds are examined for the same initial diameter $D_0 = 49$ mm and initial height $h_0 = 0.4$ mm. Here the dashed line is the prediction of the perfect plastic yield stress adhesion model with $\sigma_y = 9.12$ Pa, corresponding to the experimentally measured shear stress at the characteristic shear rate $\dot{\gamma} = 2\dot{h}R_0/h_0^2 = 3.06$ s ⁻¹ . Top plate is native aluminum surface.	236
9-9	Experimentally measured adhesive performance of the “off state” MR fluid. Various initial diameters D_0 examined for the same separation speed $\dot{h} = 10\mu\text{m/s}$ and initial height $h_0 = 0.5$ mm. Top plate covered with P2000 grit sandpaper. For reference $D_m = 12.7$ mm, but no magnet was used for these ambient tests.	237
9-10	Initial static force measurement, for data set shown in Fig. 9-9. Top plate covered with P2000 grit sandpaper. For reference $D_m = 12.7$ mm, but no magnet was used for these ambient tests.	237

9-11	Experimentally measured adhesive performance for a moderately activated MR fluid (Alnico 8 disc magnet), $B_{face} = 0.077$ T on face of magnet, but just above bottom plastic surface $B_0 = 0.061$ T. Various initial diameters D_0 examined for the same separation speed $\dot{h} = 10\mu\text{m/s}$ and initial height $h_0 = 0.5$ mm. The top plate is covered with P2000 grit sandpaper, $D_m = 12.7$ mm.	239
9-12	Experimentally measured adhesive performance for a strongly activated MR fluid (Neodymium disc magnet), $B_{face} = 0.389$ T on face of magnet, but just above bottom plastic surface $B_0 = 0.296$ T. Various initial diameters D_0 examined for the same separation speed $\dot{h} = 10\mu\text{m/s}$ and initial height $h_0 = 0.5$ mm. The top plate is covered with P2000 grit sandpaper, $D_m = 12.7$ mm. (a) Log-Log plot, (b) Linear-Linear plot of same data, which highlights the iterative sawtooth failure leading up to the peak force (for $R/R_m = 2.81, 3.97$).	240
9-13	Experimentally measured peak adhesive force (open symbols) at moderate magnetic field $B_0 = 0.61$ T, for various initial geometries h_0 and (R_0/R_m). The theoretical predictions of the current model are given by the lines (see Section 9.3). No fitting parameters are used.	242
9-14	Experimentally measured peak adhesive force (open symbols) at high magnetic field $B_0 > 0.14$ T, for various initial geometries h_0 and (R_0/R_m). The theoretical predictions of the current model are given by the lines (see Section 9.3). No fitting parameters are used. The experimentally measured adhesive strength is systematically lower than predicted by theory for these field strengths.	243
9-15	Remnant fluid patterns after adhesive failure, for various parameter values B_0 and R_0/R_m . Images shown of the surface containing the permanent magnet. Opposing top surfaces are not shown, which exhibit “clean” failure for $R_0/R_m \leq 1.5$ and remnant fluid rings for $R_0/R_m \geq 2.8$. The “flower” instability is observed for large R_0/R_m and moderate magnetic fields.	244

9-16	Demonstration of using magnetic fields for reversible adhesion to non-magnetic substrates, enabled by a viscoplastic magnetorheological fluid. Surfaces shown are aluminum, plastic, wood, ceramic tile, and glass. The suspended mass, $m = 112$ g, is a switchable permanent magnet configuration which creates a magnetic field strength on the order of $B = 0.16$ T over an area of approximately $A \sim 230$ mm ² . The holding stress is therefore at least $mg/A \sim 4.8$ kPa.	245
A-1	Chebyshev polynomials of the first kind; plots of the first few odd polynomials.	252
C-1	Non-interpolated vs. interpolated fingerprints of viscoelastic parameters.	276
C-2	Additional quantitative LAOS analysis of the xanthan gum. (a,b,c) Elastic moduli G'_1 , G'_M and G'_L respectively. (d,e) higher harmonic Chebyshev coefficients, e_3/e_1 and e_5/e_1 , respectively. Contour lines shown at ± 0.01 in (d,e).	277
C-3	Additional quantitative LAOS analysis of the xanthan gum (cf. Figures 7-7-7-8). (a,b,c) Elastic moduli η'_1 , η'_M and η'_L respectively. (d,e) higher harmonic Chebyshev coefficients, v_3/v_1 and v_5/v_1 , respectively. Contour lines shown at ± 0.01 in (d,e).	278
C-4	Smoothed Lissajous curves for the drilling fluid. LAOS test strain-sweep at constant frequency $\omega = 0.475$ rad.s ⁻¹ , increasing strain amplitude γ_0 from bottom row. (left column) Elastic perspective, 2D projection onto stress vs. strain axes; (middle column) 3D view with strain, strain-rate, and stress as the coordinate system; (right column) Viscous perspective, 2D projection onto stress vs. strain-rate axes. . .	279

C-5	Smoothed Lissajous curves for the drilling fluid. LAOS test strain-sweep at constant frequency $\omega = 4.75 \text{ rad.s}^{-1}$, increasing strain amplitude γ_0 from bottom row. (left column) Elastic perspective, 2D projection onto stress vs. strain axes; (middle column) 3D view with strain, strain-rate, and stress as the coordinate system; (right column) Viscous perspective, 2D projection onto stress vs. strain-rate axes.	280
C-6	Additional quantitative LAOS analysis of the drilling fluid (cf. Figures 7-9 and 7-10). (a,b,c) Elastic moduli G'_1 , G'_M and G'_L respectively. (d,e) higher harmonic Chebyshev coefficients, e_3/e_1 and e_5/e_1 , respectively. Contour lines shown at ± 0.01 in (d,e).	281
C-7	Additional quantitative LAOS analysis of the drilling fluid (cf. Figures 7-9 and 7-10). (a,b,c) Elastic moduli η'_1 , η'_M and η'_L respectively. (d,e) higher harmonic Chebyshev coefficients, v_3/v_1 and v_5/v_1 , respectively.	282
E-1	Newtonian oil rheological characterization.	290
E-2	Magnetic field analysis for the Neodymium magnet, $R_m = 6.35 \text{ mm}$, $L_m = 9.52 \text{ mm}$	291
E-3	Magnetic properties of the oil-based magnetorheological fluid MRF 132-DG, as given by the LORD Corporation.	291
E-4	Magnetic field analysis for the Neodymium magnet, $R_m = 6.35 \text{ mm}$, $L_m = 9.52 \text{ mm}$, including the layer of magnetorheological fluid with thickness $h = 0.5 \text{ mm}$ and various radii ($R = 2, 5, 10, 20 \text{ mm}$).	292
E-5	Magnetic field profile for the Neodymium magnet, $R_m = 6.35 \text{ mm}$, $L_m = 9.52 \text{ mm}$, including the layer of magnetorheological fluid at various radii ($R = 2, 5, 10, 20 \text{ mm}$). Localized spikes in the magnetic field strength occur near the edge of the fluid, but overall the profile appears flat above the magnet ($r < R_m = 6.35 \text{ mm}$) and decays as a cubic power law beyond the edge of the magnet ($r > R_m$).	293

E-6 Magnetic field profile for an Alnico 9 magnet, $R_m = 6.35$ mm, $L_m = 6.35$ mm, including the layer of magnetorheological fluid at various radii ($R = 2, 5, 10, 20$ mm). Localized spikes in the magnetic field strength occur near the edge of the fluid. The profile is approximately constant above the magnet ($r < R_m = 6.35$ mm), although a rise in magnetic field is observed near $r = R_m$. The field decays as a cubic power law beyond the edge of the magnet ($r > R_m$). 294

List of Tables

1.1	Creep ringing solutions for a Kelvin-Voigt model (viscoelastic solid) coupled with an inertial mass.	51
1.2	Creep ringing solutions for a Jeffreys model (viscoelastic fluid) coupled with an inertial mass.	52
1.3	Viscoelastic moduli determined from inertio-elastic creep ringing shown in Figure 1-6 using three different methods: the approximate relation using frequency and logarithmic decrement, and fitting two assumed constitutive models: Kelvin-Voigt and Jeffreys.	55
2.1	Material measures and nomenclature for characterizing nonlinear viscoelasticity with imposed oscillatory shear strain.	77
8.1	Summary of rheological properties of two simulants with similar apparent yield stresses compared with native gastropod pedal mucus. Although the concentrations and microscopic structure are different, fluids with similar yield stresses are compared since the macroscopic rheological property of a yield stress is the primary requirement for inclined adhesive locomotion, c.f. Eq. 8.1.	216
9.1	Various fluid adhesion mechanisms.	228
D.1	Details of personal data from Figure 8-3	284
D.2	Details of polymeric gels from Figure 8-3	285
D.3	Details of particulate gels from Figure 8-3	286
D.4	Details of emulsions, wet foams, and composites from Figure 8-3	287

Chapter 1

Introduction and background

A material subjected to mechanical loading may respond by storing energy (elastic deformation), dissipating energy (viscous deformation), or a combination of the two (viscoelastic deformation). Aspiring students are typically introduced to the mechanics of materials by considering either purely elastic solids or purely viscous fluids. Complete courses and textbooks focus on either of these two limits, and engineering departments subdivide along the lines of solid mechanics and fluid mechanics. Viscoelastic materials are currently treated as an advanced topic but play a central role in many systems, especially biological materials (biofluids, cells, and tissues), field-responsive “smart” materials, processing of structured materials, oil drilling operations, and soft condensed matter in general. Rheologically complex materials are not simply present in many circumstances, but also provide novel functionality due to nonlinear viscoelastic properties. This is the case for both biological and engineered systems. Figure 1-1 shows several examples in which nonlinear viscoelastic material responses are relevant.

Biomaterials are inherently structured, hierarchical, and complex, often exhibiting nonlinear mechanical properties. Physiological conditions commonly produce mechanical loading which evokes a nonlinear rheological response, and in some instances this is essential for proper biological functioning. Terrestrial gastropods depend on the dramatic viscous shear-thinning of pedal mucus for their locomotion[3] (Figure 1-1a). As another example, the strain-stiffening of arterial walls enables stability to

Examples of nonlinear viscoelastic materials

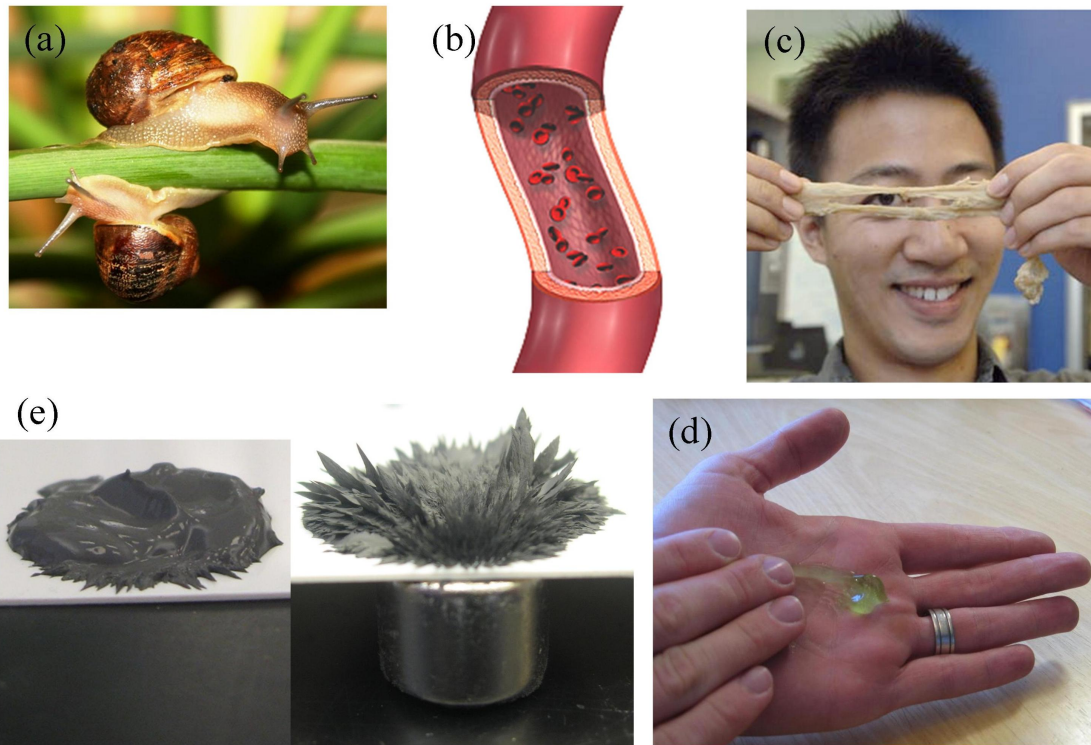


Figure 1-1: Several examples in which nonlinear viscoelastic material behavior is relevant, ranging from biological to engineered systems. (a) the adhesive locomotion of snails (see Chapter 8), (b) biomaterials and biofluids such as artery walls, blood, and cells (photo from N.I.H. Medical Encyclopedia), (c) bread dough processing (photo of Dr. Shen Kuan (Trevor) Ng by Donna Coveney), (d) personal care products such as hand lotions, (e) magnetorheological fluids (see Chapter 9).

inflation over a range of pressures[4] (Figure 1-1b).

Engineered systems and processing operations also require an understanding of nonlinear viscoelastic properties. The processing of polymers, emulsions, suspensions, and other structured materials (e.g. bread dough[5], Figure 1-1c) typically involves large deformations and nonlinear rheological responses. Some applications currently use nonlinear rheology to their advantage, for example shear-thickening fluids are used in mechanical clutches, and yield stress fluids are ubiquitous among lotions and foodstuffs (Figure 1-1d). Field-activated “smart” fluids, such as magnetorheological

fluids (Figure 1-1e) are commercially used for actively-tuned dampers, and in this thesis are used for tunable adhesion to non-magnetic substrates (Chapter 9).

The significance of nonlinear viscoelasticity is becoming increasingly apparent. However, it is less clear how to describe such complex materials most appropriately. Standard methods for characterizing nonlinear viscoelasticity are mathematically robust but lack a physical interpretation and have proven to be insufficient descriptors, especially for biological materials[6, 7]. The goal of this thesis is to transcend the limitations of current characterization methods as well as demonstrate new applications of nonlinear viscoelastic materials, including reversible adhesion and snail-like wall climbing.

1.1 Scope of thesis

Part one of this thesis describes new rheometric techniques and methods (Chapters 2-3). In particular, it introduces a complete, low-dimensional language and framework (or *ontology*) for characterizing nonlinear viscoelasticity using large amplitude oscillatory shear (LAOS) deformation. LAOS quantifies the progressive transition from linear to nonlinear rheological behavior in the 2D parameter space of deformation amplitude and frequency, known as a Pipkin space. The term rheological fingerprint is used here to describe the 2D (frequency, amplitude) mapping of viscoelastic properties. The new framework avoids the ambiguities of current state-of-the art techniques, such as Fourier-Transform rheology which hitherto has provided only a mathematical description of nonlinear viscoelastic responses. This thesis proposes physically meaningful material measures and clearly defined language such as strain-stiffening/softening and shear-thickening/thinning, which can be used in conjunction with graphical representations of response curves with strain, strain-rate, and stress as the coordinate axes (Lissajous-Bowditch curves). The new ontology is general enough to be applied to any viscoelastic material, ranging from purely elastic to purely viscous, and any complex response in-between. The framework has been packaged into a distributable data analysis program (MITlaos) to widen its use in both academic

and industrial settings.

Part two (Chapters 4-7) examines the nonlinear rheological response of various soft materials and constitutive models. The new framework is illustrated by examining prototypical nonlinear constitutive models such as the Giesekus model, the pseudoplastic Carreau model, and the elastoplastic Bingham model. Various soft materials are tested experimentally, including pedal mucus gel from terrestrial gastropods, a wormlike micelle solution, ultrasoft hagfish slime, and an oilfield drilling fluid. Rich nonlinear viscoelastic responses are revealed and meaningfully described using the new ontology. Extensions of the framework introduced in Chapter 3 are also discussed.

Part three (Chapters 8-9) describes the use of nonlinear rheological behavior to enable unique functionality, specifically for bioinspired snail-like locomotion (Chapter 8) and reversible adhesion using magnetorheological fluids (Chapter 9). Gastropods (such as snails and slugs) crawl using adhesive locomotion, a technique which exploits the nonlinear mechanical properties of excreted pedal mucus to enable their traversal of inclined and inverted surfaces. Yield stress fluids are examined here to enable the bioinspired adhesive locomotion of a self-contained mechanical device (Robosnail, developed by Brian Chan, Ph.D. '09). Field-responsive fluids are analyzed in the context of providing fast-switching reversible adhesion for use with adhesive locomotion devices and shape-changing soft robots. The adhesive performance of a field-responsive magnetorheological fluid is examined with models and experiments.

Interest in soft materials is increasing across many disciplines. The contributions presented here provide the means to a better understanding of biological and engineered systems which involve complex viscoelastic materials.

1.2 Rheological characterization techniques

The mechanical response of a material may be correlated with either deformation (elastic properties) or the rate of deformation (viscous properties). For a purely elastic material, the stress response is only a function of the imposed strain. To describe

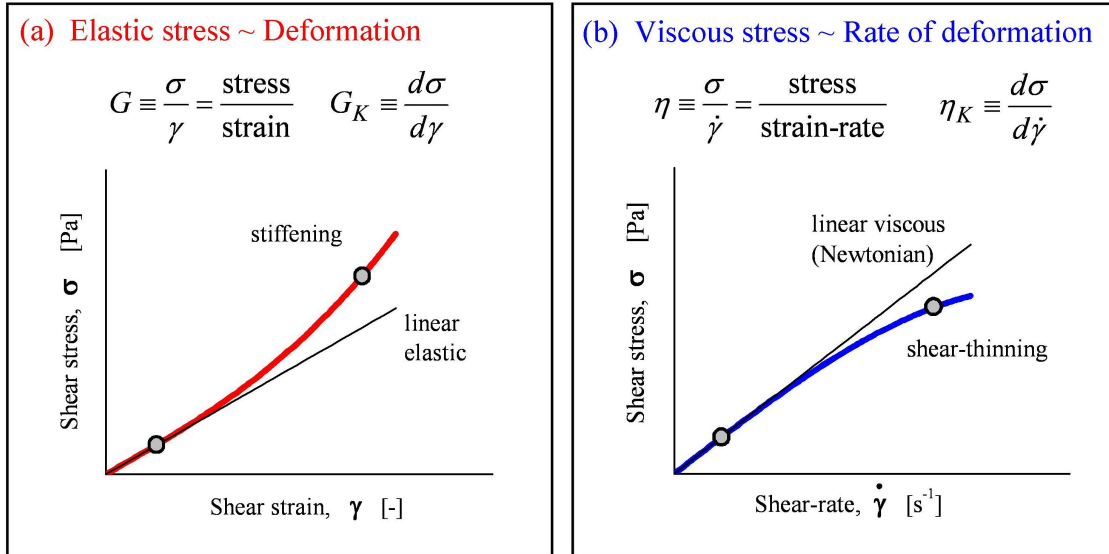


Figure 1-2: Simple shear characterization of (a) purely elastic material response, and (b) purely viscous material response.

the stress-strain relationship of a material, one may start by imposing a simple shear strain and measuring the resulting shear stress (Figure 1-2a). An intrinsic material property, the shear modulus, is then determined from $G = \sigma/\gamma$. For a linear material, G is constant independent of the amplitude of deformation. For a nonlinear response G is still defined but depends on the amplitude of deformation, e.g. $G = G(\gamma)$. It is sometimes convenient to describe the response in terms of a tangent modulus, G_K , which is equivalent to the chord modulus G in the linear regime but diverges from G for a nonlinear elastic response.

Any purely viscous material can be described by imposing a constant *rate* of simple shear deformation and measuring the resulting shear stress (Figure 1-2b). The resistance to flow is then described by the intrinsic material property $\eta = \sigma/\dot{\gamma}$. A material with a nonlinear viscosity, e.g. $\eta(\dot{\gamma})$, can still be described by this intrinsic material measure which represents resistance to flow. A tangent viscosity can also be defined for such a response, $\eta_K = d\sigma/d\dot{\gamma}$.

When a material is viscoelastic its stress response is a function of both strain *and* strain-rate, in which the material may have partial memory and exhibit a response which depends on the entire history of its deformation. Numerous testing protocols

are available to a rheologist for probing such material behavior which depends on the timescale of deformation.

Available rheometric protocols include small amplitude oscillatory shear, stress growth upon inception of steady shear flow, stress relaxation after a sudden shearing displacement, strain response to a sudden step in stress (a.k.a. a creep test), and constrained recoil after steady shear flow (a.k.a. creep recovery). The material measures associated with such tests are described in detail in the textbook *Dynamics of Polymeric Liquids*, vol. 1 [8]. In the linear viscoelastic regime the viscoelastic material functions are inter-related.

A nonlinear viscoelastic response is one for which the intrinsic material measures depend not only on the timescale of deformation, but also on the amplitude of deformation. For a nonlinear viscoelastic response, material measures cannot always be inter-related from the various test protocols. Furthermore, certain test protocols cannot systematically explore the full domain of timescale and amplitude dependence of the material properties, as discussed in the following section.

This thesis is primarily concerned with addressing the current limitations to characterization of nonlinear *shear* properties. Extensional flow properties are also relevant to many processing or use conditions. A short discussion (Section 5.1) addresses the modification of theory to apply to Large Amplitude Oscillatory Extension (LAOE), but extensional flow properties in general are beyond the scope of this work. As such, shear rheometry techniques are the focus of the following sections.

1.2.1 Non-oscillatory techniques

Test protocols other than oscillatory deformation can be used to examine nonlinear rheological behavior in shear. For example, step-strain tests or step-rate tests can examine nonlinear material responses, but neither test on its own simply reduces to both linear viscoelasticity and steady flow for all materials. Thixotropic loop tests can also examine time-dependent nonlinearities in the viscous response, e.g. by ramping the shear-rate up to a particular value over a specified time, and subsequently ramping shear-rate back down. Time dependent viscous properties are indicated by hysteresis

(i.e. loops) in the resulting curves of $\sigma(\dot{\gamma}, t)$, but the response to linear ramps of shear-rate cannot be used to connect with linear viscoelastic characterization.

1.2.2 Oscillatory shear deformation

Viscous and elastic mechanical properties can be simultaneously probed by subjecting a material sample to oscillatory deformation. Oscillatory techniques allow for the nonlinear viscoelastic response to be systematically explored and related to steady flow and linear viscoelasticity within the two-dimensional experimental space $\{\omega, \gamma_0\}$. Additionally, oscillatory shear does not involve any sudden jumps in speed or position and it is therefore a relatively easy flow to generate[9].

For shear deformation, one requires an input shear strain of the form $\gamma(t) = \gamma_0 \sin \omega t$, where γ_0 is the strain amplitude and ω is the frequency of deformation. This oscillatory shear strain consequently imposes an oscillatory strain-rate $\dot{\gamma}(t) = \dot{\gamma}_0 \cos \omega t$, where $\dot{\gamma}_0$ is the amplitude of the strain-rate. The stress resulting from this deformation will also be oscillatory, and will have a component in phase with the strain (i.e. elastic stress, $\sigma' = f'(\gamma)$) and a component in phase with the strain-rate (i.e. viscous stress, $\sigma'' = f''(\dot{\gamma})$). Note that the inputs of strain and strain-rate are exactly 90° out of phase (i.e. phase quadrature), which allows for the decomposition of the elastic and viscous stresses since elastic stress should only be a function of strain (e.g. $\sigma \sim G\gamma$ where G is the shear modulus) and viscous stress should only be a function of strain-rate (e.g. $\sigma \sim \eta\dot{\gamma}$ where η is viscosity). In the linear viscoelastic regime, the stress response is simply represented by

$$\sigma(t) = \gamma_0 (G' \sin(\omega t) + G'' \cos(\omega t)) \quad (1.1)$$

where G' is the elastic modulus and G'' is the viscous modulus[10].

This oscillatory test protocol involves only two input parameters, e.g. frequency and strain amplitude $\{\omega, \gamma_0\}$. These parameters can be mapped in a two-dimensional plane known as a Pipkin space, named after A.C. (Jack) Pipkin [1], drawn in Figure 1-3. Three boundaries of this 2D space are related to limits of viscoelastic materials

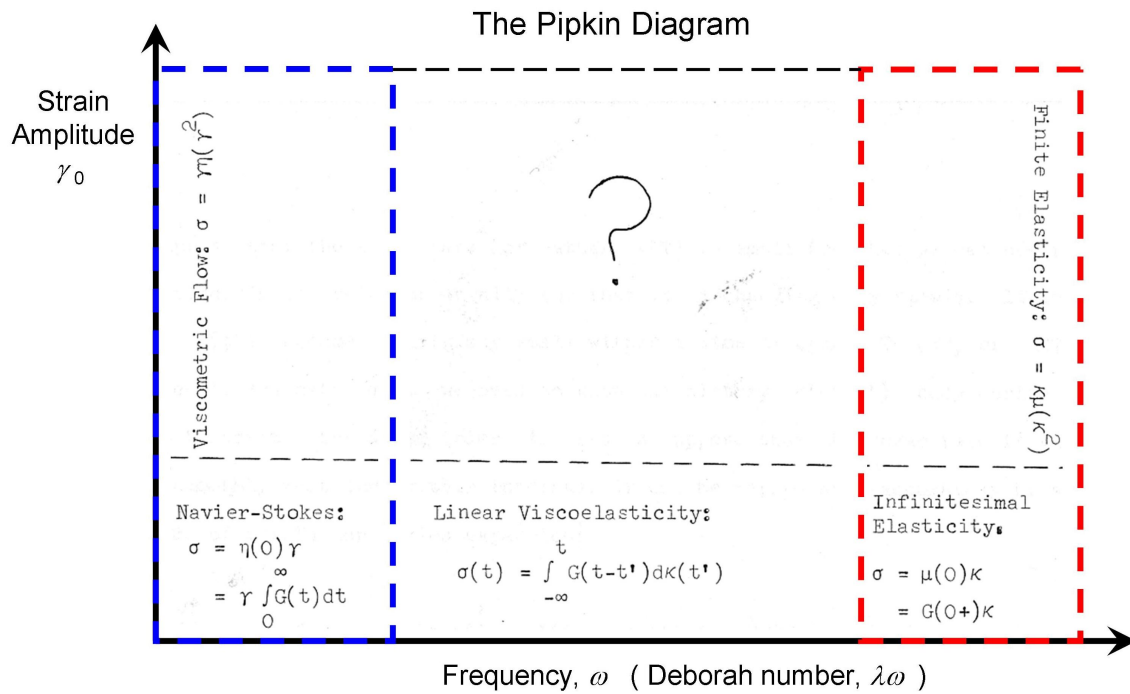


Figure 1-3: Schematic map of the input parameters for oscillatory shear rheometry, known as a Pipkin diagram (adapted from A. C. Pipkin[1]). For viscoelastic fluids, the limit of low frequency corresponds to approximately viscous behavior, whereas high frequency corresponds to approximately elastic behavior. Linear viscoelastic responses are expected at sufficiently small values of strain amplitude γ_0 . A. C. Pipkin drew a question mark in the region of intermediate frequency and large amplitude, the deformation regime in which many materials are processed and used.

responses. The first limit is that of vanishing strain-amplitude, $\gamma_0 \rightarrow 0$, which is the regime of linear viscoelasticity in which material properties are only a function of the timescale (frequency) of loading. The next limit is that of vanishing frequency, $\omega \rightarrow 0$, in which case the response of a viscoelastic liquid is quasistatic and therefore representative of a steady flow test with gradually changing shear-rate. The final boundary is that of high frequency $\omega \rightarrow \infty$, for which case a viscoelastic liquid will approach a purely elastic response. It is the middle region, away from these limiting cases, which is often the most relevant for processing and use of viscoelastic materials (i.e. the nonlinear viscoelastic region). It has been difficult to systematically describe material responses in this regime, which motivated A.C. Pipkin to include a large question mark in this region. It is this region which is of primary interest for this

thesis.

The nonlinear viscoelastic regime can be approached by systematically increasing the strain amplitude γ_0 . This results in a so-called “large amplitude oscillatory shear” (LAOS) test. Early LAOS research was initiated in 1965 by Harris[11], 1966 by Philippoff[12], and 1970 by Onogi et al.[13]. These researchers examined the nonlinear material response as the strain amplitude was increased. Such nonlinearity is exhibited by viscoelastic coefficients which depend on strain amplitude γ_0 and a non-sinusoidal stress response. For a nonlinear viscoelastic response, the stress response is more complicated and the viscoelastic moduli, G' and G'' , are no longer uniquely defined. Meaningful quantitative measures have been difficult to identify, and attempts at quantifying LAOS results tend to fall into two categories: analysis of the time-domain response $\sigma(\omega t)$ or alternatively, analysis of parametric response curves of stress vs. strain or stress vs. strain-rate (i.e. stress as a function of the orthogonal mechanical inputs).

The time-dependent oscillatory waveform $\sigma(\omega t)$ is historically the most common “perspective” used for quantitative LAOS analysis. An adequate mathematical representation for a time-dependent oscillatory stress response is a Fourier series, and the term Fourier-transform rheology (or FT-rheology)[9, 14, 15] refers to the practice of representing the periodic oscillatory stress response as

$$\sigma(t; \omega, \gamma_0) = \gamma_0 \sum_n \{G'_n(\omega, \gamma_0) \sin n\omega t + G''_n(\omega, \gamma_0) \cos n\omega t\}. \quad (1.2)$$

This FT framework is mathematically robust and reduces to the linear viscoelastic framework in the limit of small strains. However, it suffers from two drawbacks. First, although FT rheology is a very sensitive indicator of nonlinearity, as quantified by the Total Harmonic Distortion (T.H.D.) (e.g. [16]) or the normalized intensity of the 3rd harmonic (e.g. [17]), the FT framework does not result in a clear physical interpretation of the higher-order coefficients. Second, the linear viscoelastic moduli “ G' ” and “ G'' ” are not uniquely defined once the material response becomes nonlinear[18], since a nonlinear stress response is not a single-harmonic sinusoid. The

first-harmonic moduli G'_1 and G''_1 are often used as viscoelastic moduli, e.g. they are often the output of commercial rheometers. These first-harmonic measures have been used as a means to classify LAOS responses[19], and have been sufficient for describing some types of nonlinear behavior, for example using the idea of strain-rate frequency superposition[20, 21]. However, the use of first-harmonic moduli is an arbitrary choice (the meaning of this choice is outlined in Section 2.2) and can fail to capture the rich nonlinearities that are apparent in the raw data signal. Another method of using the time-series stress signal for LAOS analysis is a recently proposed decomposition into characteristic response functions[22, 23] which uses sets of sine, square, and triangular waves to describe a prototypical nonlinear response. These selected waveforms may be thought of as a set of “basis functions” used to represent a superposition of different physical phenomena. Although this provides a very useful step toward a physical interpretation, these basis functions are not mutually orthogonal, in contrast to the harmonic series that form the basis of FT-rheology. They therefore blur measurement of the linear viscoelastic response and qualitative interpretations of the progressive onset of nonlinearity. Qualitative interpretations of the non-sinusoidal shape of $\sigma(\omega t)$ has also been explored[24], however it is difficult to find physically meaningful interpretations in the time-domain.

The second “perspective” of LAOS analysis (and the one used in this thesis to provide physically meaningful parameters) is based on parametric response curves of stress vs. strain or strain-rate. These parametric plots are commonly called Lissajous curves, and are frequently used to represent the raw test data obtained from LAOS (e.g. Philippoff[12]). As a historical note, such curves are more accurately termed Lissajous-Bowditch curves, as orbital trajectories bearing J. A. Lissajous’ name were studied by N. Bowditch in 1815, before J. A. Lissajous was born and predating Lissajous’ treatment in 1857 by more than forty years[25, 26]. There have been some attempts to quantitatively analyze the LAOS response from this perspective of parametric response curves of stress as a function of the orthogonal mechanical inputs of strain and strain-rate. Tee and Dealy[27] offered three measures for quantifying viscous Lissajous-Bowditch curves of stress vs. strain-rate. Their material function

which quantified the non-elliptical shape of a single curve was useful for indicating nonlinearity but offers no physical interpretation. More recently, the so-called geometrical interpretation (also referred to as stress decomposition) was introduced by Cho et al. [28]. For a single harmonic sinusoidal strain input, the geometrical interpretation decomposes the generic nonlinear stress response into a superposition of “elastic” and “viscous” contributions using symmetry arguments (further details are provided in Section 2.2). Although this decomposition is unique, the resulting material parameters associated with the decomposition are not unique due to the non-orthogonality of the underlying basis functions, as outlined in Section 2.2.

Physical interpretation of the multitude of different material nonlinearities observed in LAOS tests is difficult, and widespread adoption of the technique has been hindered because an appropriate framework does not yet exist. It is therefore desirable to develop a complete, low-dimensional framework for quantifying nonlinear viscoelasticity which avoids these ambiguities. Chapter 2 introduces a framework to overcome the current limitations of LAOS interpretation. This framework includes a descriptive language and set of unambiguous material measures for quantifying the nonlinear viscoelastic response of soft materials using Large Amplitude Oscillatory Shear (LAOS). The framework gives meaning to some of the past attempts listed above, and inter-relations are given between various LAOS quantifiers.

In addition to LAOS, other experimental protocols exist for measuring nonlinear oscillatory rheology. The most common of these techniques is to measure a differential modulus[6, 29, 30] from a small amplitude oscillatory shear deformation that is superposed upon a fixed bias strain or stress. This protocol is quite useful for materials dominated by elasticity, but is less robust for materials which relax and flow under the constant imposed bias strain (or stress). Although the differential modulus protocol cannot be applied readily to viscoelastic fluids in general, it has been useful to describe some of the results in this thesis (e.g. hagfish slime, Chapter 6). It has recently been shown that the technique of “free oscillations” (a.k.a. creep ringing), which has traditionally been used to measure linear viscoelastic moduli, can also be used to characterize the nonlinear differential moduli[30]. A review of the general use

of inertio-elastic ringing (“free oscillations”) is provided in the following Section.

1.2.3 Inertio-elastic ringing (“free oscillation”)

This section was originally published as a review article in the *Rheology Bulletin*[31]. In addition to the review presented in this section, the method of inertio-elastic ringing is used in Chapter 6 to examine the rheology of hagfish slime networks.

Background

Inertial effects are ubiquitous and unavoidable in stress-controlled rheometry. Many rheologists will have seen the kind of phenomena shown in the experimental data of Figure 1-4. If the fluid is sufficiently viscoelastic, inertio-elastic “ringing” events (i.e. damped oscillations) are observed in the angular displacement measured at the start of a creep test, as a result of the coupling of instrument inertia and sample elasticity. Even if the fluid is a simple viscous Newtonian fluid one may have noticed that the initial strain response of any real creep test is always quadratic in time, rather than the simple linear response $J(t) \equiv \gamma(t)/\sigma_0 = t/\mu$ that is always taught in class. Although well-understood theoretically, effectively dealing with the consequences of inertio-elastic ringing is something with which practitioners of the coarse art of rheometry may not always be comfortable. This section is intended to remind the reader of the sources of these phenomena, and review some methods for extracting useful rheological information from the data rather than simply discarding or deleting it.

Inertial effects are often interpreted as undesirable, because inertia limits the ability to measure the theoretical creep response of an unknown test material at short times. However, effects such as inertio-elastic creep ringing can be exploited in order to rapidly estimate viscoelastic properties. Creep ringing can be deliberately exploited to slightly extend the accessible range of oscillatory measurements, and the data extracted can also be compared with the viscoelastic material properties measured in forced oscillation tests in order to check for self-consistency.

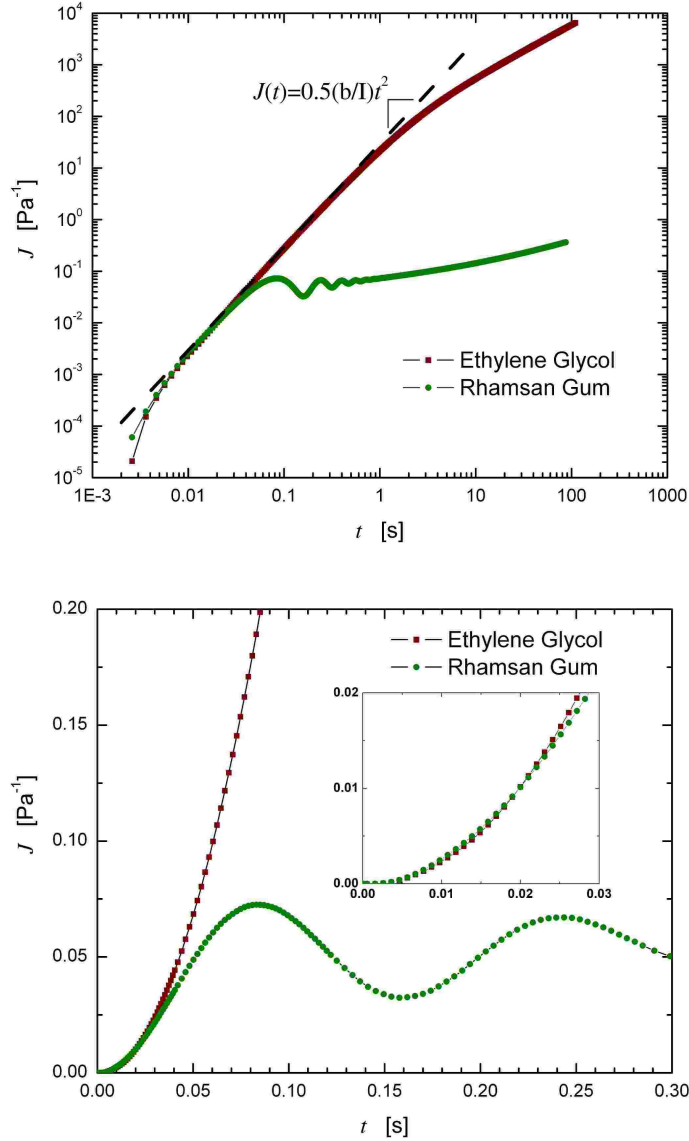


Figure 1-4: The transient creep response of a viscous Newtonian fluid and a viscoelastic polymeric gel with equivalent instrument inertia and geometry. The viscoelastic fluid exhibits underdamped oscillations but little flow at long times as shown in (a). The short time creep response, shown in (b), is identical for the two fluids and is completely determined by instrument inertia and geometry. A short time asymptotic solution proportional to t^2 is also shown by the broken line. Creep ringing is caused by the coupling of instrument inertia with the elasticity of the viscoelastic sample (Rhamsan gum (courtesy of CPKelco, San Diego, CA) at 0.75 wt% 250mM NaCl, AR-G2, $D = 6$ cm 2° cone, $T = 25^\circ\text{C}$, $\sigma_0 = 1$ Pa for each).

Review

The analysis of inertio-elastic vibrations arising in viscoelastic materials has been practiced for some time. It was apparently one of the most popular methods of (at-

tempting to) extract viscoelastic moduli, especially for low frequencies and low-loss samples, when it was difficult to measure the phase angle (see, e.g., the opening remarks by Markovitz [32]). The earliest protocols were to perform the test under *free* vibrations; that is, a predetermined force was released and the system was then allowed to return to equilibrium as it underwent damped vibrations (often referred to as 'free damped vibrations' in the literature). Some early rheometer designs incorporated torsional springs, which would exhibit free (and weakly damped) vibrations even when the sample itself had no elasticity. Instrument elasticity complicated the experimental procedure, as pointed out by Walters [33], who noted that the free vibration technique was generally only useful for extracting a viscosity coefficient. Without the torsional spring, however, the analysis and experiments are less difficult. By measuring the ringing frequency ω_* and the *logarithmic decrement* Δ associated with the ringing (to be defined in detail below), Struik [34] showed that the viscoelastic moduli can be approximated for small Δ , negligible instrument elasticity, and negligible sample inertia by the following expressions:

$$G' \approx \frac{I\omega_*^2}{b} (1 + (\Delta/2\pi)^2) \quad (1.3)$$

$$G'' \approx \frac{I\omega_*^2}{b} \left(\frac{\Delta}{\pi} \right) \quad (1.4)$$

$$\tan\delta \approx \frac{\Delta}{\pi} (1 + (\Delta/2\pi)^2)^{-1} \quad (1.5)$$

where I is the moment of inertia of the system, ω_* is the ringing frequency and Δ is the logarithmic decrement. This is defined as the natural logarithm of the ratio of two successive peaks, or more generally $\Delta = (1/n)\ln(A_1/A_{n+1})$ where A is the amplitude of the ringing above the equilibrium displacement and n is the number of cycles between peaks.

In these expressions, b is a geometry factor given by $\gamma/\sigma = b\phi/T$ that relates the raw (or measured) angular displacement ϕ and torque T to the rheological quantities of interest, i.e. strain γ and stress σ (i.e. $b = F_\gamma/F_\sigma$ where $\sigma = F_\sigma T$ and $\gamma = F_\gamma\phi$). For example the geometry factor for a cone-plate is $b_{c-p} = 2\pi R^3/(3\tan\theta)$, and for

a plate-plate, $b_{p-p} = \pi R^4/2h$. Struik also gives higher order correction terms to the approximation given above. These corrections are proportional to Δ , ω , and derivatives with respect to frequency (to access a range of frequencies, one would need to vary the instrument inertia). Struik also presents a plot of maximum relative error versus logarithmic decrement. For example, at $\Delta=1.0$ (or equivalently $\tan\delta = 0.33$ from Eqs. 1.3-1.5) the maximum relative error for the elastic modulus is 7%, and for the loss modulus 23%. These ideas are also reviewed in the treatise by Ferry [10].

Forced oscillations with precise harmonic control and measurements over many orders of magnitude in frequency are now readily provided by commercial rheometers, and therefore the free vibration technique is no longer a common method of measuring viscoelastic moduli. However, the ringing caused by the coupling of instrument inertia and sample elasticity is still part of the everyday lives of experimental rheologists. Zolzer & Eicke [35] used creep data obtained on a modern controlled stress instrument to revisit the early ideas of ringing under step stress loadings, and used the approximations developed for free vibrations to interpret their data; however, this work is not widely known or cited. Another option for obtaining estimates of viscoelastic moduli from observations of free ringing is to assume a specific rheological constitutive model for the material. The differential equation governing the evolution in the sample stress is then coupled with the differential equation of motion for the system, and the resulting time-dependent response can then be solved analytically (or numerically) and regressed to the experimental measurements in order to obtain best-fit material parameters. The resulting equation of motion is of the general form:

$$\frac{I}{b}\ddot{\gamma} = H(t)\sigma_0 - \sigma_s(t) \quad (1.6)$$

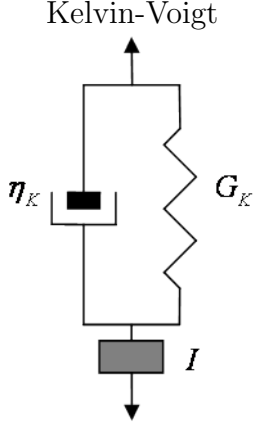
where $I = I_{\text{geometry}} + I_{\text{rheometer}}$, $H(t)$ is the Heaviside step function characterizing the imposition of the instrument stress and $\sigma_s(t)$ is the shear stress in the sample arising from deformation. It is immediately apparent that the sample stress is not a step function, $\sigma_s(t) \neq H(t)\sigma_0$, due to the finite inertia of any real rheometric instrument, although it eventually reaches the constant, desired value after the inertial

transient has decayed. The constitutive equation for sample stress is coupled with this equation of motion, and the full system of (differential) equations must be solved simultaneously. Arigo & McKinley [36] presented numerical solutions for a four-mode upper-convected Maxwell model in parallel with a solvent viscosity, along with the analytical solution for the single-mode formulation (a convected Jeffreys model). Additional rheological models were considered by Baravian & Quemada [37], including the Kelvin-Voigt and Maxwell models. Baravian & Quemada noted that creep ringing was advantageous in extending the accessible frequency range in measurements on biopolymer gels (they reported ringing at up to 75 Hz) since inertial effects limited the frequency range accessible by forced oscillations.

Illustrative examples

We turn now to some examples of creep ringing behavior. Figure 1-5 shows the creep response for three common rheological models: Newtonian, Kelvin-Voigt, and Jeffreys. For each model the ideal creep response is shown (with $I = 0$ in Eq. 1.6) alongside the actual response that arises due to a finite moment of inertia. For completeness, the analytical solutions for the Kelvin-Voigt and Jeffreys models are given in Table 1.1 and 1.2 (see e.g. [37] for detailed development of solutions). The Kelvin-Voigt model contains two parameters (a spring of modulus G_K in parallel with a dashpot η_K) and is the canonical model for a viscoelastic solid because it attains a finite strain at steady state. The Jeffreys model contains three-parameters (one spring and two dashpots), and at steady state shows a steady rate of creep as expected in a viscoelastic fluid. The three elements of the Jeffreys model can be arranged as either a Kelvin-Voigt unit in series with a dashpot, or equivalently as a Maxwell unit (i.e. a spring in series with a dashpot) in parallel with a dashpot [38]. In this work we use the former formulation because it is convenient to see how the results reduce to the Kelvin-Voigt model in the limit $\eta_2 \rightarrow \text{inf}$. Ringing is only observed in the under-damped case, corresponding to sufficient elasticity, $G_K, G_J > G_{\text{critical}}$, where G_{critical} is given in Table 1.1 and 1.2 for each model.

The envelope for determining the logarithmic decrement is also shown for the



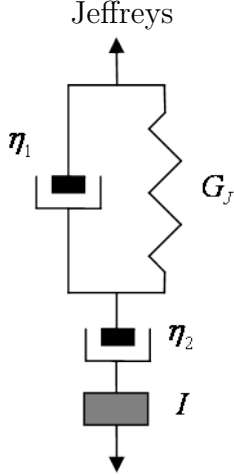
<p>For ringing, $G_K > G_{critical} = \frac{\eta_K^2 b}{4I}$</p> $\gamma(t) = \gamma_K \left\{ 1 - e^{-A_K t} \left[\cos(\omega_K t) + \frac{A_K}{\omega_K} \sin(\omega_K t) \right] \right\}$
<p>where $\gamma_K = \frac{\sigma_0}{G_K}$, $A_K = \frac{\eta_K b}{2I}$, $\omega_K = \sqrt{\frac{G_K b}{I} - A_K^2}$</p> <p>with short time response: $\gamma(t) \simeq \frac{\sigma_0}{I/b} \left[\frac{1}{2} (\delta t)^2 - \frac{1}{6} \frac{\eta}{I/b} (\delta t)^3 + \dots \right]$</p>
$G' = G_K, \quad G'' = \eta_K \omega, \quad \lambda_K = \frac{\eta_K}{G_K}$

Table 1.1: Creep ringing solutions for a Kelvin-Voigt model (viscoelastic solid) coupled with an inertial mass.

Kelvin-Voigt model in Figure 1-5(b). For an approximate viscoelastic solid creep response of the form $J(t) \approx X e^{-\frac{\Delta\omega}{2\pi} t} \sin(\omega_* t + \psi) + Y$, the logarithmic decrement Δ can be determined from the absolute value of three peaks, J_1, J_2, J_3 (as shown in Figure 1-5b) by the formula $\Delta = 2 \ln \left(\frac{J_1 - J_2}{J_3 - J_2} \right)$, which eliminates the need to know the offset bias Y . The logarithmic decrement Δ may then be used in conjunction with Eqs. 1.3,1.4 to approximate the viscoelastic moduli.

It is apparent from Figure 1-5(c) that the logarithmic decrement may be more difficult to obtain for a viscoelastic *fluid*, since an irreversible flow component is part of the response. For this case an approximate viscoelastic response is of the prototypical form $J(t) \approx X e^{-\frac{\Delta\omega}{2\pi} t} \sin(\omega_* t + \psi) + Y + Zt$. In this case, the logarithmic decrement can be determined from the absolute value of four peak points, J_1, J_2, J_3, J_4 (shown in Figure 1-5c) without knowledge of Y or Z , by the formula

$$\Delta = 2 \ln \left(\frac{J_1 - 2J_2 + J_3}{-J_2 + 2J_3 - J_4} \right). \quad (1.7)$$



<p>For ringing, $G_J > G_{critical} = A_J^2 \frac{I}{b} (1 + \eta_1/\eta_2)$</p> $\gamma(t) = \dot{\gamma}_J t - B_J + e^{-A_J t} \left[B_J \cos(\omega_J t) + \frac{A_J}{\omega_J} \left(B_J - \frac{\dot{\gamma}_J}{A_J} \right) \sin(\omega_J t) \right]$
<p>where $\dot{\gamma}_J = \frac{\sigma_0}{\eta_2}$, $\omega_J = \sqrt{\frac{G_J b}{I} \frac{\eta_2}{(\eta_1 + \eta_2)} - A_J^2}$</p> $A_J = \frac{G_J + \eta_1 \eta_2 b / I}{2(\eta_1 + \eta_2)}, \quad B_J = \frac{\sigma_0}{G_J} \frac{(\eta_1 + \eta_2)}{\eta_2} \left(\frac{2A_J I}{\eta_2 b} - 1 \right)$ <p>with short time response: $\gamma(t) \simeq \frac{\sigma_0}{I/b} \left[\frac{1}{2} (\delta t)^2 - \frac{1}{6} \frac{1}{I/b} \frac{\eta_1 \eta_2}{\eta_1 + \eta_2} (\delta t)^3 + \dots \right]$</p>
$G' = G_J \frac{(\lambda_2 \omega)^2}{1 + (\lambda_1 \omega)^2}, \quad G'' = G_J \frac{(\lambda_2 \omega) [1 + (\lambda_1^2 - \lambda_1 \lambda_2) \omega^2]}{1 + (\lambda_1 \omega)^2}$ $\lambda_1 = (\eta_1 + \eta_2) / G_J, \quad \lambda_2 = \eta_2 / G_J$

Table 1.2: Creep ringing solutions for a Jeffreys model (viscoelastic fluid) coupled with an inertial mass.

Figure 1-5(d) is a close-up of the short time response of each constitutive model presented in Figure 1-5(a) - (c). This graphically shows that the initial short time response of any model is related only to the inertia of the system and is quadratic in time. This can be readily observed from Eq. 1.6. Provided the sample being probed does not exhibit any instantaneous (or 'glassy') elastic response, then at time $t = 0^+$ the sample stress resisting the acceleration of the rheometer fixture can be ignored and the resulting second order differential equation is $(I/b)\ddot{\gamma} = \sigma_0$ which can be readily integrated to give $\gamma(t) = \frac{1}{2}(\sigma_0 b/I)t^2 + \dots$ for *any* constitutive model. As the shear strain and the shear rate build up in the material, the viscous or viscoelastic stress will retard the acceleration of the fixture. The next order correction to the short time solution is also given in Tables 1.1 and 1.2 for the Kelvin-Voigt and Jeffreys models.

It is clear from the expression above that all controlled stress rheometers undergoing a step stress loading will exhibit a quadratic response at short times. It is

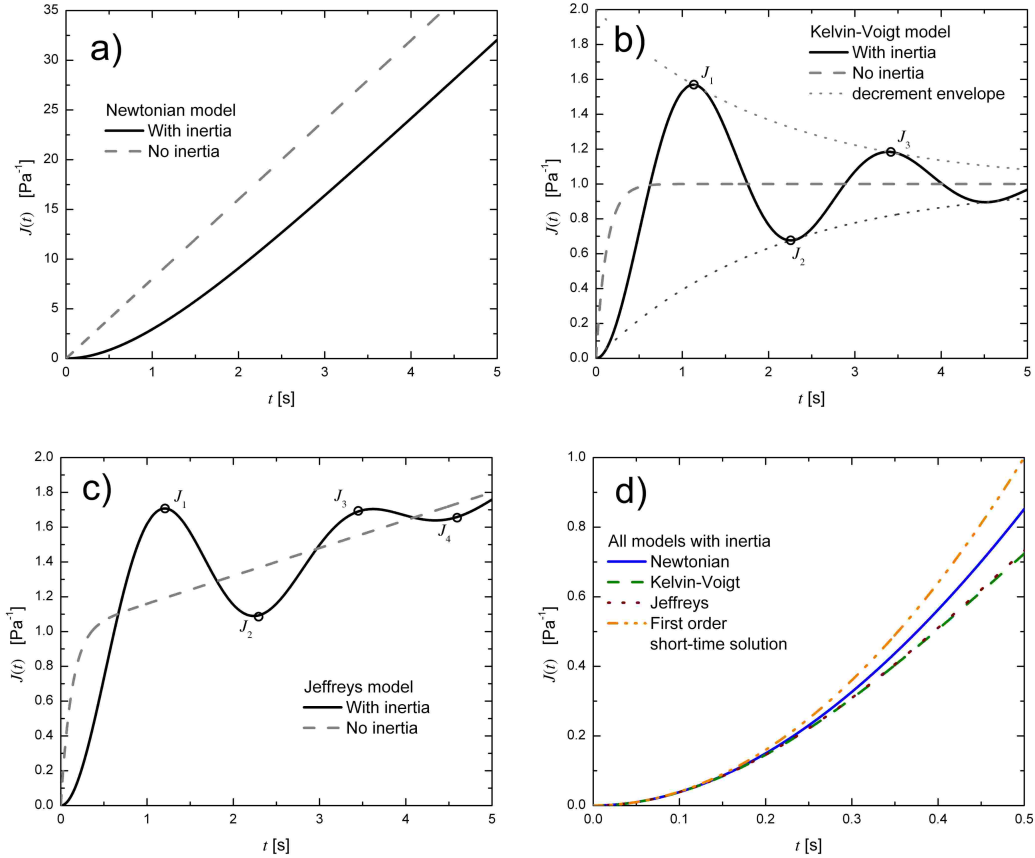


Figure 1-5: Typical data (simulated) for inertial creep responses compared to ideal non-inertial responses: a) Newtonian; b) Kelvin-Voigt viscoelastic solid, under-damped; c) Jeffreys viscoelastic fluid, under-damped; d) an enlargement of the response near the origin shows that all models have the same quadratic response at short times, which is determined purely by the instrument inertia and geometry factor.

interesting to note that the degree to which this response is actually resolved will vary with the temporal sampling rate of the data acquisition system and the minimum angular displacement (or strain) that can be resolved by the rheometer. As angular resolution and temporal sampling rates increase, inertio-elastic oscillations will become increasingly apparent in short time creep data.

As a further illustration of the creep ringing technique, Figure 1-6 shows real data from a creep test on pedal mucus (a biopolymer gel) from the terrestrial gastropod *Helix aspera* (also known as the common garden snail). This protein-polysaccharide gel exhibits an apparent yield stress on the order of 100Pa [7], but is dominated by elasticity below the yield stress. The ringing frequency is approximately $\omega_* = 2.14 \text{ rad.s}^{-1}$

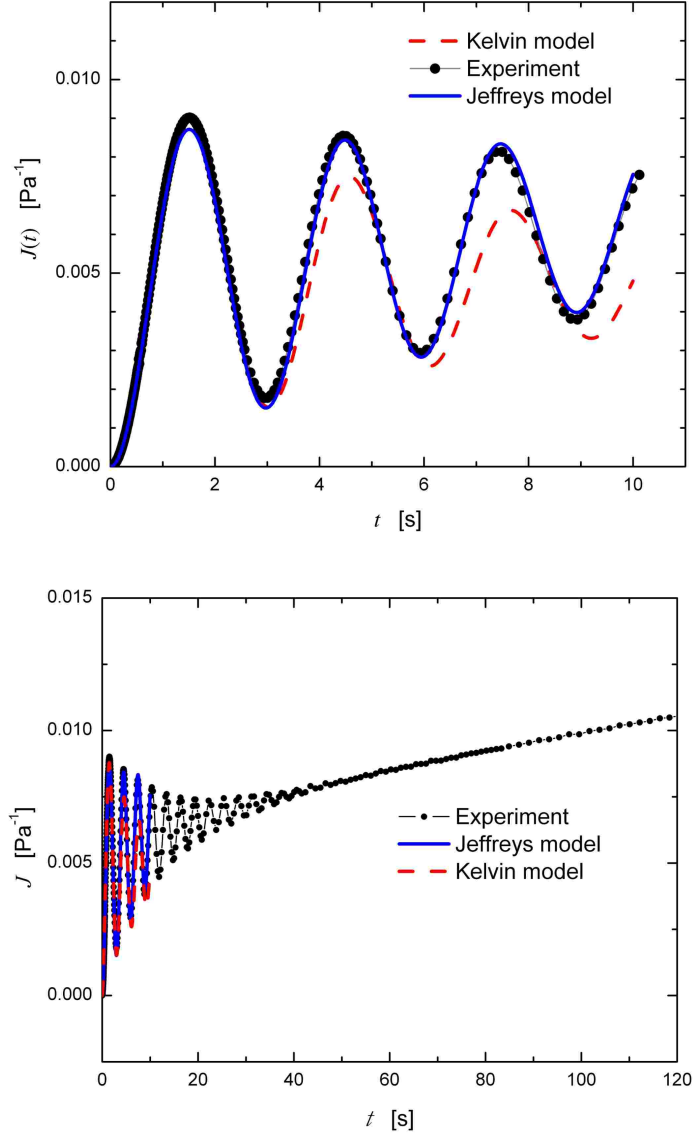


Figure 1-6: Creep test of native pedal mucus from the terrestrial gastropod *Helix aspera*; inertio-elastic ringing fit to both a Kelvin-Voigt and Jeffreys model (AR-G2, $D=0.8$ cm plate with sandpaper, $1000\mu\text{m}$ gap, $T=22^\circ\text{C}$, $\sigma_0 = 5 \text{ Pa} \ll \sigma_y$).

($f_* = 0.34$ Hz) and the slow decay in the oscillations indicates weak damping. The under-damped oscillatory response for the two-parameter Kelvin-Voigt model and three-parameter Jeffreys model (Tables 1.1 and 1.2) were fitted to the experimental data using a nonlinear fitting routine in MATLAB. Once the model parameters are determined they can be converted into values of G' and G'' (see formulae in Tables 1.1 and 1.2), and compared with the values extracted from the approximate analysis of

	ω_* [rad.s ⁻¹]	G' [Pa]	G'' [Pa]	$\tan\delta$
Approximation	2.14	231	18.2	0.08
Kelvin-Voigt	2.03	210	25.9	0.12
Jeffreys	2.11	223	17.0	0.08

Table 1.3: Viscoelastic moduli determined from inertio-elastic creep ringing shown in Figure 1-6 using three different methods: the approximate relation using frequency and logarithmic decrement, and fitting two assumed constitutive models: Kelvin-Voigt and Jeffreys.

Struik which are model-independent and use only the ringing frequency ω_* and logarithmic decrement Δ . Here the logarithmic decrement was determined from the first two cycles, using the four-point calculation (Figure 1-5(c) and Eq. 1.7) to account for the finite flow in the response. Table 1.3 shows the comparative results, using all three techniques.

The Jeffreys model achieves a satisfying fit to the data especially at short times before any finite flow effects are observed, and will therefore be used as a benchmark for comparing the results. It is interesting that the approximation, based on frequency and logarithmic decrement, does as well or better than the Kelvin-Voigt model at determining the moduli. Here the logarithmic decrement is small ($\Delta \approx 0.25 \ll 2\pi$), which satisfies the low-loss criteria for using the approximation. In addition to achieving a better fit to the data, another benefit of assuming a rheological model is the opportunity to extend the measured result from free oscillations (which are inherently limited to the single frequency, ω_*) to frequencies above and below the ringing frequency. The precision of this extrapolation certainly depends on the quality of the model fit, but at a minimum allows one to estimate the trends in frequency dependence within a small range of the ringing frequency.

Conclusions

This short section has hopefully clarified some of the key features of inertio-elastic creep oscillations that can often be discerned in the high resolution data obtained with state-of-the-art rheometers. We remind the reader that when the effects of inertia are negligible (at 'long' times $t \gg \{1/A_J, 1/A_K\}$ respectively from Tables 1.1 and 1.2),

the frequency-dependent linear viscoelastic moduli can be determined directly from the creep compliance $J(t)$ [10], although the frequency range and accuracy will still be limited by the rate of data acquisition and length of measurement. However, the presence of inertia limits the high frequency projection, since the short time response of any real creep test is dominated by inertia, and therefore the sample stress is not actually a step function, $\sigma_s \neq H(t)\sigma_0$, but instead $\sigma_s = H(t)\sigma_0 - I\ddot{\gamma}$. The creep compliance is not well defined for these short times. Of course, one way to nearly eliminate instrument inertia is to perform a step strain experiment and measure instead the relaxation modulus $G(t)$, in which case it is only the response time of the instrument and sample inertia that become the limiting factors.

As we noted earlier, one reported experimental benefit of inertio-elastic ringing is the ability to achieve higher frequencies than forced oscillations. Note, however, that the ability to resolve this frequency is important, and this depends on the rate of data acquisition of the rheometer. The ringing frequency, to first order, depends on the instrumental parameters and sample elasticity as $\omega_* \sim \sqrt{bG'/I}$. For a given material, the limiting frequency is maximized by increasing $\sqrt{b/I}$. If the inertia of the geometry is much less than the inertia of the instrument, then the choice of geometry should be made to increase b . For a cone-plate $b_{c-p} \sim R^3/\theta$, where R is the radius and θ is the cone angle, while for a plate-plate $b_{p-p} \sim R^4/h$ where h is the gap height. Thus, assuming that the total inertia is primarily from the instrument, large diameters with small gaps maximize the ringing frequency by increasing the 'stiffness' of the system. Higher ringing frequencies will also decrease the total timescale of the ringing, since higher frequencies will increase the rate of dissipation in the viscoelastic material (note also in Tables 1.1 and 1.2 that increasing b/I increases the damping rates A_K and A_J respectively). Decreasing the total ringing time will also improve the approximation of a step-sample-stress, $\sigma_s \approx H(t)\sigma_0$ (with progressively higher frequency oscillations that are dissipated increasingly rapidly and which can only be observed for short times $t < A_J, A_K$ respectively). Shifting the ringing frequency to higher values is thus useful for observing creep compliance in viscoelastic materials at shorter timescales.

When analyzing inertio-elastic ringing, the Struik approximation using frequency ω_* and logarithmic decrement Δ can be used as a very rapid manual self-consistency check to compare with forced oscillation tests. If better precision is desired, the higher order terms given by Struik could be used (which require data at multiple frequencies). Alternatively, a rheological constitutive model can be assumed a priori, and the ringing response can be fit to this model. At least one commercial software package for rheological analysis includes a routine to fit creep ringing to mechanical models such as those in Tables 1.1 and 1.2 (TA Instruments, New Castle, DE). In this particular software the user is still required to manually convert the fitted model parameters to the viscoelastic moduli $G'(\omega_*)$ and $G''(\omega_*)$. Being aware of the existence of inertio-elastic creep ringing and the quadratic short time response of any material to a step stress loading in a rheometer enables the practicing rheologist to extract useful information from data that is often obscured or ignored.

Chapter 2

New measures for characterizing nonlinear viscoelasticity with large amplitude oscillatory shear (LAOS)

2.1 Introduction

Biopolymer networks[6, 39, 40], wormlike micelles[41], colloidal gels[42], and metastable soft solids in general[21], exhibit complex nonlinear rheological responses, and as such have been of interest to experimentalists and theoreticians for many decades. The question arises of how to probe the complex viscoelastic response of such soft materials in the most appropriate way; see for example Philippoff[12]. Many of the biological and industrial processes associated with these materials cannot be described by steady shearing flow, nor by linear viscoelastic deformations constrained by small strain amplitudes. Large amplitude oscillatory shear (LAOS)[14] provides a method to quantify the progressive transition from linear to nonlinear rheological behavior as the strain amplitude γ_0 is increased at any given imposed frequency ω . The independent variables ω, γ_0 can be used to define the coordinate axes of a *Pipkin diagram*[1] which seamlessly connects steady viscometric flow (in the limit of small ω), linear viscoelasticity (in the limit of small γ_0), and nonlinear viscoelasticity. However, a

comprehensive framework does not currently exist for quantifying in a physically meaningful way the nonlinear viscoelastic response that arises from this imposed deformation protocol. In this chapter I develop a descriptive language and set of unambiguous material measures for quantifying the nonlinear viscoelastic response of soft materials, enabling the development of a unique “rheological fingerprint” of an *a priori* unknown substance.

Both the elastic and viscous characteristics of an unknown material can be examined simultaneously by imposing an oscillatory shear strain, $\gamma(t) = \gamma_0 \sin(\omega t)$, which consequently imposes an orthogonal strain-rate $\dot{\gamma}(t) = \gamma_0 \omega \cos(\omega t)$. Here ω is the imposed oscillation frequency, γ_0 is the strain amplitude, and t is time. At small strain amplitudes when the response is linear, the material is commonly characterized by the viscoelastic moduli $G'(\omega)$, $G''(\omega)$ as determined from the components of the stress in phase with $\gamma(t)$ and $\dot{\gamma}(t)$ respectively[10]. The strain amplitude γ_0 can be increased systematically to enter the nonlinear viscoelastic regime, resulting in a large amplitude oscillatory shear (LAOS) test. However, these linear viscoelastic moduli are not uniquely defined once the material response becomes nonlinear[18], since a nonlinear stress response is not a single-harmonic sinusoid. Physical interpretation of the multitude of different material nonlinearities observed in LAOS tests is difficult, and widespread adoption of the technique has been hindered because an appropriate framework does not yet exist.

The most common method of quantifying LAOS tests is Fourier transform (FT) rheology[15]. For a sinusoidal strain input $\gamma(t) = \gamma_0 \sin(\omega t)$, the stress response can be represented completely by a Fourier series[14], given in two alternate forms to emphasize either elastic or viscous scaling, respectively,

$$\sigma(t; \omega, \gamma_0) = \gamma_0 \sum_{n \text{ odd}} \{G'_n(\omega, \gamma_0) \sin n\omega t + G''_n(\omega, \gamma_0) \cos n\omega t\} \quad (2.1)$$

$$\sigma(t; \omega, \gamma_0) = \dot{\gamma}_0 \sum_{n \text{ odd}} \{\eta''_n(\omega, \gamma_0) \sin n\omega t + \eta'_n(\omega, \gamma_0) \cos n\omega t\}. \quad (2.2)$$

Only odd-harmonics are included in this representation because the stress response is

assumed to be of odd symmetry with respect to directionality of shear strain or shear-rate, i.e. the material response is unchanged if the coordinate system is reversed[8]. Even-harmonic terms can be observed in transient responses, secondary flows[43], or dynamic wall slip[44], but these conditions will not be considered here. In the linear viscoelastic regime the stress response will include only the first harmonic, $n = 1$, whereas nonlinear material responses at larger strains result in the appearance and growth of higher harmonic contributions. Although this FT framework is mathematically robust and reduces to the linear viscoelastic framework in the limit of small strains, it suffers from two drawbacks. First, although FT rheology is a very sensitive indicator of nonlinearity, as quantified by the Total Harmonic Distortion (T.H.D.) (e.g. [16]) or the normalized intensity of the 3rd harmonic (e.g. [17]), the FT framework does not result in a clear physical interpretation of the higher-order coefficients. Second, the use of the first-harmonic coefficients G'_1 and G''_1 as measures of the viscoelastic moduli in the nonlinear regime (and which are often the output of commercial rheometers) is arbitrary and often fails to capture the rich nonlinearities that are apparent in the raw data signal.

A striking example of the shortcomings of the conventional FT rheology framework, and motivation for a new approach, is provided by the nonlinear viscoelastic response of native pedal mucus gel secreted by the terrestrial slug *Limax maximus*[7]. In the present work, a series of strain-controlled oscillatory tests at a fixed frequency of $\omega = 3 \text{ rad.s}^{-1}$ is imposed and the corresponding nonlinear behavior of the physically cross-linked mucus gel is shown in Figure 2-1. The typical rheometric measures of viscoelastic moduli are shown in Figure 2-1a and appear unremarkable. By contrast Figure 2-1b shows the raw data measured by the torque transducer at each imposed frequency; the periodic stress response $\sigma(t)$ at steady state is plotted parametrically against $\gamma(t)$. These parametric plots are commonly called Lissajous curves, and are frequently used to represent the raw material test data obtained from LAOS (e.g. Philippoff[12]). Such curves are more accurately termed Lissajous-Bowditch curves, as orbital trajectories bearing J. A. Lissajous' name were studied by N. Bowditch in 1815, predating Lissajous' treatment in 1857 by more than forty years[25, 26]. A

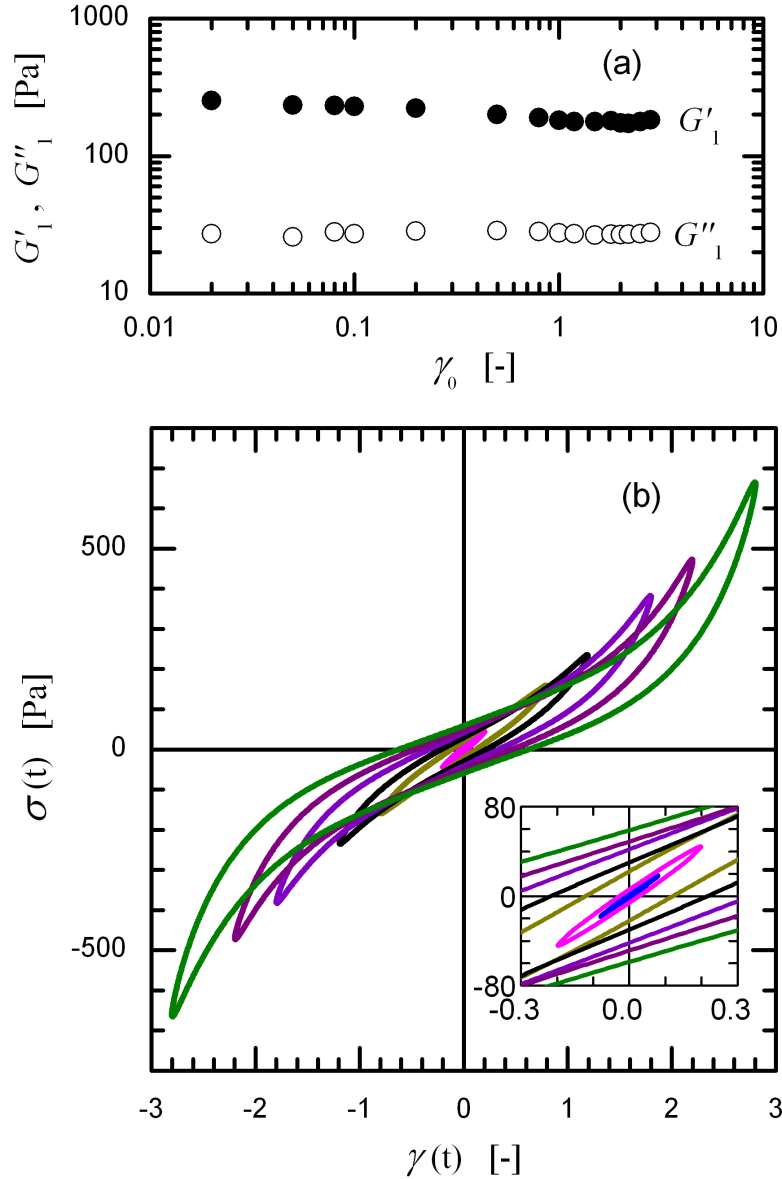


Figure 2-1: Oscillatory strain sweeps of pedal mucus from *Limax maximus* at a frequency $\omega = 3 \text{ rad.s}^{-1}$. (a) Typical rheometer output of the fluid viscoelasticity as parameterized by the first-harmonic Fourier moduli; (b) Plotting the raw data from every-other point as $\sigma(t)$ vs. $\gamma(t)$ reveals additional nonlinear characteristics that are obscured by G'_1 , G''_1 .

linear viscoelastic response appears as an ellipse, which contains two mirror planes (the major and minor axes of the ellipse). A steady nonlinear viscoelastic response loses the mirror planes and requires only that the response is periodic, $\sigma(t) = \sigma(t+T)$ where T is the period of oscillation, allowing both odd and even harmonics in the

Fourier series stress response. For the common situation of a simple fluid in which the material behaves the same in both shear directions, only odd harmonics are allowed (Eq. 2.1) and the Lissajous-Bowditch curve maintains a rotational symmetry about the origin (rotation by π radians). We refer to the curves of $\sigma(t)$ vs. $\gamma(t)$ as *elastic* Lissajous-Bowditch curves to distinguish them from the *viscous* Lissajous-Bowditch curves which represent $\sigma(t)$ as a function of the imposed shear-rate $\dot{\gamma}(t)$.

The “elastic modulus” of pedal mucus reported by a rheometer (i.e. the first harmonic elastic modulus, G'_1) decreases slightly with strain amplitude (Figure 2-1a), implying minor strain-softening. However, the raw data in the form of Lissajous-Bowditch curves (Figure 2-1b) reveal a strong nonlinear response evocative of strain-stiffening. The elastic Lissajous curves in Figure 2-1b are elliptical for small γ_0 (see inset), but become progressively distorted in the nonlinear regime. At large strains, the shear stress is greater than one would expect by projecting the center portion of the ellipse, suggesting pronounced elastic strain-stiffening at large strain amplitudes which is not captured by the first harmonic elastic modulus.

This paradoxical behavior is not unique to pedal mucus but appears to be common in soft biological materials and can be seen, for example, in data reported for a keratin filament network[45]; in both cases strain-stiffening is suggested in the elastic Lissajous-Bowditch curves even though the familiar “viscoelastic moduli” do not appear to increase as a function of imposed strain amplitude γ_0 . A quantitative measure for easily identifying and comparing this type of stiffening response does not currently exist.

In addition to FT rheology, various other methods have been proposed for quantifying nonlinear viscoelasticity in LAOS[27, 28, 22]. However, these techniques either lack physical interpretation, cannot be calculated uniquely, or do not apply generally to all viscoelastic materials. Tee and Dealy[27] offered three measures for quantifying viscous Lissajous-Bowditch curves of stress vs. strain-rate. Their material function which quantified a non-elliptical shape of a single curve was useful for indicating non-linearity but offers no physical interpretation. A recently proposed decomposition into characteristic response functions[22, 23] uses sets of sine, square, and triangu-

lar waves to describe a prototypical nonlinear response. These selected waveforms may be thought of as a set of “basis functions” used to represent a superposition of different physical phenomena. Although this provides a very useful step toward a physical interpretation, these basis functions are not mutually orthogonal, in contrast to the harmonic series that form the basis of FT-rheology. They therefore blur measurement of the linear viscoelastic response and qualitative interpretations of the progressive onset of nonlinearity. Similarly, the so-called geometrical interpretation (also referred to as stress decomposition) introduced by Cho et al. [28] suffers from non-orthogonality of the resulting material measures. For a single harmonic sinusoidal strain input, the geometrical interpretation decomposes the generic nonlinear stress response into a superposition of “elastic” and “viscous” contributions using symmetry arguments (further details are provided in Section 2.2). Although this decomposition is unique, the resulting material parameters associated with the decomposition are not unique due to the non-orthogonality of the describing basis functions, as we outline below. It is therefore desirable to develop a complete, low-dimensional framework for quantifying nonlinear viscoelasticity which avoids these ambiguities.

In this chapter I introduce a comprehensive framework for physically interpreting the deviations from a linear response to an imposed oscillatory shear deformation. This framework provides a geometric representation and a descriptive language for qualitatively familiar, but poorly defined, adjectives such as elastic stiffening/softening and viscous thickening/thinning. I also propose several new measures for reporting the first-order (linear) viscoelastic moduli in the nonlinear regime, to complement the first-order Fourier coefficients which are often insufficient to describe the material response. These additional measures all reduce to $G'(\omega)$ in the linear regime, but diverge systematically when applied to a nonlinear signal, offering additional physical insight into the underlying rheological response which would otherwise be obscured by conventional measures.

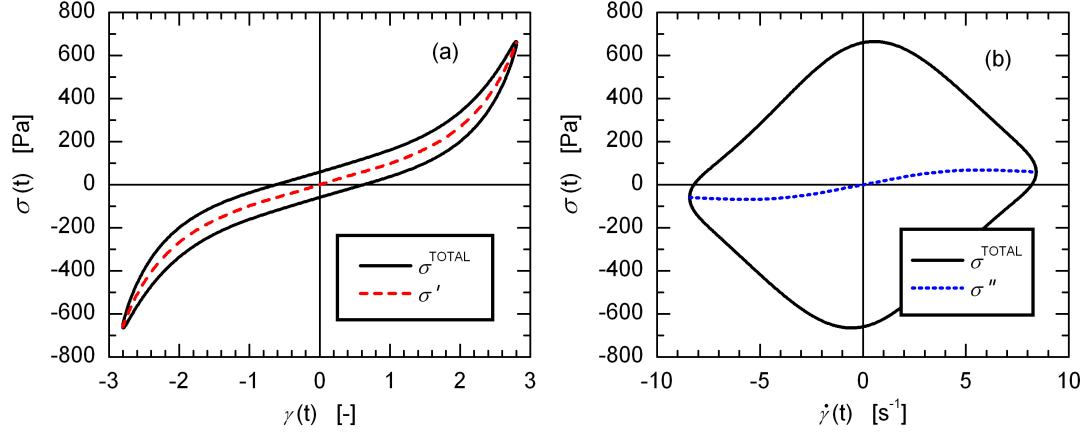


Figure 2-2: Applying the geometrical interpretation to the largest strain amplitude data point from Figure 2-1, ($\omega = 3 \text{ rad.s}^{-1}$, $\gamma_0 = 2.8$); (a) total stress and elastic stress σ' , (b) total stress and viscous stress σ'' .

2.2 Interpretation of higher harmonics using the Chebyshev polynomial representation

To interpret LAOS data in a physically meaningful way, we first extend the method of orthogonal stress decomposition[28], which uses symmetry arguments to decompose the generic nonlinear stress response into a superposition of an elastic stress $\sigma'(x)$, where $x = \gamma/\gamma_0 = \sin \omega t$, and viscous stress $\sigma''(y)$ where $y = \dot{\gamma}/\dot{\gamma}_0 = \cos \omega t$. The total oscillatory stress is the sum of the two contributions, $\sigma(t) = \sigma'(t) + \sigma''(t)$. This decomposition is based on the idea that the elastic stress σ' should exhibit odd-symmetry with respect to x and even-symmetry with respect to y , whereas viscous stress σ'' should exhibit even-symmetry with respect to x and odd-symmetry with respect to y . The decomposition is defined below[28], and using this definition, along with Eq. 2.1 we indicate here that these elastic and viscous stresses are related directly to the Fourier decomposition as follows,

$$\sigma' \equiv \frac{\sigma(\gamma, \dot{\gamma}) - \sigma(-\gamma, \dot{\gamma})}{2} = \gamma_0 \sum_{n \text{ odd}} G'_n(\omega, \gamma_0) \sin n\omega t \quad (2.3)$$

$$\sigma'' \equiv \frac{\sigma(\gamma, \dot{\gamma}) - \sigma(\gamma, -\dot{\gamma})}{2} = \gamma_0 \sum_{n \text{ odd}} G''_n(\omega, \gamma_0) \cos n\omega t. \quad (2.4)$$

Thus, in contrast to the closed loops formed by the total stress σ vs. γ or σ vs. $\dot{\gamma}$, plotting elastic stress σ' vs. x or viscous stress σ'' vs. y produces single-valued functions of strain or strain-rate respectively. Figure 2-2 illustrates this stress decomposition using the LAOS experimental data for native pedal mucus shown in Figure 2-1. The intra-cycle elastic and viscous nonlinearities (i.e. nonlinearities within a given steady state cycle at fixed ω, γ_0) are therefore related to the nonlinearity of these functional forms. Cho et al.[28] suggest a polynomial regression fit to these lines of elastic and viscous stress (see their Eq. (23)). However, the material properties represented by the polynomial coefficients are not unique since they depend on the order of the polynomial arbitrarily chosen by the user. For example, given an unknown smooth function $F(x)$, a regression fit to a first order polynomial $F = a_0 + a_1x$ will always result in different coefficients a_0, a_1 than a regression fit to the higher-order polynomial $F = a_0 + a_1x + a_2x^2 + \dots$ except in the limit of $x \ll 1$ or if the unknown function is itself a linear function. Thus, fitting higher order terms affects the values of lower order terms, and polynomial regression fits do not result in unique values for quantifying nonlinearity. A framework which breaks down beyond the limit $x \ll 1$ is not suitable for quantifying a nonlinear (viscoelastic) response.

What is desired is an approach in which one fits $F = a_0f_0(x) + a_1f_1(x) + a_2f_2(x) + \dots$ such that incorporation of higher order terms does not affect lower order terms, i.e. the $f_i(x)$ must be orthogonal over the finite integration domain, in this case $[-1,1]$. These functions $f_i(x)$ are basis functions, and for the present case in which we decompose the stress into terms $\sigma'(x)$ and $\sigma''(y)$, where $x = \gamma/\gamma_0$ and $y = \dot{\gamma}/\dot{\gamma}_0$, the domain limits are the same for each curve, $-1 \leq x, y \leq 1$. Various sets of orthogonal polynomial basis functions exist, including Laguerre, Hermite, Jacobi, Utraspherical (Gegenbauer), Legendre, and Chebyshev of the first and second kind [46]. The appropriate set of polynomials for describing $\sigma'(x)$ and $\sigma''(y)$ will exhibit (i) orthogonality over a finite domain, (ii) odd symmetry about $x = 0$ and (iii) a bounded range for higher-order contributions. By process of elimination, we argue that the logical choice for understanding LAOS is the set of Chebyshev polynomials of the first kind. Laguerre and Hermite polynomials are eliminated because their limits

of orthogonality are $[0, \infty]$ and $[-\infty, \infty]$, which contradicts the finite domain criteria. Jacobi polynomials are not appropriate, as they do not have symmetry about $x = 0$ (except for special cases in which Jacobi polynomials can be related to Ultraspherical polynomials). Ultraspherical and Chebyshev (second kind) are ill-suited for LAOS due to their values at $x = \pm 1$; higher harmonics have ever-larger maxima, or for some classes of Ultraspherical polynomials have ever-decreasing maxima. Finally, Legendre polynomials are eliminated because they are not directly related to the time-domain Fourier coefficients, thus implementation with previously reported LAOS data and comparison with other LAOS interpretations would be unnecessarily complicated. We therefore make the choice to select Chebyshev polynomials of the first kind, because these functions are bounded, exhibit symmetry about $x = 0$, are orthogonal on the finite domain $[-1, +1]$, and can easily be related to the Fourier coefficients which have dominated the discussion on quantitative LAOS analysis. Using this basis set, the elastic and viscous contributions to the measured stress response can be written as

$$\sigma'(x) = \gamma_0 \sum_{n: \text{ odd}} e_n(\omega, \gamma_0) T_n(x) \quad (2.5)$$

$$\sigma''(y) = \dot{\gamma}_0 \sum_{n: \text{ odd}} v_n(\omega, \gamma_0) T_n(y) \quad (2.6)$$

where $T_n(x)$ is the n th-order Chebyshev polynomial of the first kind, and $x = \gamma/\gamma_0$, $y = \dot{\gamma}/\dot{\gamma}_0$ provide the appropriate domains of $[-1, +1]$ for orthogonality. The first, third, and fifth Chebyshev polynomials of the first kind are shown in Appendix A for reference, in addition to their equations and orthogonality relations. The functions at each order are orthonormal and therefore the coefficients e_n , v_n are independent of each other. We refer to $e_n(\omega, \gamma_0)$ as the elastic Chebyshev coefficients and $v_n(\omega, \gamma_0)$ as the viscous Chebyshev coefficients.

In the linear regime $e_3/e_1 \ll 1$ and $v_3/v_1 \ll 1$, and Eqs. 2.5, 2.6 recover the linear viscoelastic result such that $e_1 \rightarrow G'$ and $v_1 \rightarrow \eta' = G''/\omega$. We interpret any deviation from linearity, i.e. the $n = 3$ harmonic, as follows. A positive contribution of the third-order polynomial $T_3(x) = 4x^3 - 3x$ results in a higher elastic stress at the max-

imum dimensionless strain, $x \rightarrow 1$ than is represented by the first-order contribution alone. Thus $e_3 > 0$ corresponds to intra-cycle strain-stiffening of the elastic stress, whereas $e_3 < 0$ indicates strain-softening. Similarly, a positive value for v_3 represents intra-cycle shear-thickening of the viscous stress, and $v_3 < 0$ describes shear-thinning. These physical interpretations are not apparent in the time-domain (Fourier coefficients) but become immediately apparent from the sign of the Chebyshev coefficients.

Our deliberate use of Chebyshev polynomials allows the coefficients e_n and v_n (Eqs. 2.5,2.6) to be calculated from the familiar Fourier coefficients (Eq. 2.1). We use the identity $T_n(\cos \theta) = \cos(n\theta)$, together with $\sin \theta = \cos(\pi/2 - \theta)$ which gives $T_n(\sin \theta) = \sin(n\theta)(-1)^{\frac{n-1}{2}}$ for n :odd (see Appendix A for details). The relationships between the Chebyshev coefficients in the strain or strain-rate domain and the Fourier coefficients in the time domain are thus given by

$$e_n = G'_n (-1)^{\frac{n-1}{2}} \quad n:\text{odd} \quad (2.7)$$

$$v_n = \frac{G''_n}{\omega} = \eta'_n \quad n:\text{odd} \quad (2.8)$$

Thus, just as the third-order Chebyshev coefficients provide physical insight into the deviation from linear viscoelasticity, as described above, the third-order Fourier coefficients can also now be given a physical interpretation (with appropriate sign correction for G'_3). This new framework allows Fourier coefficients to be used to calculate physically meaningful measures of nonlinearity, i.e. the elastic and viscous Chebyshev coefficients.

Some researchers report results from FT rheology in terms of amplitude and phase, e.g. [47], in which Eqs. 2.1,2.2 would take the form

$$\sigma = \gamma_0 \sum_{n:\text{ odd}} |G_n^*| \sin(n\omega t + \delta_n) \quad (2.9)$$

where $|G_n^*| = \sqrt{G_n'^2 + G_n''^2}$ is the scaled stress magnitude and δ_n is the phase with respect to the input strain signal $\gamma(t) = \gamma_0 \sin \omega t$. The variable δ_n may be interpreted as determining the initial conditions of the higher-harmonic contributions. For ex-

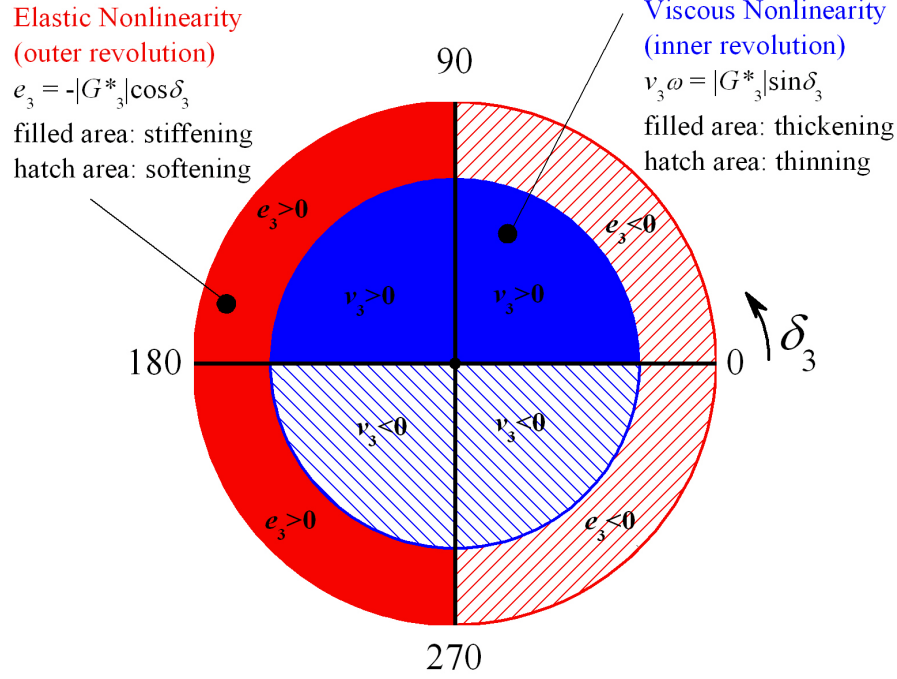


Figure 2-3: Diagram summarizing the interpretation of the third-harmonic phase angle δ_3 , as revealed by the third-order Chebyshev coefficients.

ample, at $\omega t = 0$ the third harmonic contribution is $|G_3^*| \sin(\delta_3)$, and subsequently oscillates with a frequency of $3\omega_1$ for $\omega t > 0$. Thus, δ_3 determines the initial value of the third-harmonic contribution, and must range from $0 \leq \delta_3 \leq 2\pi$.

As we noted above, only the signs of the third harmonic Chebyshev coefficients are needed to interpret the nature of elastic and viscous nonlinearities. Here they are related to the $n = 3$ phase angle and our interpretation of intra-cycle stiffening/softening and thickening/thinning can be summarized as (see also Figure 2-3)

$$e_3 = -|G_3^*| \cos \delta_3 \begin{cases} > 0 & \text{strain - stiffening} & \text{for } \pi/2 < \delta_3 < 3\pi/2 \\ = 0 & \text{linear elastic} & \text{for } \delta_3 = \pi/2, 3\pi/2 \\ < 0 & \text{strain - softening} & \text{for } -\pi/2 < \delta_3 < \pi/2 \end{cases}$$

$$v_3 = \frac{|G_3^*|}{\omega} \sin \delta_3 \begin{cases} > 0 & \text{shear - thickening} & \text{for } 0 < \delta_3 < \pi \\ = 0 & \text{linear viscous} & \text{for } \delta_3 = 0, \pi \\ < 0 & \text{shear - thinning} & \text{for } \pi < \delta_3 < 2\pi \end{cases}$$

If only torque and displacement signals are available, rather than stress and strain, it is common to report the scaled intensity of the third harmonic torque response,

I_3/I_1 , where I_n is the magnitude of the n -harmonic torque signal. One may calculate the scaled third harmonic Chebyshev coefficients as $e_3/e_1 = (I_3/I_1) \cos \delta_3 / \cos \delta_1$ and $v_3/v_1 = (I_3/I_1) \sin \delta_3 / \sin \delta_1$, the signs of which have an equivalent interpretation to e_3 and v_3 , respectively, since e_1 and v_1 are always positive.

Other attempts have been made to physically interpret the phase of the 3rd harmonic, e.g. [48]. Our interpretation is distinct in that the phase angle δ_3 indicates the nature of both the elastic and viscous nonlinearities, even when they occur simultaneously. Furthermore, in our framework this interpretation is based on the absolute phase difference relative to the excitation (δ_3). By contrast, in the work of Neidhofer et al. [48] the relative phase with respect to the first harmonic ($\delta_3 - \delta_1$) is used. Our result above suggests that the sign of both the elastic and viscous deviation from linearity is captured by a single quantity, δ_3 . The interpretation of the higher harmonic stress response (G'_3, G''_3 and the absolute phase δ_3) is thus facilitated by the use of our elastic and viscous Chebyshev coefficients e_3 and v_3 .

2.3 Meaningful viscoelastic moduli in the nonlinear regime

The second issue addressed with this new framework is the lack of clearly defined viscoelastic moduli for a nonlinear material response. The frequently used first-harmonic coefficients G'_1 and G''_1 often fail to capture the rich nonlinearities that are apparent in the raw data signal (as shown in Figure 2-1). I define here several new measures for accurately reporting the magnitudes of the first-order (linear) viscoelastic moduli in the nonlinear regime, each of which has a distinct physical interpretation and complements the often-reported first-order Fourier coefficients. These additional measures are deliberately chosen such that they reduce to the unique material functions $G'(\omega)$ or $G''(\omega)$ in the linear regime, but diverge systematically when used to analyze a nonlinear signal, offering additional physical insight beyond that captured by the average measures G'_1, G''_1 . The variation in these new measures can be reported as a

function of imposed strain amplitude γ_0 (or strain-rate amplitude $\dot{\gamma}_0$) to indicate the nature of material nonlinearity across different steady state cycles (i.e. inter-cycle nonlinearities).

2.3.1 Elastic modulus

The apparent contradiction of Figure 2-1 is addressed by first recognizing that G'_1 can be a misleading measure of the “elastic modulus” of such a material, since other harmonic components may also store energy[18]. The first-harmonic represents a sine transform $G'_1 = \omega / (\pi\gamma_0^2) \oint \sigma(t) \gamma(t) dt$, which is a measure of the average elasticity in the material response at each imposed pair of LAOS coordinates (ω, γ_0) , and is therefore unable to distinctly represent the local elastic response of a material at small and large instantaneous strains. To capture this local behavior, we define a set of elastic moduli that are geometrically-motivated and then derive their relation to both conventional FT rheology descriptions (by substituting Eq. 2.1 into the definitions) and our new Chebyshev stress decomposition (via Eqs. 2.5,2.6). The following definitions are introduced:

$$G'_M \equiv \left. \frac{d\sigma}{d\gamma} \right|_{\gamma=0} = \sum_{n \text{ odd}} nG'_n = e_1 - 3e_3 + \dots \quad (2.10)$$

$$G'_L \equiv \left. \frac{\sigma}{\gamma} \right|_{\gamma=\gamma_0} = \sum_{n \text{ odd}} G'_n (-1)^{\frac{n-1}{2}} = e_1 + e_3 + \dots \quad (2.11)$$

where G'_M is the *minimum-strain modulus* or tangent modulus at $\gamma = 0$ and G'_L is the *large-strain modulus* or secant modulus evaluated at the maximum imposed strain. The definitions of G'_M and G'_L can be considered as methods for calculating G' from available raw data, since for a linear viscoelastic response each is equivalent to G' (similarly, G'_1 is also equivalent to G' for a linear viscoelastic response). These measures can easily be visualized graphically using typical Lissajous-Bowditch curves as shown in Figure 2-4a (linear response) and Figure 2-4c (nonlinear response). These measures are deliberately chosen such that both converge to the linear elastic modulus $G'(\omega)$ in the limit of small strains ($e_3/e_1 \ll 1$), i.e. $G'_L = G'_M = G'_1 = G'(\omega)$ in the

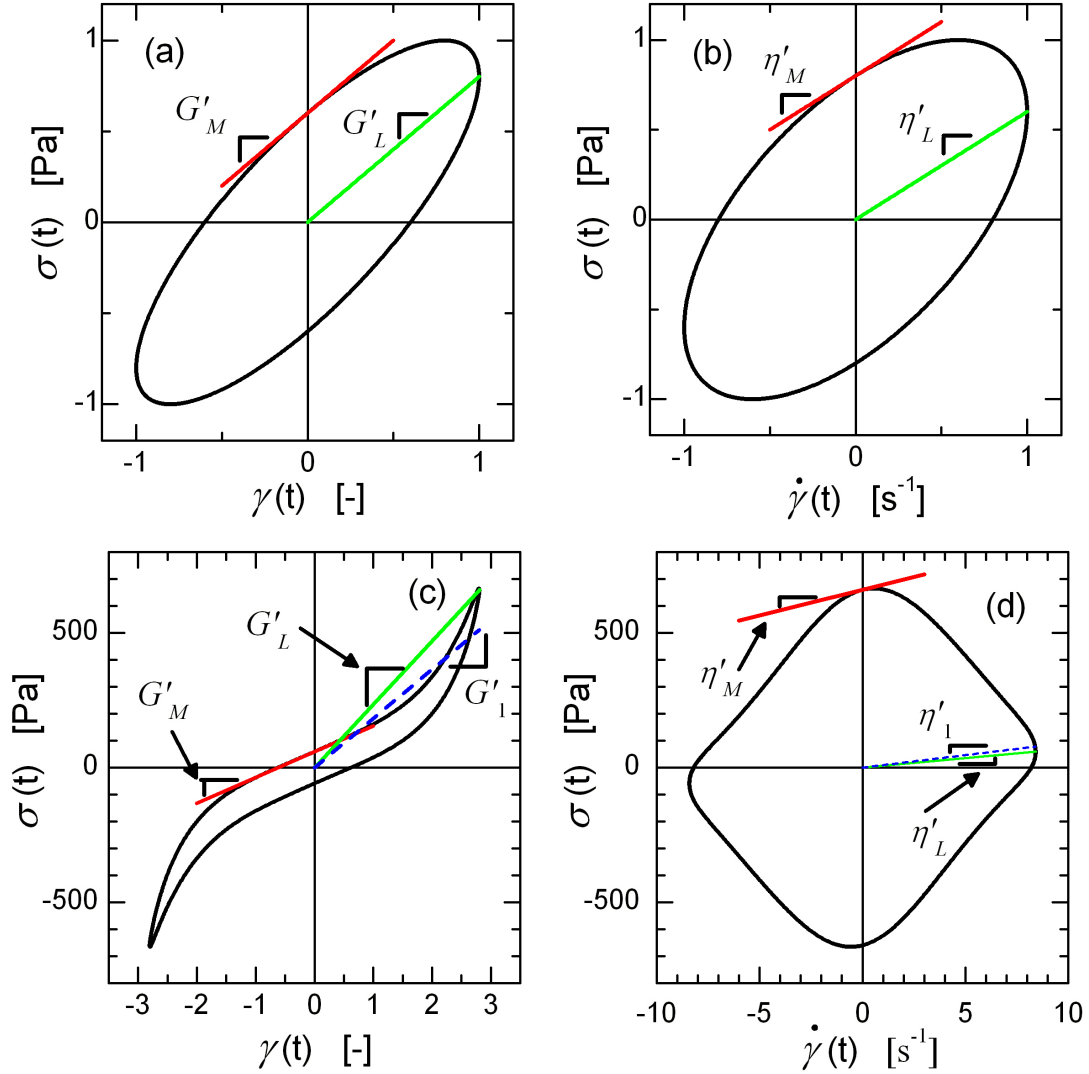


Figure 2-4: Definitions of new measures for reporting viscoelastic moduli: (a),(b) elastic moduli and dynamic viscosities, respectively, for a model linear viscoelastic response with $G' = 0.8$, $G'' = 0.6$ at $(\omega = 1 \text{ rad.s}^{-1}, \gamma_0 = 1)$; (c),(d) elastic moduli and dynamic viscosities, respectively, for a nonlinear viscoelastic response (experimental data shown is same as Figure 2-2). The first harmonic moduli are shown for comparison. In the linear regime (a,b) all measures are equivalent to the linear viscoelastic moduli. A nonlinear material response (c,d) will result in different values for each material measure.

linear regime, as seen from Eqs. 2.10-2.11. The corresponding Lissajous-Bowditch curve is an ellipse with local tangent at $\gamma = 0$ parallel to a secant at $\gamma/\gamma_0 = x = 1$. Although these new elastic measures are calculated from the total stress signal, they can also be related to the elastic stress σ' as decomposed by the geometrical

interpretation of Cho et al. [28]. Thus, another useful measure of elasticity may be the slope of the elastic stress at maximum strain, $G'_K \equiv d\sigma'/d\gamma|_{\gamma=\gamma_0}$, which is reminiscent of a differential modulus for a given strain amplitude. We note that one might be tempted to take the local slope of the total stress near maximum strain as a type of elastic modulus, however this measure does not reduce to $G'(\omega)$ in the linear regime.

The minimum-strain modulus G'_M is the tangent modulus at zero instantaneous strain. This is a natural way to measure an elastic modulus. By the nature of an oscillatory test for which $\gamma(t) = \gamma_0 \sin(\omega t)$, at the point where $\gamma = 0$ the strain-rate is at a local maximum, $d\dot{\gamma}/dt = 0$ and the viscous contribution to the stress is thus locally constant. However, the strain *is* changing, which suggests that any change in stress should be related only to elasticity. In fact, this is a possible way to measure G' in the linear regime, since for small total deformations $G'_M \rightarrow G'$, but the formulation of Eq. 2.10 offers an interpretation of the elastic modulus in the nonlinear regime which is distinct from G'_1 .

The large-strain modulus, G'_L , is the secant modulus at maximum strain. This is also a natural measurement of an elastic modulus since for $\gamma = \gamma_0$, we have $\dot{\gamma} = 0$, which suggests that the instantaneous viscous stress at this point should be zero. Accordingly, the total residual stress in the sample results only from the elastic characteristics of the soft material. The result is that $G'_L \rightarrow G'$ in the linear regime (small γ_0), but Eq. 2.11 offers an alternative and distinct view of the nonlinear elastic response.

The graphical representation of these measures aids our interpretation of Lissajous-Bowditch curves in both the linear and nonlinear regime. A Lissajous-Bowditch curve in the linear regime will appear as an ellipse. A common misconception is that the slope of the semi-major axis of this ellipse represents the elastic modulus (this slope actually represents the magnitude of the complex modulus). The elastic modulus is represented by the tangent slope at zero strain, G'_M , and the slope of the secant at maximum strain, G'_L . The secant at maximum strain is not equal to the semi-major axis of the ellipse, except for the case of a purely elastic solid whose

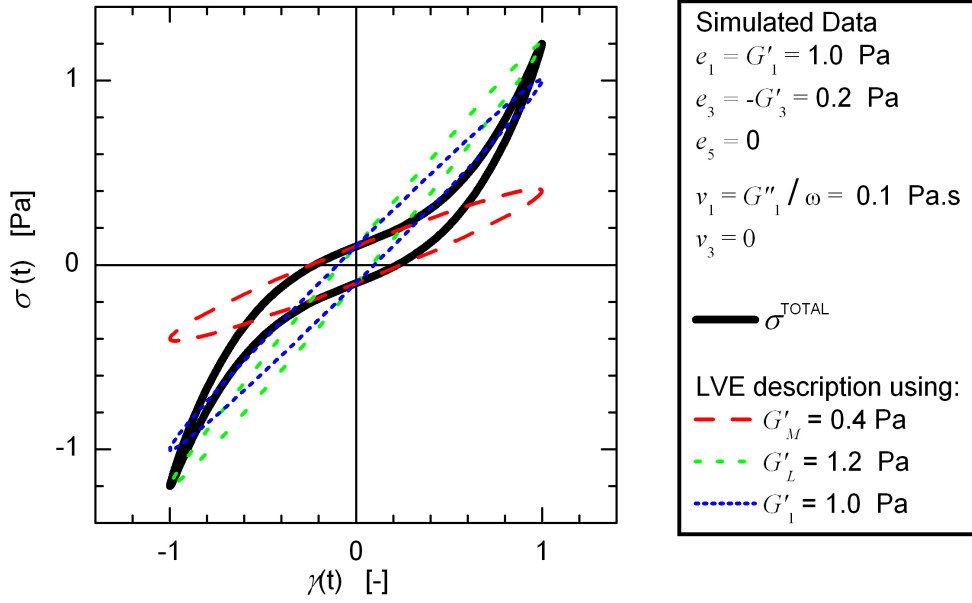


Figure 2-5: Different elliptical approximations to a nonlinear viscoelastic signal, using the newly proposed alternative measures of elastic modulus.

Lissajous-Bowditch curve would appear as a straight line.

Using these graphical interpretations, it can be observed from the elastic Lissajous-Bowditch curves of Figure 2-1b that for large imposed strain amplitude γ_0 the material is strain-stiffening within a given cycle (intra-cycle stiffening) since $G'_L > G'_M$. As the strain amplitude is varied, it is also observed that the tangent modulus G'_M decreases, indicating a type of inter-cycle softening of the elasticity at low strains. These insights can not be gained from reporting G'_1 alone.

We now have three ways to report the first-order elastic modulus: $G'_1 = e_1$, $G'_M = e_1 - 3e_3 + \dots$, and $G'_L = e_1 + e_3 + \dots$. These can be thought of as three different ways to approximate the leading order response of a nonlinear viscoelastic material. Figure 2-5 depicts the use of these three elastic moduli in the approximation of an intra-cycle strain-stiffening nonlinear model. The simulated response is described by $G'_1 = 1$ Pa, $e_3 = -G'_3 = 0.2$ Pa, $\nu_1 = G''_1 / \omega = 0.1$ Pa.s, and $\nu_3 = 0$, with all other higher harmonic contributions being identically zero. The minimum- and large-strain elastic moduli can be found from the model parameters by use of Eqs. 2.10-2.11. The linear approximation to the nonlinear viscoelastic response can

be represented by using any of the first-order elastic moduli along with the loss modulus $\{G'_1, G''\}$, $\{G'_M, G''\}$, $\{G'_L, G''\}$ to create elliptical Lissajous-Bowditch curves. As can be seen in Figure 2-5, the first-order Fourier elastic modulus is a type of average elastic response. The small-strain modulus G'_M approximates the linear viscoelastic response as an ellipse that matches the small-strain elasticity. The linear approximation using the large-strain modulus G'_L captures the large-strain elasticity by matching the stress response at maximum strain.

2.3.2 Dynamic viscosity

It has been previously shown that under oscillatory shear deformation, all of the dissipated energy is represented by the first-harmonic loss modulus G''_1 [13, 18]. The total energy dissipated per cycle per unit volume is $\pi\gamma_0^2 G''_1$. While $G''_1 = \eta'_1 \omega$ represents the total dissipation per cycle, it cannot differentiate between any local changes in the coefficient of viscous dissipation between the lowest and highest instantaneous shear-rates experienced during the oscillatory deformation. We therefore regard $G''_1 = \eta'_1 \omega$ as representing an average dissipation coefficient over the cycle. Here we introduce new measures η'_M and η'_L which indicate the instantaneous viscosity (or coefficient of viscous dissipation) at the smallest and largest shear-rates, respectively.

To represent the viscous nature of a soft viscoelastic material, we will use the framework of dynamic viscosities, as given in Eq. 2.2. We define a set of dynamic viscosities for reporting the viscous or dissipative response in a similar fashion to the framework of the previous section. The definitions are

$$\eta'_M \equiv \left. \frac{d\sigma}{d\dot{\gamma}} \right|_{\dot{\gamma}=0} = \frac{1}{\omega} \sum_{n \text{ odd}} n G''_n (-1)^{n-1/2} = v_1 - 3v_3 + \dots \quad (2.12)$$

$$\eta'_L \equiv \left. \frac{\sigma}{\dot{\gamma}} \right|_{\dot{\gamma}=\dot{\gamma}_0} = \frac{1}{\omega} \sum_{n \text{ odd}} G''_n = v_1 + v_3 + \dots \quad (2.13)$$

where η'_M is the *minimum-rate dynamic viscosity* and η'_L is the *large-rate dynamic viscosity*. These measures are represented graphically in Figure 2-4b (linear response) and Figure 2-4d (nonlinear response). Note that each measure of dynamic viscosity

reduces to $\eta' = G''/\omega$ when the response is a single harmonic, i.e. $\eta'_L = \eta'_M = \eta'_1 = \eta'(\omega)$ in the linear regime.

2.3.3 Dimensionless index of nonlinearity

These new alternative measures of elastic modulus and dynamic viscosity can be compared to quantify intra-cycle nonlinearities which distort the linear viscoelastic ellipse. For example, if the large-strain modulus G'_L is greater than the minimum-strain modulus G'_M , then the response is strain-stiffening within the particular cycle (i.e. intra-cycle strain-stiffening). We define the following *strain-stiffening ratio*:

$$S \equiv \frac{G'_L - G'_M}{G'_L} = \frac{4e_3 + \dots}{e_1 + e_3 + \dots}. \quad (2.14)$$

Note that $S = 0$ for a linear elastic response, $S > 0$ indicates intra-cycle strain-stiffening, and $S < 0$ corresponds to intra-cycle strain-softening. Users of this framework may also choose to compare the moduli using e.g. the ratio $(G'_L/G'_M)M = (1 - S)^{-1}$; we prefer the measure in Eq. 2.14 for convenience in relating the new measure to higher order Fourier/Chebyshev coefficients, and to eliminate potential singularities as $G'_M \rightarrow 0$.

We similarly define the shear-thickening ratio as

$$T \equiv \frac{\eta'_L - \eta'_M}{\eta'_L} = \frac{4v_3 + \dots}{v_1 + v_3 + \dots} \quad (2.15)$$

where $T = 0$ indicates a single harmonic linear viscous response, $T > 0$ represents intra-cycle shear-thickening, and $T < 0$ intra-cycle shear-thinning. The parameter T behaves in a comparable manner to the 3rd order viscous Chebyshev coefficient v_3 , and therefore has a similar relationship to I_3/I_1 and δ_3 as described at the end of Section 2.2.

The full framework for characterizing nonlinear viscoelasticity is summarized in Table 2.1. The table includes both terminology and definitions of material measures.

Elastic Characterization

	Material Measures	Interpretation
Linear first-order properties	$G'_1 = \frac{\omega}{\pi\gamma_0^2} \oint \sigma(t)\gamma(t)dt$ $G'_M \equiv \left. \frac{d\sigma}{d\gamma} \right _{\gamma=0}$ $G'_L \equiv \left. \frac{\sigma}{\gamma} \right _{\gamma=\gamma_0}$	<p>First-harmonic (average) elastic modulus</p> <p>Minimum-strain elastic modulus</p> <p>Large-strain elastic modulus</p>
Nonlinear properties	$e_3 = -G'_3$ $S \equiv \frac{G'_L - G'_M}{G'_L} = \frac{4e_3 + \dots}{e_1 + e_3 + \dots}$	<p>Intra-cycle <i>elastic</i> nonlinearities</p> $e_3 \text{ and/or } S \begin{cases} > 0 & \text{strain - stiffening} \\ = 0 & \text{linear elastic} \\ < 0 & \text{strain - softening} \end{cases}$

Viscous Characterization

	Material Measures	Interpretation
Linear first-order properties	$\eta'_1 = \frac{1}{\pi\omega\gamma_0^2} \oint \sigma(t)\dot{\gamma}(t)dt$ $\eta'_M \equiv \left. \frac{d\sigma}{d\dot{\gamma}} \right _{\dot{\gamma}=0}$ $\eta'_L \equiv \left. \frac{\sigma}{\dot{\gamma}} \right _{\dot{\gamma}=\dot{\gamma}_0}$	<p>First-harmonic (average) dynamic viscosity</p> <p>Minimum-rate dynamic viscosity</p> <p>Large-rate dynamic viscosity</p>
Nonlinear properties	$v_3 = -G''_3/\omega$ $T \equiv \frac{\eta'_L - \eta'_M}{\eta'_L} = \frac{4v_3 + \dots}{v_1 + v_3 + \dots}$	<p>Intra-cycle <i>viscous</i> nonlinearities</p> $v_3 \text{ and/or } T \begin{cases} > 0 & \text{shear - thickening} \\ = 0 & \text{linear viscous} \\ < 0 & \text{shear - thinning} \end{cases}$

Table 2.1: Material measures and nomenclature for characterizing nonlinear viscoelasticity with imposed oscillatory shear strain.

Chapter 3

Data analysis software: MITlaos

The descriptive framework for nonlinear viscoelastic characterization (Chapter 2) is sufficiently general to be applied to any viscoelastic material, ranging from purely elastic to purely viscous, and any complex viscoelastic response in-between. The framework has been packaged into a distributable data analysis program to widen its use in both academic and industrial settings[49]. This MATLAB-based software, “MITlaos,” is freely available for use by anyone. This author is the primary contact for distribution of MITlaos, by means of the permanent email address ‘MITlaos@mit.edu’.

The data processing used in the MITlaos software follows the protocol described in Section 4.2.1. The MITlaos software includes source code for processing data, along with a graphical user interface to improve ease of use. A manual for using MITlaos is distributed to each user. This chapter includes the contents of the MITlaos v2.2 user manual. The source code associated with the primary data processing portion of MITlaos is included in Appendix B.

The MITlaos software requires time-series signals of strain and stress, along with user-specification of some analysis parameters. A flowchart showing the program sequence is shown in Figure 3-1. The input data must be in the form of a plain text file, but the software is sufficiently flexible to accept various formats and layouts, including the standard text file export of some commercial instrumentation. Output from the software includes data files and image files. The data file outputs can be

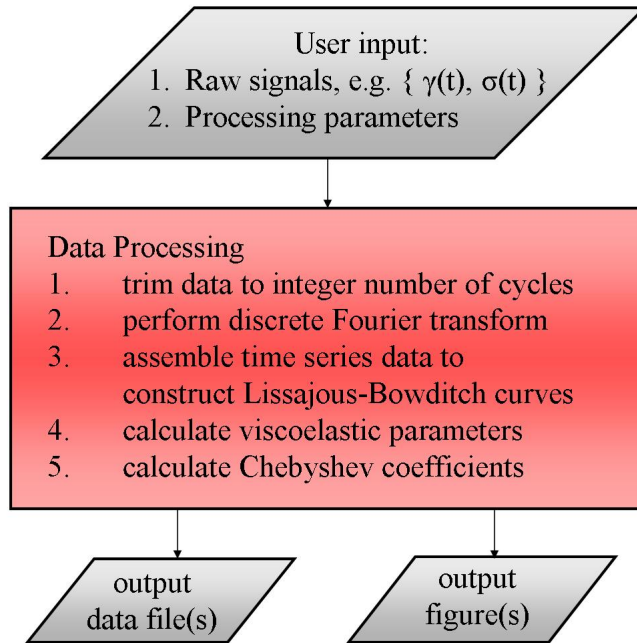


Figure 3-1: Flow chart of the processing sequence for the “MITlaos” data analysis software.

modified at the user’s discretion, and include calculated viscoelastic parameters and time-series signals of elastic and viscous stresses, $\sigma'(\gamma(t))$ and $\sigma''(\dot{\gamma}(t))$ respectively.

Image file output is also useful for documenting the analysis. Figure 3-2 shows one of the optional image outputs from the software, which includes an overview of the analysis (here for pedal mucus from *Limax maximus*, $\omega = 3 \text{ rad.s}^{-1}$, $\gamma_0 = 2.8$, c.f. Figure 4-2). The top left subplot in Figure 3-2 includes the input time-series data of strain $\gamma(t)$ and shear stress $\sigma(t)$ used for the analysis. The lower left subplot of Figure 3-2 is a Fourier spectrum of the stress response represented in terms of a power spectrum density $P(\omega)$. This Fourier spectrum provides a mathematically robust description of the response in terms of the individual harmonic contributions to the system response. However, interpreting the physical meaning directly from the phase and amplitude information encoded in the higher harmonics has proven elusive. The physically meaningful characterization is represented in the middle and far right columns of Figure 3-2. The middle column of Figure 3-2 captures the elastic behavior of the sample response, showing the elastic Lissajous-Bowditch curve at the

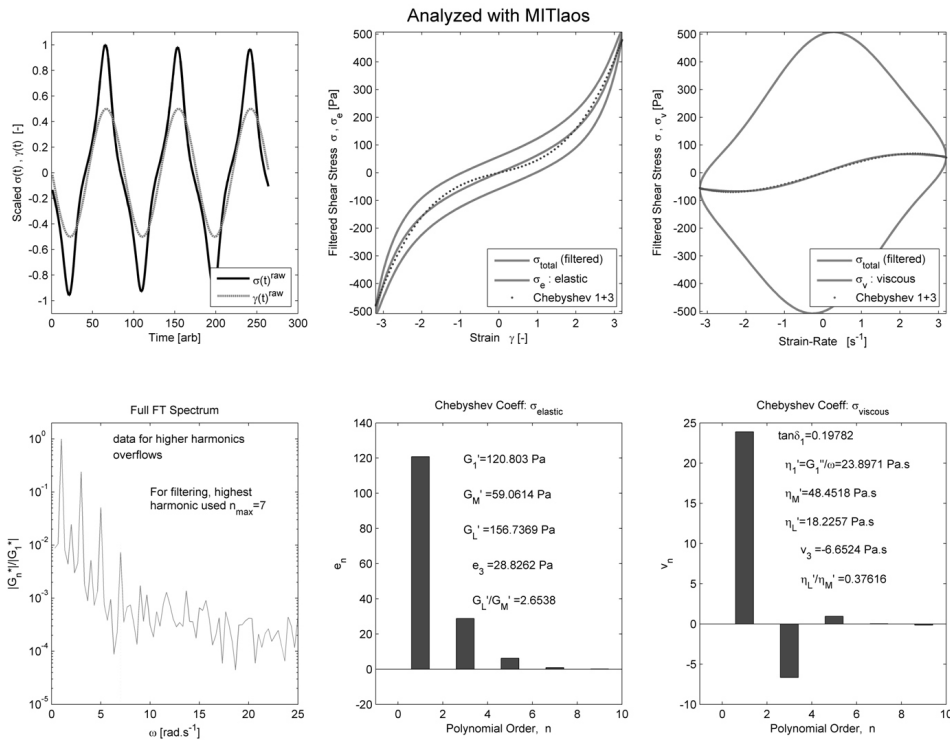


Figure 3-2: MITIaos Output: Overview plot example, shown here for pedal mucus from *Limax maximus*, $\omega = 3 \text{ rad.s}^{-1}$, $\gamma_0 = 2.8$, c.f. Figure 4-3.

top, and at the bottom containing the spectrum of elastic Chebyshev coefficients and the value of the different measures of elastic moduli. The solid red line in the elastic Lissajous-Bowditch curve, the elastic stress $\sigma'(\gamma)$, clearly shows the strain-stiffening nature of the material response. The dashed-green line labeled “Chebyshev 1+3” is the representation of the elastic stress using only first- and third-harmonic Chebyshev coefficients e_1 and e_3 ; higher harmonics also exist (e_5, e_7 , etc.) but these are negligible as shown by the near overlap of the approximate (dashed line) and actual (solid line) elastic stress $\sigma'(\gamma)$. The far right column of Figure 3-2 contains the corresponding viscous characterization of the sample response, showing the viscous Lissajous-Bowditch curve at the top and at the bottom displaying the viscous Chebyshev spectrum and the different local measures of dynamic viscosities. The software can save the overview plot of Figure 3-2 for each test at a given amplitude and frequency, (γ_0, ω) . All of the data displayed in the overview plot of Figure 3-2 can be output to data files.

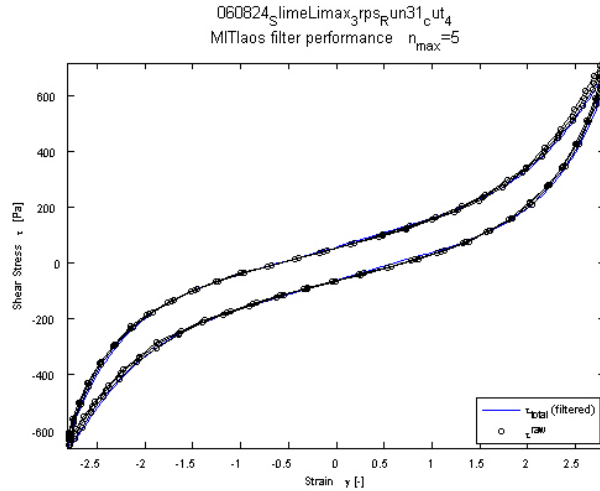


Figure 3-3: MITlaos Output: Filter performance, shown here for pedal mucus from *Limax maximus*, $\omega = 3 \text{ rad.s}^{-1}$, $\gamma_0 = 2.8$, c.f. Figure 4-3.

As a final example of figure output from MITlaos, a plot showing the performance of the comb-filter is shown in Figure 3-3. The raw data (shown as open circles) is smoothed by retaining only the odd, integer harmonics of stress up to a cutoff frequency, resulting in the smoothed stress response shown by the solid blue line. Section 4.2.1 provides a detailed discussion of the comb filter process.

The remaining portions of this chapter contain instructions for installing and using the MITlaos software.

3.1 Introduction

This manual describes the use of MITlaos (MATLAB version), a data analysis program for analyzing rheological properties in large amplitude oscillatory shear (LAOS). In addition to calculating standard viscoelastic parameters such as G'_1 , G''_1 , MITlaos calculates additional parameters for interpreting nonlinear viscoelastic behavior. For detailed information regarding definitions and interpretation please refer to Chapter 2, and [28][50].NOTE: As input, the program requires oscillatory waveforms of strain and stress from a strain-controlled oscillatory shear test.

NOTE: MITlaos requires installation of MATLAB, which can be purchased from The MathWorks at www.mathworks.com.

3.2 Installation

MITlaos is currently distributed as a ZIP folder which contains multiple subfolders and multiple MATLAB subfunctions. Installation is done by unzipping and saving the MITlaos folder to any location on the local hard drive. Although any location is acceptable, a convenient location for the MITlaos folder is ... \MATLAB\work\MITlaos.



WARNING: Do not modify the contents of the MITlaos folder. Please contact MITlaos@mit.edu regarding installation problems.

3.3 Running the program

3.3.1 Structure of Input Data File

MITlaos requires a text-based (ASCII) data file which contains columns of data. Header information is typically tolerated by the program. At a minimum, time-series data for strain (or displacement) and stress (or torque) are required. Additionally, a data column of time may be included if data are sampled at uneven intervals.

NOTE: MITlaos is flexible regarding the arrangement of columns in the data input file. The user will specify which column contains strain, stress, and time (optional).

3.3.2 Starting the Program

Once MITlaos is installed and the data input file is of the proper form, the program can be initialized with the following sequence.

1. Open MATLAB

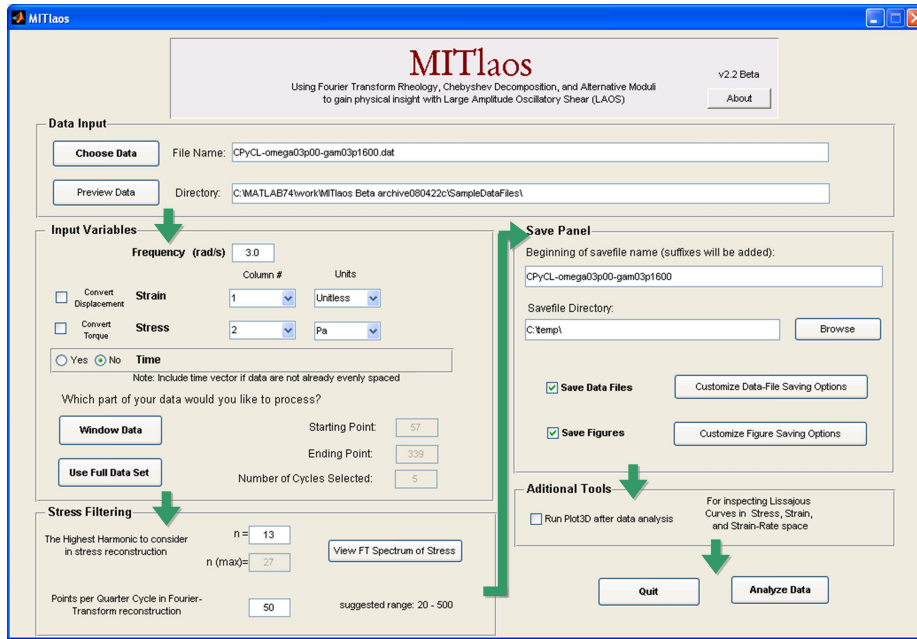


Figure 3-4: The MITlaos main window (arrows added to show the standard order of completion).

2. Change the current working directory to the MITlaos folder (e.g. ... \MATLAB\work\MITlaos\). This folder should contain MITlaos.m
3. Type MITlaos at the command prompt to start the program

3.4 Main Window Overview

The MITlaos program consists of one main window (Figure 3-4) and several side windows. The main window includes all the necessary steps for analyzing sets of data. Several buttons in the main window open side windows that provide the user with more information and with more options to customize the data analysis.

The MITlaos main window is broken into separate panels (which look like boxes) that group together related information. MITlaos was designed for filling out the information in one panel and then moving to the next one. The typical order for setting up MITlaos is to complete the Data Input panel, Input Variables panel, Stress Filtering panel (optional), Save Panel (optional), Additional Tools (optional), and then to press the ‘Analyze Data’ button. The arrows in Figure 1 show the progression

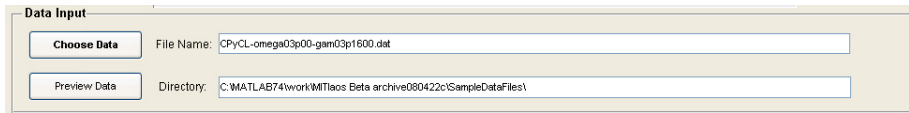


Figure 3-5: Data Input Panel.

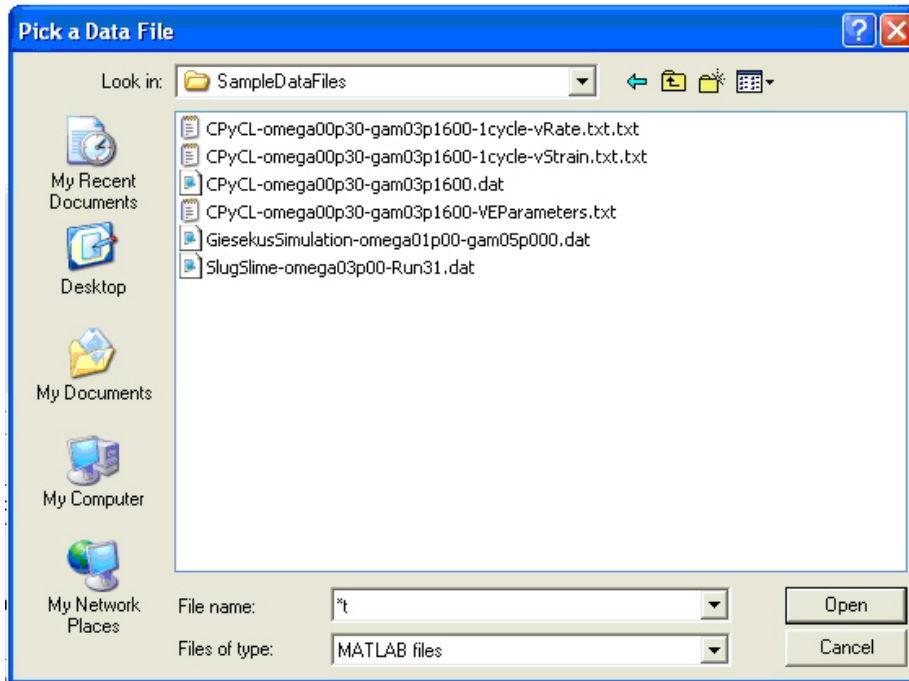


Figure 3-6: Choose Data Window.

across the main MITlaos window. This User Manual will also follow this order.

3.5 Data Input Panel

The Data Input panel lets the user select and preview the data file MITlaos will analyze. To select the data file, click either the Choose Data button or type the filename and its directory into the File Name and Path Name boxes (see Figure 3-5).

Choose Data button

Press the ‘Choose Data’ button in the Data Input panel to browse and select the file to analyze (Figure 3-6). Select the file, then click ‘Open’ and the filename and directory information will automatically be entered into the MITlaos main window.

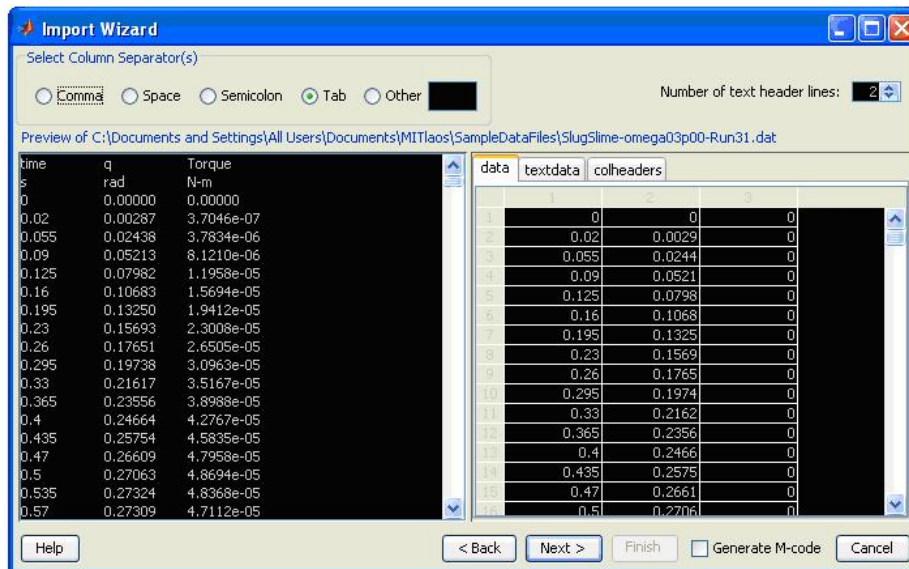



Figure 3-7: Import Wizard (only used to preview data).

Preview Data button (Optional)

The 'Preview Data' button uses a function called Import Wizard to preview the selected data file. This can be used to quickly look at the contents of the selected input file. The Import Wizard is shown in Figure 3-7.



WARNING: Import Wizard must only be used for previewing data. Press 'Cancel' when finished using the wizard; **DO NOT** click 'Next.'

In Figure 3-7, the box on the left shows the raw contents of the chosen data file. The grid on the right shows how MITlaos will load the file. In the example shown in Figure 3-7, MITlaos automatically cuts off the top rows of text containing the headers and units and reads only the numerical data below them. Note that the values of Torque are being read properly, however the numerical value is so small that Import Wizard rounds to 0 in the display on the right.

File Name edit box

The File Name edit box displays the name of the chosen data input file. Using the 'Choose Data' button will automatically fill in this box; however, the user may

Figure 3-8: Input Variables panel.

also manually type the name of the data file into this box if desired.

Path Name edit box

The Path Name edit box displays the directory of the input file. As with the File Name edit box, the ‘Choose Data’ button can be used to automatically fill in this box. The user also has the option to type the pathname of the data file into this box.

3.6 Input Variables Panel

The Input Variables panel (Figure 3-8) allows the user to specify all the information MITlaos requires for loading the data. It asks three separate questions:

- At what oscillatory frequency was the sample tested?
- Which columns in the data file contain which variables?
- What portion of the time-series data should be analyzed?

Frequency edit box

In the Frequency box, enter the oscillatory strain frequency used to test the sample, in units of [rad/s]. This input is necessary to run the analysis. It is suggested

that the user include the frequency in the input filename as a convenient reference.

Column Specification

The user must specify which columns in the data file contain the strain, stress, and (optionally) time signals. This allows MITlaos to read data files with different layouts. To identify the column in the data file corresponding to each signal, click on the dropdown menus to the right of the words ‘Strain’ and ‘Stress’, underneath the heading ‘Column #’. From the dropdown menu, select the column number corresponding to the location of the data signal in the input file. To make the Time column options visible, the user must first select the ‘Yes’ box to the left of the word ‘Time’. If the input datafile has headers labeling the columns, it is possible to see them with the ‘Preview Data’ button (in the Data Input panel) to see which column contains which variable.

NOTE: Different columns must be selected for each variable.

Strain and Stress are the two variables required by MITlaos. Time is an additional variable that can be incorporated into the analysis if necessary. If the data was NOT collected at equally spaced time intervals, then it is important to include time as an input. If time is not included, MITlaos will assume the data points are equally spaced in time. It is recommended to NOT include time if data are evenly spaced.

In order to input displacement (instead of strain), click on the ‘Convert Displacement’ checkbox to the left of the word ‘Strain’. A box allowing the input of a conversion factor will appear to the right of ‘Units’, and the word ‘Strain’ will be changed to ‘Displacement’ (Figure 3-9). Use the appropriate conversion factor such that strain is unitless (i.e. not in terms of percent), according to the equation $\gamma[-] = F_\gamma \Theta$.

If the data was collected as torque, instead of stress, click on the ‘Convert Torque’ box to the left of the word ‘Stress’. Similar changes will occur, allowing the user to specify a conversion factor between torque and stress. Use the appropriate conversion factor such that stress is in units of Pascals, according to the equation $\tau[\text{Pa}] = F_\tau T$. Note that torque may be reported in various units, but must be chosen to give stress

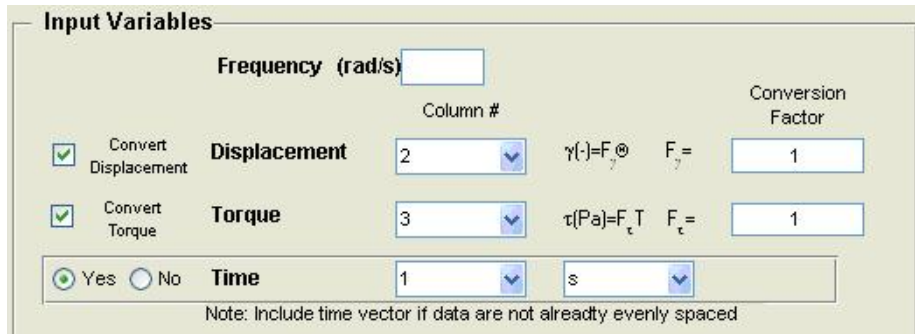


Figure 3-9: Input Variables panel, with ‘Convert Displacement’ and ‘Convert Torque’ options selected, and the ‘Time’ column input turned on.

in units of Pascals. These conversion factors depend on the type and size of geometry being used (cone-plate, plate-plate, etc.). Values for conversion factors may be found in rheology textbooks, and may sometimes be given by the geometry manufacturer.

Data Windowing

MITlaos can analyze all or part of the time-series data contained in the input file. There are two large buttons, titled ‘Window Data’ and ‘Use Full Data Set’ that allow the user to choose between these options (see Figure 3-8). To the right of these buttons are three boxes which display the starting point, ending point, and number of cycles chosen from the dataset. These boxes will be empty if no data range has yet been chosen.

NOTE: At least one complete cycle must be selected for the analysis to work properly

To analyze the full time-series data set, press the ‘Use Full Data Set’ button. The full dataset will be trimmed to an integer number of complete cycles (this is necessary for analysis), and the boxes to the right of the button will immediately display how much data will be included for analysis.

Windowing the data is required if the time-series data contains transients, or if several strain amplitudes or frequencies are contained within the same data. In these cases, only part of the data should be used for each analysis. Press the ‘Window Data’ button and a new window will open called ‘processPartDataGUI’, which allows

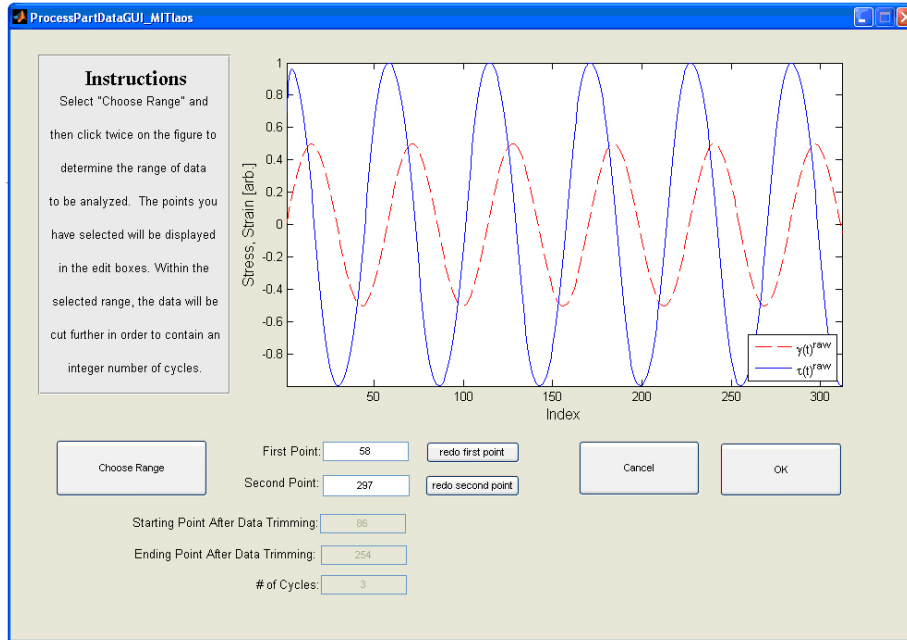


Figure 3-10: ProcessPartDataGUI window.

the user to select which portion of the time-series to include for analysis.

ProcessPartDataGUI

Stress and strain are plotted against time (or arbitrary time) in the ProcessPart-DataGUI (Figure 3-10). Since MITlaos is designed to analyze a viscoelastic system response to a sinusoidal strain input, the strain signal should appear as a sine wave and the stress response should oscillate with the same period (note that stress should simply be a shifted sine wave in the linear viscoelastic regime). By looking at this stress and strain signals, the user should be able to determine which portion of the data should be analyzed.

Click the ‘Choose Range’ button on the bottom left of the window to select the desired portion of data to analyze. The cursor will immediately change to a cross hair which will be used for selecting the limiting points of the desired range. Move the cross hair over the graph and click once at the beginning and once at the end of the desired data range (note that the vertical position of the crosshairs is irrelevant). The two chosen points will be displayed in the First Point, and Second Point edit

boxes. If desired, the user may choose to manually type the location of the chosen points into the edit boxes.

The chosen data range will be further trimmed to be an integer number of cycles. The new limits of the data to be processed will be displayed in the ‘Starting Point After Data Trimming’ and ‘Ending Point After Data Trimming’ boxes. The bottom box shows the total number of complete cycles that will be used in data analysis. An integer number of cycles is required for proper processing.

It is possible to redo either of the endpoints of the initially selected data range. To redo one point, but leave the other point as is, click ‘Redo First Point’ or ‘Redo Second Point’ and then click on the graph. When satisfied with the selected data range, click ‘OK’.

On Selecting the Data Range

The stress response reaches a steady state when the stress amplitudes of each cycle are equal and the shape of the cycle repeats itself. In Figure 3-10, steady state is reached after the first peak, which is slightly smaller than the others. For best analysis, include only cycles that have reached equilibrium.

Example: Incorrect column settings

To illustrate a possible mistake with the settings of the Input Variables panel, an example is included here (Figure 3-11) in which the columns for the data have been incorrectly assigned. As shown in Figure 3-11, a straight line running through the graph is an immediate indication that something is wrong, since both stress and strain should be oscillating. In this example the time column was incorrectly specified as the strain column.

Example: Multiple strain-amplitudes in one data file

Figure 3-12 shows an example of more advanced data processing that can be done with MITlaos. This shows the data collected from a waveform test combined with a stepwise increases in amplitude (6 cycles at each strain-amplitude). The decreasing

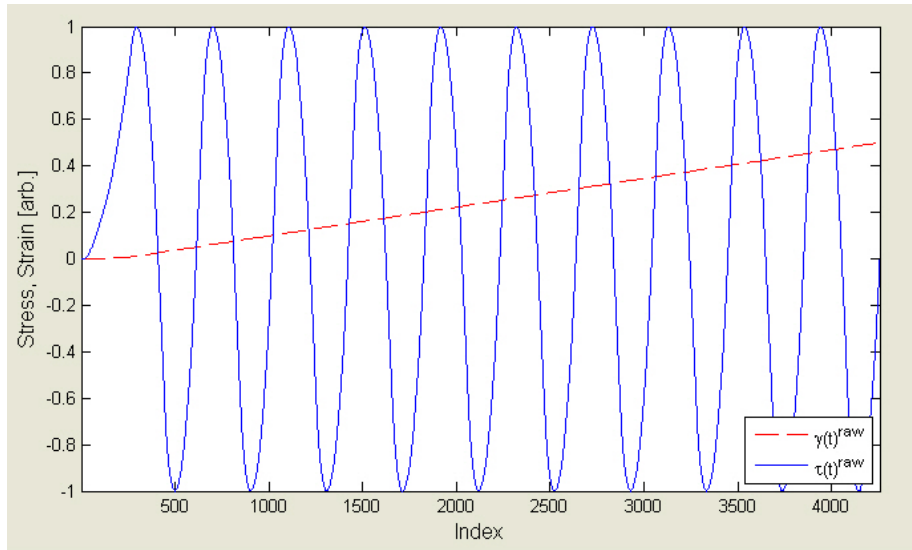


Figure 3-11: Data Set with Incorrectly Specified Columns.

stress amplitudes after each step show that the system has not reached equilibrium. MITlaos can not accurately process this entire set of data (Figure 3-12) due to the changing strain-amplitude. However, the data can manually be windowed to analyze one strain-amplitude at a time. This data set could then be used to separately analyze four different strain amplitudes. Note, however, that for best results it is recommended that the analysis be carried out on a system that has reached steady state.

Example data files are included with the distribution of MITlaos in the subfolder `...\MITlaos\subfunctions_MITlaos\`. A document in the same subfolder describes these example data files.

NOTE: The following 2 sections (Stress Filtering panel and Save panel) are OPTIONAL steps. Default values for these settings are provided when MITlaos is initialized. However, these settings are not optimal for all data.

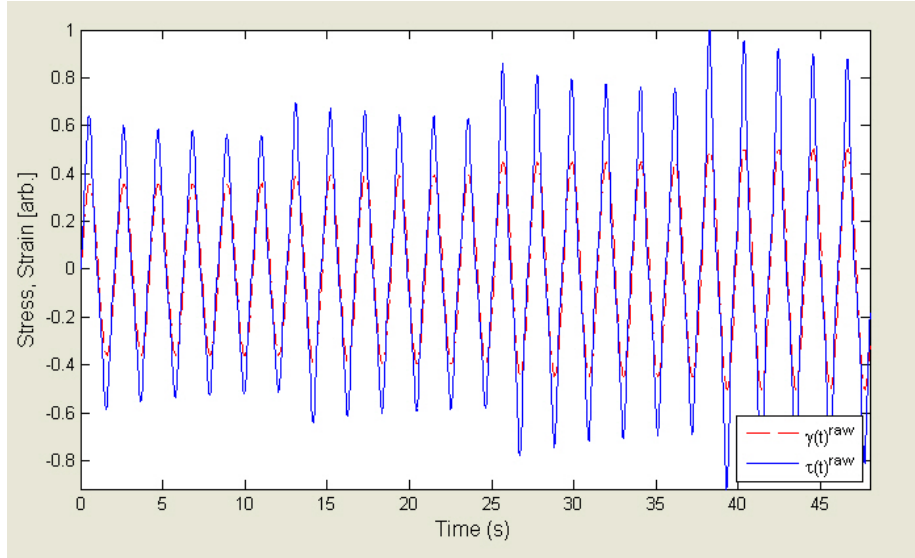


Figure 3-12: Data Set with a Stepwise Increase in Amplitude.

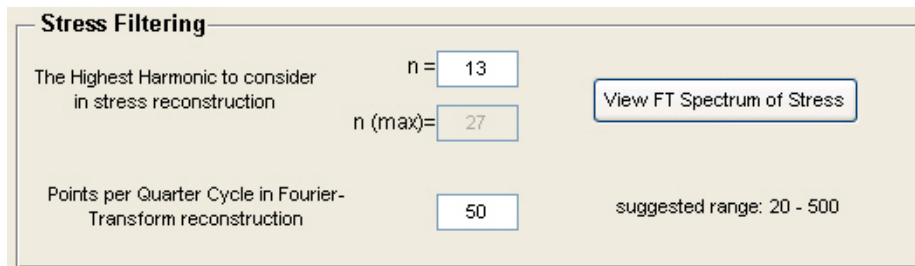


Figure 3-13: Stress Filtering panel.

3.7 Stress Filtering Panel

Stress signals are smoothed with the help of a Fourier Transform (FT). The raw stress signal is first decomposed into Fourier components. A linear viscoelastic response should have only one frequency component in its Fourier spectrum, whereas a nonlinear viscoelastic response will also contain higher harmonics. The smoothed stress signal is then reconstructed using only the odd, integer harmonics of the Fourier spectrum, since all other harmonics are the consequence of noise, unsteady oscillations, or systematic bias. This FT filtering technique eliminates noise and also aids in calculating nonlinear viscoelastic parameters. The Stress Filtering panel allows the user to change two options involved in this Fourier reconstruction (Figure 3-13).

The first setting is the value for n , the highest odd harmonic used in stress recon-

struction (i.e. $\omega_{\max} = n\omega$, where ω is the oscillatory test frequency). The maximum available value for n , labeled as ‘n (max)’ is displayed as well (this indicates the Nyquist frequency). The value of ‘n (max)’ is limited by the number of data points per cycle, and will be displayed as soon as a data range is chosen (see data windowing). Although ‘n (max)’ is the maximum possible value for n , it is common to use a lower n value than this.

Choosing a lower n will limit the number of harmonics used in the Fourier Transform (FT) reconstruction. If n is too low, the stress will be overly-smoothed and less accurate. However, if n is too high, random noise may be incorporated into the smoothed stress. For help on choosing the appropriate value for n , click the ‘View FT Spectrum of Stress’ button (see next subsection).

The second setting is the ‘Points per Quarter Cycle (PPQC) in Fourier-Transform reconstruction’. This value indicates the number of data points included in the reconstructed stress signal. A smaller number of points will decrease the resolution of the reconstruction, and a higher number of points will increase the file size. The default value is currently 50 PPQC, which is likely adequate to capture most nonlinearities. No limit is placed on size of the reconstructed Fourier-Transform, other than the operator’s ability to store the resulting data. Note that a smoothed stress signal with a large PPQC value may represent a higher time-resolution than is actually contained in the smoothed signal, since harmonics greater than n have been omitted.

View FT Spectrum of Stress

Clicking the ‘View FT Spectrum of Stress’ button opens the FTHarmonicGUI window (Figure 3-14). This window displays the Fourier Transform (FT) power spectrum of the raw stress signal, and provides the user with information to choose the appropriate value for n .

The FT spectrum will typically show a series of decreasing peaks that eventually fall into the noise floor at higher frequencies (note that a single peak at $n = 1$ is required for a linear viscoelastic response). Any data signal will have such a noise threshold. For Figure 3-14, the signal to noise ratio for the first harmonic is of the

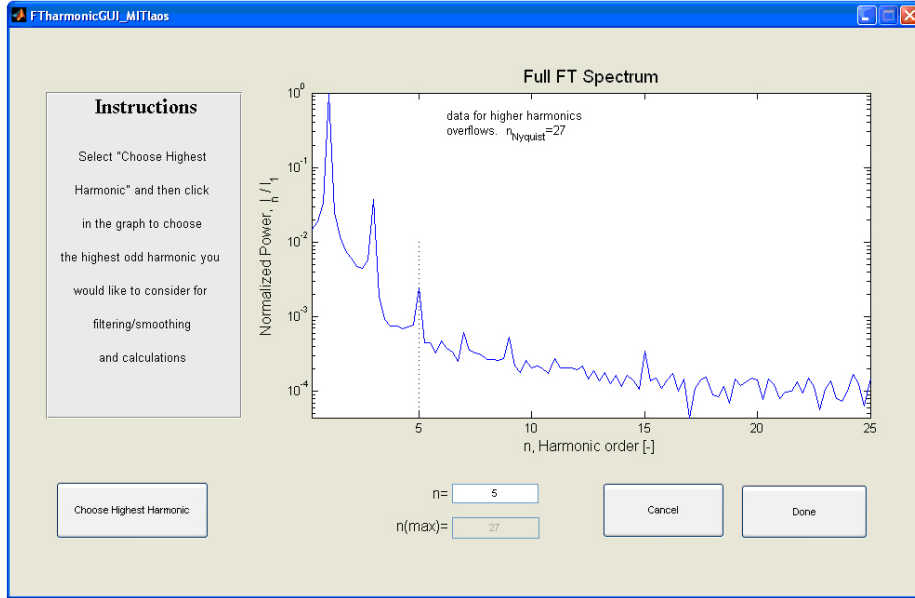


Figure 3-14: FTharmonicGUI window.

order $S/N \approx 10^4$.

An appropriate value for n , the highest harmonic to use in reconstruction, is typically a value which is low enough to avoid the noise floor, yet high enough to capture the viscoelastic nonlinearities. To select the desired n value, click the ‘Choose Highest Harmonic’ button. The pointer will turn into a set of crosshairs. Next, click on the graph at the desired n value, typically near the last big peak that stands out above the noise threshold (note that the vertical location of the crosshairs is irrelevant).

When the graph is clicked once, the value of n will automatically be rounded to the nearest odd integer and displayed in the box below the graph. The user may also manually type the desired value of n into this box.

3.8 Save Panel

The Save Panel (Figure 3-15) allows the user to select all the options for saving the analyzed data as figures and/or data files. No files will be saved until the ‘Analyze Data’ button is clicked, which is located at the bottom-right of the main window.

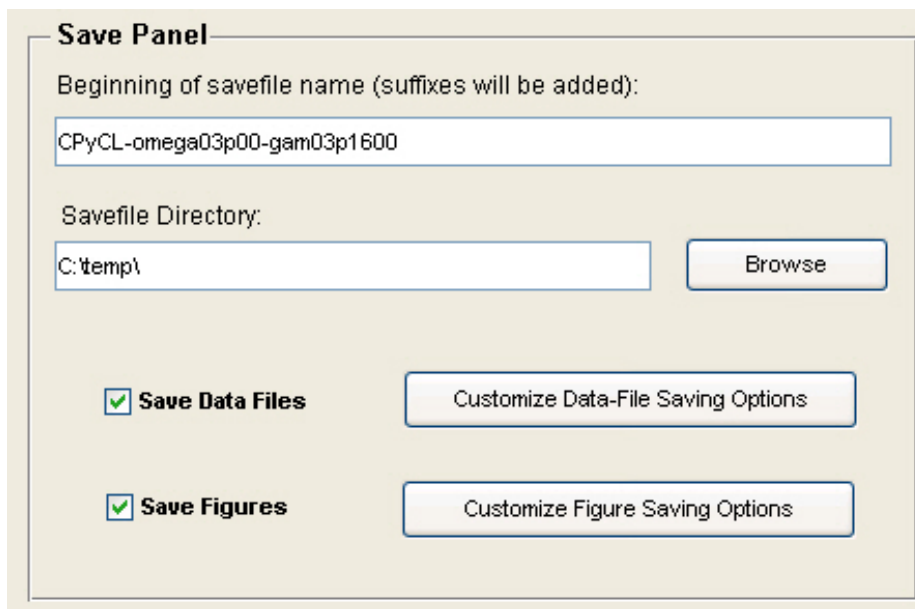


Figure 3-15: Save panel.

The data will be saved at the completion of the analysis.

The first edit box at the top of this panel allows the user to choose the beginning of the save file names. When the figures and data files are saved, each of their names will begin with the text in this box, and an appropriate suffix will be added to distinguish each file. This provides a simple way to group related files together. For example, when saving a JPEG image with suffix 'Figure1' (a setting located beneath the 'Customize Figure Saving Options' button), with the text of 'Beginning of save file name' as 'TestSample42', the final save file would be called 'TestSample42-Figure1.jpg'.

The second edit box determines the folder where figure and data output is saved. This can be chosen to be different than the original data file location.

The Save Data Files checkbox

This box must be checked to save any data files.

The Save Figures checkbox

This box must be checked to save any image files.

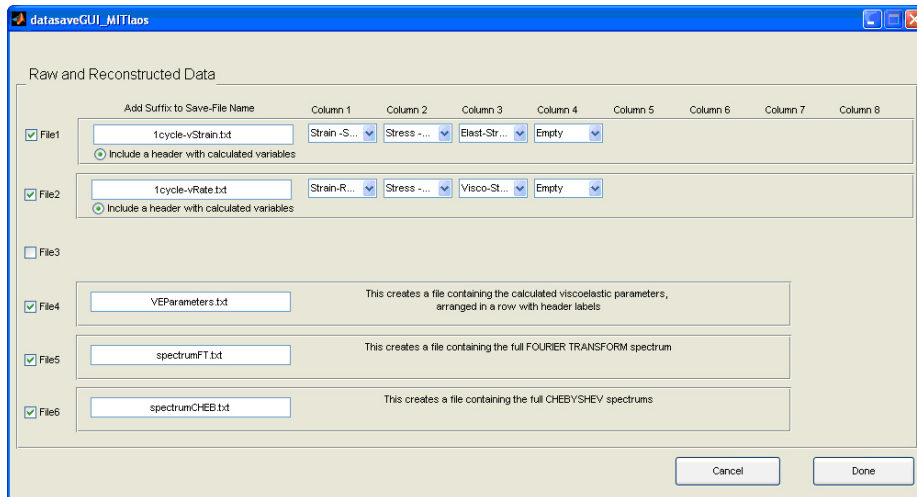


Figure 3-16: datasaveGUI window.

Details regarding the ‘Customize Data-File Saving Options’ and ‘Customize Figure Saving Options’ buttons are discussed in the following two subsections.

Customize Data-File Saving Options

When the ‘Customize Data-File Saving Options’ button is clicked, the datasaveGUI window opens, allowing the user to specify the layout and format of the saved data files (Figure 3-16).

The check boxes labeled ‘File 1’, ‘File 2’, etc. determine if each file will be saved. ‘File 1’, ‘File 2’, and ‘File 3’ are intended to contain columns of time-series data, the layout of which can be modified by using the dropdown menus associated with each file. ‘File 4’, ‘File5’, and ‘File6’ have fixed formats, since they contain the calculated viscoelastic parameters. All data files have a default file extension .txt, but this may be changed by the user.

The layout of ‘File 1’ will be determined by the box immediately to the right of the ‘File 1’ checkbox. The window shown in Figure 3-16 indicates here that ‘File 1’, ‘File 2’, ‘File 4’, ‘File5’, and ‘File6’ will all be saved. Since the ‘File 3’ checkbox is unchecked, it will not be saved and none of its information is displayed in the window.

The edit boxes underneath the header ‘Add Suffix to Save-File Name’ will deter-

mine the last part of each filename. Note that the beginning of each save file name will be identical, and can be changed in the Main Window under the Save Panel. In Figure 3-16, 'File 1' will be saved under a name ending with '1cycle-vStrain.txt'.

Files 1-3 have selectable round circles labeled 'Include a header with calculated variables' located under the save file name edit boxes. When this option is selected, a 29 line header will be printed in the file which specifies all the calculated viscoelastic parameters of the processed data.

The 'Column #' drop down menus to the right allow the choice of time-series data to be saved in each column. The drop down menu underneath the words 'Column 1' and to the right of 'File 2' will change the first column saved in the second file. Up to eight different columns can be specified for each save file.

File 4 is permanently set to create a save file containing all the calculated viscoelastic parameters, and contains two rows of text. The first row includes a text description for each parameter and the second row contains the numerical values for each parameter. This layout was chosen so that other programs could be written to easily access these viscoelastic parameters.

File 5 and File 6 are permanently set to output the Fourier Transform spectrum and the Chebyshev spectrums. The FT spectrum may contain non-integer harmonics, but the Chebyshev spectrum will contain only integer harmonics.

NOTE: If the 'Save Data Files' checkbox in the main window is not checked, none of these files will be saved regardless of what options are chosen.

Customize Figure Saving Options

The 'Customize Figure Saving Options' button opens the figuresaveGUI window (Figure 3-17). The check boxes on the left allow the choice of which figures to save. The dropdown menus underneath the header 'Image Format' allow the choice of saving each figure as JPEG or TIFF format.

The edit boxes underneath the header 'Suffix to Append to File Name' will determine the last part of the name for each file. Note that the beginning of each save

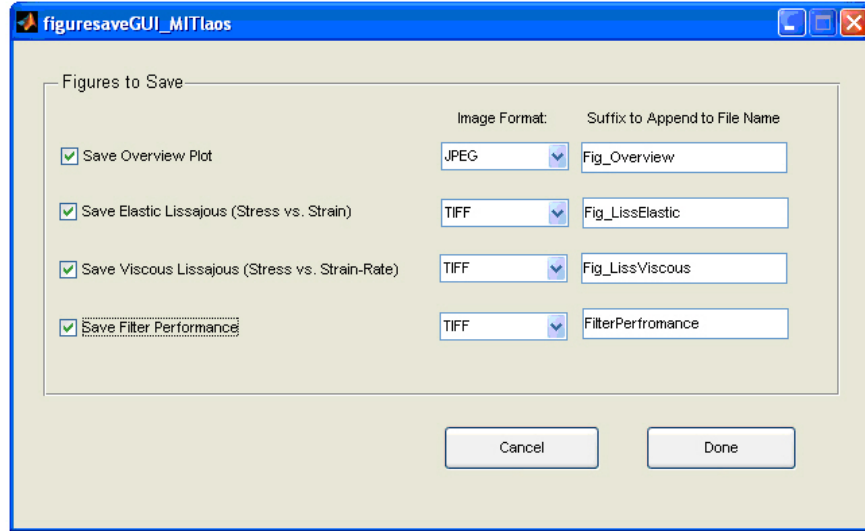


Figure 3-17: figuresaveGUI window.



Figure 3-18: Main Program Buttons.

file name will be identical, and can be changed in the Main Window under the Save panel. As prescribed in Figure 3-17, the overview plot will be saved under a name ending with 'Fig_Overview.JPEG'.

NOTE: If the 'Save Figures' checkbox in the main window is not checked, none of these figures will be saved regardless of the selected options.

3.9 Main Buttons

Once all of the details are specified, the analysis is initialized by clicking the 'Analyze Data' button, at the lower-right corner of the MITlaos main window (Figure 3-18).

Quit:

Exits MITlaos and closes main window.

Analyze Data

This processes the selected data, using the chosen analysis options, and saves the specified figures and data files. Figures chosen for saving will also be displayed on screen for viewing.

Note that inputs in the MITlaos main window are only reset if MITlaos is closed and re-opened. This allows the user to

1. Tweak processing parameters, and quickly reprocess the data with the ‘Analyze Data’ button
2. Select a different input data file while keeping the same processing parameters. This allows for quick subsequent processing of multiple data files.

NOTE: An over-abundance of figures may remain on screen when subsequently processing many data sets, thus slowing the processing. All figure files may be conveniently closed by typing ‘close all’ at the MATLAB command prompt. All of the figures will close, and the main MITlaos window will remain open.

3.10 Additional function: Plot3D

Plot3D is an additional tool for inspecting Lissajous curve trajectories in the 3D space with strain, strain-rate, and stress as the coordinate axes. Within this 3D space, three curves are shown: elastic stress, viscous stress, and total stress. The user can explore various views of the viscoelastic response within this 3D space. A screenshot of the plot3D user interface is shown in Figure 3-19.

View Options

Three default view options are available, accessible by three buttons under View Options:

- Stress vs. Strain (elastic perspective)

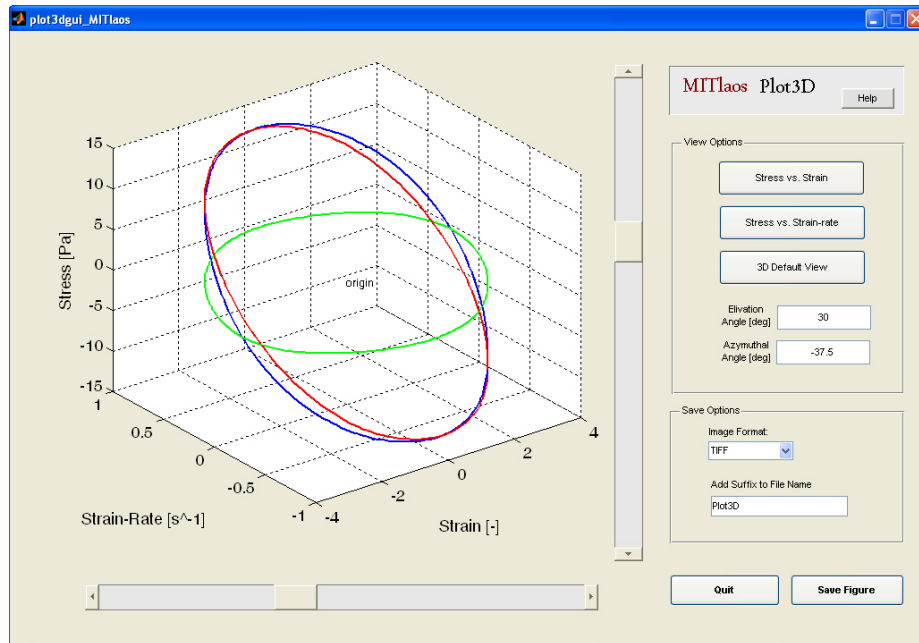


Figure 3-19: Plot3D user interface.

- Stress vs. Strain-rate (viscous perspective)
- 3D view (original view when plot3D starts)

The Azimuthal and Elevation viewing angles can be specified in the boxes under View Options. The view can be changed by typing a new angle (in units of degrees) and pressing Enter on the keyboard.

The slider bars on the bottom and right side of the display window can be used to change both the azimuthal and elevation angles. To continuously rotate the view, use the arrows at the edges of the slider bars. Dragging the indicator bars will also change the view, but will not result in a continuous change in perspective.

Save Options

The 'Image Format' dropdown menu allows the user to select either TIFF or JPEG image format for figure output.

The 'Add suffix to file name' textbox allows the user to modify the last portion of the filename for figure output. The destination folder and first portion of the filename are specified in the main MITlaos interface.

Save Figure

Outputs an image file of the current 3D view. The figure is saved and a new window is opened showing the saved image. If desired, the newly opened figure can be further modified using MATLAB's standard 3D-modification tools. This modified figure can be saved by accessing the 'File' dropdown menu and selecting the 'Save As' command

Chapter 4

LAOS ontology applied

4.1 Constitutive model examples

In this section I illustrate and reinforce the interpretation of the new quantitative framework presented in Chapter 2 with some idealized model examples.

4.1.1 Purely elastic strain-stiffening solid

Consider a purely elastic solid material, whose shearing behavior can be represented by the constitutive expression

$$\begin{aligned}\sigma &= f(\gamma) \gamma \\ f(\gamma) &= G_0 + G_\beta \left(\frac{\gamma}{\gamma^*} \right)^2\end{aligned}\tag{4.1}$$

where $f(\gamma)$ is the nonlinear elastic coefficient and γ^* is a critical strain beyond which nonlinear effects become significant. All nonlinear spring functions (e.g. FENE, wormlike chain, etc.) have leading order expansions of this form with expressions for G_β that vary with the chosen model; when G_β is positive the model is, by construction, strain-stiffening. It can be shown analytically (by using substitution and equating coefficients) that the decomposition of this nonlinear response results in the following

elastic Chebyshev coefficients

$$\begin{aligned} e_1 = G'_1 &= G_0 + \frac{3}{4} \left(\frac{\gamma_0}{\gamma^*} \right)^2 G_\beta \\ e_3 = -G'_3 &= +\frac{1}{4} \left(\frac{\gamma_0}{\gamma^*} \right)^2 G_\beta. \end{aligned} \tag{4.2}$$

All higher coefficients e_5, e_7 are zero as the function in Eq. 4.2 can be expressed exactly by the first two Chebyshev polynomials. As we expect for elastic strain-stiffening, e_3 is positive. However, because of the functional form of the Chebyshev basis functions the material nonlinearity corresponding to G_β is distributed between the first and third order terms. Accordingly, the first harmonic Fourier component G'_1 in fact represents a combination of both the zero-strain elastic modulus and a contribution from this nonlinear term[33]. In the limit of small imposed strain amplitudes, $\gamma_0 \ll \gamma^*$, $e_1 = G'_1 \rightarrow G_0$ and $e_3 \rightarrow 0$ as we expect. It is clear that the first Chebyshev coefficient $e_1 = G'_1$ could be used to indicate inter-cycle stiffening if multiple data points were plotted against strain amplitude, but the degree of intra-cycle strain-stiffening is immediately apparent from one data point as indicated by the sign of e_3 . It is also noteworthy that the third order Chebyshev and Fourier coefficients contain only 1/4 of the total nonlinear contribution to the stress amplitude. Thus, simply considering the magnitude of the third harmonic (e_3 or e_3/e_1) significantly underestimates the actual nonlinear contribution to the material response.

In contrast to the first-order Fourier elastic modulus, the alternative measures for reporting elastic modulus, G'_M and G'_L , distinctly capture the small-strain elasticity $f(\gamma \rightarrow 0)$ and the large-strain elasticity $f(\gamma \rightarrow \gamma_0)$, respectively. That is,

$$G'_M = \sum_{n \text{ odd}} n G'_n = e_1 - 3e_3 = G_0 \tag{4.3}$$

$$G'_L = \sum_{n \text{ odd}} G'_n (-1)^{n-1/2} = e_1 + e_3 = G_0 + \left(\frac{\gamma_0}{\gamma^*} \right)^2 G_\beta. \tag{4.4}$$

Thus, the minimum-strain modulus $G'_M = f(\gamma = 0)$ equates to the zero-strain elasticity, whereas the large-strain modulus $G'_L = f(\gamma = \gamma_0)$ captures the large strain

elasticity. Furthermore, the strain-stiffening ratio S correctly captures the true relative magnitude of the intra-cycle strain-stiffening,

$$S = \frac{\left(\frac{\gamma_0}{\gamma^*}\right)^2 G_\beta}{G_0 + \left(\frac{\gamma_0}{\gamma^*}\right)^2 G_\beta} \quad (4.5)$$

where $S \rightarrow 0$ in the limit of $\gamma_0 \ll \gamma^*$.

This simple example demonstrates how the interpretation of these new elastic material measures extract the key features of a nonlinear elastic response, and they can now be applied to any unknown material or constitutive model.

4.1.2 Purely viscous shear-thinning fluid

We next consider a purely viscous, but nonlinear, constitutive equation represented by

$$\begin{aligned} \sigma &= g(\dot{\gamma}) \dot{\gamma} \\ g(\dot{\gamma}) &= \eta_0 - \eta_\beta \left(\frac{\dot{\gamma}}{\dot{\gamma}^*}\right)^2 \end{aligned} \quad (4.6)$$

where $\dot{\gamma}^*$ is a critical strain-rate for shear-thinning to appear. This constitutive equation for shear stress is that of a generalized Newtonian fluid (GNF) and in particular it is an example of a Third-Order Fluid in simple shear[8]. Any GNF model (in which viscosity can be written as a function of shear-rate) has a Taylor series expansion in the form of Eq. 4.6. For example the Carreau model for the viscosity coefficient has the following expression for $g(\dot{\gamma})$ and associated Taylor expansion

$$g(\dot{\gamma}) = \eta_\infty + (\eta_0 - \eta_\infty) \left[1 + \left(\frac{\dot{\gamma}}{\dot{\gamma}^*}\right)^2\right]^{\frac{n-1}{2}} \simeq \eta_0 - \frac{1-n}{2} (\eta_0 - \eta_\infty) \left(\frac{\dot{\gamma}}{\dot{\gamma}^*}\right)^2 + \dots \quad (4.7)$$

Eq. 4.6 is only intended to represent the initial deviation from linear behavior observed in a real material. It applies only for small values of $\dot{\gamma}_0$ such that shear stress is always

monotonically increasing with shear-rate, i.e. $d\sigma/d\dot{\gamma} > 0$. This constrains the upper limit of oscillatory shear-rate amplitude in this example to values $\dot{\gamma}_0 < \dot{\gamma}^* (\eta_0/3\eta_\beta)^{1/2}$.

Applying the Chebyshev decomposition of Eq. 2.6 to Eq. 4.6 results in the following viscous material coefficients

$$\begin{aligned} v_1 = \eta'_1 &= \eta_0 - \frac{3}{4}\eta_\beta \left(\frac{\dot{\gamma}_0}{\dot{\gamma}^*}\right)^2 \\ v_3 = \eta'_3 &= -\frac{1}{4}\eta_\beta \left(\frac{\dot{\gamma}_0}{\dot{\gamma}^*}\right)^2. \end{aligned} \quad (4.8)$$

As expected, for shear-thinning the 3rd order viscous Chebyshev coefficient v_3 is negative. Again, the nonlinearity is distributed between the first and third order terms, whereas the alternative measures for reporting the first order viscous contribution, η'_M and η'_L , distinctly represent the instantaneous zero-rate and maximum-rate viscosities, respectively

$$\eta'_M = \frac{1}{\omega} \sum_{n \text{ odd}} n G''_n (-1)^{n-1/2} = v_1 - 3v_3 = \eta_0 \quad (4.9)$$

$$\eta'_L = \frac{1}{\omega} \sum_{n \text{ odd}} G''_n = v_1 + v_3 = \eta_0 - \eta_\beta \left(\frac{\dot{\gamma}_0}{\dot{\gamma}^*}\right)^2. \quad (4.10)$$

Thus, the minimum-rate dynamic viscosity accurately captures the viscous material coefficient at zero shear-rate, $\eta'_M = g(\dot{\gamma} = 0) = \eta_0$ (i.e. the zero-shear rate viscosity), whereas the large-strain-rate dynamic viscosity represents the viscous material coefficient at maximum strain-rate, $\eta_L = g(\dot{\gamma} = \dot{\gamma}_0)$. Finally, the shear-thickening index equates to

$$T = \frac{\eta'_L - \eta'_M}{\eta'_L} = \frac{-\eta_\beta \left(\frac{\dot{\gamma}}{\dot{\gamma}^*}\right)^2}{\eta_0 - \eta_\beta \left(\frac{\dot{\gamma}}{\dot{\gamma}^*}\right)^2} \quad (4.11)$$

which will have a negative value for a shear-thinning fluid. As we noted above, these new viscous material measures can now be applied to any unknown material or constitutive model.

4.1.3 Nonlinear viscoelastic Giesekus model

The purely elastic and purely viscous models above can be superposed to construct a nonlinear model of Kelvin-Voigt form, $\sigma = f(\gamma)\gamma + g(\dot{\gamma})\dot{\gamma} = \sigma' + \sigma''$. For this simple nonlinear viscoelastic solid model, the elastic and viscous contributions will decompose exactly as shown previously, since the geometrical interpretation (stress decomposition) is immediately apparent by construction. To look beyond the simple decomposition of a nonlinear Kelvin-Voigt model we consider a prototypical nonlinear viscoelastic constitutive equation such as the Giesekus model which is commonly used for constitutive modeling of nonlinear viscoelastic fluids (see for example [51, 52]). We examine the output of numerical simulations of this model in LAOS flow to illustrate our new interpretation and nomenclature (intra- and inter-cycle nonlinearities, stiffening/softening, and thickening/thinning) with the application of the Chebyshev decomposition and 2-D Pipkin diagrams.

The constitutive equation for the Giesekus model, as presented by [8], is given by

$$\begin{aligned}\boldsymbol{\sigma} &= \boldsymbol{\sigma}_s + \boldsymbol{\sigma}_p \\ \boldsymbol{\sigma}_s &= \eta_s \dot{\boldsymbol{\gamma}} \\ \boldsymbol{\sigma}_p + \lambda_1 \boldsymbol{\sigma}_{p(1)} + \alpha \frac{\lambda_1}{\eta_p} \{\boldsymbol{\sigma}_p \cdot \boldsymbol{\sigma}_p\} &= \eta_p \dot{\boldsymbol{\gamma}}.\end{aligned}\tag{4.12}$$

Here $\boldsymbol{\sigma}_s$ is the solvent stress tensor, $\boldsymbol{\sigma}_p$ is the polymer stress tensor, $\boldsymbol{\sigma}_{p(1)}$ is the upper convected time derivative of the polymer stress, η_s is the solvent viscosity, η_p is the polymer viscosity, λ_1 is the relaxation time, and α is the mobility factor which gives rise to a nonlinear viscoelastic response (for $\alpha \neq 0$). In the linear viscoelastic regime, the Giesekus model reduces to the linear Jeffreys model. The mechanical analog of the Jeffreys model is a Maxwell element representing the polymer (i.e. a spring in series with dashpot) in parallel with a Newtonian solvent (dashpot).

The Giesekus model was simulated under imposed oscillatory simple shear strain, $\gamma_{yx} = \gamma_0 \sin \omega t$, across a range of frequencies and strain amplitudes using the following model parameters, $\lambda_1 = 1$ s, $\eta_s = 0.01$ Pa.s, $\eta_p = 10$ Pa.s, and $\alpha = 0.3$. These four independent parameters result in a retardation time scale $\lambda_2 = \lambda_1 \eta_s / (\eta_s + \eta_p) = 0.001$ s

and a polymer shear modulus $G = \eta_p/\lambda_1 = 10$ Pa. The coupled system of differential equations was solved numerically with MATLAB for the range of $De_1 = \lambda_1\omega = [10^{-2}, 10^3]$ and $\gamma_0 = [10^{-3}, 10]$. The ‘ode15s’ multistep solver was used with relative and absolute tolerances of 10^{-10} , and a maximum time step $t_{max} = (0.004)2\pi/\omega$ to ensure at least 250 points per cycle. Integration was continued until a steady oscillatory response was achieved (the shorter of $t = 18\lambda_1$ or $N = 1000$ cycles). For analysis of viscoelastic parameters, the final 10 oscillation periods were used (see Section 4.2.1 regarding data filtering and processing). The nonlinear term involving α in the polymer stress equation contributes to rich phase behavior in the 2-dimensional (ω, γ_0) parameter space (i.e. the Pipkin space). Material measures can be plotted as surfaces or contours within the Pipkin diagram [47, 53, 54, 55]. Two dimensional rheological fingerprints of the Giesekus model, as represented by contour plots of G'_1 , η'_1 , e_3/e_1 , v_3/v_1 , and $I_3/I_1 = |G_3^*|/|G_1^*|$ are given in the Pipkin diagrams of Figure 4-1.

The linear viscoelastic regime is indicated first by the vertical contour lines in Figure 4-1a,b which show that G'_1 and η'_1 are independent of strain amplitude γ_0 . The linear regime is more strictly confirmed by Figure 4-1c,d,e which show the regions in which e_3/e_1 , v_3/v_1 , and I_3/I_1 are negligibly small. A linear scale is used for e_3/e_1 and v_3/v_1 to emphasize the sign of the nonlinearity which is needed for a physical interpretation. It is observed that e_3/e_1 and v_3/v_1 are more sensitive indicators of material nonlinearities than I_3/I_1 , since the third-order Chebyshev coefficients reach values of 0.001 at smaller strain amplitudes. The lower sensitivity of I_3/I_1 is attributed to the comparison of the total nonlinearity with the total magnitude of the fundamental harmonic, which allows a nonlinear subdominant component to be masked by a linear dominant component, e.g. a finite e_3/e_1 may be obscured if $v_1\omega \gg e_1$, since $I_3/I_1 = \sqrt{e_3^2 + (v_3\omega)^2} / \sqrt{e_1^2 + (v_1\omega)^2}$.

The linear viscoelastic (Jeffreys-like) response of the Giesekus model is observed for sufficiently small strain amplitude γ_0 . In Figure 4-1a the elastic modulus plateaus at the value of the polymer modulus ($G'_1 \rightarrow G = 10$ Pa) for $De_1 = \lambda_1\omega \gg 1$, $\gamma_0 \ll 1$. In Figure 4-1b the low frequency dynamic viscosity plateaus at the total steady viscosity $\eta'_1 \rightarrow \eta_s + \eta_p = 10.01$ Pa ($De_1 = \lambda_1\omega \ll 1$, $\gamma_0 \ll 1$). At sufficiently

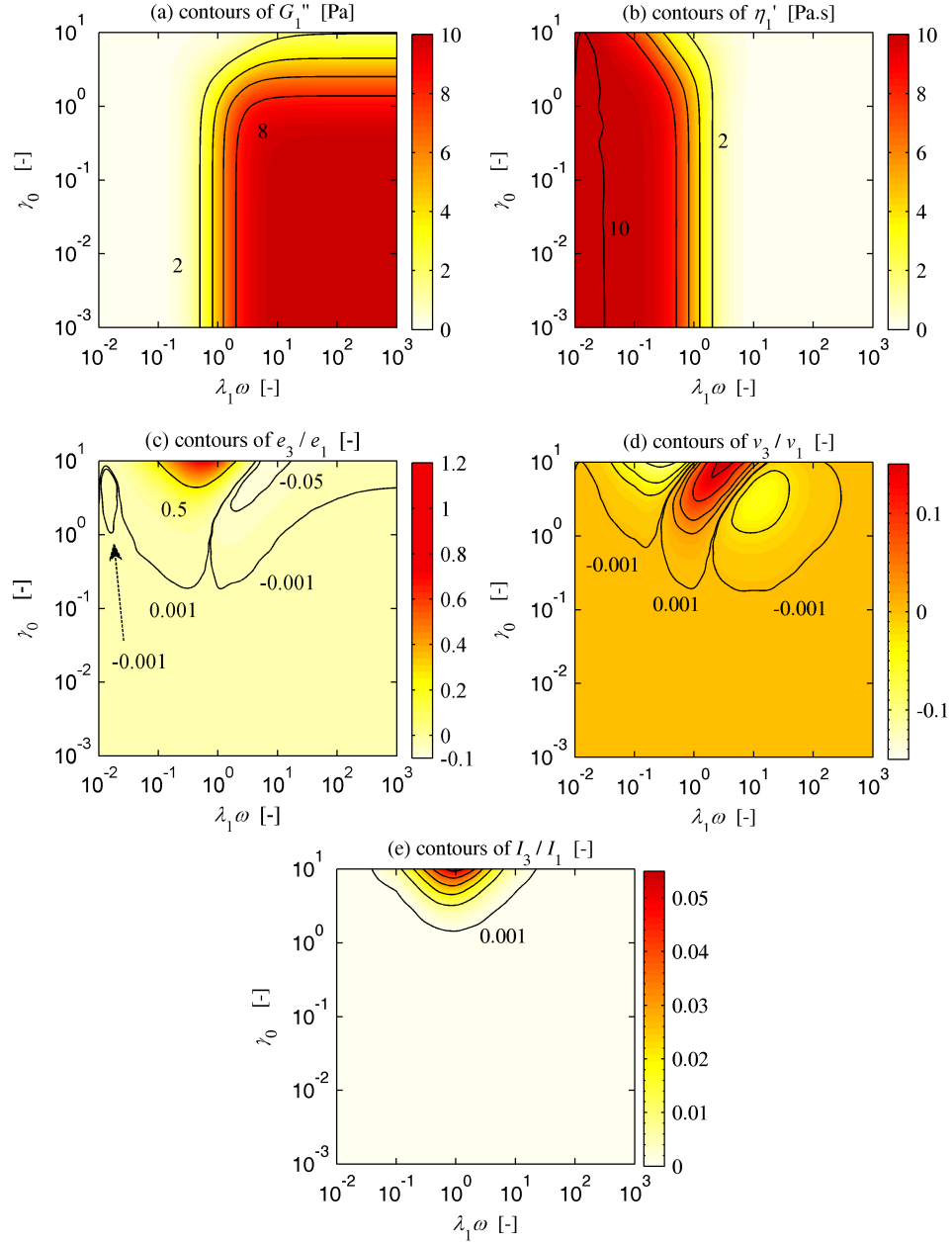


Figure 4-1: Pipkin diagram plots of resulting viscoelastic parameters for a simulated nonlinear viscoelastic fluid (Giesekus model, $\lambda_1 = 1$ s, $\eta_s = 0.01$ Pa.s, $\eta_p = 10$ Pa.s, and $\alpha = 0.3$); (a) first order elastic modulus G_1'' , contours shown at increments of 2 Pa (b) first order dynamic viscosity η_1' , contours shown at increments of 2 Pa (c) normalized third-order elastic Chebyshev coefficient e_3/e_1 , contours as labeled, (d) scaled third-order viscous Chebyshev coefficient v_3/v_1 , contours shown at ± 0.001 , ± 0.025 , ± 0.05 , ± 0.1 , and ± 0.15 , and (e) normalized intensity of the third harmonic I_3/I_1 , contours shown at 0.001, and increments of 0.01.

high frequencies ($De_1 = \lambda_1\omega \gg 1$, $\gamma_0 \ll 1$) we expect only the solvent viscosity to contribute to the dissipation, such that $\eta'_1 \rightarrow \eta_s = 0.01$ Pa.s, which is shown by the lower plateau for η'_1 in this region.

The boundary demarcating the limits of the linear regime is a function of frequency, as clearly seen from the contour plots in Figure 4-1. For example, the linear viscoelastic regime extends to larger strain amplitudes γ_0 at lower frequencies. Indeed, at sufficiently low frequency one would expect a viscoelastic fluid to be dominated by its viscous characteristics. Thus nonlinearities at low frequency are triggered by a critical strain-rate amplitude $\dot{\gamma}_0$, rather than strain amplitude γ_0 . Lines of constant strain-rate amplitude, such that $\dot{\gamma}_0 = \gamma_0\omega = \text{constant}$, would appear as diagonal lines of slope=-1 from the upper left to the lower right of the Pipkin diagrams in Figure 4-1. The contours of the first-order dynamic viscosity η'_1 (Figure 4-1b) reflect this response and show that a critical strain-rate triggers nonlinear effects at low frequency ($De_1 < 1$). At these low frequencies the viscous nonlinearities of the Giesekus model become apparent near a Weissenberg number $We_1 = \lambda_1\omega\gamma_0 \leq 1$. Conversely, at higher frequency, $De_1 > 1$ when the fluid is dominated by elasticity, the nonlinear regime is determined by a critical strain amplitude γ_0 , as seen by the horizontal contours in Figure 4-1a ($De \gg 1$).

The inter-cycle nonlinearities (i.e. the dependence of the material response on the imposed values of γ_0 or $\dot{\gamma}_0$), are indicated by the gradients of the contours in Figure 4-1. Strain-softening results in a progressive decrease in the magnitude of the elastic modulus G'_1 for strains $\gamma_0 > 1$ (Figure 4-1a), i.e. the average elasticity decreases with strain-amplitude. This softening occurs more readily at higher frequencies. The fact that the contours of $G'_1(\omega, \gamma_0)$ are not self similar is an indication that the relaxation modulus of the Giesekus model cannot be written in a time-strain separable form, i.e. $G'_1(\omega, \gamma_0) \neq G'(\omega)h(\gamma_0)$ [56]. Figure 4-1b captures the inter-cycle nonlinearity of the average viscous dissipation, showing inter-cycle shear-thinning of η'_1 . Inter-cycle shear-thinning is not observed in the higher frequency regime, presumably because at sufficiently high frequencies only the Newtonian solvent dissipates energy and the viscous response becomes linear once more (i.e. $|v_3/v_1 < 10^{-3}|$), even for large am-

plitudes up to $\gamma_0 = 10$.

The contours of the normalized third-order Chebyshev coefficients e_3/e_1 and v_3/v_1 (Figure 4-1c,d) give deeper insight into the viscoelastic nonlinearities of the Giesekus model. At any given location (ω, γ_0) in the Pipkin diagram, these Chebyshev coefficients quantify the intra-cycle nonlinearities (i.e. the nonlinearities in the material response within a steady oscillatory cycle). Elastic nonlinearities are revealed in Figure 4-1c where regions of both intra-cycle strain-stiffening and intra-cycle strain-softening are present, as indicated by the sign of e_3/e_1 being positive or negative, respectively. Intra-cycle strain-softening is predominant at higher frequency. The onset of this strain-softening appears to be mediated primarily by the strain-amplitude at the highest frequencies, as shown by the nearly horizontal contours of e_3/e_1 at high frequency. Intra-cycle stiffening is observed at moderate to low frequencies, creating a region where the sign of e_3/e_1 must change from negative to positive. Thus, a contour of e_3/e_1 exists at large strain-amplitudes, showing that an individual oscillatory response may appear to be linearly elastic even deep into the nonlinear viscoelastic regime. To fully explore viscoelastic material nonlinearity it is thus essential to perform a full series of frequency and strain amplitude sweeps. The intra-cycle viscous nonlinearities of Figure 4-1d show two regions of intra-cycle shear-thinning ($v_3/v_1 < 0$) and one region of intra-cycle shear-thickening ($v_3/v_1 > 0$). This necessitates two transition regions where v_3/v_1 changes sign, again demonstrating that even at large amplitudes the intra-cycle response can be linearly viscous.

The Giesekus model response is determined by four model parameters ($G, \lambda_1, \alpha, \eta_s$). However, the response to a range of deformations (ω, γ_0) is not immediately apparent from inspection of the constitutive equation and knowledge of the values of these parameters. We have used our new framework (physically meaningful measures of nonlinearity, contour plot “fingerprints” of the material coefficients, and unambiguous nomenclature) to characterize the response of the Giesekus model under imposed oscillatory shear deformation, and can smoothly map the steady flow, linear viscoelastic, and nonlinear viscoelastic response. Our framework is able to describe the nonlinear viscoelastic response in general terms, i.e. without *a priori* knowledge of

the material behavior in LAOS. Thus, the scheme can be applied to both constitutive models and experimental data, providing physically meaningful measures for comparison. Furthermore, the physical insight gained from examining experimental data in this way may help motivate the selection of an appropriate constitutive model. We now proceed by using our new framework to describe experimental measurements of the material response in two representative complex fluids.

4.2 Experimental examples

To illustrate the experimental utility of our proposed new framework for describing LAOS tests, we apply it to data taken with a wormlike micellar solution and a natural biopolymeric hydrogel, gastropod pedal mucus. These analytic techniques may be applied to any rheologically complex material that is subjected to oscillatory simple shearing deformation.

4.2.1 Materials and Methods

Materials

Slugs were collected in Cambridge, MA, kept in an indoor terrarium maintained at room temperature, and supplied with a diet of green leaf lettuce. Pedal mucus was collected by placing a slug on a glass plate and enticing it to crawl with a piece of food. Trail mucus was collected after the slug had crawled more than one body length to ensure that no debris remained in the sample.

The wormlike micelle solution (prepared as in [57]) consists of cetylpyridinium chloride (CPyCl) and sodium salicylate (NaSal) dissolved in brine. The ratio of CPyCl/NaSal is 100 mM/50 mM (3.2 wt%/0.76 wt%) in a 100 mM (0.56 wt%) NaCl aqueous solution.

Rheometry

All experiments were performed on a strain-controlled ARES rheometer (TA Instruments) equipped with a Peltier plate maintained at $T=22^{\circ}\text{C}$, using a solvent trap to inhibit evaporation. The pedal mucus was tested with a plate-plate geometry (diameter $D = 8$ mm, gap $h = 550\mu\text{m}$). To eliminate slip, the plate-plate surfaces were covered with adhesive-backed waterproof sandpaper, 600 grit (ARC Abrasives Inc). The micellar solution was tested with a cone-plate geometry (diameter $D = 50$ mm, cone angle $\theta = 0.0402\text{rad} = 2.30^{\circ}$, truncation $48.8\mu\text{m}$).

Data acquisition

The analysis requires raw strain and stress signals. However, the standard oscillatory test setup available from the instrument control software (TA Orchestrator software) does not capture raw stress and strain waveforms; it only outputs the calculated viscoelastic parameters such as “elastic modulus” G' . In order to capture the stress and strain waveforms under oscillation we used the Arbitrary Waveshape Test capability of the TA Orchestrator software. With this test procedure the user can specify an equation for the strain input, and the raw strain and stress waveforms are saved to a data file. Note that this test procedure is part of the standard software which accompanies every ARES rheometer, making the technique broadly accessible to ARES users. Another option for capturing the time series waveforms, on the ARES and also some other rheometers, is to connect to voltage outputs of torque and displacement. Although higher sampling rates and larger signal to noise ratios may be obtained by collecting oversampled raw voltage signals of torque and displacement output [15, 58], the Arbitrary Waveshape Test has the advantage of directly collecting stress and strain data (rather than voltages) and does not require additional hardware such as an Analog-to-Digital Converter. Maximum sampling rates of the Arbitrary Waveshape Test were adequate for our experiments, with a maximum sampling rate near 100 samples/s. Multiple steady-state waveforms were used for data analysis (typically 4 cycles) at each coordinate pair (ω, γ_0) .

Data filtering and processing

In preparation for Fourier transform (FT) processing, strain and stress data signals were first trimmed to contain an integer number of cycles, N , by identifying the zero crossings of the strain signal. The discrete FT operation further requires that the strain and stress signals have data points which are equally spaced in time. Linear time spacing was inherent in the data collected experimentally, as a result of the analog to digital converter within the rheometer. However, the numerical integration routines used for the Giesekus simulation utilized a variable time stepper, and consequently the output strain and stress signals were interpolated to create data with equal time spacing. The prepared data signals were then analyzed with the 'fft' function in MATLAB which returns the discrete Fourier transform of the input vector, from which the trigonometric Fourier coefficients were determined (note that a vector with 2^m data points is *not* required for this operation). The resulting Fourier spectrum contains discrete information for frequencies up to the Nyquist frequency $\omega_{\text{Nyquist}} = \omega_1 n/2$, where ω_1 is the imposed frequency and n is the number of data points per cycle, with a frequency resolution $\Delta\omega = \omega_1/N$, where N is the integer number of cycles.

The trimmed strain signal has a small but finite phase lag (imaginary component), since the first data point is not identically zero but instead a small positive number. This phase lag of the strain signal must be considered for precisely calculating the Fourier coefficients G'_n, G''_n . These Fourier coefficients are then directly used to calculate viscoelastic parameters such as G'_M and G'_L . The Fourier coefficients are particularly convenient for calculating parameters such as the minimum-strain modulus G'_M . This parameter would otherwise need to be calculated as the slope of a line via numerical differentiation (Figure 2-4), but the experimental error is substantially reduced by calculating tangent properties such as G'_M and η'_M from the odd-harmonic Fourier coefficients as shown in Eqs. 2.10 and 2.12. The Chebyshev coefficients, e_n, v_n are also calculated from the Fourier spectrum c.f. Eqs. 2.7 and 2.8, since this avoids the multiple processing steps of stress decomposition (Eqs. 2.3

and 2.4), followed by the determination of Chebyshev coefficients using numerical integration of the corresponding orthogonality relation (see Appendix A) combined with Eqs. 2.5 and 2.6.

The stress decomposition of Cho et al. [28] is also conveniently calculated from the odd, integer Fourier coefficients using Eqs. 2.3 and 2.4. This stress decomposition is typically calculated by using the “find-and-subtract” method given by the first portion of Eqs. 2.3 and 2.4 [28, 59]. The find-and-subtract method is easily implemented with simulated data [59], but is more difficult to use with real experimental data sets because of two principal difficulties. First, it is unlikely that the available set of data points will have the appropriate strain/strain-rate symmetry, which necessitates the use of local interpolation methods. Second, subtracting two individual data points (from a data series that has not been smoothed or filtered) results in amplification of random noise. Accordingly, the elastic stress $\sigma'(\gamma)$ and viscous stress $\sigma''(\dot{\gamma})$ curves may not appear as smooth lines, but rather as scatter plots. Thus, in contrast to the findings of Kim et al. [59], we find that the discrete Fourier transform approach provides greater accuracy than the find-and-subtract methodology. Using the odd, integer Fourier coefficients to construct the individual elastic and viscous stress contributions (Eqs. 2.3 and 2.4) eliminates both the problem of interpolation and noise amplification, resulting in smooth processed data containing corresponding information from the entire periodic stress signal (one may also consider reconstructing the strain and total stress time data from the FT coefficients, and thereafter using the Cho et al. subtraction algorithm, but an identical output is more quickly obtained by directly using Eqs. 2.3 and 2.4). Strain and strain-rate signals are also constructed to have data points at spacing which corresponds to the stress decomposition signals; the first-harmonic coefficients of the strain signal are used for this reconstruction.

Furthermore, we construct a smoothed total stress signal by utilizing only the odd, integer-harmonic components, up to a cutoff frequency, c.f. Eq. 2.1. This process can be described as applying a discrete comb filter to the raw data, allowing only particular frequency components to pass through to the smoothed stress signal. Frequency information corresponding to even-harmonics and non-integer harmonics

are neglected in the signal reconstruction because they contain only random noise and are non-physical for a material response devoid of transients, dynamic wall slip, and secondary flows, as mentioned in Section 2.1. Selecting a cutoff frequency removes the high frequency components of the signal in which noise obscures any real signal. The use of multiple cycles N input to the FFT allows for data averaging, and an increase in the signal to noise ratio[60]. This data averaging of multiple cycles contributes to the digital filter’s ability to smooth the total stress signal.

4.2.2 Gastropod pedal mucus (a biopolymer hydrogel)

The apparent contradiction of the data shown in Figure 2-1 can be resolved by applying the framework introduced in Chapter 2. As shown in Figure 2-1, slug pedal mucus exhibits substantial intra-cycle strain-stiffening as suggested by the Lissajous-Bowditch curves of stress vs. strain (Figure 2-1b), but the elastic modulus, as captured by the first harmonic coefficient G'_1 , is approximately flat when plotted against strain-amplitude γ_0 (Figure 2-1a).

The inter-cycle variations of the elastic moduli are shown in Figure 4-2a where we plot G'_1 , G'_M , G'_L as a function of imposed strain amplitude γ_0 . It can be seen that these measures converge in the linear regime (though G'_M suffers from more experimental noise at these low strain amplitudes). The onset of material nonlinearity is indicated by the divergence of these three different measures of elastic modulus as the strain amplitude increases. In this biopolymer gel G'_M decreases with γ_0 (softening at small strains), whereas G'_L first decreases then increases, i.e. the large-strain elasticity of the network first softens then stiffens (see Figure 4-2a). The first-harmonic elastic modulus G'_1 falls between the two other measures, supporting its interpretation as an average measure of elasticity throughout the oscillatory cycle.

The intra-cycle nonlinearities which distort the familiar linear viscoelastic ellipse are also quantified (Figure 4-2c,d). Both S and e_3 are positive at the largest strain amplitudes (Figure 4-2c), indicating strain-stiffening. These indicators of nonlinearity should be equal to zero in the linear regime (c.f. Eq. 2.14). We see that the parameter S suffers more from noise than e_3 , due to the error in calculating G'_M which is in the

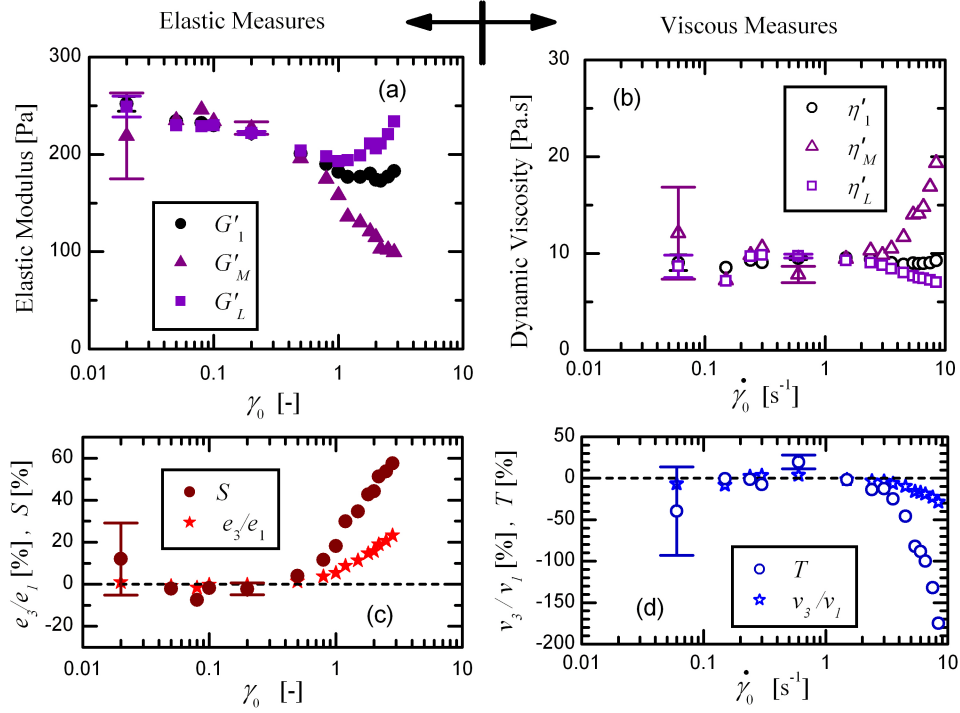


Figure 4-2: Oscillatory shear test of pedal mucus from Figure 2-1, $\omega = 3 \text{ rad.s}^{-1}$, analyzed within the new framework; (a) Elastic moduli: minimum-strain and large-strain elastic moduli compared to first harmonic elastic modulus (b) Dynamic viscosities: minimum-rate and large-rate dynamic viscosities compared to first harmonic dynamic viscosity, (c) Intra-cycle elastic nonlinearity measures: scaled 3rd order elastic Chebyshev coefficient e_3/e_1 and strain-stiffening ratio S , both indicate intra-cycle strain-stiffening; (d) Intra-cycle measures of viscous nonlinearity: 3rd order viscous Chebyshev coefficient v_3/v_1 and shear-thinning ratio T , both indicate intra-cycle shear-thinning. Error bars are determined from the noise in the Fourier spectrum and are shown for representative points. The data point size exceeds the error margins at larger amplitudes. For e_3/e_1 and v_3/v_1 (star symbols) the data point size exceeds the error for all amplitudes.

denominator of the calculation for S . However, both measures clearly indicate a strain-stiffening deviation from linear elasticity, with both measures taking positive values for large strain-amplitudes. This rich behavior in the elastic response of the gel is revealed and physically described only by the use of the present framework.

From Figure 4-2b it is apparent that the dissipation at small strain-rates η'_M increases with increasing $\dot{\gamma}_0$, whereas the dissipative nature at large strain-rates (represented by η'_L) decreases from one cycle to the next. At small strain-amplitudes these quantities suffer from residual noise, with greater perturbations than observed with

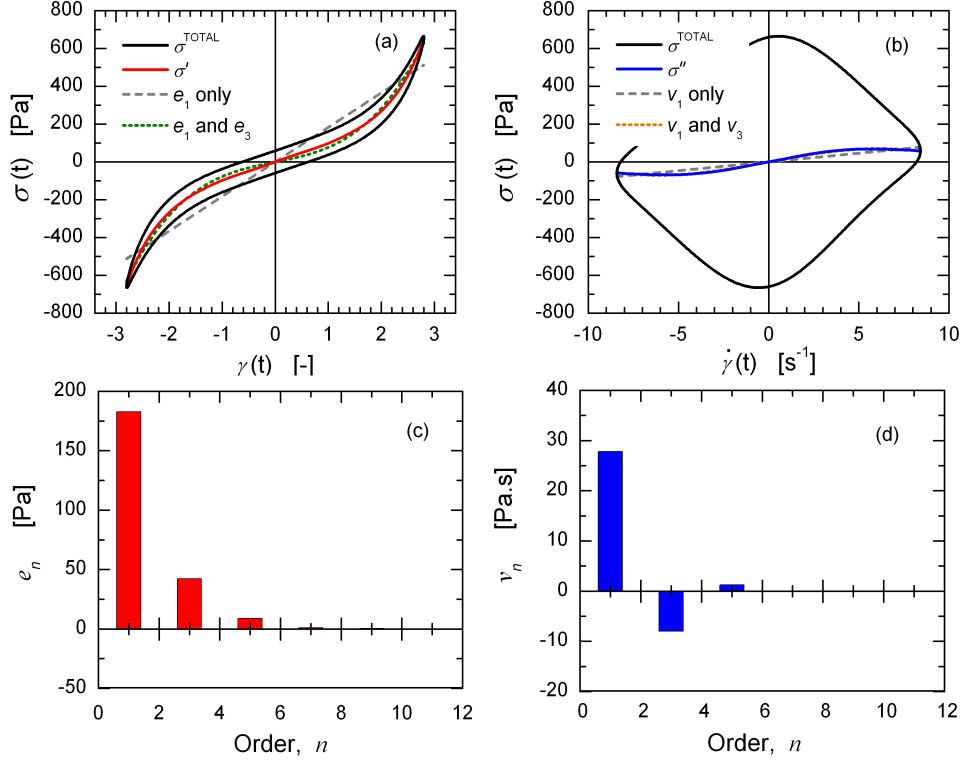


Figure 4-3: Reconstruction of (a) elastic and (b) viscous stresses using the Chebyshev spectrum of each signal (c,d). The nonlinearity of each signal is predominantly described by including only the third-order contribution; contributions higher than $n = 3$ are comparably insignificant ($e_5, e_1, v_5/v_1 < 0.005$) (same experimental data as Figure 2-2).

the elastic quantities since the viscous contribution to the measured signal is comparatively smaller and the gel is predominantly elastic at these strain-amplitudes. At sufficient strain-amplitude, however, the values converge with each other before the nonlinear regime is reached at strain-rate amplitudes $\dot{\gamma}_0 > 2\text{s}^{-1}$. In the nonlinear regime the measures clearly diverge, with an increasing value of η'_M , a nearly constant η'_1 , and a slightly decreasing value of η'_L . This increase of η'_M suggests that at small instantaneous strain-rates (corresponding to strains close to the maximum strain γ_0) the deformed material becomes progressively more dissipative.

The intra-cycle nonlinear viscous measures T and v_3 (Figure 4-2d) are both negative at large strain amplitudes, indicating intra-cycle shear-thinning. This is consistent with the fact that $\eta'_L < \eta'_M$ in the nonlinear regime. Again, the true rheological behavior of the nonlinear viscoelastic material could be ascertained only by using the

present framework. Insights such as these will help guide constitutive model development, since a physical picture of the nonlinear response is now readily apparent.

The utility of elastic and viscous Chebyshev decomposition is illustrated further by showing a Lissajous-Bowditch plot at a single coordinate point ($\omega = 3\text{rad.s}^{-1}$, $\gamma_0 = 2.8$) for native pedal mucus (Figure 4-3). The total and decomposed stresses are displayed in Figure 4-3a and Figure 4-3b against the strain and strain-rate respectively. Overlaid on these figures are the reconstructions of the elastic and viscous stresses using only the 1st and 3rd order contributions for each signal. In Figure 4-3c and Figure 4-3d we report the spectrum of the elastic and viscous Chebyshev coefficients, respectively. It can be seen that the 1st and 3rd order contributions describe the nonlinear curves fairly well, thus giving confidence that they represent the predominant departure from linearity.

4.2.3 Wormlike micellar fluid

In small amplitude oscillatory shear (SAOS) the viscoelastic behavior of this CPyCl wormlike micelle solution is well described by a single mode Maxwell model with $\lambda_1 = 0.64$ s, while in steady shear the solution shear bands at a critical stress of approximately $\sigma \approx 20$ Pa [61].

Here we test the micellar solution in LAOS under strain-controlled conditions. Tests are performed over a frequency range of $\omega = [0.15, 15]$ with three points per decade, and a strain-amplitude range $\gamma_0 = [0.0056, 10]$ with four points per decade. We first use Lissajous-Bowditch curves to summarize the rich viscoelastic response of the material as a function of both frequency and strain-amplitude. These Lissajous-Bowditch curves allow a visual inspection of the response prior to applying our quantitative analytic techniques. The full set of raw data, covering four tests per decade of imposed strain, is shown in Figure 4-4) A subset of the elastic Lissajous-Bowditch curves are shown in Figure 4-5, and the corresponding viscous Lissajous-Bowditch curves are displayed in Figure 4-6. The individual orbits ($\sigma(t)$ vs. $\gamma(t)$ or $\sigma(t)$ vs. $\dot{\gamma}(t)$) are arranged in Figure 4-5 and Figure 4-6 so that they are centered about the independent coordinates (ω, γ_0) to form a Pipkin diagram [1] of the material response

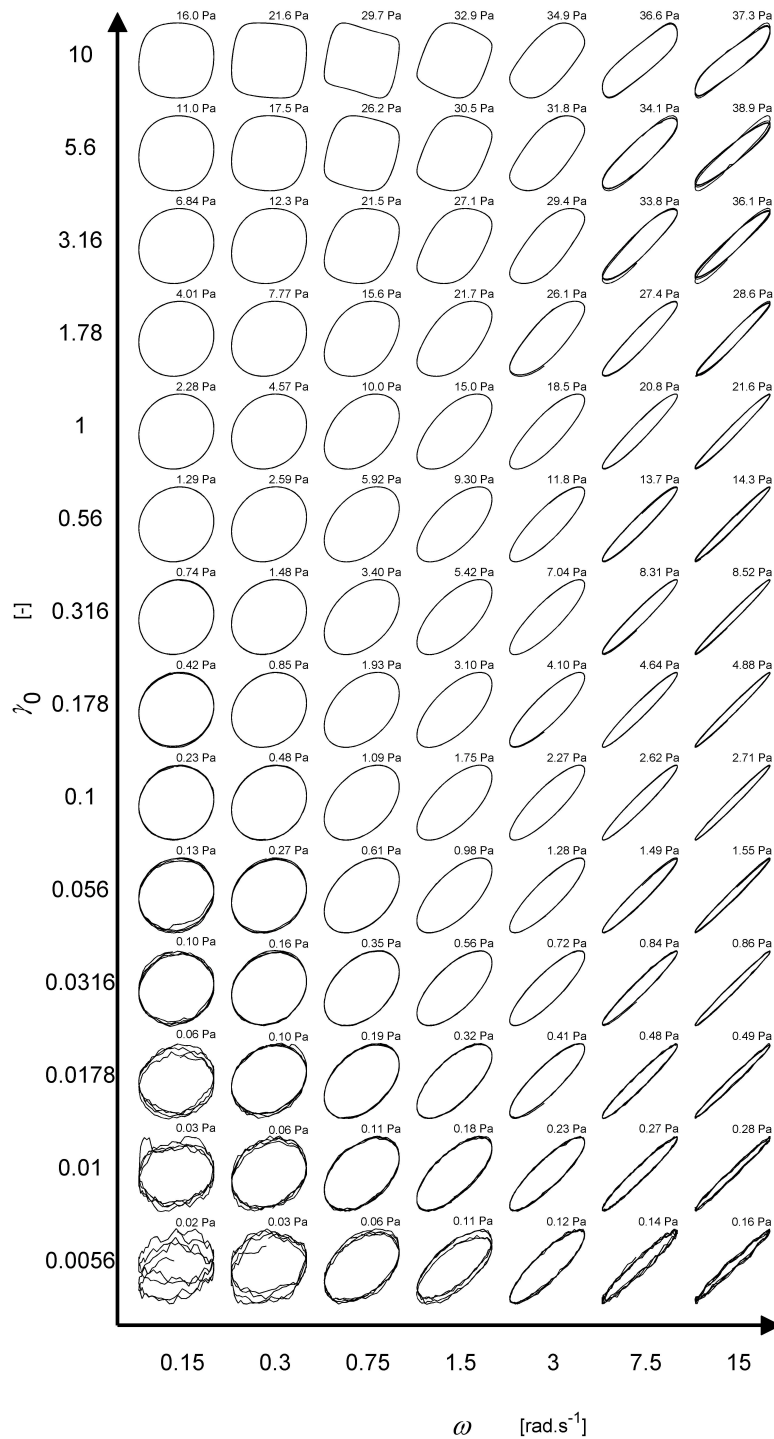


Figure 4-4: Raw LAOS data for the micellar solution, shown as elastic Lissajous-Bowditch curves generated from experimental oscillatory tests. Each trajectory is positioned in a Pipkin space according to the imposed values (ω, γ_0) . Solid lines are total stress $\sigma(t)/\sigma_{\max}$ vs. $\gamma(t)/\gamma_0$. The maximum stress, σ_{\max} , is indicated above each curve.

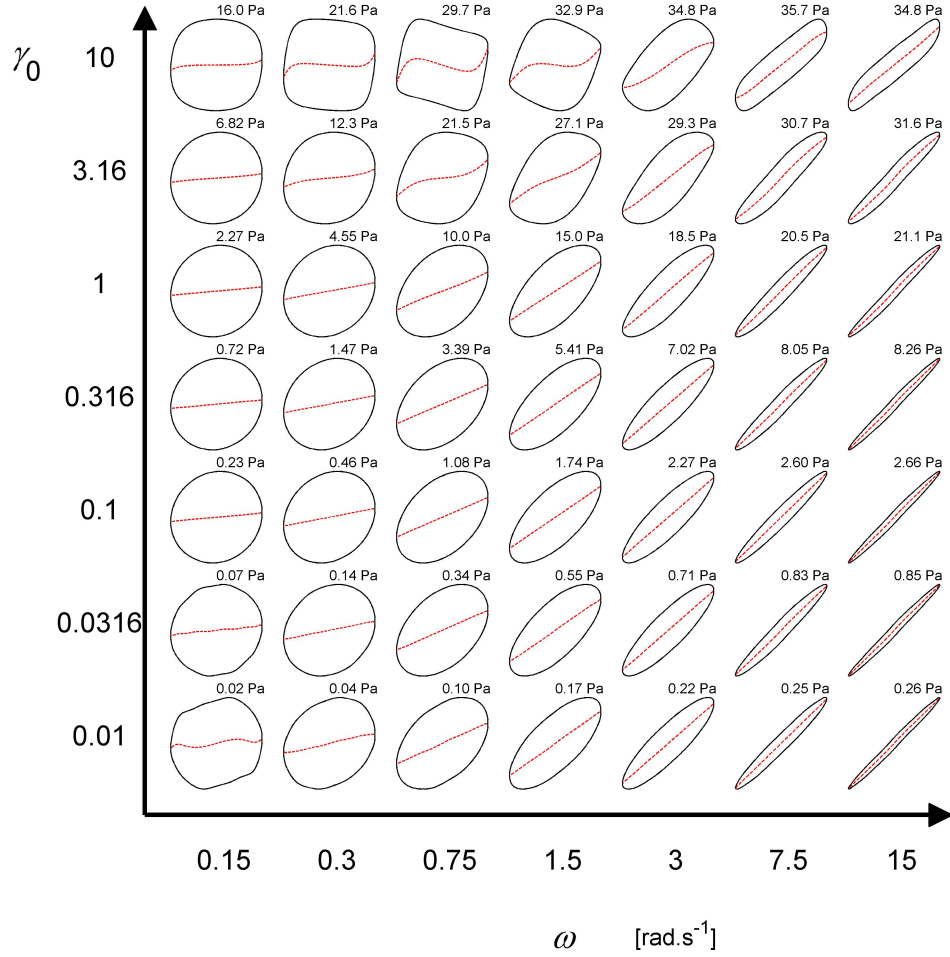


Figure 4-5: Elastic Lissajous-Bowditch curves generated from experimental oscillatory tests of the micellar solution, displayed in a Pipkin space. Each trajectory is positioned according to the imposed values (ω, γ_0) . Solid lines are total stress (filtered) $\sigma(t)/\sigma_{\max}$ vs. $\gamma(t)/\gamma_0$, dashed lines are elastic stress $\sigma'(t)/\sigma_{\max}$ vs. $\gamma(t)/\gamma_0$. The maximum stress, σ_{\max} , is indicated above each curve.

over a range of frequency and strain. The linear viscoelastic regime is approached at adequately small strains, and is indicated in both Figure 4-5 and Figure 4-6 by elliptical curves that are independent of imposed strain amplitude γ_0 while frequency ω is held constant. The data suffers from noise in the lower left portions of Figure 4-5 and Figure 4-5 when $\sigma_{\max} < 0.10$ Pa, i.e. maximum torque $T_{\max} < 3.3\mu\text{N.m}$. The onset of material nonlinearity can be visually observed for strains $\gamma_0 \geq 1$, at which point the shapes of the curves change and the elastic and viscous stress contributions to the total stress each become progressively more nonlinear. The nature of the

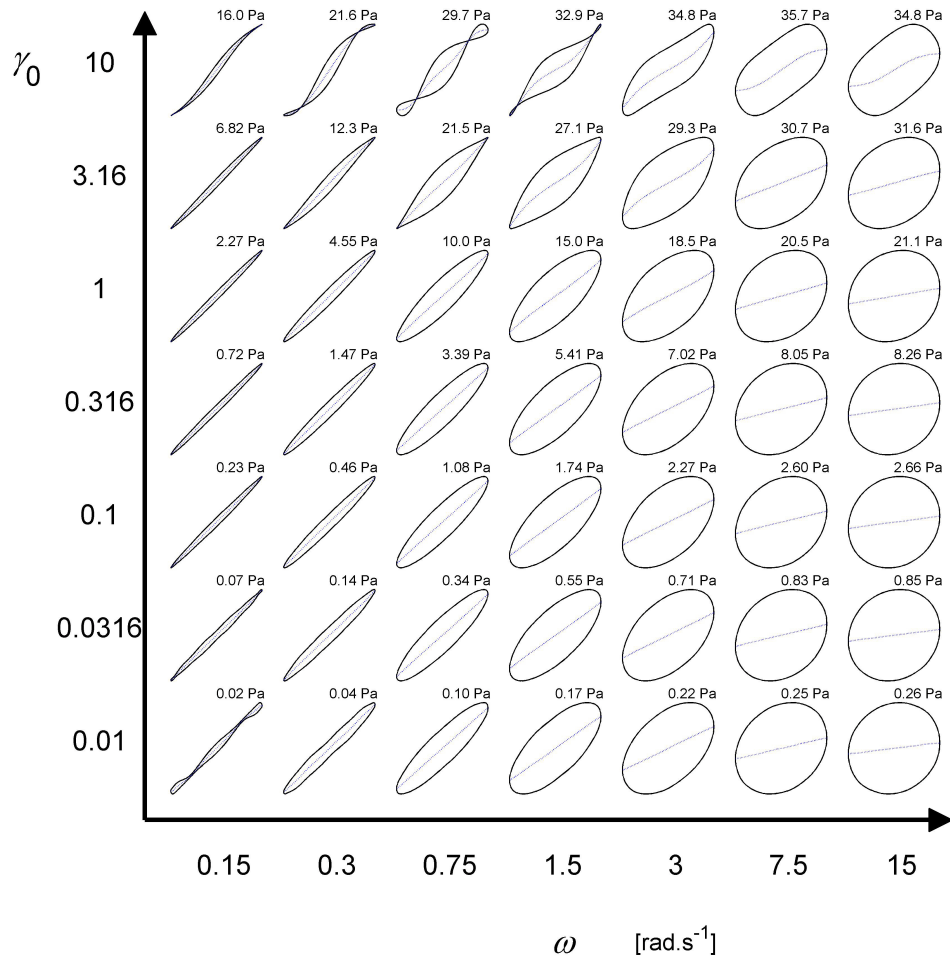


Figure 4-6: Viscous Lissajous-Bowditch curves generated from experimental oscillatory tests of the micellar solution, displayed in a Pipkin space. Each trajectory is positioned according to the imposed values (ω, γ_0) . Solid lines are total stress (filtered) $\sigma(t)/\sigma_{\max}$ vs. $\dot{\gamma}(t)/\dot{\gamma}_0$, dashed lines are viscous stress $\sigma''(t)/\sigma_{\max}$ vs. $\dot{\gamma}(t)/\dot{\gamma}_0$. The maximum stress, σ_{\max} , is indicated above each curve.

initial deviation from linearity depends on the frequency, creating an extremely rich nonlinear response. For example, at $\omega = 0.75 \text{ rad.s}^{-1}$ ($\omega < 1/\lambda_1$) the initial elastic departure from linearity is strain-stiffening, whereas at $\omega = 3.0 \text{ rad.s}^{-1}$ ($\omega > 1/\lambda_1$) the initial nonlinearity is strain-softening.

The elastic properties of the micellar fluid are shown as contour plots, or “rheological fingerprints,” in the two-dimensional Pipkin diagram of Figure 4-7, and the corresponding viscous properties are shown in Figure 4-8. Essential characteristics of the expected Maxwell behavior in the linear viscoelastic regime can be seen from the

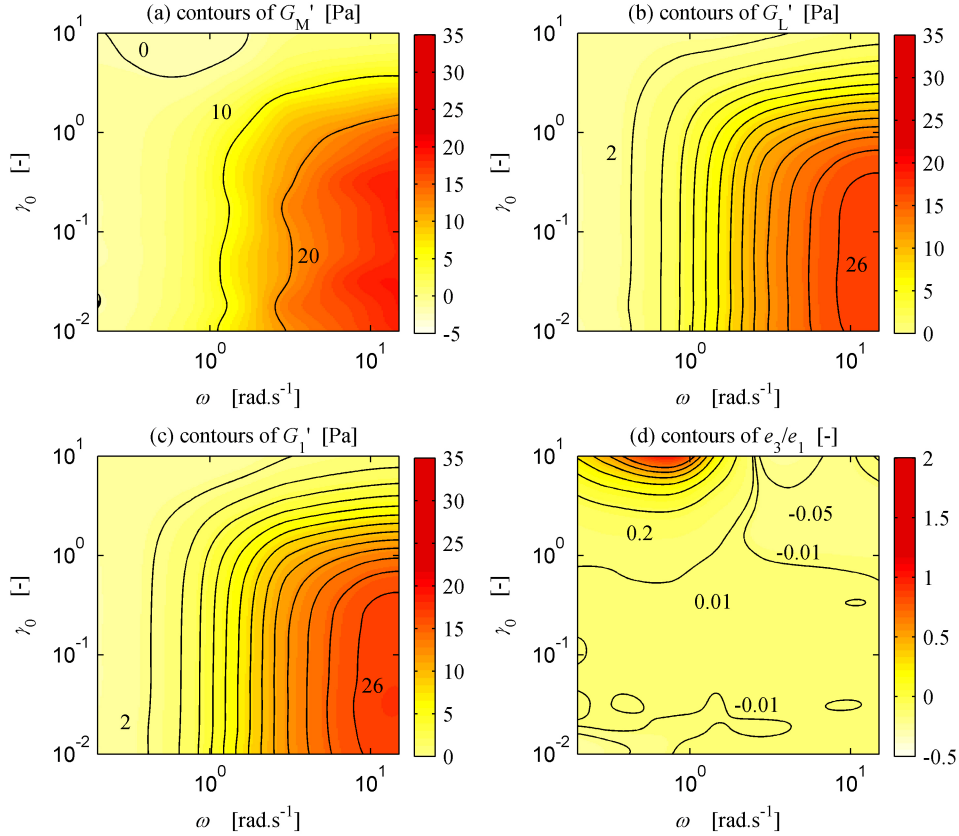


Figure 4-7: “Rheological Fingerprints” of the elastic properties of the micellar solution in large amplitude oscillatory shear. Each parameter is plotted in a Pipkin diagram as a function of the imposed frequency and strain amplitude. (a,b,c) Elastic moduli G'_M , G'_L , and G'_1 respectively; unlabeled contours shown at increments of 2 Pa (d) Intra-cycle elastic nonlinearity as indicated by the normalized third-order elastic Chebyshev term, e_3/e_1 ; contours shown at -0.05, ± 0.01 , and increments of 0.2.

monotonically increasing value of G'_1 with frequency and the approach to a plateau modulus. Furthermore, the contour plots of the third order elastic Chebyshev coefficient e_3 in Figure 4-7d show contrasting nonlinear trends for low and high frequencies. For low frequencies, $\omega < 2\text{rad.s}^{-1}$, the elastic nonlinearity is strain-stiffening with $e_3 > 0$, whereas for higher frequency the elastic nonlinearity is strain-softening with $e_3 < 0$. The values of e_3 in the nonlinear regime are consistent with our visual inspections of the elastic Lissajous-Bowditch curves in Figure 4-5.

Reporting more than the common first-order viscoelastic moduli G'_1 and $G''_1 = \eta'_1\omega$ also reveals behavior which might otherwise be hidden. The Lissajous-Bowditch curves of Figure 4-5 and Figure 4-6 show a curious behavior at ($\omega = 0.75\text{ rad.s}^{-1}$,

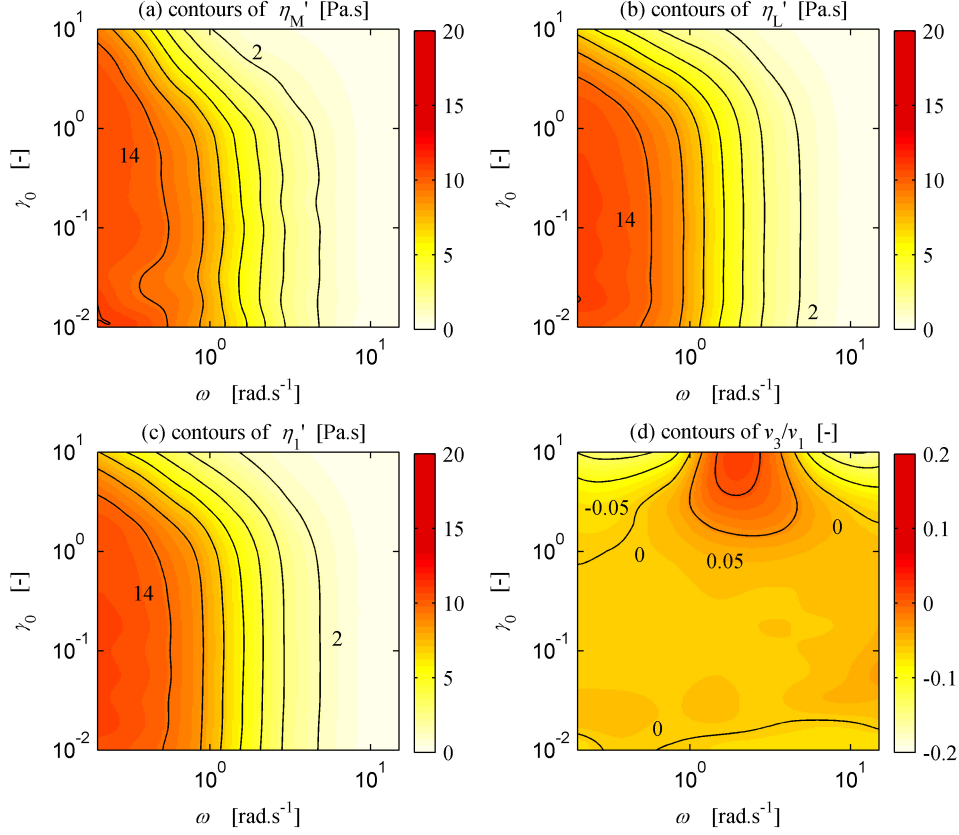


Figure 4-8: Viscous properties of the micellar solution in large amplitude oscillatory shear, each parameter plotted in a Pipkin space; (a,b,c) Dynamic viscosities η'_M , η'_L , and η'_1 respectively; contours shown at increments of 2 Pa.s. Inter-cycle nonlinearities are indicated by gradients of these measures. Inter-cycle thinning is shown for sufficiently large and increasing values of the shear rate amplitude $\dot{\gamma}_0 = \gamma_0\omega$. (d) Intra-cycle viscous nonlinearity as indicated by the normalized third-order viscous Chebyshev term, v_3/v_1 ; contours shown at increments of 0.05. Intra-cycle thickening is indicated by $v_3/v_1 > 0$, whereas intra-cycle thinning is shown by $v_3/v_1 < 0$.

$\gamma_0 = 10$), in which self-intersection appears in the viscous Lissajous-Bowditch curves (leading to loops) and a negative slope appears in the elastic Lissajous-Bowditch curves at instantaneous strain value $\gamma = 0$. There is nothing in the contour plot of G'_1 (Figure 4-7c) or η'_1 (Figure 4-8c) which hints at such behavior; the contours of G'_1 and η'_1 appear unremarkable in this region of the Pipkin diagram. However, the small-strain elastic modulus G'_M takes a negative value at this point (Figure 4-7a), which corresponds to the negative slope in the elastic Lissajous-Bowditch curve at $\gamma = 0$, and leads to the self-intersection in the viscous Lissajous-Bowditch curve. A

negative modulus G'_M indicates that the material is unloading elastic stress faster than new deformation is being accumulated. This behavior can easily be hidden by the commonly reported viscoelastic parameters of G'_1 or $G''_1 = \eta'_1\omega$, but is revealed quantitatively with the alternative measures of viscoelastic moduli proposed in this work.

The physical insight provided by these material measures informs a microstructural picture of the material, which in turn helps to motivate the choice of a constitutive model. Furthermore, these measures can be used to help test the robustness of a constitutive model, to see if the model is capable of predicting the same nonlinear response over a range of imposed strains and timescales.

Chapter 5

Nonstandard Large Amplitude Oscillations

5.1 Even-harmonics

Transient, non-periodic, or asymmetric responses will exhibit even-harmonics in the Fourier-series representation of shear stress. This occurs in general for a response which is not strictly periodic and does not close on itself, such as oscillations with decaying amplitude. Periodic responses may also show even harmonics. For example, large amplitude oscillatory extension or compression may exhibit asymmetric Lissajous curves [62, 63, 64] due to the nonlinearity $F \sim 1/h^3$. Additionally, the LAOS normal stress difference inherently involves even harmonics, due to the even symmetry of the elastic stresses and the independence on the direction of shearing deformation [65]. Although the analysis of such circumstances with Large Amplitude Oscillations is not yet in common practice, the ontology presented in Chapter 2 can be generalized to include even harmonics in order to enable the characterization of such phenomena in the future.

Asymmetric Lissajous curves will exhibit even harmonics, and are of interest for both asymmetric materials and also large amplitude oscillatory extension (LAOE) about zero strain $\gamma = 0$. Although shear deformations are typically symmetric with respect to the direction of deformation, extension and compression will likely behave

differently as the response becomes nonlinear. This asymmetry with respect to strain direction will result in even harmonics in the Fourier spectrum. For completeness, we restate the Fourier series representing a stress response to harmonic strain deformation $\gamma(t) = \gamma_0 \sin \omega t$ (we continue to represent the response in terms of shear strain and shear stress, but the results are applicable to other deformations as well, such as tension). The Fourier series includes both odd and even harmonics,

$$\sigma(t; \omega, \gamma_0) = \sum_n G'_n \sin(n\omega t) + G''_n \cos(n\omega t), \quad (5.1)$$

in which $n = 0$ must also be included. The term G'_0 is meaningless, since it is the coefficient of $\sin(0) = 0$, but the term G''_0 must be retained. The double-prime notation does not necessarily indicate a connection to dissipation. Instead, the G''_0 term can be considered as a bias stress, since it is always multiplied by $\cos(0) = 1$. This is particularly important for normal stresses which oscillate about a non-zero mean[10, 65].

The stress decomposition is more complicated when even-harmonics are included. This has been considered recently by Yu et al. [66]. The connection to a Chebyshev polynomial representation is yet to be worked out. Here we focus on the viscoelastic moduli and dynamic viscosities introduced in Section 2.3, which will help to provide some interpretation of the even harmonic contributions. An asymmetric LAOS response (e.g. a material which responds differently in each strain direction) will have Lissajous-Bowditch curves without 180° rotational symmetry, and therefore the local measures of moduli and viscosities can take separate values on either side of the cycle. Thus, G'_M can take two values, G'_{M+} , at $\gamma = 0$, $\dot{\gamma} > 0$, and also G'_{M-} , which is associated with $\gamma = 0$, $\dot{\gamma} < 0$. For $\gamma(t) = \gamma_0 \sin \omega t$, G'_{M+} occurs at $\omega t = 2\pi m$, and G'_{M-} occurs at $\omega t = \pi + 2\pi m$, where m is an arbitrary integer. Substituting this into the definition of the minimum strain modulus gives

$$G'_{M\pm} \equiv \left. \frac{d\sigma}{d\gamma} \right|_{\gamma=0, \dot{\gamma}=\pm\dot{\gamma}_0} = \sum_{n:\text{odd}} nG'_n \pm \sum_{n:\text{even}} nG'_n. \quad (5.2)$$

where the n :odd and the n :even terms have been grouped separately to show the deviations due to even harmonics. A similar case exists for G'_L , in which $G'_{L\pm}$ refers to the instantaneous point in the cycle in which $\gamma = \pm\gamma_0$. For the sinusoidal deformation, these points occur at $\omega t = \pi/2 + 2\pi m$ and $\omega t = 3\pi/2 + 2\pi m$, respectively. The large-strain elastic modulus is then

$$G'_{L\pm} \equiv \frac{\sigma}{\gamma} \Big|_{\gamma=\pm\gamma_0} = \sum_{n:\text{odd}} G'_n (-1)^{\frac{n-1}{2}} \pm \sum_{n:\text{even}} G''_n (-1)^{\frac{n}{2}}. \quad (5.3)$$

It is quite interesting that the possible elastic asymmetry of $G'_{L\pm}$ originates from G''_n (n :even), the double-prime coefficients. It is evidently incorrect to associate the double-prime coefficients solely with dissipative behavior, as is also the case for G''_0 which represents a bias stress. In fact, the combination of single-prime and double-prime coefficients also occurs with the minimum-rate dynamic viscosity $\eta'_{M\pm}$. The full results for the minimum-rate and large-rate dynamic viscosities are given as follows,

$$\eta'_{M\pm} \equiv \frac{d\sigma}{d\dot{\gamma}} \Big|_{\dot{\gamma}=0, \gamma=\pm\gamma_0} = \frac{1}{\omega} \sum_{n:\text{odd}} nG''_n (-1)^{\frac{n-1}{2}} \mp \frac{1}{\omega} \sum_{n:\text{even}} nG'_n (-1)^{\frac{n}{2}} \quad (5.4)$$

$$\eta'_{L\pm} \equiv \frac{\sigma}{\dot{\gamma}} \Big|_{\dot{\gamma}=\pm\dot{\gamma}_0} = \frac{1}{\omega} \sum_{n:\text{odd}} G''_n \pm \frac{1}{\omega} \sum_{n:\text{even}} G'_n. \quad (5.5)$$

To aid in the understanding of the nonlinear and asymmetric influences of higher harmonics, the *leading order* terms are explicitly shown for each of the results in Eqs. 5.2 – 5.5.

$$G'_{M\pm} = G'_1 \pm 2G'_2 + 3G'_3 \pm \dots \quad (5.6)$$

$$G'_{L\pm} = \pm G''_0 + G'_1 \mp G''_2 - G'_3 \pm \dots \quad (5.7)$$

$$\omega\eta'_{M\pm} = G''_1 \pm 2G'_2 - 3G''_3 \pm \dots \quad (5.8)$$

$$\omega\eta'_{L\pm} = \pm G''_0 + G''_1 \pm G''_2 + G'_3 \pm \dots \quad (5.9)$$

In this section we begin an exploration of the influence of these even harmonics, by

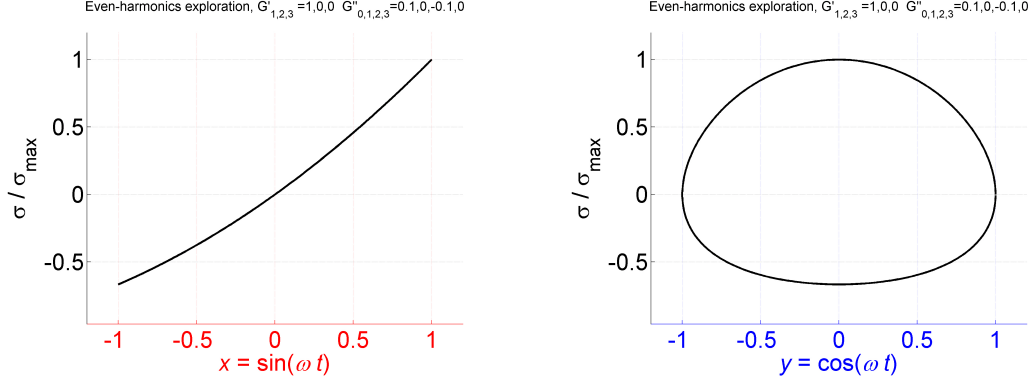


Figure 5-1: A purely elastic oscillatory response for $G_2'' = -G_0'' = -0.1$, $G_1' = 1$, and all other terms equal to zero. (a) elastic Lissajous curve of stress vs. strain, (b) p viscous Lissajous curve of stress vs. strain-rate.

way of a few examples.

The first example we construct is that of a purely elastic response, for which $\sigma(\gamma)$ is a single valued function. We will seek to construct an asymmetric curve, such that the response is more stiff in the positive strain direction, and examine the constraints which are then imposed on the leading order harmonics. The criteria for our desired response are as follows. First, we will neglect the third harmonics G_3' and G_3'' for the sake of simplicity. Next, we impose the condition $G_{M+}' = G_{M-}'$, since for a purely elastic response we might expect the tangent modulus at zero strain to be equivalent independent of shearing direction. The condition that $G_{M+}' = G_{M-}'$ then forces $G_2' = 0$ (Eq. 5.6). A purely elastic material response dissipates no net energy, $E_d = \pi\gamma_0^2 G_1'' = 0$, and therefore $G_1'' = 0$. Furthermore, no dissipation should occur at any point in the cycle, which requires that $\eta_{M\pm}' = 0$ (which is already satisfied by previously discussed values $G_1'' = G_2' = G_3'' = 0$), and also $\eta_{L\pm}' = 0$. Equation 5.9 for $\eta_{L\pm}'$ therefore requires that $G_0'' = -G_2''$. The condition that $\eta_{L\pm}' = 0$ is equivalent to the condition that $\sigma(\gamma = 0) = 0$, i.e. zero remnant stress should exist at zero strain for a purely elastic material. Finally, to create asymmetry, we desire $G_{L+}' > G_{L-}'$, i.e. the stiffness is higher in the positive strain direction. This condition forces $G_2'' < 0$, from Eq. 5.7.

All that is left now is the choice of G_1' and G_2'' . We choose $G_1' = 1$ and $G_2'' = -0.1$

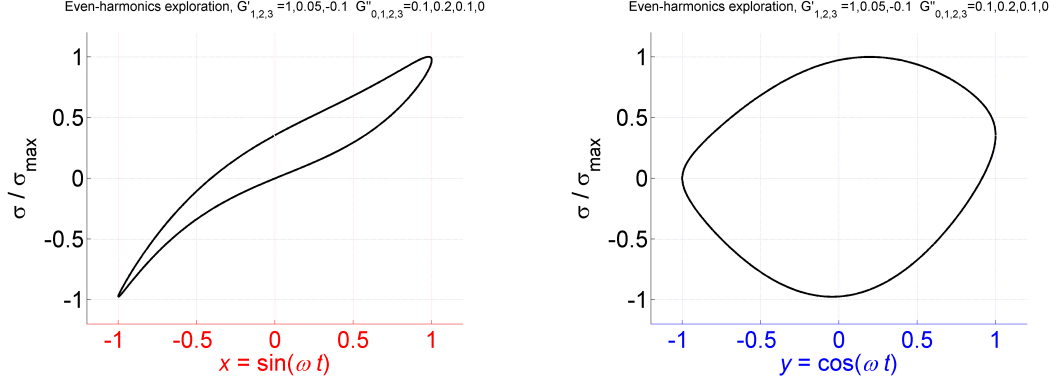


Figure 5-2: Oscillatory response of arbitrary construction which includes even harmonics.

for illustrative purposes. Units are arbitrary throughout this section and plotted results are always scaled as σ/σ_{max} , $x = \gamma/\gamma_0 = \sin(\omega t)$, and $y = \dot{\gamma}/\dot{\gamma}_0 = \cos(\omega t)$, as defined in Section 2.2. Figure 5-1 shows both the elastic and viscous Lissajous-Bowditch curves for this purely elastic asymmetric response. Indeed, the response is that of an asymmetric purely elastic material for which the elastic modulus is larger for large positive strains. The resulting non-zero moduli are $G'_{M\pm} = 1$, $G'_{L+} = 1.2$, $G'_{L-} = 0.8$ (cf. Eqs. 5.6 – 5.7).

In the previous example, forcing $G'_{M+} = G'_{M-}$ required that the leading order term $G'_2 = 0$. This result consequently forces a similar condition on the minimum rate dynamic viscosity, i.e. $\eta'_{M+} = \eta'_{M-}$ for $G'_2 = 0$ (when terms $n \geq 3$ are zero, Eq. 5.8). This may be considered a natural connection, considering that the symmetry of the minimum-strain and minimum-rate coefficients is grounded in the idea that a smooth transition must exist at both $\gamma = 0$ and $\dot{\gamma} = 0$, and that asymmetries in the response occur only at large strains or strain-rates (to leading order). This would then predict that for a typical asymmetric material response, the double-prime coefficients G''_2 and G''_0 should be the most significant, and $G'_2 = 0$. This is because G''_2 and G''_0 are associated with asymmetries at the largest strains and strain-rates within the oscillatory cycle, i.e. $G'_{L\pm}$ and $\eta'_{L\pm}$.

A complex viscoelastic response may allow the minimum-strain modulus and minimum-rate viscosity to become asymmetric (i.e. $G'_{M+} \neq G'_{M-}$ and $\eta'_{M+} \neq \eta'_{M-}$),

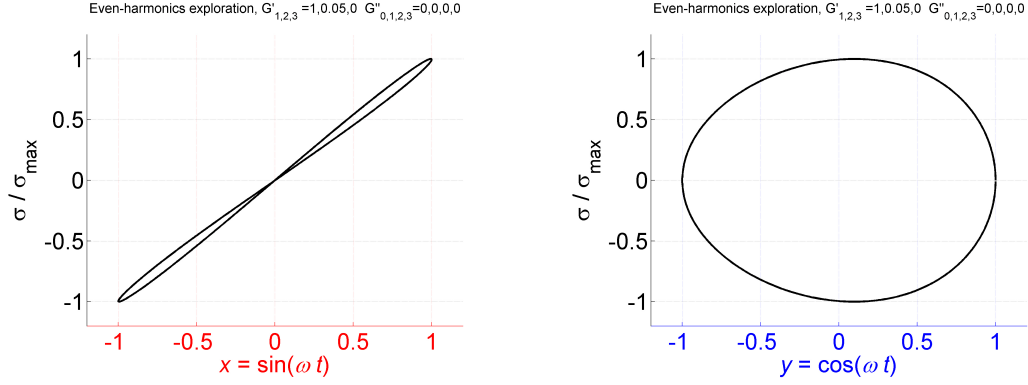


Figure 5-3: Oscillatory response of arbitrary construction which includes even harmonics.

in which case $G'_2 \neq 0$. Figure 5-2 shows an example of this for the parameter values $G'_1 = 1$, $G'_2 = 0.05$, $G'_3 = -0.1$, and $G''_0 = 0.1$, $G''_1 = 0.2$, $G''_2 = 0.1$, and $G''_3 = 0$. The presence of the third-harmonic introduces a known amount of symmetric nonlinearity (strain-stiffening in this case, revealed by $e_3 = -G'_3 > 0$, cf. Section 2.2). The response includes asymmetries from both G'_2 (affecting minimum-strain and minimum-rate coefficients), and also G''_0 and G''_2 which affect the large-strain and large-rate coefficients. The resulting material coefficients for the response in Figure 5-2 are:

$$\begin{aligned}
 G'_{M\pm} &= 0.8, 0.6 \\
 G'_{L\pm} &= 1.1, 1.1 \\
 \omega\eta'_{M\pm} &= 0.4, 0 \\
 \omega\eta'_{L\pm} &= 0.4, 0
 \end{aligned} \tag{5.10}$$

While exploring the possible behavior of even harmonics and asymmetric responses, it became apparent that some combinations of even harmonics may violate physical laws. For example, with the Fourier coefficients $G'_1 = 1$ and $G'_2 = 0.05$, and all other harmonics equal to zero, the resulting response stores energy across half of an oscillatory cycle which begins and ends at $\gamma = 0$ (during which $\dot{\gamma} > 0$). This describes a situation in which stress begins and ends at zero, yet mechanical energy was stored during the deformation and therefore the response is not physically pos-

sible (one may also look at the physical implausibility by considering this half-cycle to be repeated indefinitely with increasing stored mechanical energy, and if stopped at zero strain the stress state would still be zero). The response for this (unphysical) situation is shown by the Lissajous-Bowditch curves in Figure 5-3.

There is much more to be explored and explained in the realm of even-harmonics within a nonlinear response. For the purpose of this thesis, such efforts will be considered as future work.

5.2 Stress-controlled LAOS

Another limitation to the current use of LAOS is the restriction that *strain-controlled* LAOS is required to produce the higher harmonic coefficients e_n, v_n (or G'_n, G''_n), which were given a physically meaningful interpretation in Chapter 2. Load-controlled (or stress-controlled) instrumentation is also very common, and it is therefore useful to extend the framework of LAOS to include physically meaningful material measures under load-control LAOS.

For load-control circumstances, the natural material measures are compliance, $J \equiv \gamma/\sigma$ (for an elastic response, units Pa^{-1}), and fluidity $\phi = \dot{\gamma}/\sigma$ for a viscous response, units $[\text{Pa}\cdot\text{s}]^{-1}$. For oscillatory deformation the imposed stress can be represented as

$$\sigma(t) = \sigma_0 \cos \omega t \quad (5.11)$$

in which case the linear viscoelastic response is

$$\gamma(t) = \gamma_0 \cos(\omega t - \delta) \quad (5.12)$$

$$\gamma(t) = \sigma_0 (J' \cos \omega t + J'' \sin \omega t). \quad (5.13)$$

Here Eq. 5.11 uses $\cos \omega t$ so that the J' and J'' terms are additive and positive in Eq. 5.13. The magnitude of the complex compliance is $|J^*| = (J'^2 + J''^2)^{1/2}$. It is important to note that $J' \neq 1/G'$ and $J'' \neq 1/G''$ in general[10]. For a linear

viscoelastic response the interrelationship is

$$|G^*||J^*| = 1 \quad (5.14)$$

$$G' = \frac{J'}{J'^2 + J''^2} \quad (5.15)$$

$$G'' = \frac{J''}{J'^2 + J''^2}. \quad (5.16)$$

For a nonlinear response the Fourier series is represented in terms of higher-harmonic compliance coefficients (or fluidity coefficients),

$$\gamma(t; \omega, \gamma_0) = \sigma_0 \sum_{n \text{ odd}} \{J'_n(\omega, \gamma_0) \cos n\omega t + J''_n(\omega, \gamma_0) \sin n\omega t\} \quad (5.17)$$

$$\dot{\gamma}(t; \omega, \gamma_0) = \sigma_0 \sum_{n \text{ odd}} \{-\phi''_n(\omega, \gamma_0) \sin n\omega t + \phi'_n(\omega, \gamma_0) \cos n\omega t\} \quad (5.18)$$

in which case the the coefficients are related by $\phi''_n = n\omega J'_n$, and $\phi'_n = n\omega J''_n$.

Here again we are faced with the problem of interpreting the higher-harmonic coefficients, and also the choice of characterizing compliance and fluidity for a nonlinear viscoelastic response. The method and interpretation of stress decomposition is complicated for a nonlinear response to oscillatory stress. Using analogous arguments to that described by Cho et al.[28], it is possible to write

$$\gamma(t) = \gamma'(\sigma) + \gamma''(-\dot{\sigma}), \quad (5.19)$$

where $\sigma \sim \cos \omega t$ is the stress and $-\dot{\sigma} \sim \sin \omega t$ is the stress-rate, but it is initially unclear how to interpret the superposition. It is easy to consider $\gamma'(\sigma)$ as an “elastic” strain response, since it only depends on the imposed stress σ , i.e. a purely elastic strain response should only depend on the instantaneous stress input. However, the interpretation of $\gamma''(-\dot{\sigma})$ is not immediately clear, since rates of stress do not in general correspond with a viscous instantaneous strain response. What is desired is a relationship between the strain-*rate* and the imposed stress (recall that fluidity is $\phi \equiv \dot{\gamma}(\sigma)/\sigma$). It is possible to construct such a representation by taking the derivative

of the superposition of strains in Eq. 5.19, to give

$$\dot{\gamma}(t) = \dot{\gamma}'(\dot{\sigma}) + \dot{\gamma}''(-\ddot{\sigma}). \quad (5.20)$$

The interpretation of the $\dot{\gamma}''$ term is still not revealed by this representation, as there is no general interpretation of strain-rate which instantaneously depends on the second time derivative of stress. We must exploit the fact that our test is sinusoidal, and in fact $-\ddot{\sigma}(t) = \sigma(t)$, and therefore Eq. 5.20 can instead be written as

$$\dot{\gamma}(t) = \dot{\gamma}'(\dot{\sigma}) + \dot{\gamma}''(\sigma), \quad (5.21)$$

which now represents the second term as a viscous property, with strain-rate a function of stress. This representation provides a means of physically interpreting the nonlinear strain response to oscillatory stress input, in which $\dot{\gamma}'(\sigma)$ is the decomposed elastic strain, and $\dot{\gamma}''(\sigma)$ is the decomposed viscous strain-rate. The details of this are saved as future work, especially the question of the appropriate coordinate space for plotting response curves. For example, is it preferable to plot the orthogonal stress inputs and the strain output $[\sigma(t), \dot{\sigma}(t), \gamma(t)]$, or the strain-rate output $[\dot{\sigma}(t), \sigma(t), \dot{\gamma}(t)]$, or perhaps the most interpretable curve would be the strain and strain-rate as a function of the input stress $[\sigma(t), \gamma(t), \dot{\gamma}(t)]$?

As for quantitative material measures, the decomposition and material parameters will be analogous to the framework proposed in Chapter 2. In terms of nonlinear compliances,

$$J'_1 = \frac{\omega}{\pi\sigma_0^2} \oint \gamma(t) \sigma(t) dt \quad (5.22)$$

$$J'_{M\pm} \equiv \left. \frac{d\gamma}{d\sigma} \right|_{\sigma=0, \dot{\sigma}=\pm\dot{\sigma}_0} \quad (5.23)$$

$$J'_{L\pm} \equiv \left. \frac{\gamma}{\sigma} \right|_{\sigma=\pm\sigma_0} \quad (5.24)$$

$$(5.25)$$

and for the nonlinear fluidities

$$\phi'_1 = J_1'' \omega = \frac{\omega}{\pi \sigma_0^2} \oint \sigma(t) \dot{\gamma}(t) dt \quad (5.26)$$

$$\phi'_{M\pm} \equiv \left. \frac{d\dot{\gamma}}{d\sigma} \right|_{\sigma=0, \dot{\sigma}=\pm\dot{\sigma}_0} \quad (5.27)$$

$$\phi'_{L\pm} \equiv \left. \frac{\dot{\gamma}}{\sigma} \right|_{\sigma=\pm\sigma_0} \quad (5.28)$$

$$(5.29)$$

An LAOS framework for load-controlled tests will be extremely valuable for materials which fundamentally respond to the stress input, and also to allow the ubiquitous “torque-controlled rheometer” to confidently examine, and quantify, the nonlinear viscoelastic response to large amplitude oscillatory shear stress. Inertia artifacts must be carefully handled for torque-controlled large amplitude oscillations, since it is the *sample* stress which must be a single-harmonic sinusoidal input (Eq. 5.11), rather than the instrument torque. Of particular note is the fact that the instrument torque may be sinusoidal, but inertial artifacts combined with a nonlinear strain response (and therefore non-sinusoidal $\dot{\gamma}$) will cause a non-sinusoidal sample stress. This can be addressed by avoiding inertial artifacts, i.e. using sufficiently low frequencies, or using very precise feedback control which accounts for this phenomena to provide a sinusoidal sample stress.

Finally, it is important to note that in the linear viscoelastic regime the strain-control and stress-control tests are interchangeable, since inter-relations exist between compliances and moduli[10], e.g. $|G^*||J^*| = 1$. However, for a nonlinear viscoelastic response it is unclear if a direct relation will exist between nonlinear compliances and nonlinear moduli (or between nonlinear fluidities and nonlinear dynamic viscosities). Thus, strain-control and stress-control tests may not be interchangeable in general with large amplitude oscillations, and may therefore provide distinct information.

Chapter 6

Hagfish slime - an ultrasoft material

6.1 Background

Hagfishes are marine animals that inhabit the cool or deep parts of the oceans of both hemispheres[67]. They have long bodies (Figure 6-1), and are sometimes called “slime eels” although they are not eels at all . Hagfishes are well known for their ability to produce large amounts of slime when they are provoked or stressed. They do this by ejecting a small amount of slime exudate which can mix into a large volume of the surrounding water, forming a mucus-like cohesive mass[68, 69, 70]. The slime glands line both sides of the animal’s body (Figure 6-1c). Hagfish slime is distinct from other mucus-like materials. In addition to mucin-like molecules it also contains a fibrous component made of intermediate filaments[71, 72](Figure 6-2). The fibrous component originates within specialized cells in the slime glands known as gland thread cells. These unique cells express intermediate filament proteins that assemble into 10 nm intermediate filaments, which then bundle into a single protein polymer thread. The threads are wrapped into an egg-shaped “ball of yarn” that takes up the majority of the cytoplasm volume in mature cells. The thread diameter ranges from 1-3 μ m, and when fully unraveled it can be about 15 cm long[73]. The details of producing a continuous 15 cm long thread within the cytoplasm are still unknown.

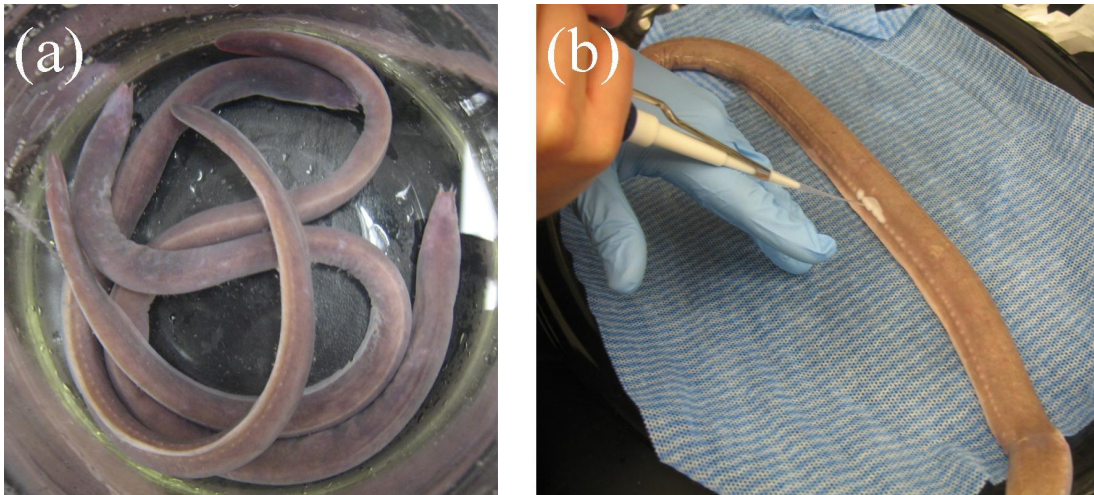


Figure 6-1: Photos of Atlantic hagfish used for this research. (a) top-down view of three hagfish in a large glass beaker, (b) collection of fresh slime exudate.

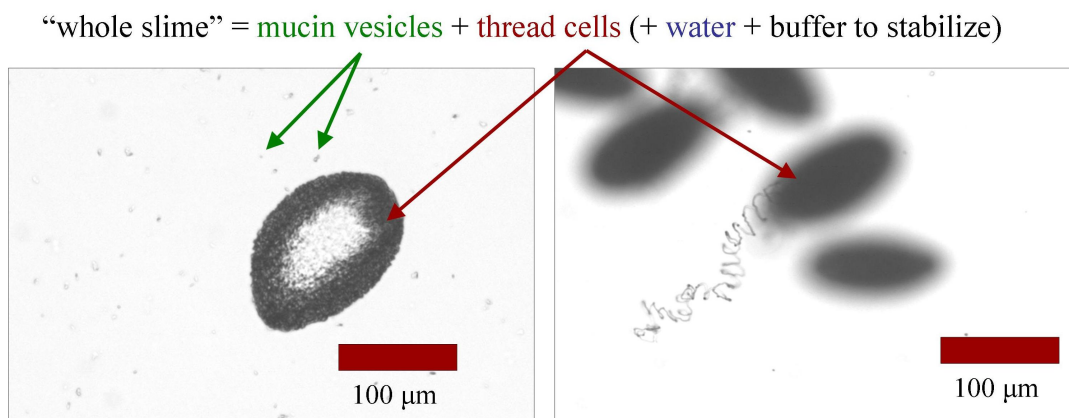


Figure 6-2: Microscope images of stabilized hagfish slime. The primary constituents of whole slime exudate are mucin vesicles and wound-up threads. Each egg-shaped thread winding is composed of a continuous filament of diameter $1\text{-}3\mu\text{m}$, with length up to 15 cm when fully unraveled.

One remarkable thing about hagfish slime is that small volumes of exudate can entrain large volumes of water. A typical slime mass created by a hagfish has a volume of about 0.9 L, but this total mass of exudate and entrained water contains only 20 mg of slime threads and 15 mg of mucins (dry weight)[73]. In contrast, typical mucus secretions contain about the same mass of mucins per *milliliter*, i.e. typical human mucin concentrations are about 1000x larger (47 mg/ml for gastric, 37 mg/ml for duodenal, and 20 mg/ml for colonic mucus respectively)[74]. Hagfish

slime exudate can absorb 26,000x its weight in water, in comparison to commercially available absorbent materials (e.g. those used in diapers) which can absorb 50x their weight in water[75]. However, the method of water entrainment is different between these materials, and for hagfish slime the water is bound less tightly and will drain out over timescales of minutes under suitable driving pressure (e.g. as when lifted into the air)[73]. It appears that bulk seawater is entrained within minute spaces in the slime, and it is the viscous resistance to the flow of water through this porous network that allows the slime to be (momentarily) lifted into air.

The viscous entrainment of large volumes of water enable the most likely function of hagfish slime, which is to thwart attacks by gill-breathing predators[76]. Suction feeding is such a fast event that most prey typically have little chance of evasion once the attack has been detected. Hagfishes have evolved a counter-attack strategy to inhibit the suction feeding mechanism. Lim et al.[76] have shown that hagfish slime dramatically increases the hydrodynamic resistance of gills, at least in freshly dead specimens, and the likely result for a predator that gets a mouthful of slime is suffocation. The slime achieves this effect not by binding seawater tightly, but rather by simply decreasing the size of the pores through which the water must flow[76].

A slime mass network (of exudate mixed with water) can accommodate large stretch ratios. When lifted into the air (Figure 6-3), the slime mass remains a cohesive mass. At sufficiently short times there is minimal draining of water. Stretch ratios up to approximately $\lambda = L_f/L_i \approx 60\text{cm}/1.5\text{cm} = 40$ can be observed while the network remains a cohesive mass, as shown in Figure 6-3.

6.2 Materials and methods

Atlantic hagfish were collected and provided by Prof. Douglas Fudge (University of Guelph). For slime collection, hagfish were removed from a salt water containment bath, placed on a cold tray, and patted dry with a towel. Hagfish were then induced to produce slime exudate by electrical stimulation. Exudate was collected directly from the skin of the animal. For some tests, hagfish were kept in the lab at MIT and



Figure 6-3: Hagfish slime networks can sustain large stretch ratios while maintaining a cohesive mass. This photo shows Tim Winegard (hagfish wrangler, University of Guelph) raising the rheometer test geometry after experiments.

“fresh” exudate could be used for rheometry tests. Other tests were performed on exudate collected at the University of Guelph from the lab of Prof. Fudge, in which case “stabilized” exudate was maintained under mineral oil and shipped to MIT.

A precise volume of exudate ($V_e = 10\mu\text{L}$) was acquired using a micropipette, and this exudate was added to a predetermined volume of salt water ($V_{sw} = 12\text{ mL}$) in a Falcon tube. The tube was closed and the contents mixed to establish the slime gel network. The concentration was chosen to consistently entrain the full volume of salt water into the slime network. Mixing was generated by sloshing the contents back and forth along the container axis by repeatedly inverting the tube. After mixing for six oscillations, the entire volume of sample material appeared fibrous and behaved

as a cohesive mass.

Viscoelastic properties of the slime were measured with a torque-controlled rheometer (AR-G2, TA Instruments) using a concentric-cylinder geometry (a.k.a. cup-and-bob). The geometry consists of an outer cup with flat bottom (radius $R_o = 15$ mm). The inner cylinder has radius $R_i = 14$ mm, length $L = 41.5$ mm over which the radius is constant, and a protruding conical bottom with half angle $\alpha/2 = 60^\circ$.

The mixed sample of slime was placed in the cup, and the inner cylinder lowered into the sample until the bottom conical point reached a distance $h = 5$ mm from the bottom of the cup, pushing the sample into the 1 mm gap between the inner and outer cylinders. The volume $V_{sw} = 12$ mL was chosen such that the sample exactly reached the top of the inner cylinder. The sample is thus contained around and below the inner cylinder. It is the portion of the sample confined in the small gap which dominates the resistance to deformation, and this deformation is approximately described as simple shear, $\dot{\gamma} \simeq \Omega R_i / (R_o - R_i)$, where Ω is the angular velocity, R_i is the inner radius, and R_o is the outer cylinder radius.

6.3 Results

The results presented here are the first tests to characterize the intrinsic material properties of mature hagfish slime. Fig. 6-4 contains the results from a single creep test on “fresh” slime, in which a small constant load was imposed (shear stress $\sigma_0 = 0.01$ Pa) and the resulting strain $\gamma(t)$ observed as a function of time. Figure 6-4 shows the creep compliance, defined as $J(t) = \gamma(t)/\sigma_0$. At long times the compliance (strain) approaches a constant, $J(t) \rightarrow J_{ss} \approx 55 \text{Pa}^{-1}$. The equilibrium elastic modulus of the sample is then approximated by $G = 1/J_{ss}$. We measured this elastic modulus to be $G = 0.018$ Pa, which is about five orders of magnitude more compliant than materials like gelatin, making it one of the softest elastic biomaterials known.

The inertio-elastic ringing response of Fig. 6-4 was also analyzed following the procedures outlined in Section 1.2.3, Eqs. 1.3-1.4, by estimating the logarithmic decrement using four peak points (Eq. 1.7). The “ringing” modulus is interpreted

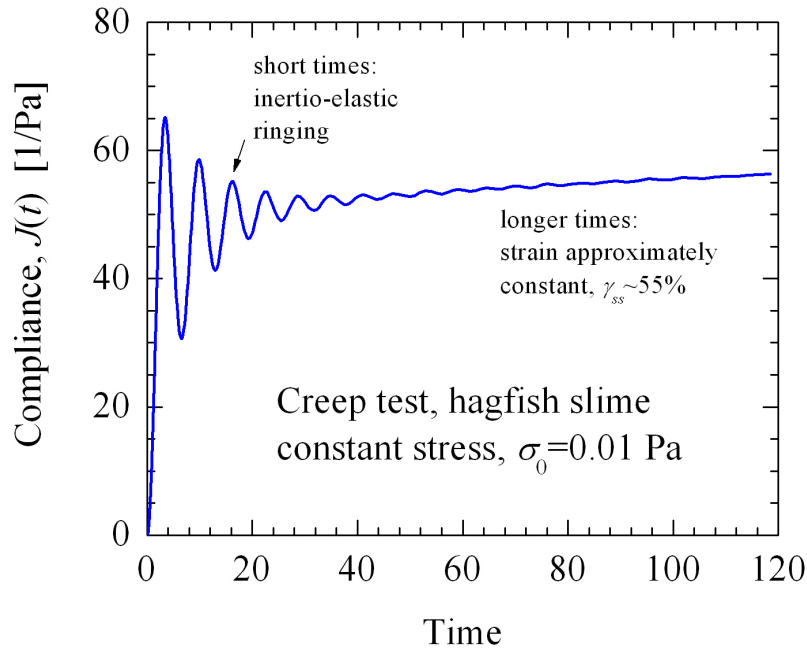


Figure 6-4: Results of a creep test conducted with “fresh” hagfish slime reconstituted from exudate mixed with seawater in the lab. At short times the strain oscillates due to inertio-elastic ringing, in which the sample elasticity couples with the finite instrument rotational inertia to “ring” at a resonant frequency, just like a mass at the end of a spring (see Section 1.2.3). At longer times the strain is approximately constant, γ_{ss} , and this is representative of a primarily elastic material response.

here as the differential modulus about an imposed stress (i.e. the tangent modulus at $\sigma_0 = 0.01$ Pa)[30]. For a nonlinear elastic response the tangent elastic modulus $K' \sim d\sigma/d\gamma$ is different than the secant modulus $G = \sigma_0/\gamma$. For the results of Fig. 6-4 it is found that the ringing frequency is $\omega^* = 0.99$ rad.s⁻¹, $K'_c = 0.032$ Pa, and $K''_c = 0.007$ Pa. The hagfish slime creep response even at $\sigma_0 = 0.01$ Pa is in fact nonlinear, as indicated by the differential modulus $K' = 0.032$ Pa being larger than the secant modulus $G = 0.018$ Pa.

The same “fresh” sample used for the creep tests of Figure 6-4 was also used for a linear viscoelastic frequency sweep (Figure 6-5) and large amplitude oscillatory shear (LAOS) (Figure 6-6). The hagfish slime sample is so soft that inertia easily dominates the response, as indicated by the raw phase angle $> 130^\circ$ above a critical frequency (note that this critical frequency corresponds to the inertio-elastic ringing

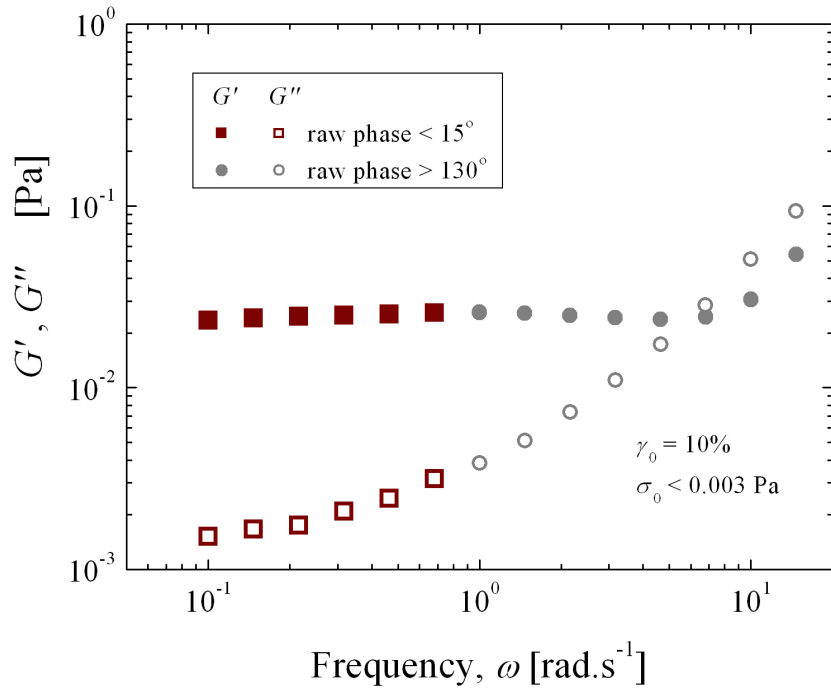


Figure 6-5: Frequency sweep results with hagfish slime reconstituted from fresh exudate. The strain amplitude was prescribed ($\gamma_0 = 10\%$). The mechanical resistance is so low ($G' < 0.03$ Pa) that inertial effects from the rheometer spindle easily appear in the data, with a sharp jump in raw phase angle from $\delta = 14.7^\circ$ to $\delta = 134.9^\circ$ at $\omega = 1 \text{ rad.s}^{-2}$, corresponding to the resonant frequency of the material-instrument system $\omega^* = 0.99 \text{ rad.s}^{-1}$ (Fig. 6-4).

frequency shown in Figure 6-4, $\omega^* = 0.99 \text{ rad.s}^{-1}$). With such large raw phase angles the accuracy of inertia corrections becomes questionable, and for this reason such data points with exceedingly large raw phase angles are distinguished as grey circles in Figure 6-5. The linear viscoelastic moduli for this sample show weak frequency dependence, and the value of $G' \approx 0.02$ Pa corresponds well with the results of the creep test of Figure 6-4 for which $G = 0.018$ Pa.

The LAOS results for this fresh sample are given in Figure 6-6. The test protocol specified a strain amplitude as the controlled input parameter, since the sample stress amplitude is not easily controlled when inertia plays such a dominant with such soft samples as this. It is important to note that the LAOS tests are performed on a torque-controlled instrument and therefore the strain is not strictly sinusoidal. Thus, the LAOS ontology cannot be applied since neither the stress nor the strain are controlled

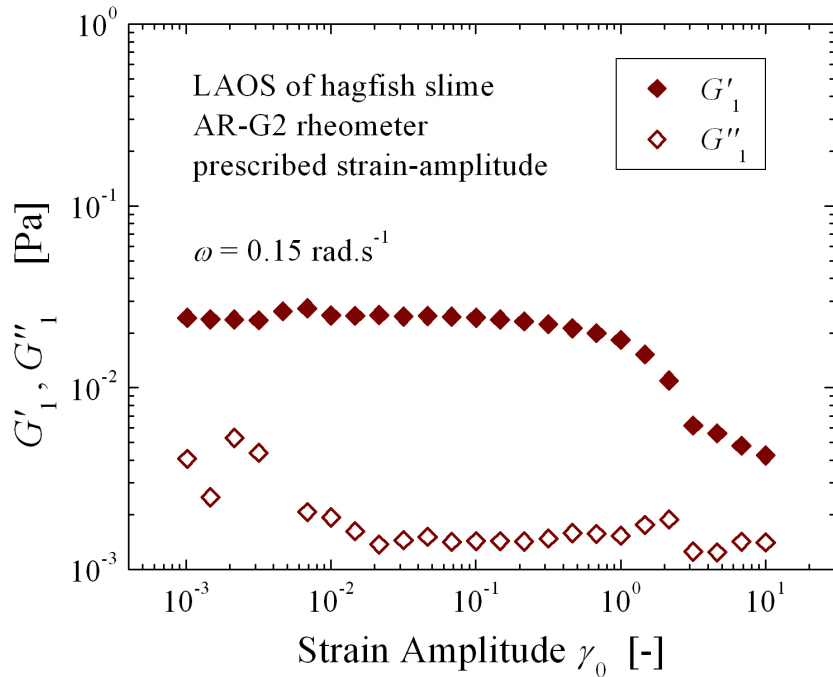


Figure 6-6: Large amplitude oscillatory shear test with hagfish slime reconstituted from fresh exudate. The strain amplitude was prescribed as indicated on the abscissa ($\omega = 0.15 \text{ rad.s}^{-1}$).

with sufficient precision in this case (i.e. neither is a smooth sinusoid). We are therefore limited to look only at the first-harmonic moduli output from the rheometer software. Figure 6-6 shows that the hagfish slime network degrades above a critical strain-amplitude $\gamma_0 \approx 1$, which corresponds to a stress amplitude $\sigma_0 \approx G' \gamma_0 \approx 0.02 \text{ Pa}$. This intercycle softening of G'_1 might initially seem to contradict the results obtained with the creep test in Figure 6-4, in which $K' > G$ indicated strain-stiffening. Recall however that the first-harmonic modulus can overshadow the true nonlinear behavior of the sample, as was the case for slug pedal mucus (Chapter 2, Figure 2-1).

Creep tests were performed over a range of input stress amplitude to better explore the nonlinear viscoelastic behavior of hagfish slime networks using the torque-controlled rheometer. Stabilized slime was used for the creep tests in Figure 6-7 (fresh samples were not available at that time). Note that the creep response of the stabilized slime (at $\sigma_0 \leq 0.01 \text{ Pa}$) corresponds well with the fresh slime creep response shown in Figure 6-4. This gives confidence that the stabilized slime exudate

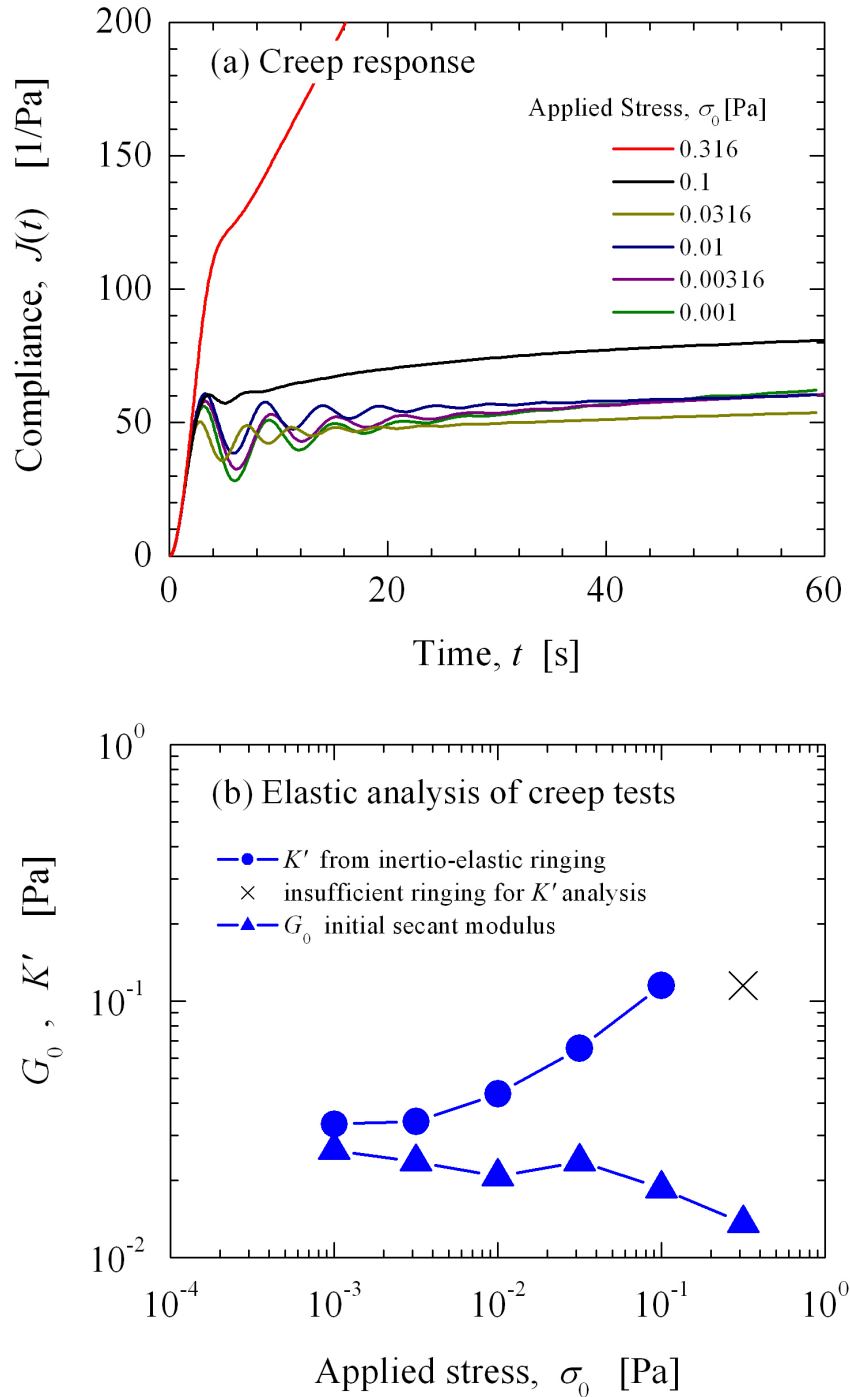


Figure 6-7: Creep tests conducted with hagfish slime reconstituted from stabilized exudate mixed with seawater in the lab. Various stress amplitudes are imposed to examine the nonlinear rheological response. (a) time dependent creep response curves at each imposed stress, (b) elastic analysis of each curve including the differential modulus K' (Eq. 6.12) and initial secant modulus G_0 (Eq. 6.11).

can be used in place of fresh exudate, and therefore future research can avoid the maintenance and care of hagfish at multiple sites.

As shown in Figure 6-7a, the slime network responds as a predominantly elastic material for sufficiently small values of stress. The material softens, i.e. becomes more compliant, at larger stresses near $\sigma_0 = 0.1$ Pa, which is a slightly larger stress than observed in Figure 6-6 in which softening initiates near $\sigma_0 = 0.02$ Pa. The sample eventually yields and flows at large imposed stress, e.g. at $\sigma_0 = 0.316$ Pa. Inertio-elastic ringing is observed in all of these tests, and was used for analysis of each curve except $\sigma_0 = 0.316$ Pa which had insufficient ringing information available. The four-point method of identifying successive peak/valley data points was used to determine the differential moduli K' and K'' . Additionally, an underlying Maxwell-like behavior was assumed to analyze the secant modulus and fluidity of the sample. Specifically, the prototypical curve assumes a Maxwell response superimposed with decaying oscillations,

$$J(t) = X \exp\left(\frac{-\Delta\omega}{2\pi}t\right) \sin(\omega t + \Psi) + Y + Zt \quad (6.1)$$

in which X is the ringing amplitude, Y is the initial compliance, Z is the fluidity, and Ψ is an arbitrary phase. Identifying four successive peak/valley data points from the experimental data, $t_1 \rightarrow t_4$ and $J_1 \rightarrow J_4$, provides sufficient information to determine all of the parameters of interest. The ideal time spacing forces the following relationships of the time points, $t_2 = t_1 + \pi/\omega$, $t_3 = t_1 + 2\pi/\omega$, and $t_4 = t_1 + 3\pi/\omega$. These four data points then provide the following system of equations

with the assumed underlying model (using Eq. 6.1),

$$J_1 = X \exp\left(\frac{-\Delta\omega}{2\pi}t_1\right) (+1) + Y + Zt_1 \quad (6.2)$$

$$J_2 = X \exp\left(\frac{-\Delta\omega}{2\pi}(t_1 + \pi/\omega)\right) (-1) + Y + Z(t_1 + \pi/\omega) \quad (6.3)$$

$$J_3 = X \exp\left(\frac{-\Delta\omega}{2\pi}(t_1 + 2\pi/\omega)\right) (+1) + Y + Z(t_1 + 2\pi/\omega) \quad (6.4)$$

$$J_4 = X \exp\left(\frac{-\Delta\omega}{2\pi}(t_1 + 3\pi/\omega)\right) (-1) + Y + Z(t_1 + 3\pi/\omega) \quad (6.5)$$

The inertio-elastic ringing frequency is determined from the total time-span of the data points,

$$\omega^* = \frac{2\pi}{t_4 - t_1} 1.5. \quad (6.6)$$

The logarithmic decrement, Δ , can be determined through a proper elimination of the variables X , Y , and Z . Two independent methods of eliminating Y and Z are used, namely $J_1 + J_3 - 2J_2$, and $-J_2 - J_4 + 2J_3$. The ratio of these two terms further eliminates X and allows for Δ to be calculated as a function of the four point $J_1 \rightarrow J_4$. This result was given in Eq. 1.7 and is repeated here for convenience,

$$\Delta = 2 \ln \left(\frac{J_1 - 2J_2 + J_3}{-J_2 + 2J_3 - J_4} \right). \quad (6.7)$$

Knowing Δ and t_1 , we can than use the $J_1 + J_3 - 2J_2$ expression to solve for X .

$$X = \frac{J_1 + J_3 - 2J_2}{\exp\left(\frac{-\Delta\omega}{2\pi}t_1\right) (1 + \exp(-\Delta) + 2 \exp(-\Delta/2))}. \quad (6.8)$$

Next, Z can be determined as a function of X and Δ , using $J_2 - J_1$ which eliminates the variable Y ,

$$Z = \frac{\omega}{\pi} \left[J_2 - J_1 + X \exp\left(\frac{-\Delta\omega}{2\pi}t_1\right) (1 + \exp(-\Delta/2)) \right]. \quad (6.9)$$

Finally, Y is determined directly from the J_1 expression,

$$Y = J_1 - X \exp\left(\frac{-\Delta\omega}{2\pi}t_1\right) - Zt_1. \quad (6.10)$$

The initial secant modulus is given by

$$G_0 = 1/Y. \quad (6.11)$$

The local differential moduli are determined from inertio-elastic ringing analysis, and depend on Δ and ω . This analysis was described in Section 1.2.3 and the result is repeated here for convenience, in which the differential moduli are explicitly indicated,

$$K' \approx \frac{I\omega_*^2}{b} (1 + (\Delta/2\pi)^2) \quad (6.12)$$

$$K'' \approx \frac{I\omega_*^2}{b} \left(\frac{\Delta}{\pi}\right) \quad (6.13)$$

$$\tan\delta \approx \frac{\Delta}{\pi} (1 + (\Delta/2\pi)^2)^{-1} \quad (6.14)$$

The ringing analysis of the creep curves results in stress-amplitude dependent values of the secant modulus G_0 and differential modulus K' , which are both given in Figure 6-7b. At sufficiently small stress, the values of G_0 and K' would be expected to converge, and indeed this is approximately the case for the measured data here. As stress amplitude is increased, the values diverge. The secant modulus G_0 is initially constant and eventually decreases, which compares well with the LAOS results of G'_1 (Figure 6-6). The nonlinear behavior is quite rich as the differential modulus is larger than the secant modulus for all tests, and increases as a function of stress amplitude indicating nonlinear elastic stiffening. The elasticity stiffens by about one order of magnitude before the sample response is dominated by flow and the differential modulus can no longer be measured.

Shear flow tests were attempted, but were unsuccessful due to the wrapping of the slime threads around the inner rotor of a cup-and-bob geometry. A cone-plate geometry was also used, but in this case the solid mucus/thread components wrapped

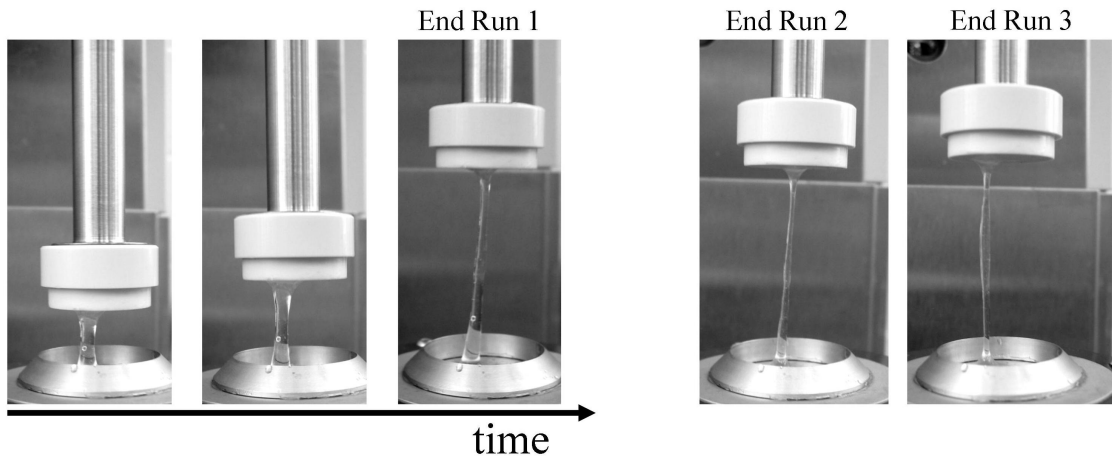


Figure 6-8: Photos of successive extensional flow tests performed on a single sample of hagfish slime, made from fresh slime exudate. The shape of the filament at the end of each run changes slightly; note that after Run 3 the shape is convex near the center of the filament due to the gel-like nature of the slime mass.

around themselves and aggregated in the center of a saltwater puddle. Extensional flow tests were more successful. Figure 6-8 displays photos taken during successive extensional flow tests performed on a single sample of “fresh” hagfish slime. The sample shows adequate adherence to the upper geometry surface. The experimental measurements corresponding to these extensional flow tests are shown in Figure 6-9. The plate separation is given by the equation $L(t) = L_0 \exp(+\dot{\epsilon}t)$, in which $\dot{\epsilon}$ is the extensional strain rate for homogeneous deformation. For the results in Figure 6-9, $\dot{\epsilon} = 0.2 \text{ s}^{-1}$, and the force curves nearly overlap. The peak force of each successive experiment is $F_{max} = 0.0416 \text{ N}$, 0.0464 N , 0.0489 N , and 0.0474 N , respectively for Runs 1-4.

Although the plate separation $L(t)$ is precisely controlled, the kinematics of material deformation may not ideally proceed, as suggested by the photos in Figure 6-8 and by observations during the experiments. For example, a remnant bulge can be seen in the filament at the end of Run 3. Furthermore, it is possible that a filament of slime is lifted out of a puddle resting on the bottom plate, i.e. the ultrasoft material sags in response to gravity, in which case the extensional flow kinematics are non-ideal. In future experiments, such kinematics can be more closely monitored by a laser mi-

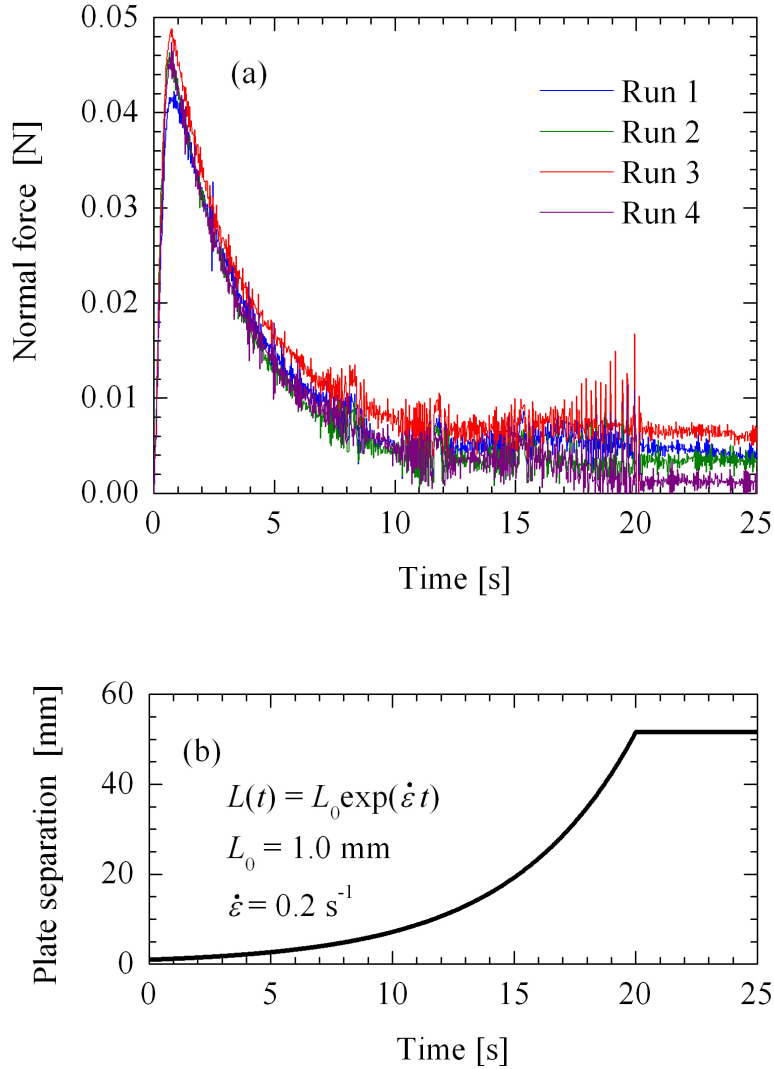


Figure 6-9: Extensional flow results for hagfish slime, corresponding to the tests shown in Figure 6-8. (a) Successive tests on the same sample show repeatable results. (b) The plate separation imposes a constant extensional deformation rate, $\dot{\epsilon} = 0.2 \text{ s}^{-1}$, if homogeneous deformation is assumed.

rometer. Keeping these possibilities in mind, we will none-the-less assume idealized kinematics for the present data set, in which stresses and rates should be considered as “apparent” values. For the idealized case the deformation is homogeneous and volume conserving, thus the radius evolves according to $R(t) = R_0 \exp(-\dot{\epsilon} t/2)$. The stress difference is determined by $\Delta\sigma(t) = F(t)/(\pi R(t)^2)$, and the apparent extensional viscosity is found from $\eta_E = \Delta\sigma(t)/\dot{\epsilon}$. These processed results are given in Figure 6-10 for Run 1. The apparent stress (and corresponding viscosity) approxi-

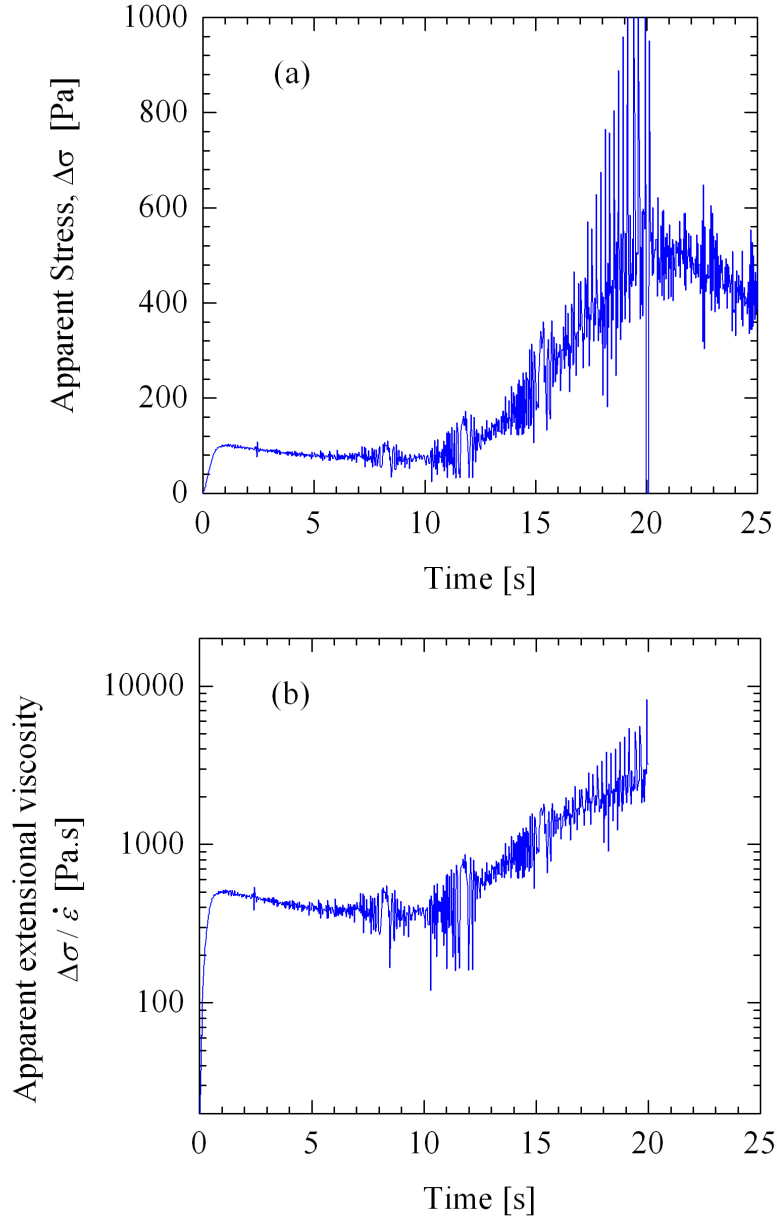


Figure 6-10: Analysis of the extensional flow measurements shown in Figure 6-9 (Run 1), with standard assumptions for kinematics of radial deformation, $R(t) = R_0 \exp(-\dot{\epsilon}t/2)$. (a) apparent stress difference, and (b) apparent extensional viscosity.

mately plateaus until time $t = 10$ s, after which it increases by one order of magnitude. Such a response indicates extensional hardening, so long as deformation kinematics can be assumed as ideal.

These tests represent the first reported intrinsic property measurement of hagfish slime, and include both linear and nonlinear rheological responses. The fresh and

stabilized slime exudate seem to have comparable mechanical properties, especially as indicated by the secant modulus $G \approx 0.02$ Pa for each. A number of items are left as future work. The most important short term goal would be the development of a microstructural model which can describe the nonlinear response measured with these tests. This ultrasoft nonlinear material may also serve as inspiration for soft materials applications which require large stretch ratios, including the DARPA Chemical Robots program which funded a portion of this thesis work.

In the context of the rheometry methods discussed in this thesis, the hagfish slime network is yet another example of the fact that the typical first-harmonic analysis of LAOS tests (Figure 6-6) can be insufficient to describe the true nonlinear viscoelastic material response. Here it is elastic strain-stiffening which is revealed by the tangent modulus analysis of inertio-elastic ringing (Figure 6-7b). Although the LAOS ontology introduced in Chapter 2 could not be used for this sample due to instrumentation limits, namely the lack of a cup-and-bob geometry for the strain-controlled ARES rheometer, we see that appropriately considering the raw oscillatory data can allow for accurate characterization of complex materials. In this case, it is the inertio-elastic oscillations (free ringing) which is amenable to analysis on a torque-controlled instrument.

Chapter 7

LAOS of pseudoplastic and elastoviscoplastic materials

This chapter explores the utility of strain-controlled large amplitude oscillatory shear (LAOS) deformation for identifying and characterizing apparent yield stress responses in elastoviscoplastic materials. The approach emphasizes the visual representation of the LAOS stress response within the framework of Lissajous curves with strain, strain-rate, and stress as the coordinate axes, in conjunction with quantitative analysis of the corresponding limit cycle behavior. This approach enables us to explore how the material properties characterizing the yielding response depend on both strain amplitude and frequency of deformation. Canonical constitutive models (including the purely viscous Carreau model and the elastic Bingham model) are used to illustrate the characteristic features of pseudoplastic and elastoplastic material responses under large amplitude oscillatory shear. A new parameter, the perfect plastic dissipation ratio, is introduced for uniquely identifying plastic behavior. Experimental results are presented for two complex fluids, a pseudoplastic shear-thinning xanthan gum solution and an elastoviscoplastic invert-emulsion drilling fluid. The LAOS test protocols and the associated material measures provide a rheological fingerprint of the yielding behavior of a complex fluid that can be compactly represented within the domain of a Pipkin diagram defined by the amplitude and timescale of deformation.

7.1 Introduction

This work examines the response of “yield stress fluids” to large amplitude oscillatory shear (LAOS) deformation. Without seeking to be drawn into an extended debate, the term “yield stress fluid” is used pragmatically to refer to any material or model which exhibits a dramatic change in viscosity (orders of magnitude) over a small range of applied stress[77, 78]. This definition might include pseudoplastic (dramatically shear-thinning) liquids, or elastoviscoplastic materials which effectively behave as elastic solids for applied stresses below a critical yield stress $\sigma < \sigma_y$, but are viscoplastic and irreversibly deform and flow for applied stress above the yield stress $\sigma > \sigma_y$.

Yield stress behavior is sometimes desired in order to achieve particular performance with complex fluids. For example, oilfield drilling fluids are often formulated to be yield stress fluids to meet the needs of an intermittent drilling process. While drilling ahead, relatively long periods of fluid flow will be interrupted by short periods (usually less than ten minutes) when the fluid is not pumped as pipe connections are made. During non-drilling activities (tripping pipe, running casing, etc.) the drilling fluid may lie stagnant in the hole for hours or even days. During this period, settling of solids can be especially problematic if the fluid does not have sufficient yield structure to support both large and small particulate matter. However, a fluid with an excessive yield stress can also provide problems; for example, if a large stress is required to break the structure and initiate fluid flow in the well annulus, the result is tremendous pressure surges which may fracture the formation and lead to further problems. The balance between minimizing these swab and surge pressures while maintaining suspension of weight materials (high specific gravity solids, primarily barite) and drilled cuttings can be difficult to maintain in fluids that are thixotropic and exhibit a yield stress[79].

What is needed is a test protocol for characterizing the elastic, viscous, and yielding characteristics of a prototypical mud in the field or in the formulation laboratory. Large amplitude oscillatory shear (LAOS) is a test method which systematically interconnects familiar material measures such as steady flow viscosity

$\eta(\dot{\gamma})$, linear viscoelastic moduli $G'(\omega)$ and $G''(\omega)$, as well as nonlinear viscoelastic properties[14], allowing for nonlinear viscous and elastic effects to be characterized simultaneously. In strain-controlled LAOS deformation, the imposed strain takes the form $\gamma(t) = \gamma_0 \sin \omega t$, which consequently imposes a phase-shifted strain-rate $\dot{\gamma}(t) = \gamma_0 \omega \cos \omega t$. The resulting oscillatory shear stress $\sigma(t; \omega, \gamma_0)$ is recorded and analyzed. LAOS tests are completely defined by two input parameters, e.g. frequency and amplitude $\{\omega, \gamma_0\}$. These two parameters define an experimental test space in which results can be compactly represented, which is now known as the Pipkin diagram[1]. The steady flow curve, $\eta(\dot{\gamma})$, is recovered in the limit of small frequency, $\omega \rightarrow 0$, whereas the familiar measures of linear viscoelasticity, $G'(\omega)$ and $G''(\omega)$, are recovered in the limit of small strain amplitude, $\gamma_0 \rightarrow 0$. Many complex fluids are processed or utilized outside of these limiting regions, e.g. the oilfield drilling fluids discussed above experience large strains and strain-rates on the order of the reciprocal of the characteristic timescales in the material. LAOS offers a systematic methodology for characterizing viscoelastic material responses over the full domain of amplitudes (γ_0) and timescales ($1/\omega$) of the imposed shearing deformation.

Methods for analyzing LAOS include Lissajous curves[12, 27], Fourier transform rheology (e.g. [15]), Stress decomposition[28, 50, 66], computation of viscoelastic moduli[19, 50], decomposition into characteristic waveforms[22], and analysis of parameters related to Fourier transform rheology[16, 80]. A unifying framework, or ontology, for LAOS was recently proposed by Ewoldt et al.[50] (see Chapter 2) which introduced a number of physically-meaningful material measures for LAOS tests and identified the inter-relation between some of the different approaches listed above. The physical meaning of some of these measures was highlighted by considering graphically the raw test data in the form of Lissajous-Bowditch curves, which are parametric plots of stress $\sigma(t)$ vs. strain $\gamma(t)$ or strain-rate $\dot{\gamma}(t)$. This inherently visual approach allows for qualitative interpretations of quantitative material measures such as Fourier or Chebyshev coefficients.

Steady state LAOS responses can be visualized as parametric curves in a 3-D space with strain, strain-rate, and stress as the coordinate axes, $\{\gamma(t), \dot{\gamma}(t), \sigma(t)\}$ [28].

We use the term “elastic Lissajous-Bowditch curve” to denote the projection of the oscillatory response curves onto the stress $\sigma(t)$ vs. strain $\gamma(t)$ plane, whereas viscous Lissajous-Bowditch curves denote parametric plots of stress $\sigma(t)$ vs. strain-rate $\dot{\gamma}(t)$. A linear elastic material response, $\sigma = G\gamma$, appears as a straight line on the elastic Lissajous curve of $\sigma(t)$ vs. $\gamma(t)$, or a circle in a suitably scaled plot of $\sigma(t)$ vs. $\dot{\gamma}(t)$. In the linear viscoelastic regime, the Lissajous figures are elliptical when the stress response is a sinusoidal function, $\sigma(t) = \sigma_0 \sin(\omega t + \delta)$ and is plotted against $\gamma(t)$ or $\dot{\gamma}(t)$.

A nonlinear viscoelastic response will distort the elliptical shape of a Lissajous curve. The particular nonlinear LAOS signature associated with yield stress fluids such as drilling muds can be identified and better understood by first considering representative constitutive models. Here we consider two canonical models: a purely viscous Carreau model and the elastic Bingham plastic model. We determine the hallmark responses of these yield stress fluid models in LAOS tests and explore suitable measures for quantifying typical yield-like responses for any material in LAOS. We examine the experimental response of two material samples using these measures; a shear-thinning aqueous xanthan gum solution and a pseudoplastic oilfield drilling mud. We show that the LAOS protocol can be used to identify regimes within the shear deformation space $\{\omega, \gamma_0\}$ in which a complex material most closely approximates the response of a yield stress fluid.

7.2 Materials and Methods

7.2.1 Materials

The aqueous xanthan gum solution (0.2 wt%) was provided by CPKelco, San Diego, CA in solution form. An oilfield drilling fluid was provided by Baker Hughes Drilling Fluids, Houston, TX. The invert emulsion drilling fluid (IEDF) was obtained as a sample from field operations and had a density of 1.53 g/ml. The fluid component of the drilling mud is an invert emulsion with a continuous mineral oil phase surrounding

an internal phase of calcium chloride brine (17%wt, 1.76 molar). The oil/water ratio was 76/24 (by vol). The drilling mud contained high specific gravity solids (barite) at $\sim 15\%$ wt and organophilic clays $\sim 2\%$ wt. Drilled solids, which primarily consist of a mixture of reactive and non-reactive clays, composed greater than 5%wt of the IEDF.

7.2.2 LAOS protocol

Large amplitude oscillatory shear (LAOS) tests were performed using an ARES-LS displacement controlled rheometer (TA Instruments). A cone-plate geometry was used for the aqueous xanthan gum solution, diameter $D = 50$ mm, cone angle $\theta = 0.0402$ rad, truncation $h = 0.049$ mm. Xanthan gum tests were performed at $T=22^\circ\text{C}$.

For the drilling fluid, a plate-plate geometry was selected (diameter $D = 25$ mm, gap $h = 0.5$ mm) because of the presence of a significant particulate phase. Adhesive-backed, waterproof sandpaper (600 grit) was attached to both the top and bottom plates to inhibit slip at the surface. In an attempt to avoid edge fracture artifacts, the gap was deliberately over-filled with the fluid sample. An outer ring ($D = 30$ mm) was used to contain the over-filled sample. The ring was sealed to the bottom sandpaper surface using vacuum grease. Using a Peltier plate, the temperature of the drilling fluid was maintained at 48.9°C (i.e. 120°F which is recommended as standard practice by the American Petroleum Institute[81]).

The strain field for the rotational parallel plate geometry is inhomogeneous, and angular displacement and torque are the naturally measured quantities. For the intrinsic variables of strain and stress, we report (and use in subsequent analysis) the strain at the edge of the plate, σ_R , and the apparent stress which would exist at the edge of the plate assuming a linear response, $\sigma_A = 2M/\pi R^3$. The possible artifacts of this approach are given more detailed consideration in a subsequent section below.

Raw data was collected with the native rheometer control software (TA Orchestrator) using the Arbitrary Waveshape test as described in Section 4.2.1 and [50]. Although extremely high sample rates can be achieved by acquiring raw voltage signals from the BNC outputs on the back of the ARES, we find that the Arbitrary

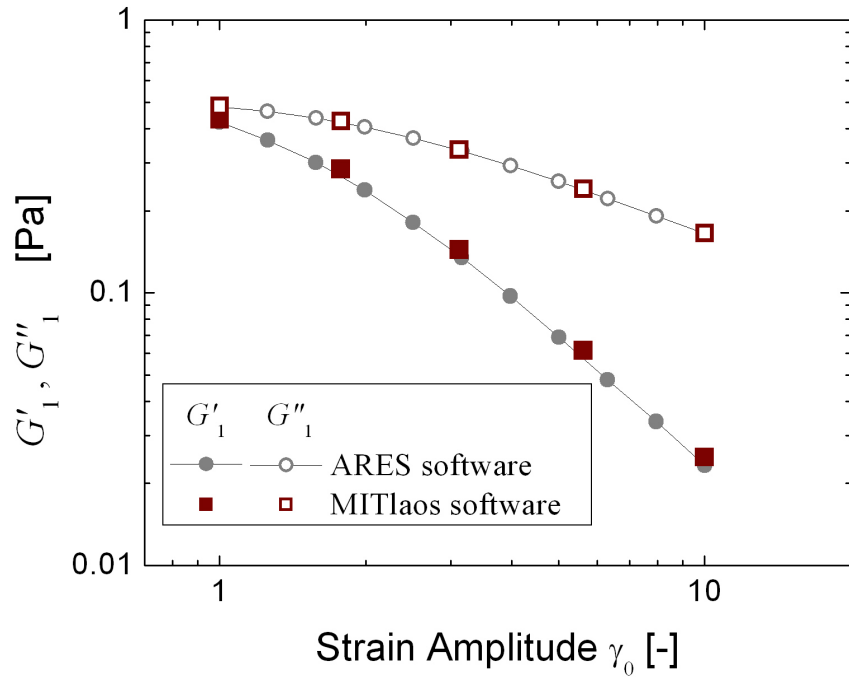


Figure 7-1: Validation of the MITlaos software (Chapter 3), using a strain sweep for xanthan gum solution (0.2 wt%) at $\omega = 3.75 \text{ rad.s}^{-1}$. MITlaos software is used to analyze the raw stress and strain waveforms resulting from Arbitrary Waveshape tests (squares). A duplicate test was performed with the typical oscillation test mode of the ARES rheometer software (circles), which provides viscoelastic parameters but no raw data or assessment of higher harmonic content. The superposition of results indicates the validity of the Arbitrary Waveshape test and the MITlaos software for analyzing both linear and nonlinear LAOS results.

Waveshape test sequence allows for sufficiently high sample rates for our analysis without the requirement of a separate data acquisition system.

7.2.3 Data processing

The raw data exported from the rheometer control software was processed using MATLAB. The majority of data processing is performed using a freely available LAOS data analysis package, MITlaos (Section 4.2.1 and [49]). The MITlaos software is used to determine the Fourier coefficients, Chebyshev coefficients, elastic/viscous stress decomposition, and the corresponding viscoelastic moduli. For a specified pair of LAOS input parameters, $\{\omega, \gamma_0\}$, the sample is subjected to multiple deformation

cycles. The initial transient response is monitored and allowed to decay so that a steady-state limit cycle is reached. Six complete strain cycles in the periodic steady state regime are used for the data processing. MITlaos uses the higher-harmonic information, up to a user-specified cutoff harmonic $n_{max} = \omega_{max}/\omega$, to calculate the desired viscoelastic material parameters. For the drilling fluid, the cutoff frequency was chosen to be $n_{max} = 11$ or higher depending on the noise floor of the power spectrum, in order to capture of all the meaningful information in the response signal while avoiding noise. For the xanthan gum solution the cutoff frequency was chosen to be $n_{max} = 9$, except for the lowest frequency test at $\{\omega = 0.15 \text{ rad.s}^{-1}, \gamma_0 = 1.0\}$ in which $n_{max} = 5$ was used to filter unnecessary noise in the (small) torque signal.

In order to validate the procedure of using MITlaos to analyze raw stress and strain waveforms we first compared the results from a pair of strain sweep tests performed using the ARES software. One test used the Arbitrary Waveshape protocol with offline processing by MITlaos, and the other test used the standard oscillation protocol of the ARES software, which does not capture the raw waveforms. The results from these duplicate tests are shown in Fig. 7-1 for the xanthan gum solution at $\omega = 3.75 \text{ rad.s}^{-1}$ and increasing values of strain amplitude γ_0 . Good correspondence between the two protocols is obtained for both $G'_1(\omega, \gamma_0)$ and $G''_1(\omega, \gamma_0)$ across the full range of strain amplitudes.

7.3 Response of model fluids with yield stress characteristics

Before we examine experimental LAOS measurements, it is instructive to explore the characteristic features of Lissajous curves for model yield stress fluids. This helps build intuition when examining results from experiments or other proposed constitutive models. Here we consider two models which are simpler limits of a general elastoviscoplastic response. One model is a purely-viscous Generalized Newtonian Fluid which exhibits pseudoplasticity (shear-thinning) and can approach plastic be-

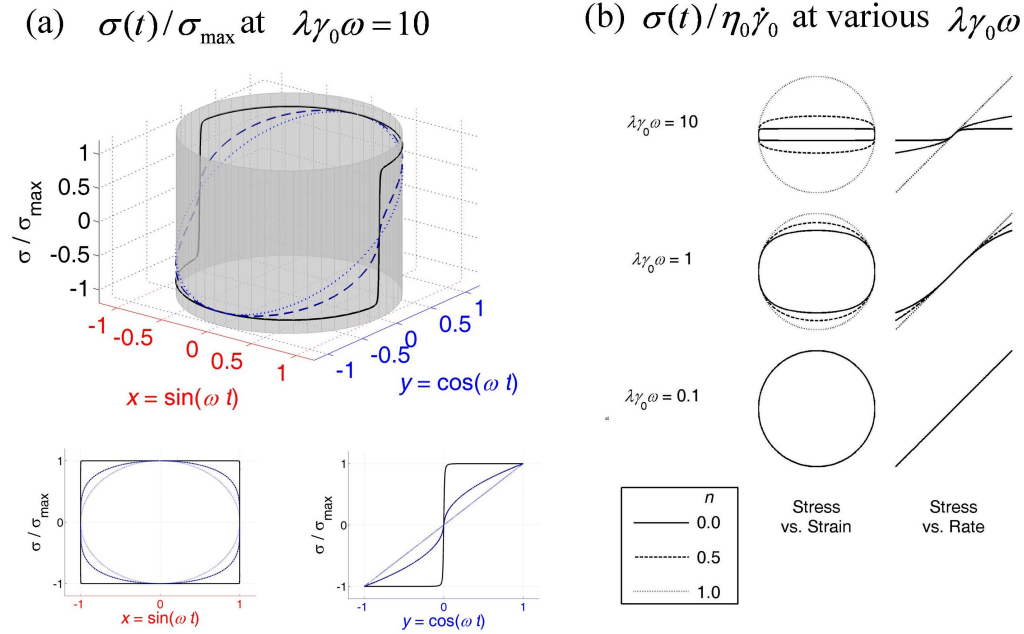


Figure 7-2: Lissajous-Bowditch curves of the Carreau pseudoplastic model (Eq. 7.2) for various values of the Carreau number $Cu = \lambda\gamma_0\omega$ and power law index n . Here $n = 1.0$ is Newtonian (dotted lines), $n = 0.5$ is shear-thinning (dashed lines), and $n = 0.0$ is the limiting case of viscoplastic yield stress behavior (solid lines). (a) 3D trajectories of the stress response $\sigma(t)/\sigma_{\max}$ as a function of the normalized LAOS inputs $\{x(t), y(t)\}$, shown for $\lambda\gamma_0\omega = 10$. Note that the maximum stress σ_{\max} is different for each value of n , as shown in (b), which depicts 2D Lissajous curves projected onto the planes of stress vs. strain ($\tilde{\sigma}(t)$ vs. $x(t)$) and stress vs. strain-rate ($\tilde{\sigma}(t)$ vs. $y(t)$). In (b) the stress is scaled by the Newtonian stress $\eta_0\dot{\gamma}_0$, rather than the maximum stress, at each value of the Carreau number $Cu = \lambda\gamma_0\omega$.

havior. The second model is elastoplastic, behaving as a linear elastic solid before yield with a rate dependent stress after yield. Each model can be allowed to approach the canonical Bingham plastic constitutive response in an appropriate limit.

7.3.1 Purely viscous Carreau model

Many Generalized Newtonian Fluid models can approach the familiar Bingham plastic limit, for example the Cross model[82]), Papanastasiou model[83], and Carreau-Yasuda model[8]. Bird et al. 1983[84] and Mitsoulis 2007[85] provide comprehensive reviews of the relative merits of many of these different models and their utility in solving flow problems. Here we select the Carreau model because of its familiarity and

its ability to describe pseudoplastic (shear-thinning) data as well as materials with a critical plastic stress. Furthermore, the model requires only two variables to fully describe a response to LAOS deformation, as shown below. The Carreau-Yasuda model is a Generalized Newtonian Fluid which describes a non-Newtonian viscosity as an instantaneous single-valued function of shear rate[8]. The non-Newtonian viscosity is given as

$$\frac{\eta - \eta_\infty}{\eta_0 - \eta_\infty} = (1 + (\lambda\dot{\gamma})^a)^{\frac{n-1}{a}} \quad (7.1)$$

where η_0 is the low-rate Newtonian plateau viscosity, η_∞ is the high-rate plateau viscosity, λ is a characteristic timescale (or more accurately the inverse of a characteristic shear-rate, $\lambda = 1/\dot{\gamma}^*$) beyond which non-Newtonian behavior becomes important, n is the power-law exponent, and a is correlated with the sharpness (concavity) of the transition from Newtonian to power-law behavior. Many good fits can be found for $a = 2$ and $\eta_\infty = 0$, especially for polymer solutions and melts[8]. For $a = 2$, the model reduces to the Carreau model.

The Carreau model reduces to the Newtonian fluid for $n = 1$ and describes shear-thinning for $n < 1$. For $n \rightarrow 0$, and $\eta_0 \gg \eta_\infty$, the model represents a yield stress fluid in which the viscosity dramatically changes within a small range of stress. The apparent yield stress of the Carreau model (Eq. 7.1) for $n = 0$ can be found by considering the power-law regime, $\lambda\dot{\gamma} \gg 1$, and determining the shear stress from $\sigma = \eta(\dot{\gamma})\dot{\gamma}$. The apparent shear yield stress is found to be $\sigma_y = \eta_0/\lambda$ in the limit $n = 0$. The Carreau model gives a purely viscous response, because stress only depends on the instantaneous value of the shear-rate, $\sigma(\dot{\gamma})$. The elastic modulus G' is therefore always zero, even in the nonlinear regime.

The LAOS material response of the Carreau model (Eq. 7.1, $a = 2$) can be concisely represented by two parameters when we set $\eta_\infty = 0$ for simplicity. For $x(t) = \gamma(t)/\gamma_0 = \sin \omega t$, $y(t) = \dot{\gamma}(t)/\dot{\gamma}_0 = \cos \omega t$ the dimensionless stress response is

$$\tilde{\sigma}(t; n, Cu) = y(t) \left(1 + (Cu y(t))^2\right)^{\frac{n-1}{2}} \quad (7.2)$$

where $\tilde{\sigma} \equiv \sigma/\eta_0\dot{\gamma}_0$ and $Cu \equiv \lambda\gamma_0\omega$ is the Carreau number. The normalized stress waveform is therefore a function of two non-dimensional parameters. The stress response of Eq. 7.2 is represented in terms of a family of Lissajous-Bowditch plots in Fig. 7-2. Fig. 7-2a depicts the 3D response curve of the normalized stress response as a function of the two orthogonal LAOS inputs, $\sigma(\gamma(t), \dot{\gamma}(t))$. When suitably scaled so that $x(t) = \sin \omega t$ and $y(t) = \cos \omega t$, the periodic system output corresponds to trajectories on the surface of the bounding cylinder shown in gray (Fig. 7-2a). In the limit $n = 1$, the response corresponds to a plane curve sectioned through the cylinder with $\sigma_{max} = \eta_0\dot{\gamma}_0$. As n is decreased, the trajectory becomes increasingly distorted and the maximum stress decreases.

The Carreau model approaches a yield stress fluid response as $n \rightarrow 0$ and the Carreau number $Cu = \lambda\gamma_0\omega$. For this yield stress response, the maximum stress becomes $\sigma_{max} \rightarrow \eta_0/\lambda$ and the trajectory approaches two plane semicircles (Fig. 7-2a, top) offset by $2\sigma_{max} = 2\eta_0/\lambda$. For this yield-like response, normalized elastic Lissajous-Bowditch curves of stress vs. strain appear as squares (Fig. 7-2a, bottom-left, $n = 0$). The viscous Lissajous-Bowditch curves of stress vs. strain-rate enclose no area and are single-valued functions of the instantaneous strain-rate $y(t) = \dot{\gamma}(t)/\dot{\gamma}_0$ (see Eq. 7.2) as expected for all Generalized Newtonian Fluid constitutive models. For this purely viscous response, the slope of any local secant line equals the viscosity, $\eta \equiv \sigma(\dot{\gamma})/\dot{\gamma}$. Near $|\dot{\gamma}| \rightarrow 0$ it is the tangent line of the viscous Lissajous curve which represents the low-rate Newtonian plateau viscosity, η_0 ; however, this becomes increasingly difficult to resolve. The apparent viscosity at the minimum resolvable rate, $\eta'_M \equiv d\sigma/d\dot{\gamma}|_{\dot{\gamma}=0}$, and at the largest imposed rate, $\eta'_L \equiv \sigma/\dot{\gamma}|_{\dot{\gamma}=\dot{\gamma}_0}$, are two useful measures of the nonlinear response which are generally applicable to any viscoelastic LAOS response, as discussed in Section 2.3.2 and [50].

The limiting yield stress behavior of the Carreau model is representative of a viscoplastic yield stress response. A corresponding elastoplastic limit is considered in the following section.

7.3.2 Elastic Bingham model - homogeneous strain

The elastic Bingham model responds as a linear elastic solid below the yield stress and transitions to a Bingham plastic response above the yield stress in which recoverable elastic strain is stored during flow[2]. This model incorporates material elasticity below yield and in this sense represents a more general yield stress response than the Carreau model presented in the previous section. A number of more general elastoviscoplastic models have also been proposed in the literature (see for example [86, 87]); however for simplicity we focus here on the canonical elastoplastic model.

The shear stress-strain relationships for the elastic Bingham model are described by

$$\begin{aligned} \sigma &= G\gamma^E & |\gamma^E| < \gamma_Y \\ \sigma &= G\gamma_Y + \mu_p\dot{\gamma} & |\gamma^E| = \gamma_Y \end{aligned} \quad (7.3)$$

where G is the elastic modulus, γ^E is the recoverable elastic strain, γ_Y is the yield strain, and μ_p is the plastic viscosity. The yield stress for this model is $\sigma_y = G\gamma_Y$. The elastic strain γ^E is found by integrating the shear-rate with respect to time, but saturates at $|\gamma^E| = \gamma_Y$ during flow. When the flow stops and reverses direction, the accumulated elastic strain is recovered and the response is linear elastic until the material is re-yielded again, when $\gamma^E = \pm\gamma_Y$.

The response of the model to LAOS flow is completely governed by two non-dimensional parameters, representing the normalized strain amplitude and normalized strain-rate amplitude[2],

$$\begin{aligned} \Gamma_0 &= \frac{\gamma_0}{\gamma_Y} \sim \frac{\text{maximum imposed strain}}{\text{yield strain}} \\ N &= \frac{\mu_p \dot{\gamma}_0}{\sigma_Y} \sim \frac{\text{max viscous stress}}{\text{yield stress}}. \end{aligned} \quad (7.4)$$

N is related to the inverse of the characteristic Bingham number for LAOS, $N = 1/Bi$ [84]. Here we use N to parameterize the flow since it directly corresponds to an input of the LAOS deformation, strain-rate amplitude $\dot{\gamma}_0$.

The elastic Bingham model is simulated in homogeneous LAOS flow to produce

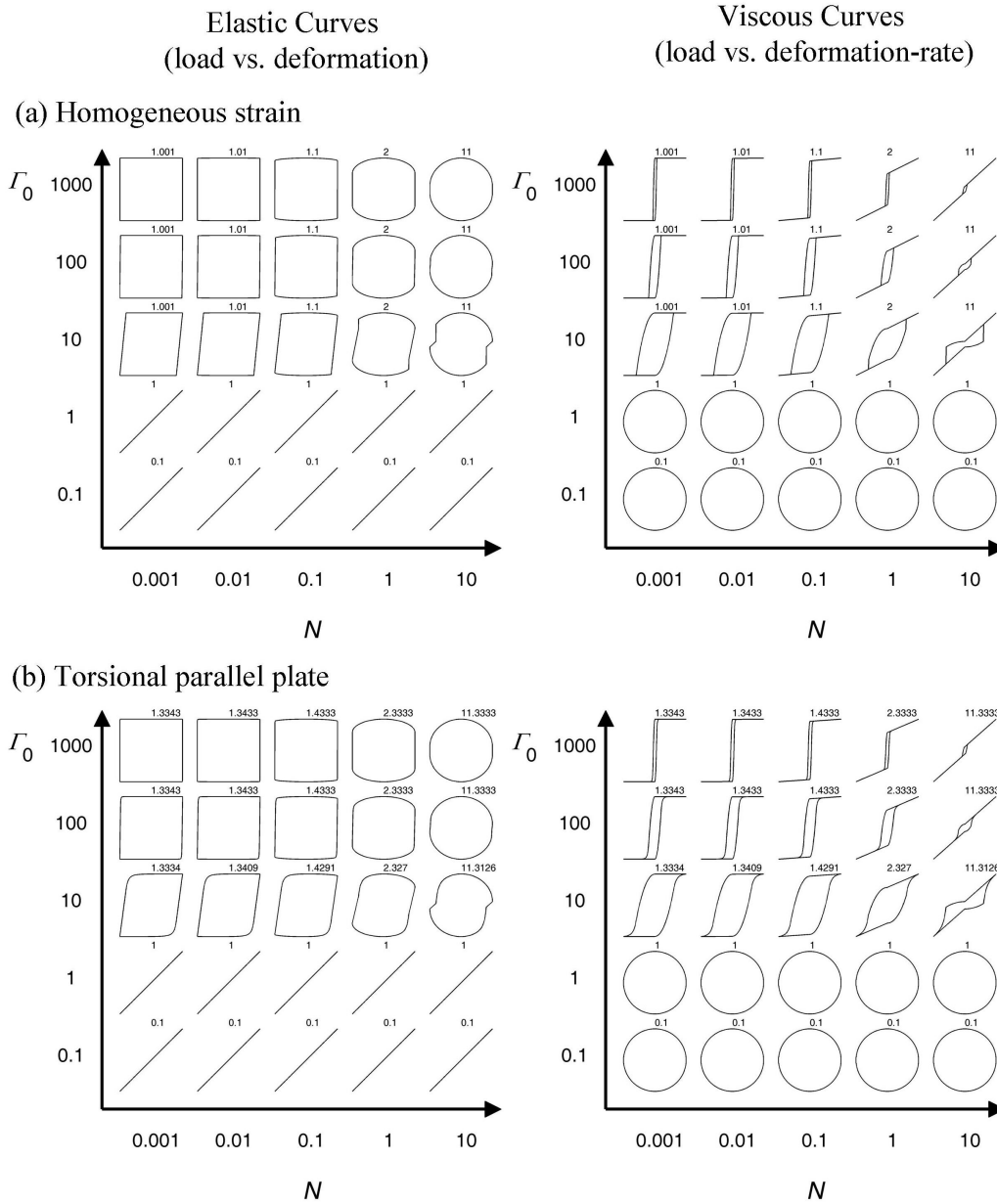


Figure 7-3: Lissajous-Bowditch curves for the elastic Bingham model in terms of the variables $\Gamma_0 = \gamma_0/\gamma_Y$, $N = \mu_p \dot{\gamma}_0/\sigma_Y$ defined by Yoshimura and Prudhomme[2]. (a) Homogeneous strain (e.g. cone-plate) response showing individual limit cycles of the oscillatory stress vs. strain (elastic curves) and stress vs. strain-rate (viscous curves). Maximum normalized stress $(\sigma/\sigma_Y)_{\max}$ is shown above each curve. (b) Steady oscillatory response of plate-plate deformation (inhomogeneous strain), curves of torque vs. displacement (elastic curves) and torque vs. displacement-rate (viscous curves). The maximum normalized torque shown above each curve, $(2M/\pi R^3 \sigma_Y)_{\max}$.

the Lissajous curves shown in Fig. 7-3a. For ease of comparison, each Lissajous curve is normalized once again by the maximum stress which is shown above each trajectory. The curves are arranged across the two-dimensional parameter space of strain-rate-amplitude and strain-amplitude (N, Γ_0) , which represents the appropriate Pipkin space for the elastic Bingham model response.

The elastic Bingham model reduces to a traditional Bingham plastic as the yield strain goes to zero, $\gamma_Y \rightarrow 0$, which corresponds to large values of Γ_0 and the top of the Pipkin space in Fig. 7-3a. In this viscoplastic limit the stress is only a function of strain rate, $\sigma(\dot{\gamma})$, since the yield criteria is satisfied for almost all times.

The elastic Bingham model further reduces to a perfect plastic model with a constant flow stress after yield as $\mu_p \rightarrow 0$, corresponding to $N \rightarrow 0$ and $\Gamma_0 \gg 1$ (the top left corner of the Pipkin space of Fig. 7-3a). In this limit the constitutive equation of the perfect plastic model is written as $\sigma = \sigma_y \text{sgn}(\dot{\gamma})$.

The most prominent feature of the yielded response ($\Gamma_0 > 1$) is a rectangular elastic Lissajous curve, which is approached exactly in the limit of the perfect plastic response ($N \rightarrow 0$ at $\Gamma_0 \gg 1$). The elastic Lissajous curve of the perfect plastic response has vertical sides ($G \rightarrow \infty$) and a flat top and bottom ($\mu_p \rightarrow 0$). The limit of a Bingham plastic model ($\Gamma_0 \gg 1$, arbitrary N) also has vertical sides, but is rounded on the top and bottom because the flow stress is proportional to shear-rate, $\sigma(t) = \sigma_y + \mu_p \dot{\gamma}(t)$. The full elastoplastic Bingham model response includes an additional feature, sloped sides, which are caused by the finite elasticity, $d\sigma/d\gamma = G$, for stresses below the yield stress.

For completeness, the viscous representation of the Lissajous curves are also shown in Fig. 7-3a. For the viscous Lissajous curves of stress vs strain-rate, $\sigma(t)$ vs. $\dot{\gamma}(t)$, the importance of the plastic viscosity μ_p term in flow is indicated by the slope of linear portions of the curves (for $\Gamma_0 > 1$). The enclosed area in the center of the viscous Lissajous curves is indicative of the finite elasticity below yield. Elasticity is negligible at $\Gamma_0 \gg 1$, which corresponds to the limit of the (purely viscous) traditional Bingham plastic response. The response is approximately Newtonian in the limit of $\Gamma_0 \gg 1$, $N \gg 1$ (upper-right portion of the Pipkin diagram). In this limit the flow

stress dominates, rendering the yield stress negligible. Even though the underlying constitutive model is elastoviscoplastic, the yielding behavior is insignificant for shear deformations at $\Gamma_0 \gg 1$, $N \gg 1$, and in this part of the deformation space, the LAOS behavior of a material that is described by the elastoplastic Bingham model would instead appear almost Newtonian.

7.3.3 Elastic Bingham model - torsional plate-plate response

Because of the high volume fraction of solid particulates in many elastoviscoplastic materials such as the drilling fluid considered in the present work, it is typically necessary to use a parallel plate configuration in which the shearing deformation is inhomogeneous. It is therefore necessary to address the possible Lissajous curve artifacts which are introduced by inhomogeneous torsional shear flow. Exploring LAOS plate-plate artifacts is important because this geometry is often used for materials which are susceptible to wall slip and the parallel disk surfaces are easily modified to increase the roughness (e.g. with adhesive-backed sandpaper as used in this work for the drilling fluid). LAOS plate-plate artifacts have been considered in terms of both the harmonic response [88, 89] and the oscillatory response in the time domain [2]. Our work here is concerned specifically with Lissajous curves, and we therefore examine the parallel disk artifacts introduced in the form of the Lissajous curves for the elastic Bingham model. The elastic Bingham model (Eq. 7.3) under torsional shearing is simulated in the plate-plate geometry following the same procedure as [2]. Yield begins at the plate edge for sufficiently large angular displacements, and the radial position separating yielded and un-yielded regions is time dependent. For the plate-plate geometry, the non-dimensional parameters governing the LAOS torque response involve the relative magnitude of the yield strain γ_Y and the strain amplitude at the edge of the plate, given by $\gamma_0 = \theta_0 R/h$, where R is the plate radius, h is the gap and θ_0 is the maximum angular displacement of the plate. The inhomogeneous strain torque response for the elastic Bingham model is shown in Fig. 7-3b.

Comparing the plate-plate responses of Fig. 7-3b with the homogeneous (e.g. cone-plate) responses of Fig. 7-3a, we observe that the plate-plate artifacts are small, and

there is little qualitative difference in the general shapes of Lissajous curves for cone-plate vs. plate-plate deformations with this model. In general, the inhomogeneous kinematics of the plate-plate geometry tend to smooth the linear-to-nonlinear transitions, for instance by rounding some otherwise sharp corners, but otherwise do not introduce any qualitative new features. The strong similarities between the Lissajous curves for cone-plate and plate-plate can be rationalized as follows. First, the range of strain within a plate-plate geometry always varies from $\gamma = 0$ at the center of rotation to $\gamma = \gamma_0$ at the edge of the fixture. Although the strain amplitude at the edge of the plate may transition into the nonlinear regime, e.g. the yielded regime $\Gamma_0 > 1$, part of the sample will always be in the linear regime at sufficiently small radial position r . Any dramatic linear-to-nonlinear transition will first occur at the outer edge of the plate, while the majority of the sample remains in the linear elastic (un-yielded) regime. The torque response of any purely strain-dependent transition will therefore be smoothed in LAOS tests with the plate-plate geometry.

Second, the measured torque M is weighted by the magnitude of the stress at large radius r (i.e. the shear stress in the yielded region). A torque balance between the applied torque and sample stress (neglecting inertia) gives $M = 2\pi \int_0^R \sigma(r)r^2 dr$. The material first yields at the maximum radius $r = R$, and the nonlinear constitutive response will quickly dominate the torque response for the plate-plate geometry. The characteristic shapes of the nonlinear Lissajous curves for the plate-plate and cone-plate flows thus closely resemble each other.

We can quantitatively compare the maximum values of the normalized curves, by examining the peak value of normalized stress shown above each curve, $(\sigma/\sigma_y)_{max}$. For the cone-plate geometry this value approaches $(\sigma/\sigma_y)_{max} \rightarrow 1$ in the yielded region ($\Gamma_0 > 1$) and at low strain-rate amplitudes ($N < 1$). For the plate-plate response, the peak value of the normalized torque $(2M/\pi R^3 \sigma_Y)_{max}$ is shown above each curve, or equivalently $(\sigma_A/\sigma_Y)_{max}$ where $\sigma_A = 2M/\pi R^3$ is the apparent stress which would exist at $r = R$ for a linear material response at a given torque M (this corresponds to the typical method of estimating the stress at the plate edge based on a torque measurement[8]). In the yielded region at low strain-rate amplitude ($N < 1$),

we observe from Fig. 7-3b that $(\sigma_A/\sigma_Y)_{\max} \rightarrow 4/3$. That is, the assumed edge stress is larger than the actual model yield stress by only 33%[90]. This numerical value $4/3$ can be understood by determining the torque response M for a perfect plastic material in which the shear stress is constant throughout the sample with magnitude $\sigma(r) = \sigma_y$. Substituting into the normalized torque expression gives

$$\left(\frac{2M}{\pi R^3 \sigma_Y} \right)_{\max} = \frac{2}{\pi R^3 \sigma_Y} \frac{2\pi R^3 \sigma_Y}{3} = \frac{4}{3} \quad (7.5)$$

Note that the plate-plate results in the yielded region for high strain-rates ($N \geq 1$, upper-right of the Pipkin space, Fig. 7-3b) are also slight overestimates of the actual maximum stress (compare to Fig. 7-3a), but the difference is smaller in this region. The difference between cone-plate and plate-plate is smaller here because the material response for $\Gamma_0 > 1$, $N > 1$, becomes dominated by the plastic viscosity term, which is inherently a linear response in this model.

This analysis provides a broad interpretation of the artifacts in Lissajous curves that can be expected to be introduced from LAOS tests in a parallel plate rheometer. In general, the inhomogeneous strain field softens the nonlinear features of the response and leads to small overestimation of stresses for shear-thinning or yield stress materials. The preceding analysis will aid in the interpretation of the LAOS response for the drilling fluid examined in this work, and also for future LAOS tests using parallel plate fixtures.

7.4 Quantitative indicators of plastic behavior in LAOS

The rheological response of a complex fluid in LAOS can be characterized by numerous material parameters, including strain- and frequency-dependent viscoelastic moduli and higher-harmonic coefficients[15]. In this section we consider the expected behavior of such viscoelastic parameters for a yield stress fluid in response to large amplitude deformation. We also introduce a measure that we refer to as the perfect plastic

dissipation ratio, ϕ , which acts as a metric for quantifying how closely a particular LAOS response is to the perfect plastic response of an idealized yield stress fluid.

7.4.1 Harmonic analysis and Chebyshev coefficients

For strain-controlled LAOS, $\gamma(t) = \gamma_0 \sin \omega t$, the stress response can be represented in the time domain by a Fourier series[14] of the form

$$\sigma(t; \omega, \gamma_0) = \gamma_0 \sum_n \{G'_n(\omega, \gamma_0) \sin n\omega t + G''_n(\omega, \gamma_0) \cos n\omega t\}. \quad (7.6)$$

On the basis of symmetry arguments it can be shown that the series contains only odd harmonics (n : odd) for typical behavior in which the material response is unchanged if the coordinate system is reversed. Even harmonic terms can be observed in transient rheological responses (when the oscillatory waveforms are not strictly periodic), in the presence of secondary flows[43], or with dynamic wall slip events[44] due to the existence of transient events.

Even harmonics have been discussed as possible indicators of wall slip or yield stress[91, 89, 92, 22]. However, the presence of even harmonics does not specifically indicate a wall slip or yield stress material response in general, nor does the absence of even harmonics indicate the lack of wall slip. For example, Yoshimura and Prudhomme [93] examined the LAOS response of a simple slip layer at the surface of a linear viscoelastic model and did not observe even harmonics. Even-harmonics are only related to non-periodic or asymmetric slip/yield responses. Any stress response which is steady, periodic, and unchanged if the coordinate system is reversed (e.g. a perfect plastic yield stress) will result in only odd, integer harmonics in the Fourier series representation (Eq. 7.6).

The harmonic material coefficients in Eq. 7.6 have a characteristic form for fluids exhibiting idealized yield stress behavior. As we have shown, the ideal perfect plastic yield stress response appears as a square wave in the time domain, $\sigma(t) = \sigma_Y \text{sgn}(\dot{\gamma}(t))$.

The spectrum of Fourier coefficients for this square wave behavior is

$$\begin{aligned} G'_n &= 0 \\ G''_n &= \frac{4}{\pi} \frac{\sigma_Y}{\gamma_o} \frac{1}{n} (-1)^{\frac{n-1}{2}} \quad n : \text{odd} \end{aligned} \quad (7.7)$$

which indicates that the higher order viscous Fourier coefficients decay as $1/n$ [22]. The third-harmonic Fourier coefficients have been given a physical meaning through the use of Chebyshev polynomial analysis (Section 2.2 and [50]). The signs of the third-order Chebyshev coefficients, $e_3 = -G'_3$ and $v_3 = G''_3/\omega$, indicate how the nonlinear contributions to the elastic and viscous stresses evolve. For the perfect plastic, $e_3 = 0$ which confirms the absence of elastic contributions to the stress and $v_3 = -4\sigma_Y/3\pi\dot{\gamma}_0$ is negative and therefore correctly indicates shear-thinning. Although the single parameter v_3 correctly indicates that a plastic-like material is strongly shear-thinning, it is not per se a sensitive discriminator of a yield stress response. Other materials including pseudoplastic liquids will give rise to negative values of v_3 . More specifically, it is the scaling in the decay of the higher viscous harmonics, $v_n \sim 1/\gamma_0\omega n$, rather than the value of a single coefficient, which indicates a Lissajous curve approaching the perfect plastic yield stress response limit associated with the rectangular shape shown in Fig. 7-3a.

7.4.2 Viscoelastic moduli

The presence of a critical stress or yield stress intrinsically leads to nonlinear behavior, and we therefore consider more general LAOS measures which quantify material nonlinearity within a periodic limit cycle (i.e. a single closed Lissajous curve). Section 2.3.3 and [50] introduced several dimensionless indexes of nonlinearity which can be applied broadly to any complex fluid response and which approach limiting values for idealized yield stress behavior. These indexes depend on local definitions of the elastic modulus and dynamic viscosity within a single periodic LAOS cycle. The elastic modulus at the minimum resolvable strain G'_M , and the largest imposed strain

G'_L , respectively, are given by

$$G'_M \equiv \left. \frac{d\sigma}{d\gamma} \right|_{\gamma=0} = e_1 - 3e_3 + \dots, \quad G'_L \equiv \left. \frac{\sigma}{\gamma} \right|_{\gamma=\gamma_0} = e_1 + e_3 + \dots \quad (7.8)$$

The apparent viscosity at the minimum resolvable shear rate and the largest imposed shear rate, respectively, are given by:

$$\eta'_M \equiv \left. \frac{d\sigma}{d\dot{\gamma}} \right|_{\dot{\gamma}=0} = v_1 - 3v_3 + \dots, \quad \eta'_L \equiv \left. \frac{\sigma}{\dot{\gamma}} \right|_{\dot{\gamma}=\dot{\gamma}_0} = v_1 + v_3 + \dots \quad (7.9)$$

These measures (Eqs. 7.8,7.9) make use of the Lissajous curves to provide a physically meaningful interpretation of each parameter, and for a linear viscoelastic response the definitions reduce identically to G' and η' , respectively (Section 2.3 and [50]). The dimensionless indexes of nonlinearity compare the elastic moduli (or dynamic viscosities) at large and minimum strain (or strain-rate), according to

$$S \equiv \frac{G'_L - G'_M}{G'_L} = \frac{4e_3 - 4e_5 + \dots}{e_1 + e_3 + e_5 + \dots}, \quad T \equiv \frac{\eta'_L - \eta'_M}{\eta'_L} = \frac{4v_3 - 4v_5 + \dots}{v_1 + v_3 + v_5 + \dots} \quad (7.10)$$

in which nonlinearities are indicated by non-zero values, and the nature of nonlinearity is captured by the signs of the strain-stiffening index S and shear-thickening index T .

We first discuss the limiting value of the strain-stiffening measure S . For an idealized perfect plastic model ($\sigma = \sigma_Y \text{sgn}(\dot{\gamma})$) or any Generalized Newtonian Fluid model (i.e. solely shear-rate dependent such as the Carreau model), $G'_M = 0$ and $G'_L = 0$, thus $S = 0/0$ and is formally undefined. However, for any real experiment with finite data acquisition rates (or in the limiting case of the elastic Bingham model approaching a perfect plastic), $G'_M = 0$ and $G'_L \approx \sigma_Y/\gamma_0 = \text{finite}$. Thus in the limit of a perfect plastic response ($\Gamma_0 \gg 1$, $N \rightarrow 0$ corresponding to the upper-left region of Fig. 7-3a), we expect $S = (G'_L - 0)/G'_L \rightarrow 1$.

The limiting value of the shear-thickening coefficient T is also undefined for the perfect plastic model. The large-rate dynamic viscosity is readily determined to be $\eta'_L = \sigma_Y/\dot{\gamma}_0$, but the minimum-rate viscosity is undefined due to the discontinuous

analytical response at $\dot{\gamma} = 0$. We therefore consider the apparent minimum-rate dynamic viscosity which would be determined from the finite data acquisition rate (or the spacing of simulated data). In fact, η'_M diverges as the resolution of the shear-rate increases, and thus represents the dynamic viscosity at the minimum strain-rate which can be resolved by the number of data points available. In such a case η'_M will be finite but very large, $\eta'_M \gg \eta'_L$. We find that T is then a function of data-acquisition rate, which is undesirable in a material measure. As sampling rate of a given experiment improves (or for the elastic Bingham model in the limit of $\Gamma_0 \gg 1$, $N \gg 1$), the value of T would behave as $T = (\eta'_L - \eta'_M)/\eta'_L \approx -\eta'_M/\eta'_L \rightarrow -\infty$ for a perfect plastic. The value of T evaluated for the Carreau model (Fig. 7-2) also depends on the sampling rate. With sufficiently fine data spacing, $\eta'_M \rightarrow \eta_0$; in this limit $T = (\eta'_L - \eta'_M)/\eta'_L \approx -\eta_0/\eta(\dot{\gamma}_0) = -(1 + Cu^2)^{\frac{1-n}{2}}$ for the Carreau model.

The nonlinear viscoelastic measures discussed in this section are all well-defined for an arbitrary elastoviscoplastic response. However, for yield stress materials, the parameters systematically approach limiting values which depend on the data acquisition rate, making it difficult to compare results from different tests. In the following section we propose a material measure which is well-defined and has almost no sensitivity to the data acquisition rate.

7.4.3 Perfect plastic dissipation ratio

We consider here a scalar metric for quantifying how close a measured material response corresponds to perfect plastic yield stress behavior. We compare the energy dissipated in a single LAOS cycle to the energy which would be dissipated in a perfect plastic response with equivalent strain amplitude γ_0 and maximum stress σ_{max} . The perfect plastic response represents the maximum possible dissipated energy for a given strain amplitude γ_0 and maximum stress σ_{max} .

The energy dissipated per unit volume in a single LAOS cycle, $E_d = \oint \sigma d\gamma$, can be visualized by the area enclosed by the Lissajous curve of stress vs. strain. The Lissajous curve for the corresponding perfect plastic reference response is always a rectangle which circumscribes the measured response. An example is shown in Fig. 7-

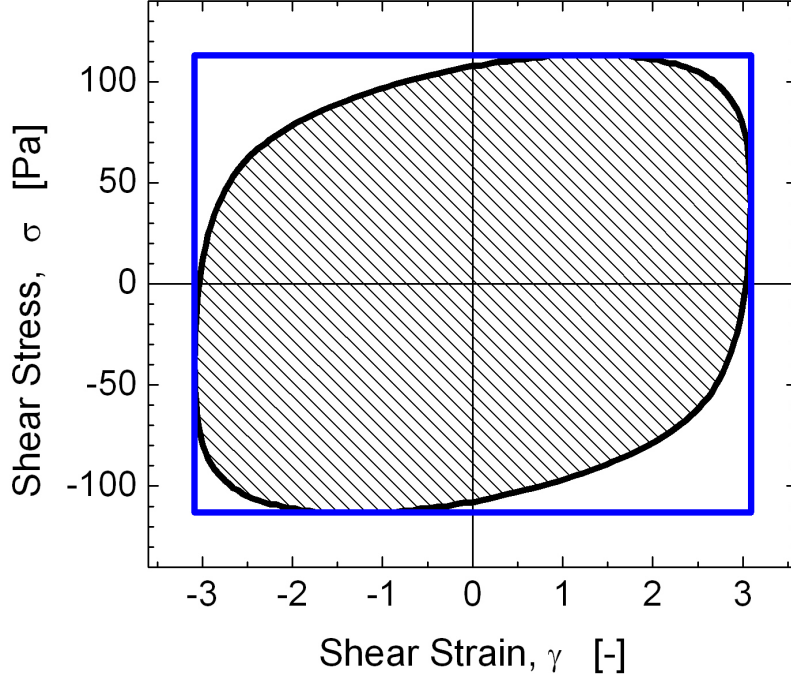


Figure 7-4: The energy dissipated by a single LAOS response is represented by the area enclosed in a Lissajous curve of stress vs. strain. For a given strain amplitude γ_0 and maximum stress σ_{\max} , the maximum possible dissipated energy is the circumscribing rectangle of the perfect plastic model response, with strain amplitude γ_0 and yield stress $\sigma_Y = \sigma_{\max}$. The example shown here is the measured steady LAOS response of the drilling fluid at $\omega = 15 \text{ rad.s}^{-1}$, with $\gamma_0 = 3.16$, $\sigma_{\max} = 113 \text{ Pa}$, and $\phi = 0.829$.

4. The energy dissipated by the perfect plastic in large amplitude oscillatory shear is $(E_d)_{pp} = (2\gamma_0)(2\sigma_{\max})$. In general, the energy dissipated per cycle by an arbitrary strain-controlled LAOS response is only a function of the first-order viscous Fourier coefficient[18], and is given by $E_d = \pi\gamma_0^2 G_1''$.

Comparing the actual dissipated energy and the perfect plastic dissipation gives a dissipation ratio, ϕ , which takes the following values for some simple model responses:

$$\phi \equiv \frac{E_d}{(E_d)_{pp}} = \frac{\pi\gamma_0 G_1''}{4\sigma_{\max}} \begin{cases} \rightarrow 1 & \text{PerfectPlastic} \\ \rightarrow \pi/4 = 0.785 & \text{Newtonian} \\ \rightarrow 0 & \text{PurelyElastic} \end{cases} \quad (7.11)$$

This scalar measure is well-behaved for any arbitrary LAOS response, since the strain

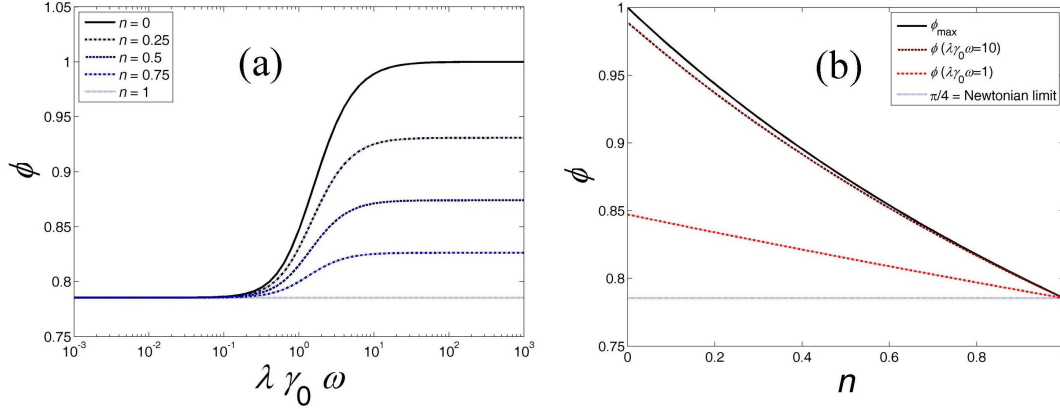


Figure 7-5: Carreau model response, characterized by the perfect plastic dissipation ratio, ϕ (Eq. 7.12). (a) Behavior of ϕ with respect to normalized shear-rate amplitude. (b) Behavior of ϕ as a function of n , shown for various values of the Carreau number $Cu = \lambda\gamma_0\omega$: ϕ_{\max} , $\phi(\lambda\gamma_0\omega = 10)$, $\phi(\lambda\gamma_0\omega = 1)$.

amplitude and maximum stress are always well-defined and easily determined from the data. This dimensionless measure ϕ can be universally applied to any measured LAOS response, as it compares the unknown response with the maximum possible energy dissipation, which is represented by the perfect plastic model. For a general LAOS response, we expect $\phi = \phi(\gamma_0, G_1'', \sigma_{\max})$. As an example, for a linear viscoelastic response, $\sigma_{\max} = \gamma_0|G^*|$ and thus $\phi = \frac{\pi G''}{4|G^*|} = \frac{\pi}{4} \sin \delta$. For a more general nonlinear viscoelastic response, $\sigma_{\max} = f(\gamma_0, G_n', G_n'')$ and thus ϕ is a complicated function of the higher-order coefficients.

A closed form expression for ϕ can be derived for the Carreau model response to LAOS (Eq. 7.2), given by

$$\phi_{\text{Carreau}}(n, Cu) = \frac{1}{4} \frac{\int_0^{2\pi} \cos^2 \omega t (1 + (Cu \cos \omega t)^2)^{\frac{n-1}{2}} d(\omega t)}{(1 + (Cu)^2)^{\frac{n-1}{2}}} \quad (7.12)$$

where the Carreau number is $Cu = \lambda\dot{\gamma}_0 = \lambda\gamma_0\omega$. Fig. 7-5 shows the behavior of Eq. 7.12, which will serve as a reference for interpreting ϕ for a predominantly viscous LAOS response. As the power law index $n \rightarrow 0$ and the Carreau number $Cu \gg 1$, the value of ϕ smoothly and monotonically approaches the limit $\phi \rightarrow 1$. This measure thus gives an unambiguous method of assessing how close a given material response

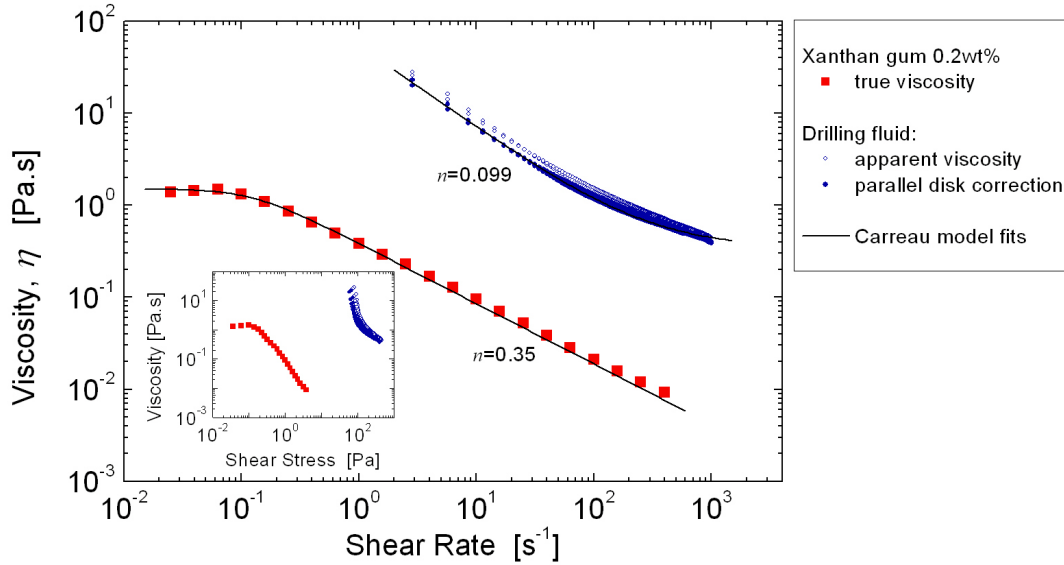


Figure 7-6: Viscosity flow curves for the 0.2wt% xanthan gum solution (squares, step shear rate for each data point) and the invert emulsion drilling fluid (circles, thixotropic loop test). Fits to the Carreau model are shown for each fluid (lines).

is to that of a perfect plastic under LAOS deformations.

7.5 Experimental results

In this section we examine experimentally the nonlinear oscillatory response of two fluids, a strongly shear-thinning (pseudoplastic) fluid and an elastoviscoplastic drilling fluid. We use the various material measures introduced above for indicating the yield-like character of the fluid response in LAOS.

Fig. 7-6 depicts a purely viscous perspective of the fluid characterization, showing flow curves of shear viscosity η for each fluid sample along with fits to the Carreau model of Eq. 7.1 (for $a = 2$). For the xanthan gum, a constant shear rate was applied and the steady state value of the viscosity was recorded, after which a higher shear-rate was applied and the process repeated. For the drilling mud, a thixotropic loop test was performed to match experimental conditions for tests on other drilling fluids[79]. The drilling fluid sample was pre-sheared at $\dot{\gamma}_R = 1022 \text{ s}^{-1}$ for 60 s (where $\dot{\gamma}_R$ is the shear-rate at the rim of the plate), followed by a 10 minute wait time. The

shear-rate was then linearly ramped up from $\dot{\gamma}_R = 0 - 1000 \text{ s}^{-1}$ over 450 seconds, and immediately ramped down, linearly from $\dot{\gamma}_R = 1000 - 0 \text{ s}^{-1}$. The time between data points limits the minimum resolution of shear-rate to approximately $\Delta\dot{\gamma}_R = 3 \text{ s}^{-1}$.

Each material exhibits pronounced shear thinning behavior. For the xanthan gum, a Carreau model fit (forcing $\eta_\infty = 0$) results in the parameters $\eta_0 = 1.50 \text{ Pa}\cdot\text{s}$, $\lambda = 8.0 \text{ s}$, $n = 0.35$ (c.f. Eq. 7.1). The power law exponent does not approach yield-like behavior, which would be indicated by $n \rightarrow 0$.

In contrast, the drilling fluid is closer to viscoplastic and approaches a yield stress fluid response. The apparent and corrected flow curves for the drilling fluid are shown in Fig. 7-6 (open symbols are apparent stress, closed symbols show the corrected stress). For steady flow between parallel plates, the true stress can be determined from $\sigma_R = \sigma_A \frac{1}{4} (3 + d \ln \sigma_A / d \ln \dot{\gamma}_R)$ (e.g. see Macosko[94]), where σ_R is the true stress at the edge of the disk and σ_A is the apparent stress determined by $\sigma_A = 2M/\pi R^3$ where M is the measured torque and R is the disk radius. Applying this correction requires derivatives of the apparent stress data. To calculate the required derivatives, we fit a fifth order polynomial function to the raw data of $\ln \sigma_A$ vs. $\ln \dot{\gamma}_R$, since this allows calculation of the derivative of a smooth analytical function rather than differentiating discrete raw data. A Carreau fit to the corrected viscosity (filled symbols) of the drilling fluid (allowing for the term η_∞) results in the parameters $\eta_0 = 3.29 \cdot 10^7 \text{ Pa}\cdot\text{s}$, $\lambda = 2.60 \cdot 10^6 \text{ s}$, $\eta_\infty = 0.337 \text{ Pa}\cdot\text{s}$, and $n = 0.099$. The experimental data lacks a Newtonian plateau in the limit of low shear rates, and therefore the values of η_0 and λ cannot independently be fit with high precision. However, a low value of the rms error is associated with a specific combination of these two parameters in the power-law shear thinning region for which experimental data is available. For $\lambda\dot{\gamma} \gg 1$, $\eta_0 \gg \eta_\infty$, the viscosity is approximately $\eta(\dot{\gamma}) \simeq \eta_0(\lambda\dot{\gamma})^{n-1}$ before the approach to the high shear-rate plateau. For the drilling fluid $n = 0.099$, and therefore $\eta_0\lambda^{-0.901} = 55.4 \text{ Pa}\cdot\text{s}^{-0.901}$ gives the lowest value of the rms error between the model and the data in the power-law shear-thinning region. Additional rheological tests, which approach the Newtonian plateau in the limit of low shear rate, are required to precisely determine η_0 and λ independently. LAOS tests at low frequencies and large

strains (so that the material is yielded) can provide such information and can thus be used to refine the values of the constitutive parameters as we show below.

The strongly shear-thinning nature of the drilling fluid is apparent from the very low power law exponent $n \ll 1$. The yield-like behavior is readily observed by replotting the flow curve in the form of viscosity vs. stress $\eta(\sigma)$ (Fig. 7-6, inset); the viscosity of the drilling mud changes by more than a factor of ten while the stress changes by less than a factor of two. LAOS tests over a range of frequency and strain amplitude can be used to further explore the behavior of these materials, from linear to nonlinear viscoelastic responses, to reveal how much each material acts like a yield stress fluid for some fraction of the relevant deformation parameter space $\{\omega, \gamma_0\}$.

7.5.1 Xanthan gum LAOS response

LAOS results for the 0.2% xanthan gum are shown in Fig. 7-7 (steady state smoothed data), and Fig. 7-8 (rheological fingerprints of potential yield stress indicators). LAOS tests were performed at four frequencies and five strain amplitudes, which are all shown in Fig. 7-7. For each frequency and strain amplitude $\{\omega, \gamma_0\}$, the final six steady state cycles are processed to produce the Lissajous curves in Fig. 7-7. Fig. 7-7a shows the 3D Lissajous curve traces at $\omega = 3.75 \text{ rad.s}^{-1}$. The full Pipkin space response is shown in Fig. 7-7b,c, which includes elastic Lissajous curves of the total stress (and the corresponding elastic stress contribution) vs. strain and also viscous Lissajous curves of stress (and viscous stress) vs. strain-rate. The response is linear viscoelastic at all strain amplitudes $\gamma_0 \leq 1$, as shown by the elliptical Lissajous figures and the linear shape of the elastic and viscous stress contributions. The frequency domain $\omega = 0.15 - 18.75 \text{ rad.s}^{-1}$ encompasses a range of phase angle $41^\circ \leq \delta \leq 61^\circ$ (in the linear viscoelastic regime), and therefore includes the $G' = G''$ crossover frequency at which $\tan \delta = 1$. For strains $\gamma_0 > 1$ the response becomes increasingly nonlinear and pseudoplastic in nature. The onset of non-linearity in the elastic stress and viscous stress functions are quickly identified by visual inspection, and correlate with the distortion of the elliptical shape of the limit cycles showing the periodic variations in the total stress. As the strain-amplitude increases, the curves of total stress vs.

Shear-thinning xanthan gum solution

(a) $\omega = 3.75 \text{ rad.s}^{-1}$

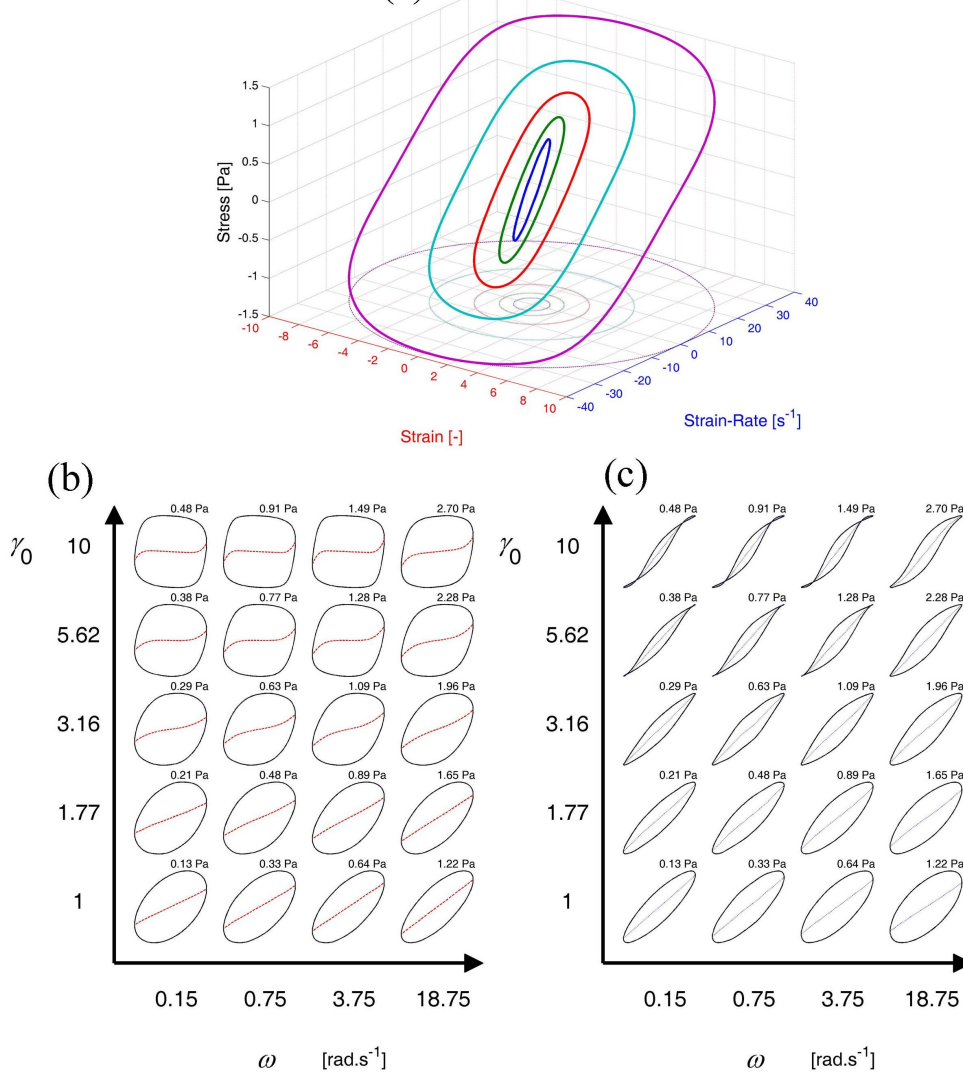


Figure 7-7: Steady-state Lissajous curves for the xanthan gum solution (0.2wt% aqueous). (a) Un-normalized 3D Lissajous curves at $\omega = 3.75 \text{ rad.s}^{-1}$. (b,c) Normalized curves arranged in a Pipkin space at the corresponding input parameters of frequency and strain-amplitude, $\{\omega, \gamma_0\}$. (b) individual plots of normalized stress (solid lines) and elastic stress (dashed lines) vs. strain; (c) individual plots of normalized stress (solid lines) and viscous stress (dotted lines) vs. strain-rate. The maximum stress σ_{\max} in each test is shown above each limit cycle.

strain become increasingly rectangular with strongly rounded corners (consistent with the Carreau model with $0 < n < 1$, c.f. Fig. 7-2). The Lissajous curves of stress vs.

Shear-thinning xanthan gum solution

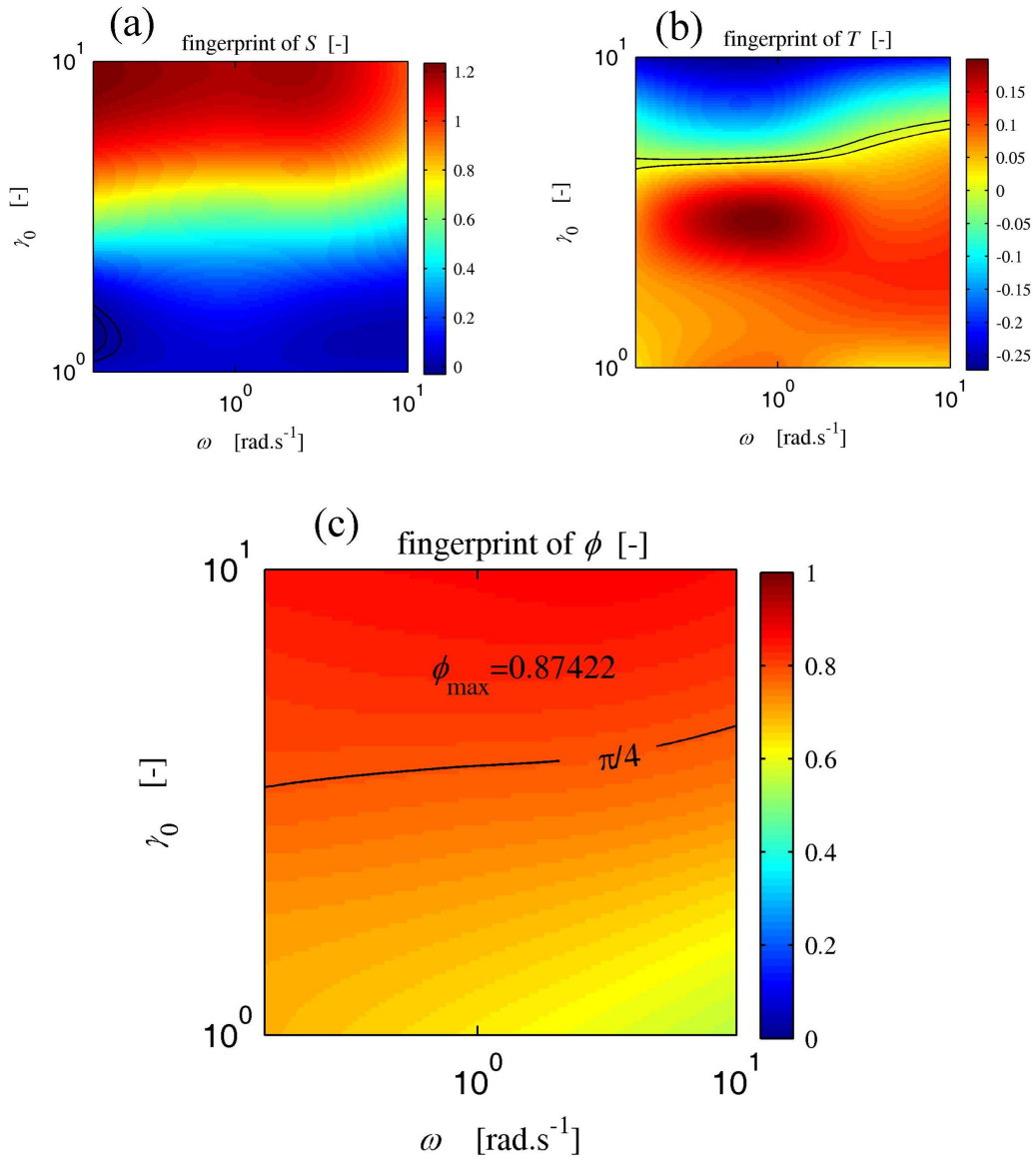


Figure 7-8: Yield stress indicators for the xanthan gum solution (0.2wt% aqueous), shown as a function of the LAOS input parameters $\{\omega, \gamma_0\}$. (a,b) Stiffening index and Thickening index, respectively, lines shown at ± 0.01 . (c) perfect plastic dissipation ratio ϕ . $\phi > \pi/4$ indicates a region in which the xanthan gum solution is shear-thinning. The maximum observed value, $\phi_{\max} = 0.97$ at $\{\omega = 3.75 \text{ rad.s}^{-1}, \gamma_0 = 10\}$, does not indicate an idealized yield stress response, which would appear as $\phi_{PP} = 1$.

strain-rate (Fig. 7-7c) appear as shear-thinning at the largest strain amplitude. The response is primarily viscous in the low frequency, large amplitude regime, since the

single-valued curves of viscous stress $\sigma''(t)$ vs. strain-rate $\dot{\gamma}(t)$ closely correspond with the loops of total stress $\sigma(t)$ vs. strain-rate $\dot{\gamma}(t)$ (Fig. 7-7c). The xanthan gum solution is therefore a shear-thinning viscoelastic liquid.

The similarity to a yield-like response can be quantified by examining contour plots of S , T , and ϕ , as shown in Fig. 7-8 (other viscoelastic parameters (e_1 , e_3 , δ , etc.) can be shown as contours in the 2-D space of $\{\omega, \gamma_0\}$, but are omitted here for clarity and brevity). For a perfect plastic response, these parameters are expected to approach the limiting values $S \rightarrow 1$, $T \rightarrow -\infty$, and $\phi = 1$. Within the limits of the linear regime ($\gamma_0 = 1$), we observe $S \approx 0.05$ and $T \approx 0.05$ indicating an approximately linear viscoelastic response as expected. At low strain amplitude the perfect plastic dissipation ratio, shown in Fig. 7-8c, is less than expected for a Newtonian fluid ($\phi < \pi/4$) as expected for a material response that is, in fact, partially elastic (and stores energy).

At larger strain amplitudes, values of $S \sim O(1)$ indicate strain-stiffening in the elastic response and $T \approx -0.25$ indicates shear-thinning. At these large strains, the plots in Fig. 7-8b,c indicate a region in which the xanthan gum solution is pseudoplastic in nature ($T < 0$, $\phi > \pi/4$). However, the maximum observed value, $\phi = 0.87$, does not indicate an idealized yield stress response. This experimentally measured maximum value of $\phi(\omega = 15 \text{ rad.s}^{-1}, \gamma_0 = 10) = 0.87$ is close to (but slightly lower) than predicted by the parameters of the Carreau model fit (Fig. 7-6, $n = 0.35$, $\lambda = 8.0 \text{ s}$), which results in $\phi(n = 0.35, Cu = 12) = 0.90$ (c.f. Fig. 7-5 and Eq. 7.12). This suggests that elasticity plays a weak role in this region of the deformation space, which is consistent with the Lissajous curves at ($\omega = 0.15 \text{ s}^{-1}$, $\gamma_0 = 10$). The significance of elasticity in the fluid at large Carreau numbers is also indicated by the observed functional dependence of ϕ , shown by the contours in Fig. 7-8c. For a purely viscous fluid such as the Carreau model, the dissipation ratio is only a function of the shear-rate amplitude, $\phi(\dot{\gamma}_0 = \gamma_0\omega)$. For such a case, ϕ would be constant along lines of constant shear-rate amplitude which correspond to lines with slope -1 on the log-log plot of Fig. 7-8c. Instead, lines of constant ϕ are approximately horizontal, and ϕ is a strong function of the strain amplitude, $\phi \approx \phi(\gamma_0)$ which indicates the significance

of elastic behavior for the range of deformation parameters $\{\omega, \gamma_0\}$ shown in Fig. 7-7 and Fig. 7-8.

Consistent with the inspection of the steady flow curves shown in Fig. 7-6, the xanthan gum solution is best described as a shear-thinning viscoelastic liquid but without a distinguishable yield stress behavior. We conclude that the dissipation ratio ϕ correctly distinguishes a moderately shear-thinning material response from a yield stress response.

7.5.2 Drilling fluid LAOS response

LAOS results for the drilling fluid are shown in Fig. 7-9 (processed Lissajous curves) and Fig. 7-10 (rheological fingerprints of yield stress indicators). A predominantly elastic regime can be observed at sufficiently small strain amplitudes. At the minimum imposed strain amplitude, $\gamma_0 = 0.01$, the material response is already weakly nonlinear and viscoelastic as indicated by the nonlinearities in the curves of elastic stress (dashed line) and viscous stress (dotted line) in Fig. 7-9b,c. It is typical for a filled system to exhibit a nonlinear material response at such small strain amplitude.

As the strain amplitude is increased, the material exhibits a rich nonlinear response in which the elastic stress curves indicate a strong elastic strain stiffening for strain amplitude $\gamma_0 \approx 0.1$. Furthermore, the Lissajous curves exhibit pronounced stress overshoots in the stress vs. strain curves, which correspond to apparent self-intersection of the trajectories when projected along the stress vs. strain-rate axes (Fig. 7-9c). Animations of these three-dimensional space curves are provided as supporting material. The complexities of this transition regime could not be observed by a steady flow viscosity curve, but are revealed here by the LAOS protocol.

As the deformation amplitude continues to increase ($\gamma_0 \approx 1$), the sample becomes increasingly plastic as indicated by the increasing area enclosed by the elastic Lissajous curves (Fig. 7-9) and the corresponding increase in the values of the dissipation ratio, ϕ (Fig. 7-10). However, for strains $\gamma_0 \approx 1$ none of the Lissajous responses are representative of a perfect plastic material, and moreover the dissipation ratio is smaller than the Newtonian benchmark, $\phi(\gamma_0 = 1) < \phi_{\text{Newtonian}}$. The material is thus

Elastoviscoplastic drilling fluid

(a) $\omega = 4.75 \text{ rad.s}^{-1}$

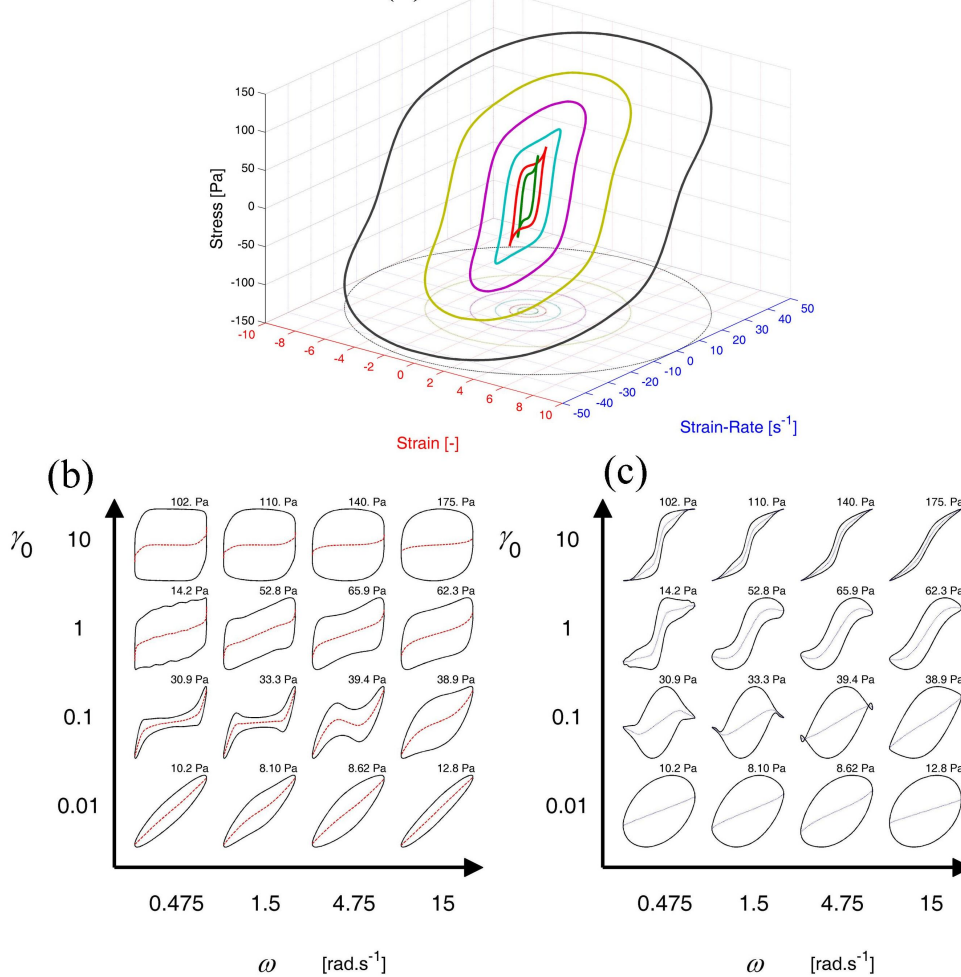


Figure 7-9: Steady-state Lissajous curves for the drilling fluid, shown for a selected range of strains and frequencies. (a) Un-normalized 3D curves for fixed $\omega = 4.75 \text{ rad.s}^{-1}$ and strain-amplitudes $\gamma_0 = 0.562, 1, 1.78, 3.16, 5.62, 10$. (b,c) Normalized 2D projections of σ/σ_{\max} arranged in a Pipkin space at the corresponding input parameters $\{\omega, \gamma_0\}$ which generated each response curve. The maximum stress is shown above each curve. (b) individual plots of normalized stress (solid black lines) and elastic stress (dashed red lines) vs. strain; (c) individual plots of normalized stress (solid black lines) and viscous stress (dotted blue lines) vs. strain-rate.

properly denoted as elastoplastic in nature.

In order to observe behavior close to perfect plastic, the strain amplitude must be further increased ($\gamma_0 = 10$) so that the sample fully yields. At this amplitude, the drilling fluid visually appears to behave as a viscoplastic fluid (Fig. 7-9). The shapes of

Elastoviscoplastic drilling fluid

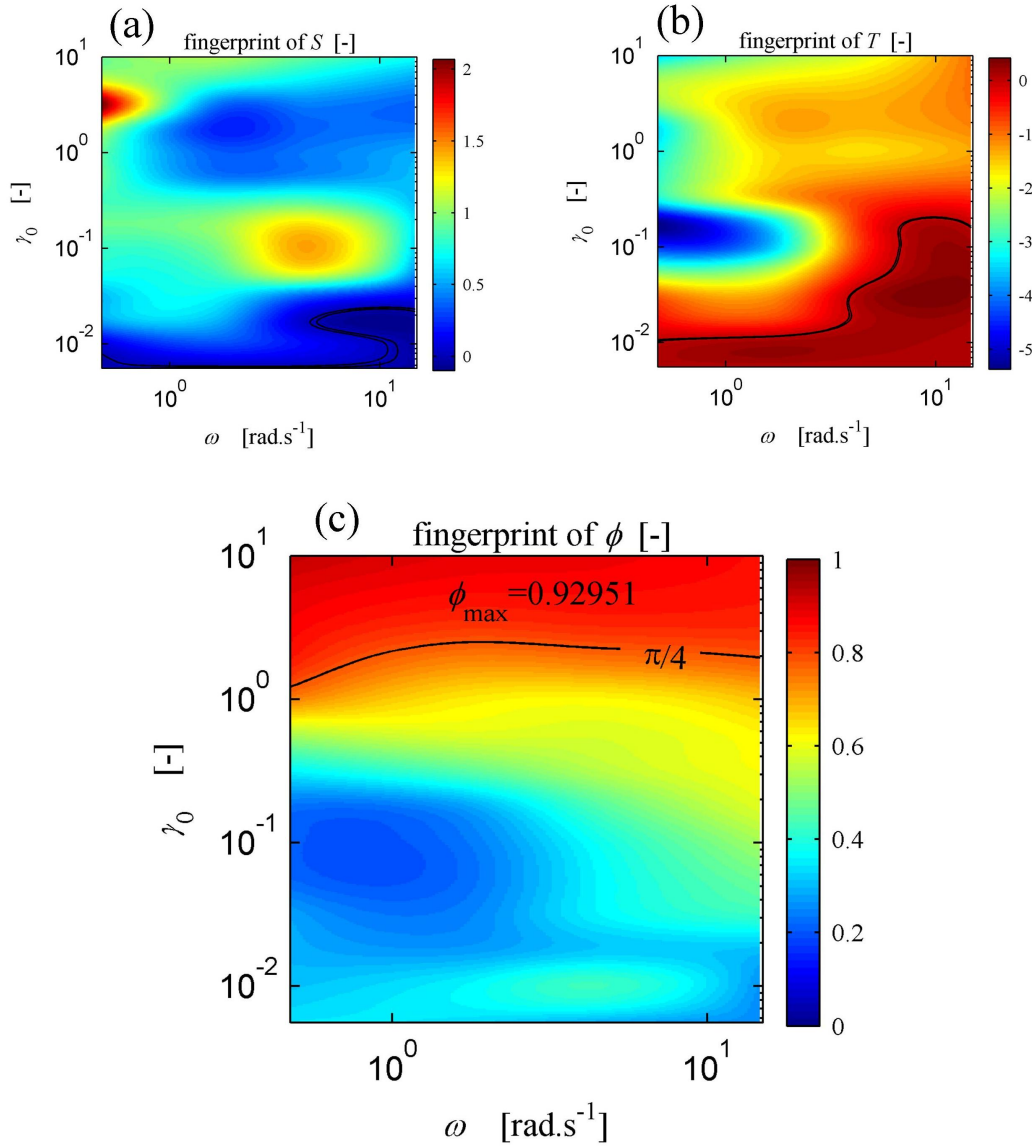


Figure 7-10: Quantitative LAOS analysis of the drilling fluid. (a,b) Stiffening index and Thickening index, respectively, lines shown at ± 0.01 . (c) Perfect plastic dissipation ratio, ϕ , shown as contours in a Pipkin space. At small strain amplitude ϕ takes very small values indicated a predominantly elastic response, which at larger strain amplitude gives way to a predominantly viscous response and eventually a maximum dissipation ratio, $\phi_{\max} = 0.93$, nearing the behavior of an idealized perfect plastic response.

Lissajous curves at $\gamma_0 = 10$ are consistent with the elastic Bingham model (c.f. Fig. 7-3). Here the Lissajous curves of stress vs. strain become increasingly rectangular in

the upper-left of the Pipkin space with additional rounding from viscous stress at high deformation rate amplitudes (upper-right of the Pipkin space).

Fig. 7-10 shows the rheological fingerprints of the potential discriminators of yield-like behavior, S , T , and ϕ . As previously discussed, for yield-like behavior, these parameters take the limiting values $S \rightarrow 1$, $T \rightarrow -\infty$, and $\phi = 1$. In Fig. 7-10a, the value of S approaches $S = 1$ in the upper left of the Pipkin space. At $\gamma_0 = 10$, we measure $S = 0.94, 1.07, 0.90$ at $\omega = 0.475, 1.5, 4.75 \text{ rad.s}^{-1}$, respectively. However, the stiffening ratio S inherently represents elastic nonlinearities, and therefore also takes the value $S \geq 1$ at other locations in the Pipkin space over which sufficient strain-stiffening is observed, notably in the region $\gamma_0 \approx 0.1$. Thus, for complex nonlinear viscoelastic material responses, $S \sim O(1)$ is associated with, but does not uniquely identify, a yield-like response.

The shear thickening ratio, T , captures intra-cycle viscous nonlinearities. From Fig. 7-10b, it is clear that T does become negative for a yield-like response in the drilling fluid (upper left region of the Pipkin space). However, the most negative values of T occur at moderate strain amplitudes, $\gamma_0 \approx 0.1$, and lower frequencies where the drilling fluid response exhibits a strongly nonlinear viscoelastic response (see Fig. 7-9b,c) but not a yield-like response specifically. We therefore conclude that negative values of T may be associated with a strong pseudoplastic response, but local extrema cannot be used to precisely indicate a yield-like response.

In Fig. 7-10c we investigate the ability of the perfect plastic dissipation ratio to uniquely identify a yield-like response. The value of ϕ is strictly related to the energy dissipated per cycle, rather than other intra-cycle nonlinearities, and is therefore robust to complex nonlinear viscoelastic responses such that $\phi \rightarrow 1$ is uniquely associated with a perfect plastic response. For the drilling fluid, the maximum dissipation ratio is $\phi_{max} \approx 0.93$ which is observed at moderate frequencies and large strains $\{\omega = 0.475 \text{ rad.s}^{-1}, \gamma_0 = 10\}$. The corresponding maximal value of the measured apparent stress at $\{\omega = 0.475 \text{ rad.s}^{-1}, \gamma_0 = 10\}$ is $\sigma_{A,max} = 102 \text{ Pa}$, which is higher than the prediction from the purely viscous Carreau model fit from Fig. 7-6, in which $\sigma_A = 84 \text{ Pa}$ at $\dot{\gamma} = \dot{\gamma}_0 = 4.75 \text{ s}^{-1}$. This provides a measure of the dynamic yield stress

in the fluid at these deformation conditions.

The perfect plastic indicator, ϕ , typically reaches its maximum value for large strain-amplitude γ_0 and low frequency ω . This is the case for the viscous and viscoelastoplastic constitutive models as well as the experimental results shown in Fig. 7-10c. This asymptotic limit $\phi \rightarrow 1$ at large strain-amplitude γ_0 and low frequency ω can be understood by considering the response of the elastic Bingham model (Fig. 7-3). For this model, the elastic portion of the yielded response is negligible as $\gamma \gg \gamma_Y$ (creating vertical sides of the Lissajous curves), and the viscous stress is approximately constant for small values of $\dot{\gamma}_0 = \gamma_0\omega$ (corresponding to small values of ω at a given γ_0), which creates a flat top to the Lissajous curve. In contrast, for large shear-rate amplitudes $\dot{\gamma}_0$, the elastic Bingham model response is predominantly Newtonian, since the instantaneous rate-dependent plastic viscosity ($\mu_p\dot{\gamma}(t)$) dominates the pre-yield elastic stress ($G\gamma_Y$). Thus, the elastic Bingham model approaches the perfect plastic response in the upper-left corner of the Pipkin space (large amplitude γ_0 and small frequency ω), in agreement with the experimental response of the elastoviscoplastic drilling fluid.

Finally we note that LAOS results can be used to augment the rheological measurements in steady shear (Fig. 7-6) by providing measurements of the viscous response at progressively lower values of the shear rate $\dot{\gamma}_0 = \gamma_0\omega$. In Fig. 7-11 we show the agreement between measurements of the apparent steady shear viscosity $\eta(\dot{\gamma})$ (limited to $\dot{\gamma} \geq 1 \text{ s}^{-1}$) and the apparent dynamic viscosity $v_1(\dot{\gamma}_0) = \eta'_1(\dot{\gamma}_0)$ for oscillatory shear-rate amplitudes down to $\dot{\gamma}_0 = 3 \cdot 10^{-3} \text{ s}^{-1}$. Good overlap in the data is observed, especially at larger strain amplitudes. This is a manifestation of the so-called Rutgers-Delaware rule (or 'extended Cox-Merz' rule) for yield stress fluids[95]. The plateau at the minimum LAOS shear-rate amplitudes is used to determine a lower bound for the Carreau model estimates of η_0 and λ the values of which are independently imprecise from the results of Fig. 7-6. As previously discussed, the value $\eta_0\lambda^{-0.901} = 55.4 \text{ Pa}\cdot\text{s}^{-0.901}$ is required to match the true viscosity of the drilling fluid response in the shear-thinning region. Fig. 7-11 suggests a lower bound of $\eta_0 \approx 1 \cdot 10^3 \text{ Pa}\cdot\text{s}$ which corresponds to $\lambda \approx 53 \text{ s}$. This modified Carreau model (for

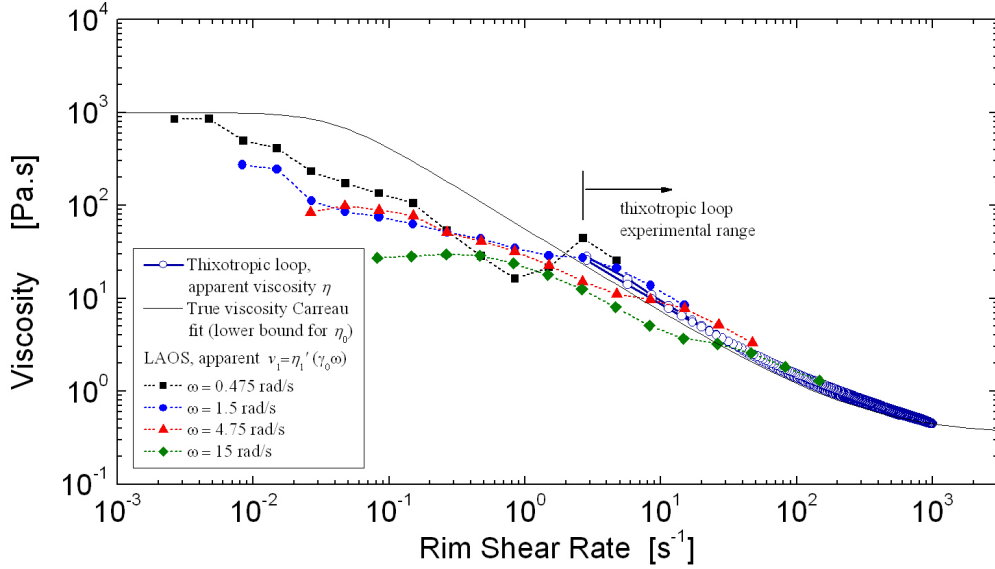


Figure 7-11: First-harmonic dynamic viscosity $v_1(\dot{\gamma}_0) = \eta'_1(\dot{\gamma}_0)$ from LAOS tests (closed symbols) compared to the apparent shear viscosity $\eta(\dot{\gamma})$ from the thixotropic loop test (open circles). Good correspondence is found between the tests at sufficiently large strain amplitudes $\gamma_0 \geq 3$, consistent with the Rutgers-Delaware rule. The viscosity at low shear-rates gives a lower bound for the Carreau model fitting parameter η_0 . The Carreau fit for $\eta_0 = 10^3$ Pa.s, $\lambda = 53.5$ s, $n = 0.099$, and $\eta_{\text{inf}} = 0.377$ Pa.s is given by the solid line.

the true viscosity) is shown in Fig. 7-11.

Closer inspection of the data in Fig. 7-11 shows that as the strain-amplitude is reduced (at fixed frequency) the LAOS data in fact systematically deviate *below* the extrapolated viscous response. This is because the material is not really yielded at these strains but is deforming elastoplastically. From Fig. 7-10 it is clear that we need to impose strains $\gamma_0 \geq 3$ to achieve $\phi > \pi/4$, corresponding to a yielded elastoplastic material that is dissipating at least as much energy per cycle as a Newtonian fluid. One of the necessary conditions for the validity of the Rutgers-Delaware rule is “high strain amplitude” [86, 95], i.e. strain amplitudes much larger than the yield strain. The absolute value of the “large strain” required to successfully apply this rule will be different between materials, but the material measure ϕ helps to unambiguously identify highly-yielded regimes (corresponding to $\phi > \pi/4$) in which the Rutgers-Delaware rule will be most applicable.

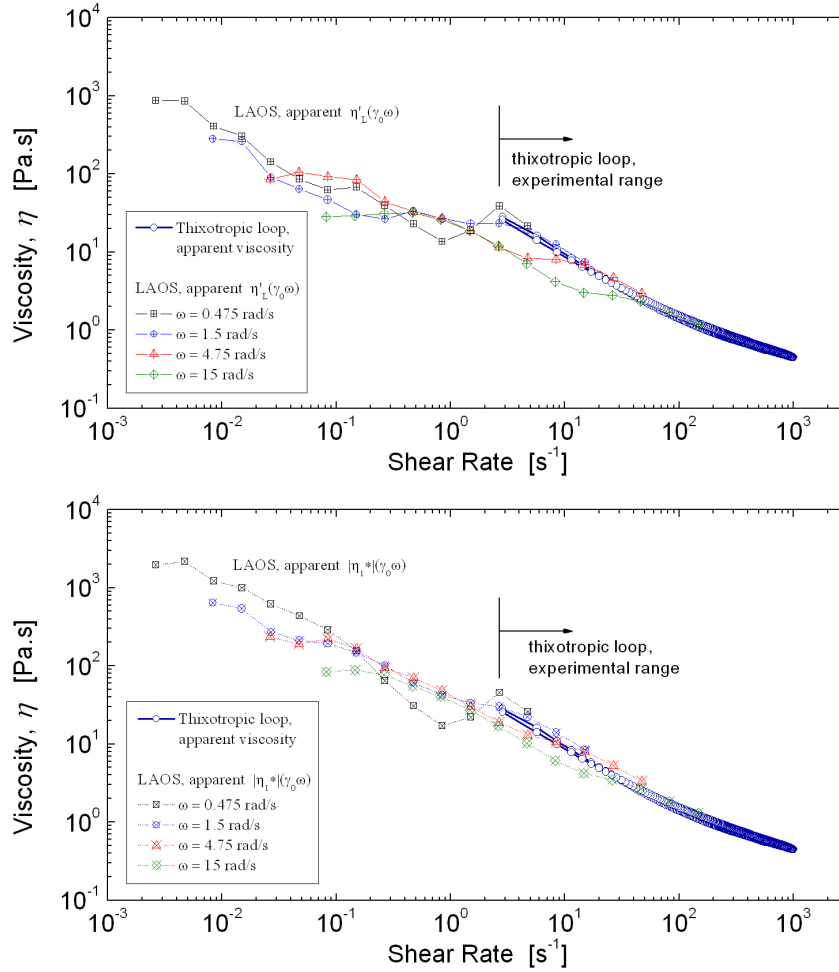


Figure 7-12: Dynamic viscosity from LAOS tests (crossed symbols) compared to the apparent shear viscosity $\eta(\dot{\gamma})$ from the thixotropic loop test (open circles). (a) Large-rate dynamic viscosity η'_L , which shows excellent correspondence in the yielded regime, $\gamma_0 > 3$. (b) Magnitude of the first-harmonic complex viscosity, which slightly over-predicts the flow viscosity in the yielded regime, but suffers from less under-prediction in the unyielded regime.

7.5.3 Rutgers-Delaware rule

In this brief section some ideas are proposed relating to the theory and applicability of the Rutgers-Delaware rule.

First, from the theoretical point of view, there are many methods of reporting viscous dissipation with a nonlinear LAOS response, e.g. η'_M , η'_L , η'_1 , and $|\eta_1^*|$ (Section 2.3). This author suggests that η'_L might be the best choice for correlating steady flow viscosity information of $\eta(\dot{\gamma})$ to LAOS dynamic viscosity at $\dot{\gamma} = \dot{\gamma}_0$, since η'_L corresponds

to the dynamic dissipation occurring at the largest instantaneous shear-rate within the cycle, $\dot{\gamma}_0$. Such a plot is shown for the drilling fluid data set in Fig. 7-12. As we have seen here, the steady flow viscosity is systematically *under-predicted* from the LAOS dynamic viscosity (by any measure of the dynamic viscosity, see Figs. 7-11,7-12). For a shear-thinning material, $|\eta_1^*| > \eta_1' > \eta_L'$, and therefore the best way to hide the systematic deviation is to choose the measure of dynamic viscosity which is largest, despite the fact that $|\eta^*|$ represents both viscous *and* elastic character. This may act as a diversion from the best theoretical choice for correlating steady viscosity and nonlinear viscous dissipation under LAOS.

The second point noted here is that of the systematically lower values of LAOS dynamic viscosity compared to steady shear viscosity within the un-yielded regime. Yang et al.[96] show comparable results to our drilling fluid results (Fig. 7-11), in that $|\eta_1^*|$ lies below $\eta(\dot{\gamma})$ at low strain amplitudes. Yang et al. use a shift in the effective shear-rate to match the LAOS and steady flow data sets (i.e. the LAOS data are moved to the *right*). In contrast, the author of this thesis postulates that the LAOS data should be shifted *upwards* to match the viscosities at the comparable rates. The reason for this upward viscosity shift would correspond to a thixotropic timescale, e.g. in steady shear the viscosity takes a long time to grow to its equilibrium steady state value[97]. Unlike steady shear, in LAOS the material structure is not given enough time to fully develop, because the flow continuously ramps up and down over a finite timescale. Thus, in LAOS the 'viscosity' (from $|\eta_1^*|$ or η_L' , etc.) will likely be lower than the 'steady state' value. This idea would predict the form of a shift factor for $|\eta_1^*|$, which would correspond to the shape of the transient viscosity curve $\eta^+(t)$, with frequency of LAOS related to timescale of the transient viscosity curve. If successful, such correspondence would be intellectually satisfying due to the underlying meaning of the shift.

7.6 Conclusions

Large amplitude oscillatory shear (LAOS) deformations provide a rich picture of the yielding transitions in a complex viscoelastoplastic fluid in terms of variations with respect to the strain amplitude and frequency of imposed deformation. This rich behavior can be represented in terms of 3D Lissajous curves $\sigma(\gamma(t), \dot{\gamma}(t))$ or 2D projections of Lissajous curves arranged in a Pipkin diagram (e.g. Fig. 7-3, Fig. 7-9). The LAOS characterization provides a more complete “rheological fingerprint” which is especially important for understanding materials which exhibit elastic solid-like behavior at low strains, as this cannot be captured by steady flow curves.

We have considered various measures for identifying yield-like viscoplastic behavior as a function of the imposed LAOS deformation conditions, $\{\omega, \gamma_0\}$. Although the strain-stiffening ratio S and the shear-thickening ratio T accurately represent the measured intra-cycle nonlinearities in the elastic and viscous properties of a complex fluid such as the oil-based drilling mud, they do not uniquely indicate yield stress behavior (Fig. 7-10).

We have introduced a new scalar parameter for identifying a plastic yield-like response under large amplitude oscillatory deformations, the perfect plastic dissipation parameter, $\phi = E_d / (E_d)_{pp}$, which uniquely identifies a plastic yield-like response as $\phi \rightarrow 1$. Calculations with simple pseudoplastic and elastoplastic constitutive models, as well as experimental measurements, correspond to increasingly rectangular Lissajous curves. For regions of the Pipkin space in which $\phi \rightarrow 1$, the dynamic yield stress in LAOS can be determined from the maximum value of the stress, $\sigma_{max} = \sigma_Y$. Of the measures considered here, we conclude that ϕ is the best choice for clearly identifying yield-like behavior in large amplitude oscillatory shear flow. The parameter ϕ is straightforward to calculate, stable to dramatic nonlinear responses, and is associated uniquely with perfect plastic behavior.

For any material of interest, the relevant processing or in-use conditions can be related to the material response in an appropriate region of the Pipkin space $\{\omega, \gamma_0\}$. For such a set of conditions, the Lissajous curves and perfect plastic indicator, ϕ , can

be used in both a qualitative and quantitative fashion to identify if a specific fluid will appear (or feel, or process) like a perfect plastic material that yields at a given stress. We conclude that the LAOS protocol, and the parameter $\phi = E_d / (E_d)_{pp}$, can be used to provide more complete rheological fingerprints of an elastoviscoplastic material, and identify regimes within the shear deformation space $\{\omega, \gamma_0\}$ in which any material can be usefully considered to behave as a fluid with a critical or “yield” stress.

Chapter 8

Snail-like wall climbing with bioinspired slime simulants

Many gastropods, such as snails and slugs, crawl using a technique called adhesive locomotion, in which a thin layer (typically 10-20 μm) of excreted mucus serves both as glue and lubricant[98, 99], allowing the animals to climb walls and crawl across ceilings. These gastropods exert shear stresses on this thin layer of structurally-sensitive mucus that holds the organism to the substrate. The pedal mucus has an effective yield stress; at high applied stresses the network structure breaks, enabling the foot to glide forward over a fluid layer; whereas in regions of low applied stress the network structure reforms into a solid-like layer connecting the foot to the substrate (Figure 8-1). Gastropod pedal mucus films are physically crosslinked gels containing 0.3-9.9% (by weight) solid matter in water[100]. The solid constituent which dominates the mechanical properties is a mucus protein-polysaccharide complex. The glycoconjugates present in pedal mucus share similarities with both mucin glycoproteins and glycosaminoglycans in vertebrates[100].

A mechanical crawler has recently been constructed which crawls using the principle of adhesive locomotion[101]. The success of the mechanical crawler depends critically on both the mechanical design of the robot and the rheological properties of the slime simulant. In this chapter I compare the rheological properties of natural pedal mucus from terrestrial gastropods with two bioinspired slime simulants that

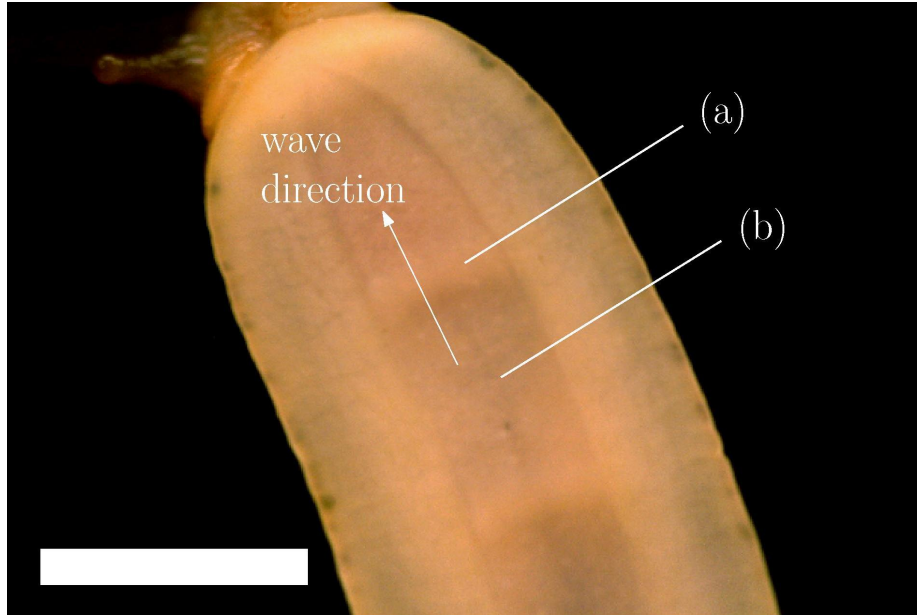


Figure 8-1: Bottom view of a crawling terrestrial slug *Limax maximus*, 1 cm scale bar; a) muscular contractions compress the foot parallel to the substrate, creating an area of high shear stress which ruptures the mucus network structure; b) an interwave of low stress allows the network structure to reform into a solid-like material which holds the organism to the substrate. Compression waves move toward the head (top of picture) during locomotion.

have been employed as adhesives by the mechanical crawler. The first is a polymeric gel based on Carbopol 940 and the second is a colloidal gel based on the synthetic clay LaponiteRD. Carbopols are a family of high molecular weight polymers consisting of cross-linked poly(acrylic acid) differing in crosslink density and degree of branching[102], which are used to modify the rheology of a variety of personal care products. Carbopol dispersions are typically interpreted as microgels[102, 103], in which soft crosslinked polymer particles are formed and swell in water. The outside of each particle exposes dangling ends which overlap with the dangling ends of other particles above a critical concentration, producing a sample-spanning network structure. LaponiteRD is a disc-shaped colloidal particle measuring approximately 300 Å in diameter and 10 Å in thickness[104]. Laponite clay particles form a fractal network when mixed with water at sufficient concentration[105]. If the colloidal dispersion is properly filtered, however, it forms a colloidal glass[106].

A series of linear and nonlinear rheological tests are used to construct a “fin-

gerprint” of the materials. With steady-state flow viscosity tests it is shown that both slime simulants satisfy a minimum yield stress criteria needed for wall climbing. In addition, I demonstrate that the linear viscoelastic behavior at low strain amplitudes of both simulants is similar to native slime. However, adhesive locomotion imposes large stresses and strains upon the material, and thus the nonlinear rheological response of slime is relevant to the dynamics of adhesive crawling. The relevant conditions for characterizing the mucin gel and simulants is large amplitude oscillatory shear (LAOS), and our measurements show that the mechanical response leading up to yield is different for the simulants compared to native slug slime; the native slime exhibits pronounced strain-stiffening as observed with Lissajous curves, and neither simulant mimics this. Other recent rheological studies have shown that similar strain-stiffening responses are ubiquitous in biopolymer gels[39].

8.1 Experimental

Pedal mucus was collected from the terrestrial snail *Helix aspera* and the terrestrial slug *Limax maximus*, which were kept in glass terrariums and supplied with a diet of green leaf lettuce and occasionally carrots. A single animal was removed from the containment area, placed on a glass plate, and allowed to crawl toward a piece of food. No mucus was collected until the gastropod had traveled a minimum of one body length so that no debris from the containment area remained in the sample, and to help ensure that locomotive mucus was present, rather than adhesive mucus which has been shown in some cases to have different compositional and mechanical properties[107]. The deposited trail mucus was gathered by scraping with a razor blade behind the crawling animal until an adequate sample size was obtained. The sample was immediately deposited on the Peltier plate of a rheometer for testing.

Carbopol 940 was obtained from the Noveon corporation (Cleveland, OH). Slime simulants based on Carbopol were prepared at various concentrations ranging from 0.5% - 4% (w/w), where w/w refers to weight of the additive with respect to the total weight of the mixture. The polymer was obtained as a white powder, and was added

to deionized water being agitated with a magnetic stirrer. Samples were mixed for a minimum of 30 minutes. The Carbopol-water mixtures initially have a pH near 3, and each was neutralized with 4 M NaOH solution to achieve a pH=7, producing a clear gel at the targeted concentration. The rheology of Carbopol mixtures depends on the pH, with maximum thickening occurring within a pH range of 5-9[108].

LaponiteRD was obtained from Rockwood Specialties Group, Inc. (Princeton, NJ). Simulants based on Laponite were prepared at concentrations ranging from 1% - 7% (w/w). Dispersions were prepared by adding Laponite powder to deionized water being agitated with a magnetic stirrer. Samples were mixed for 30 minutes and degassed to remove air bubbles. In all cases a clear solution was formed. Laponite dispersions were brought to pH=10 by addition of NaOH to make them chemically stable[109]. Dispersions were kept in a sealed container and allowed to rest for a minimum of 6 hours before testing.

Rheological measurements were performed with stress-controlled AR1000-N and AR-G2 rheometers, and a strain-controlled ARES-LS rheometer (all TA Instruments, New Castle, DE). Samples were tested between both plate-plate and cone-plate geometries, at all times using a solvent trap to stifle evaporation. For plate-plate geometries, diameters ranged from 0.8 cm to 4 cm, and gaps ranged from 200 μm to 1000 μm . When necessary, adhesive-backed waterproof sandpaper (2000 grit, Eastwood Co., Pottstown, PA) was attached to the top and bottom plates to help avoid slip at the boundaries. Cone-plate geometries were used for low viscosity Laponite mixtures. Two cones were used; a 4 cm 2° cone with 57 μm truncation and a 6 cm 1° cone with 28 μm truncation. All samples were tested at $T=22^\circ\text{C}$. Immediately before testing, Laponite samples were subjected to a controlled pre-shear at a shear rate $\dot{\gamma} = 5\text{s}^{-1}$ for 25 seconds, followed by three minutes of recovery. This pre-shear and recovery sequence helped to mitigate strain history and aging effects, as Laponite is known to be thixotropic and to exhibit rheological aging, even under quiescent conditions[105]. A carefully controlled and documented sample preparation history is thus essential in order to achieve reproducible results. It is likely that Laponite continues to slowly age after the three minutes of recovery, but this was not observed to affect the primary

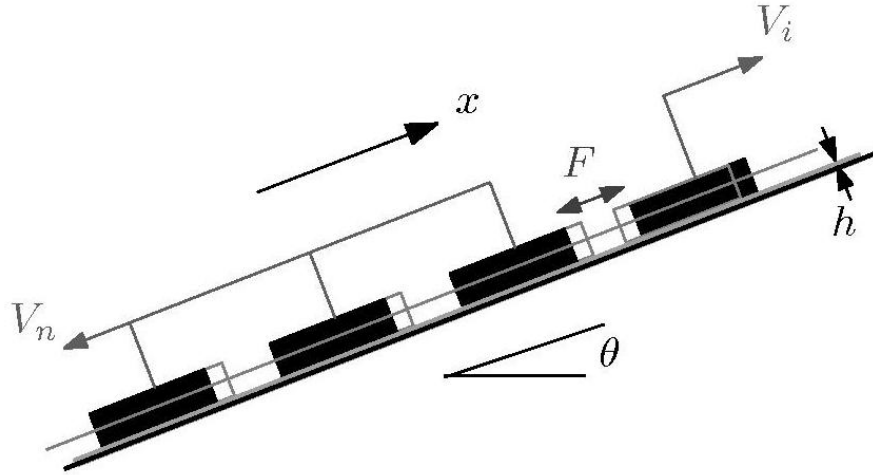


Figure 8-2: Simple model of an adhesive locomotion system - the crawler consists of N discrete pads and rests on a fluid with thickness h . An internal controlled force iteratively moves one pad forward with respect to the rest.

results of this work.

8.2 Results and discussion

8.2.1 Requirements of slime simulants

A simple model is used to determine which fluid properties are desired for adhesive locomotion. The model consists of discrete pads actuated by an internal force (Figure 8-2), which may be interpreted as a discrete form of gastropod locomotion or a generalized model of Chan’s Robosnail II [101]. The crawler rests on a layer of fluid, and a controlled internal force F separates one pad away from the rest, while the rest are rigidly connected. The controlled force might come from muscles in real gastropods or from the actuators of a mechanical crawler. This internal force acts in equal and opposite directions on the two portions that are “rearward tending” and “forward tending.” It is assumed that the pads are rigid and the no-slip condition is satisfied across the surface of each pad. The actuation force balances instantaneously with the shear resistance of the fluid and the weight of the pads when inertial effects are negligible.

It can be shown that adhesive locomotion requires, at a minimum, a non-Newtonian fluid viscosity[110]. Here we consider the case of idealized inclined locomotion. If the crawler is to passively keep its place on an inclined surface, yet move forward while attempting to crawl, the fluid must exhibit a rheologically-reversible apparent yield stress. This is a specific form of the rheoreversibility discussed by Carretti et al[111]; the material for this application must regain its solid-like properties at low stress without the need to change environmental variables such as temperature or pH. A rheologically-reversible yield stress is characteristic of weak gels, as opposed to strong gels[112]. While strong gels are solid-like and may rupture at a critical stress, they do not flow above the rupture stress, nor do they regain their solid-like nature when the stress is removed. For example, gelatin ruptures above a critical stress, but the temperature must be cycled for the pieces to recombine into a unified solid.

Inclined adhesive locomotion requires a minimum yield stress. The minimum static yield stress that is required for the crawler to rest on an inclined surface is $\sigma_y = Mg \sin \theta / A$, where A is the total contact area. The minimum yield stress required to move forward, however, is higher than the minimum static yield stress. Consider a crawler with total contact area A , consisting of N pads (Figure 8-2), each bearing an equal portion of the total weight Mg , traversing a surface inclined at an angle θ with the horizontal. Although we consider our model to be general, some relevant dimensions for Robosnail II are $Mg = 0.31$ N, $A \approx 35$ cm², $N = 5$, and overall length approximately 15 cm[113]. The discrete pad model can be generalized with $\phi = 1/N$, which represents the fraction of the crawler that is moving forward during actuation. If the crawler is connected to the substrate via a complex fluid having a yield stress σ_y , then to move forward a minimum actuation force must support the pad weight and exceed the yield stress, $F_{/textmin} = \sigma_y \phi A + \phi Mg \sin \theta$. The force can not be too large, however, or the rearward-tending pads will also cause the fluid under them to yield. The maximum actuating force is then expressed as $F_{\max} = \sigma_y (1 - \phi) A - Mg \sin \theta (1 - \phi)$. When these two forces are equal, the crawler is unable to make progress since the material under all pads would yield simultaneously. This critical point, at which $F_{/textmin} = F_{\max}$, can be recast in terms of a minimum

dynamic yield stress which is required for locomotion, given by

$$(\sigma_y)_{\min} = \frac{Mg \sin \theta}{A} \left[\frac{1}{1 - 2\phi} \right] \quad (8.1)$$

The minimum dynamic yield stress is therefore a factor of $1/(1 - 2\phi)$ larger than the static yield stress. This can be used as a design criteria when choosing a slime simulant. For example, with Robosnail II, which has five pads, the required locomotive yield stress is approximately 67% higher than the necessary static yield stress for inclined locomotion. The assumption of equipartition of weight among the pads makes Eq. 8.1 a lower bound; a higher yield stress is required if any pad carries more than the equipartition weight. The upper bound for the required yield stress occurs when one pad happens to support the entire weight of the crawler, $(\sigma_y)_{\min} = Mg \sin \theta / (\phi A)$. Although the simplest models of yield stress fluids assume affine yielding of the material, the model results presented above are independent of the nature of yield. For example, if the material experiences adhesive yielding (i.e. slip at the wall) the above analysis still applies provided the adhesive nature of the yield event is reversible and the pad can passively reattach at low stress.

Once the forward-tending pad has yielded the fluid, the speed of the crawler is inversely proportional to the flow viscosity. The center of mass velocity is $V_{cm} = hF/(A\eta)$, assuming steady viscous Couette flow above the yield point and a crawler mass equally distributed among the pads. For non-affine yielding and flow the velocity expression must be modified. However, velocity is still inversely related to the resistance to relative motion (viscosity or sliding friction). Thus, another material property to be considered for optimization is the post-yield viscosity, which should be minimized to increase the speed of the crawler.

The final property considered here is the restructuring time required for the sheared fluid to regain its yield stress. This time-dependent character of viscometric material functions in which structure breaks down during flow and builds up during rest is known as thixotropy, and is ubiquitous in yield stress materials[114, 115]. This finite restructuring time imposes limits on the maximum velocity of an adhesive lo-

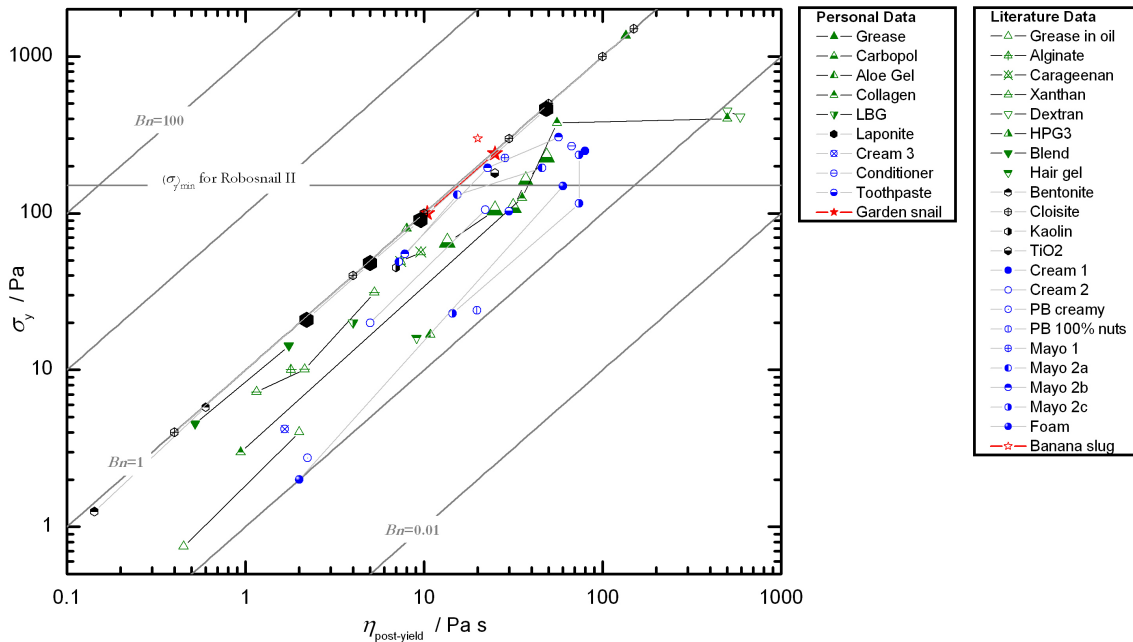


Figure 8-3: Material selection space comparing yield stress fluids; Stars: native mucus gels, Triangles: polymeric solutions and gels, Hexagons: Particulate suspensions and gels, Circles: soft glassy materials. A suitable simulant will meet a minimum yield stress requirement and have a low post-yield viscosity. See Appendix D for material preparation and reference details.

comotion crawler. After moving a portion of its foot forward, a crawler must wait for the material to regain an adequate yield stress before actuating the next portion. Thus, the restructuring time must also be minimized to increase crawler speed. It should be noted that living gastropods may optimize pedal mucus properties with respect to an alternative cost function, since the organisms must expend significant energy to produce the mucus[3, 116] unlike a mechanical crawler.

Figure 8-3 is a nomogram that represents candidate slime simulants in terms of two of the important fluid properties: yield stress and post-yield viscosity; for clarity the restructuring time is not shown in this two-dimensional projection. Post-yield viscosity values are taken at a shear rate $\dot{\gamma} = 10\text{s}^{-1}$, which is a representative shear rate for Robosnail II, since the pad velocity is $V_i \approx 1 \text{ cm}\cdot\text{s}^{-1}$ and the fluid thickness is $h \approx 1 \text{ mm}$. A line of minimum locomotive yield stress for vertical wall climbing can be drawn for Robosnail II, such that any simulant below this line will not meet the

criteria for vertical wall climbing. Lines of constant Bingham number are plotted on the figure as a guide to the eye. The Bingham number is motivated by the Bingham model for a yield stress fluid[8], and is given by $Bn = \sigma_y/\eta\dot{\gamma}$, where σ_y is the yield stress, η is the viscosity, and $\dot{\gamma}$ is the shear rate, again we take $\dot{\gamma} = 10 \text{ s}^{-1}$ for the Bingham numbers to be consistent with the post-yield viscosity data. For the case of a vertical climber the Bingham number represents a comparative measure of support forces and resistive forces, therefore high Bn values are desirable; increasing the yield stress contributes (linearly) to the factor of safety of wall-climbing whilst decreasing viscous stress increases crawler speed, as noted above.

It can be seen from Figure 8-3 that there are slime simulants which meet the minimum rheological criteria for a wall climbing mechanical crawler that uses adhesive locomotion. Thus, although native slug slime could be used for a mechanical crawler, harvesting slime is not required to operate a mechanical wall climbing device. Furthermore, from Eq. 8.1 it is clear that the minimum required yield stress scales with the areal mass density, and therefore scales as the characteristic length of the crawler, $\sigma_y \propto Mg/A \propto L$. Thus, for geometrically similar devices a smaller crawler will require a lower yield stress and a wider range of fluids will be appropriate for use as adhesive lubricants.

8.2.2 Rheological material functions

Two promising slime simulants, a particulate gel based on Laponite and a polymeric gel based on Carbopol, were examined in detail and compared with native pedal mucus from the terrestrial snail *Helix aspera* and the terrestrial slug *Limax maximus*.

Steady shear flow

The steady shear viscosity of the Carbopol-based and Laponite-based simulants and native pedal mucus from *Helix aspera* are shown in Figure 8-4. Data is shown for two different samples of pedal mucus. At sufficient concentration, each simulant exhibits a very large viscosity at low stress. For $\sigma \ll \sigma_y$ the viscosity for these

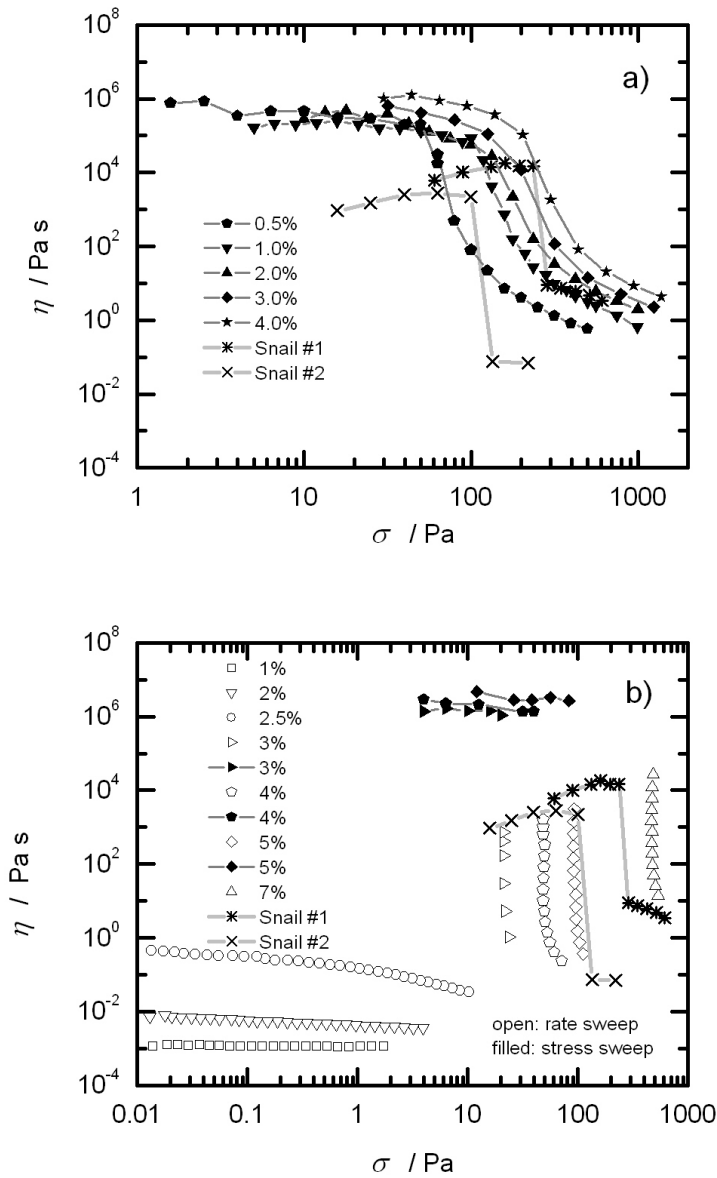


Figure 8-4: Steady shear viscosity of simulants compared to native pedal mucus from *Helix aspera*; native slime collected from two snails, tested with plate-plate fixtures $D = 0.8$ mm with sandpaper, $h = 100\mu\text{m}$; a) Carbopol-based simulant, plate-plate with sandpaper, solvent trap, $h = 1000\mu\text{m}$, $D = 4$ cm for 0.5%-2%, $D = 2$ cm for 3%-4%; b) Laponite-based simulant, solvent trap, $D = 6$ cm 1° cone-plate for 1%-2%, $D = 4$ cm 2° cone-plate for 2.5%, $D = 4$ cm plate-plate, $h = 1000\mu\text{m}$ with sandpaper for 3%-7%.

materials is so high that they are solid-like for timescales on the order of seconds, which is the relevant timescale of locomotion for natural gastropods[117] and for

Chan's mechanical crawler. For example, with a viscosity $\eta \approx 10^6$, and a fluid thickness $h = 1$ mm, Chan's crawler would slump down a vertical wall at a rate of only 0.3 mm.hr^{-1} . However, at a critical stress the viscosity decreases by several orders of magnitude. Since flow exists for any finite stress, none of these materials exhibits a true yield stress. However, this behavior may be described as an apparent yield stress, since the flow at low applied stresses may be difficult to observe, and it is followed by a dramatic drop in viscosity over a narrow range of stress. The critical stress at which the viscosity dramatically changes will henceforth be referred to as the yield stress[77, 78].

Some flow curves appear to be slightly shear-thickening below the yield stress (e.g. native slime). This is not uncommon for yield stress fluids, because the stress is incrementally increased after the apparent steady-state flow is achieved, and a very large equilibration time exists below the yield stress[97]. Native slime and the Laponite gel share a steep and dramatic drop in viscosity at the yield stress (Figure 8-4b), whereas the viscosity of the Carbopol solutions drops less quickly as stress is increased (Figure 8-4a). The drop in viscosity of Laponite occurs over such a narrow range of stress that a stress-sweep could not capture the behavior. Thus, a rate-sweep was performed from high shear-rates down to low shear-rates. This technique enables large changes in the steady shear viscosity to be measured over a small change in stress. A stress-sweep was used to explore the high viscosity region of the flow curve, since the data was beyond the minimum resolvable range of the rate-sweep.

Each of these materials is rheologically reversible, so that solid-like properties are regained when the stress is reduced below the yield stress, and the test can be repeated to give the same data. The timescale over which the material restructures is known as the thixotropic timescale[114], which may affect the value of the measured yield stress[115]; this will be discussed further in Section 8.2.2.

The data for both simulants show that the yield stress is a strong function of concentration. The maximum yield stress of each simulant is limited by the impracticality of increasing the concentration beyond a certain point. Extremely high yield stress materials are also difficult to test, since they suffer from slip at the boundaries[118].

Wall slip can be witnessed by observing the edge of the sample during the test[119]; this method indicates that Laponite at 7% is prone to slippage at the solid boundary. Thus, the data reported in Figure 8-4b give the apparent viscosity for a large gap $h = 1000\mu\text{m}$; if slip is occurring then the measured viscosity will become a function of gap height[93].

Linear viscoelasticity

The linear viscoelasticity of the materials was examined with small amplitude oscillatory shear (SAOS). The native slime is compared here to simulants which have similar yield stress values: a Carbopol-based simulant at 2% and a Laponite-based simulant at 5%, each having a yield stress $\sigma_y \approx 100$ Pa. The linear rheological regime is defined such that the material properties are not a function of the input stress amplitude, and thus each oscillation test in the linear regime is performed below the yield stress ($\sigma_0 \ll \sigma_y$).

The linear viscoelastic moduli, G' and G'' , were examined over a range of frequencies using SAOS. Both the elastic and viscous contributions to the complex modulus were found to be weak functions of frequency for each sample below the yield stress, as shown in Figure 8-5. Although each material has approximately the same yield stress, the storage moduli vary by over an order of magnitude; native slime has the lowest elastic modulus, near 200 Pa, whereas the particulate gel Laponite has a storage modulus ten times larger, $G' \approx 2000$ Pa. The mesh size of a polymer gel may be estimated from the expression $G \approx kT/\xi^3$, where ξ is the characteristic length scale of the mesh[120] resulting in $\xi \approx 30$ nm for pedal mucus and $\xi \approx 20$ nm for Carbopol.

Large amplitude oscillatory shear (LAOS)

A crawling slug subjects the pedal mucus film to shear stresses that exceed the yield stress, and thus the large amplitude, nonlinear viscoelastic properties of both native slime and slime simulants are relevant in adhesive locomotion. The shear stress exerted by a crawling slug can exceed 2000 Pa, as measured by Denny[117]. Furthermore, the strain amplitude under a crawling slug can be estimated from the speed

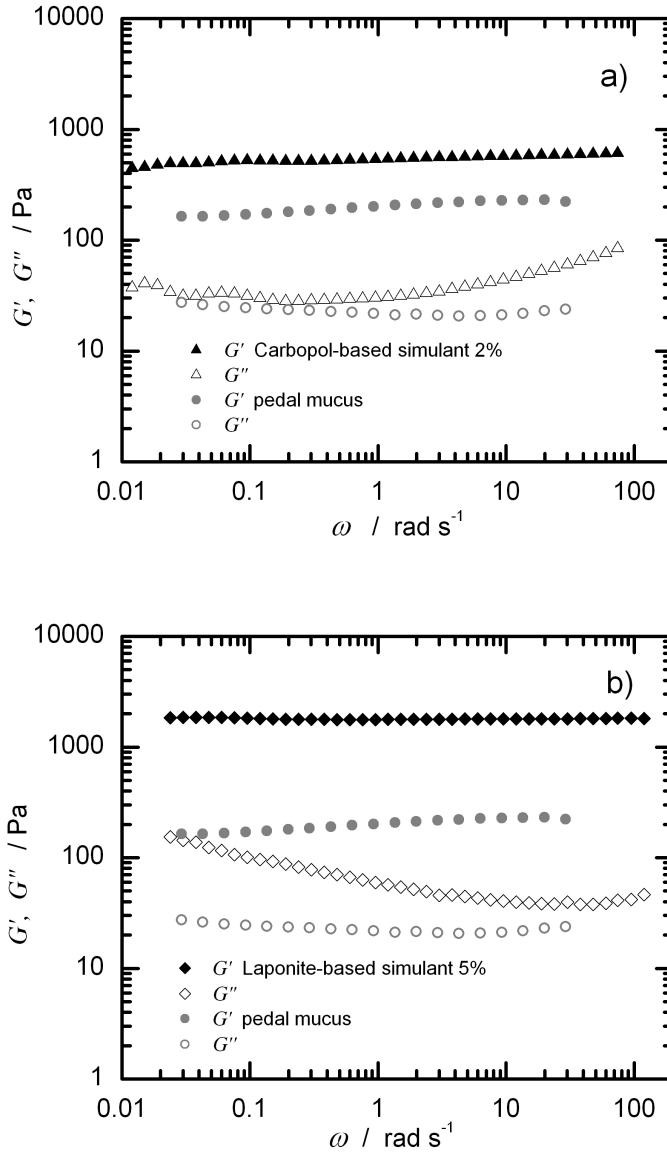


Figure 8-5: Linear viscoelastic moduli of simulants compared with native pedal mucus from *Limax maximus*; pedal mucus tested with $D = 2$ cm plate with sandpaper, solvent trap, $h = 200\mu\text{m}$, $\sigma_0 = 5$ Pa; simulants tested with $D = 4$ cm plate with sandpaper, $h = 1000\mu\text{m}$, solvent trap; a) Carbopol-based simulant, $\sigma_0 = 5$ Pa; b) Laponite-based simulant, $\sigma_0 = 20$ Pa.

versus time profile reported by Denny[117]. Using this data, and assuming the pedal mucus thickness $h = 20\mu\text{m}$, a strain amplitude $\gamma \approx O(10^2)$ is imposed on the pedal mucus with each pulsatile wave.

The response of a material to oscillatory shear is considered nonlinear if the stor-

age and loss moduli depend on the input stress (or strain) amplitude. Additionally, the strain (or stress) response may be observed to contain higher harmonics than the input frequency, rather than exhibiting a pure harmonic response. In this nonlinear regime the linear viscoelastic moduli G' and G'' are not uniquely defined. The complex fluid response can be analyzed with a Fourier transform[15], and the real and imaginary coefficients of the higher harmonic contributions can be represented as G'_n and G''_n respectively (for $n = 1, 2, 3, \dots$) (c.f. Eq. 2.1). To be precise, we will therefore report the first harmonic elastic and loss moduli, G'_1 and G''_1 , for LAOS results, which reduce to G' and G'' in the limit of a small amplitude deformation history. The new LAOS framework introduced in Chapter 2 cannot strictly be used for these data sets because they were performed with controlled oscillatory stress ($\sigma(t) = \sigma_0 \cos \omega t$), rather than controlled strain which is required for the theory of Chapter 2. However, the qualitative shapes of Lissajous-Bowditch curves can still be interpreted within the framework presented in Chapter 2.

The first harmonic of the storage modulus G'_1 and loss modulus G''_1 are shown in Figure 8-6 as a function of stress amplitude σ_0 at a fixed frequency of $\omega = 1 \text{ rad.s}^{-1}$. At low stresses each material shows little or no dependence on the input stress amplitude. Each material undergoes a transition at a critical stress at which the elastic response dramatically decreases. However, no data could be collected for native slime beyond this critical stress since the material was ejected from the gap. The critical stress amplitude for this transition corresponds approximately to the apparent yield stress observed in steady flow tests (Figure 8-4). The sharpness of the transition also corresponds with the steady shear flow results; the polymer gel simulant exhibits a gentle stress softening, whereas the slime and particulate gel simulant show a very sharp transition at a critical stress.

The critical yield strain may be expected to obey the relationship $\sigma_y \propto G\gamma_y$ where G is the nominal elastic modulus of the material. This is approximately true for the simulants. The yield stresses are similar and the elastic modulus of the Laponite gel is approximately three times that of the Carbopol. This difference in elastic modulus is therefore compensated by changes in the critical strain. The critical yield strain for

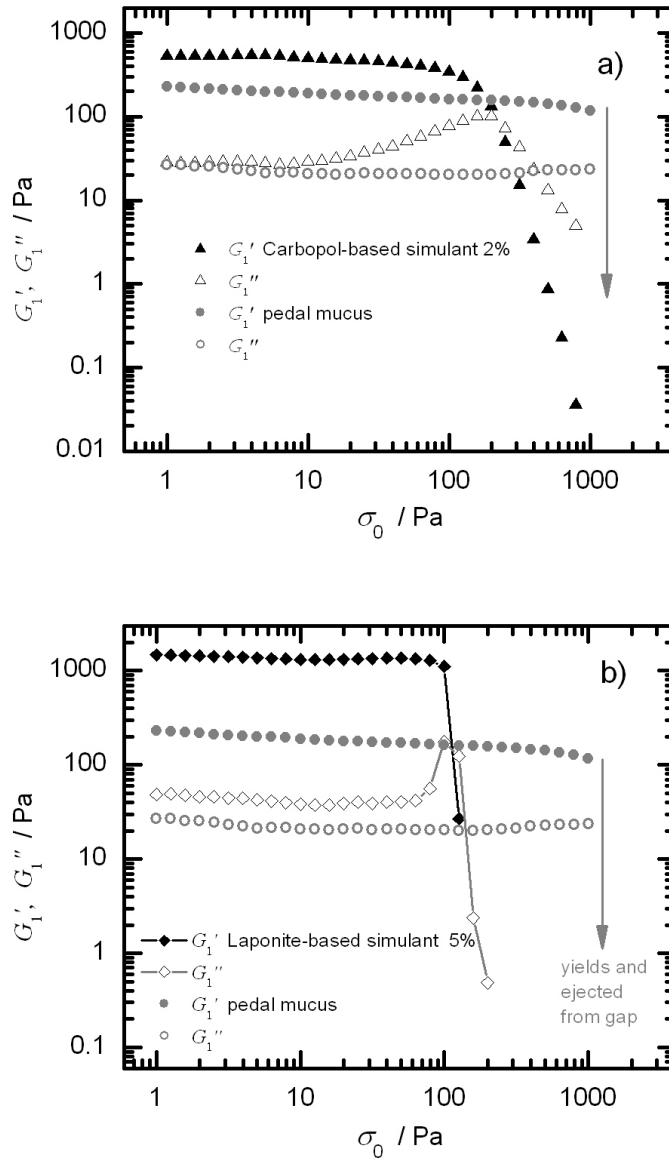


Figure 8-6: Large amplitude oscillatory shear (LAOS) of simulants compared with native pedal mucus from *Limax maximus*, same geometries as Figure 8-5, all samples tested at $\omega = 1 \text{ rad}\cdot\text{s}^{-1}$; a) Carbopol-based simulant; b) Laponite-based simulant.

the particulate gel Laponite is smaller (by approximately six times) than the polymer-based Carbopol gel; the particulate-based material requires a smaller imposed strain to disrupt the equilibrium microstructure.

As the oscillatory stress amplitude approaches the yield stress, small differences can be seen in the behavior of G_1' and G_1'' for each material. The loss modulus G_1'' ap-

pears to increase just before yield for each material; this increase is most pronounced with the Carbopol simulant. The increase in G_1'' prior to yield, combined with a decrease in G_1' , has been observed in other materials and is classified as type III LAOS behavior by Hyun and coworkers[19]. This type III behaviour can be qualitatively explained by considering a relaxation time that is shear-rate dependent, as is likely the case for metastable yield stress fluids; a peak in G_1'' can then be reproduced by simply modifying a Maxwell model in this way[20]. The variation of the first harmonic storage modulus is less interesting as the yield stress is approached; in each case G_1' is a weak function of stress amplitude for $\sigma_0 < \sigma_y$. However, upon closer inspection, a dramatic difference in the material response leading up to failure becomes apparent.

With the aid of Lissajous curves one can immediately see the substantial difference in each material's non-linear response to an oscillatory stress input $\sigma(t) = \sigma_0 \cos \omega t$, as demonstrated in Figure 8-7a, Figure 8-7b, and Figure 8-8. These Lissajous curves are parametric plots of stress versus strain, with each curve corresponding to an oscillatory shear test with a sinusoidal stress input at a particular frequency and amplitude. The trajectory is elliptic for a linear viscoelastic material, approaching the limiting case of a straight line with slope G for a Hookean elastic solid and an ellipse with axes aligned with the coordinate axes for a Newtonian fluid. A nonlinear material response to a harmonic forcing input will distort this ellipse. The cyclic integral of a Lissajous curve, in which stress is plotted against strain, is equal to the energy dissipated per unit volume per cycle, E_d , and is directly related to the loss modulus G_1'' as $E_d = \pi \gamma_0^2 G_1''$ [18].

The Lissajous curves for each material at low stress appear as tight ellipses (see insets in Figure 8-7 indicating $G' \gg G''$; only a small area is enclosed and the response is dominated by elasticity. As the imposed stress amplitude is increased toward the yield stress each material exhibits distinctive behavior. The Laponite simulant maintains tight elliptical curves almost all the way up to yield, and subsequently undergoes a quick transition to predominantly viscous behavior, as shown by a dramatic increase in the area enclosed by the curve. This transition is consistent with the sudden drop in viscosity for the steady state flow curves (Figure 8-4b), and is re-

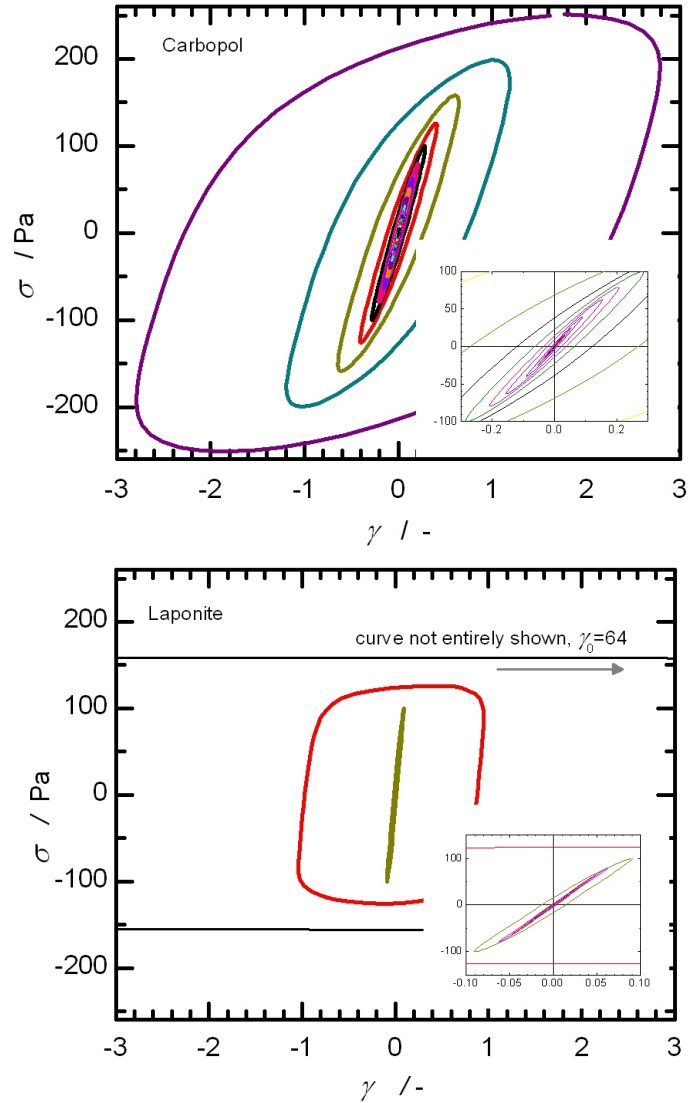


Figure 8-7: Lissajous curves resulting from the large amplitude oscillatory shear tests shown in Figure 8-6 for the polymer gel simulant(a) and the particulate gel simulant(b).

lated to the fragility of the colloidal gel microstructure. The Lissajous curves for the Carbopol (Figure 8-7a) progressively broaden to enclose more area, and thus show a gradual transition from elastic to viscous behavior. This soft transition is consistent with the steady state flow tests (Figure 8-4a) and the behavior of G'_1 and G''_1 as the oscillatory stress amplitude is increased (Figure 8-6a). To aid comparison, we use the same ranges on the abscissa and ordinate of Figure 8-7a,b; Figure 8-8 shares the same aspect ratio but with a larger range.

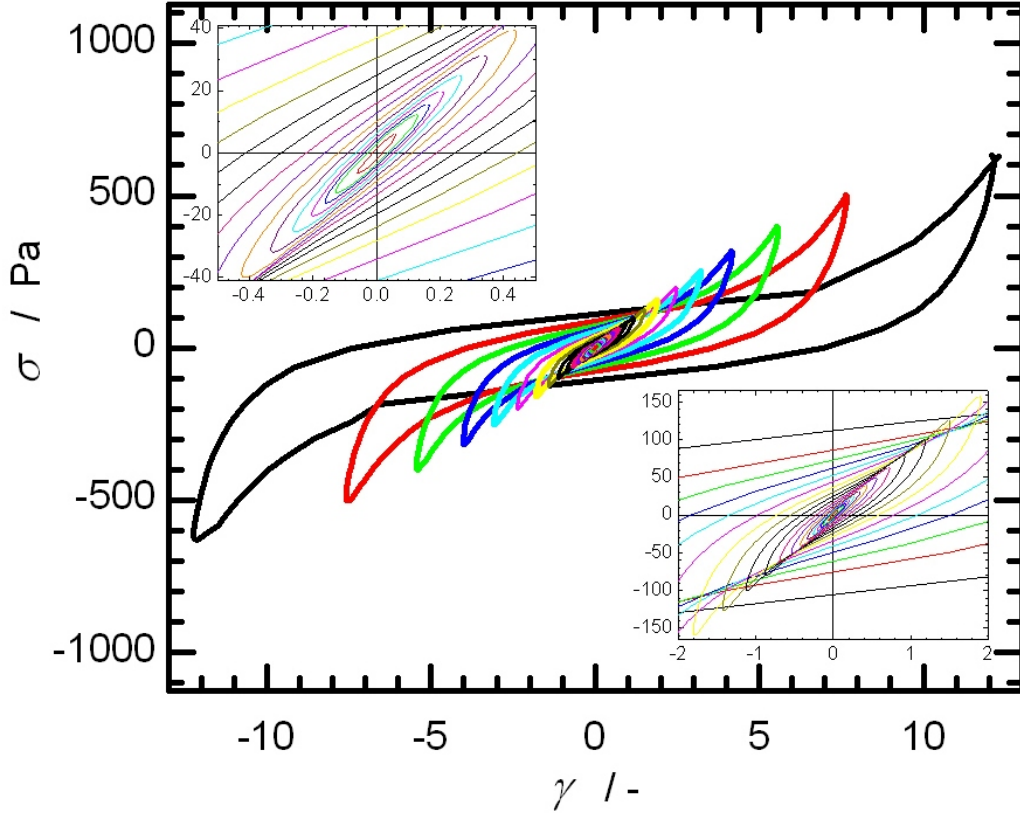


Figure 8-8: Lissajous curves resulting from the large amplitude oscillatory shear tests shown in Figure 8-6 for native pedal mucus from *Limax maximus*.

In contrast to the two simulants, the native pedal mucus exhibits a strongly nonlinear response leading up to yield. For native slime the elliptical curves which are present at low stresses become progressively distorted as the stress amplitude is increased. The distortion is such that the stress increases sharply at large strains. This upturn in stress can be interpreted as a form of strain-stiffening, since the maximum stress is higher than would be expected if the small strain response were fit to an ellipse and projected to large strains. It is significant to note that this nonlinear response is not captured by monitoring G'_1 , as shown in Figure 8-6, in which the first harmonic storage modulus of native slime is a very weak function of stress amplitude (this is consistent with the strain-controlled test of pedal mucus reported in Section 4.2.2). The strain-stiffening reported for native slime is not mimicked by either of the Carbopol or Laponite gel simulants. Although strain-stiffening is required in

other biomaterial applications (e.g. arterial walls[4]), and may also be important in biological adhesive locomotion, our simple adhesive locomotion model is not affected by this behavior.

It is important to point out that nonlinear LAOS behavior depends on (at least) two parameters: stress (or strain) amplitude and frequency. Here we have only explored one-dimension of this parameter space; i.e. the rheological response to increasing oscillatory stress amplitudes at a constant frequency. A framework for exploring the two-dimensional experimental space, along with quantifying the nonlinear stiffening behaviour, is the subject of Chapter 2.

Time dependency of yield stress

The apparent yield stress of a material is likely to depend on how long the sample has been at rest since it was last yielded, i.e. there is a natural timescale of restructuring (thixotropy) to regain a yield stress[114, 115]. Furthermore, our simple model shows that the maximum velocity of a mechanical crawler is inversely related to the restructuring time[110].

The restructuring times of the Carbopol and Laponite gel simulants were examined using shear stress overshoot tests[121]. The sample is first pre-sheared to break down structure, i.e. it is “shear rejuvenated”[122], to yield the material and erase any strain history effects. The pre-shear is abruptly “quenched,” or brought to a halt, at which point the sample is allowed to age for a waiting time t_w . A step-strain-rate is then imposed, which destroys the existing microstructure and causes the sample to flow. The resulting overshoot stress $\Delta\sigma$ is then determined as the difference between the peak shear stress and the steady flow stress, and is expected to depend on the time t_w that the microstructure has been allowed to equilibrate. The overshoot stress is not quantitatively equivalent to the yield stress as defined in this work. However, it is closely correlated to the yield stress, as it is the peak stress which occurs as the strain is increased and the material microstructure is ruptured.

The results of time-dependent overshoot tests for the simulants are shown in Figure 8-9. The Laponite sample (3%) was pre-sheared at $\dot{\gamma} = 5\text{s}^{-1}$ for 60 seconds.

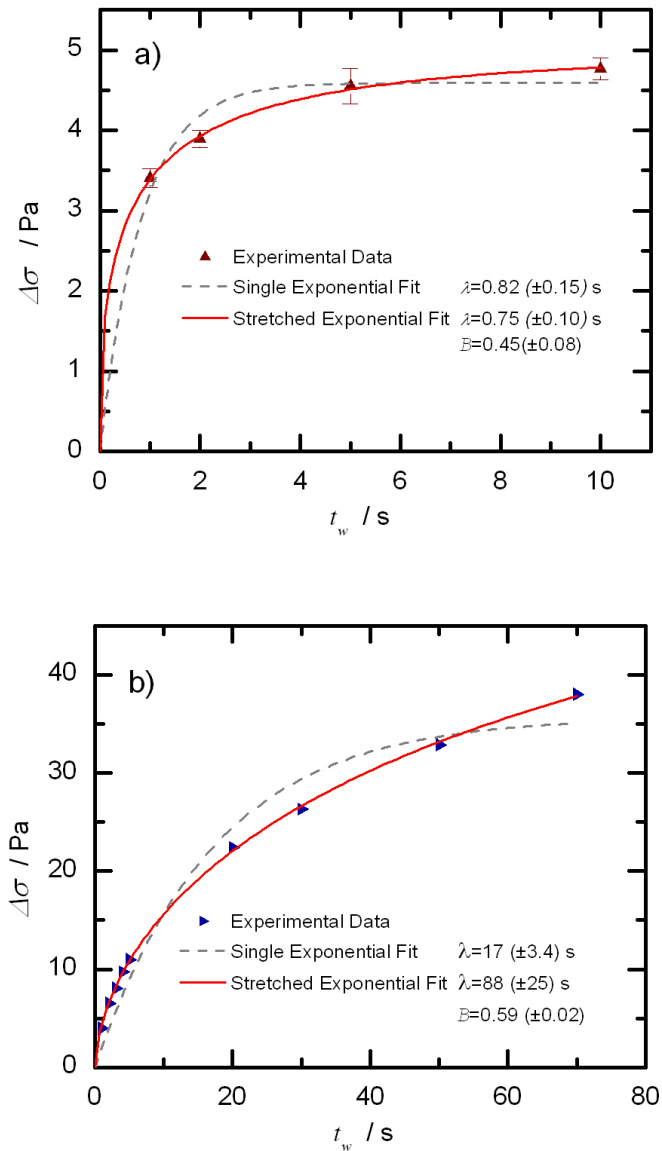


Figure 8-9: Time-dependent stress overshoot of simulants, $D = 5$ cm 1° cone-plate; a) Carbopol 2%, error bars shown at one standard deviation; b) Laponite 3%.

Less shearing was needed to eliminate strain history effects with the Carbopol, which was pre-sheared at $\dot{\gamma} = 5\text{s}^{-1}$ for five seconds. Each was allowed to rest for a specified time and then sheared once more at $\dot{\gamma} = 5\text{s}^{-1}$. Each Carbopol test was repeated three times and error bars are shown. The minimum waiting time allowed by the rheometer is one second, which provides a lower bound for measurement of thixotropic recovery.

An appropriate form of the rheological aging observed in the samples is a stretched

exponential approach to an asymptotic value observed at long rest times

$$\Delta\sigma(t_w, \dot{\gamma}) = \Delta\sigma_\infty(\dot{\gamma}) \left(1 - e^{-(t_w/\lambda)^B}\right) \quad (8.2)$$

where $\Delta\sigma_\infty$ is the maximum overshoot stress at long rest times, t_w is the rest time, λ is the characteristic restructuring time, and B is the stretching exponent. Stretched exponentials have been observed experimentally in both polymeric[123] and colloidal[124] systems and have been associated with the presence of fractal networks[125]. When $B = 1$, Eq. 8.2 represents a single exponential aging timescale, which has previously been used to describe the aging of the yield stress[126]. Each data set in Figure 8-9 has been fitted to Eq. 8.2 as both a single exponential ($B = 1$) and a stretched exponential. The regression results are shown in Figure 8-9.

For a yield stress that grows in a similar fashion to Eq. 8.2, the restructuring time λ is inversely related to the maximum velocity of a mechanical crawler[110]. The polymer gel has a much faster restructuring time than the particulate gel. The single exponential restructuring timescale of Carbopol is $\lambda \approx 0.8$ s, whereas the restructuring time of Laponite dispersions is $\lambda \approx 17$ s. Thus, the maximum velocity of a mechanical crawler on Carbopol would (theoretically) be approximately 20 times that of a crawler on Laponite. The stretched exponential timescales are also dramatically different.

The restructuring timescale of native pedal mucus could not be reliably measured as a result of technical difficulties. However, Denny performed similar overshoot tests with gastropod pedal mucus and found that peak stress as a function of wait time could be fit to a power law[127]. In order to extract a timescale of restructuring for comparison, a single exponential timescale can be fit to the first ten seconds of this power law giving $\lambda \approx 0.85$ s with $R^2 = 0.74$. Although there is biological variability and a low R^2 value, it is apparent that pedal mucus and the Carbopol gel share restructuring times of the same order of magnitude.

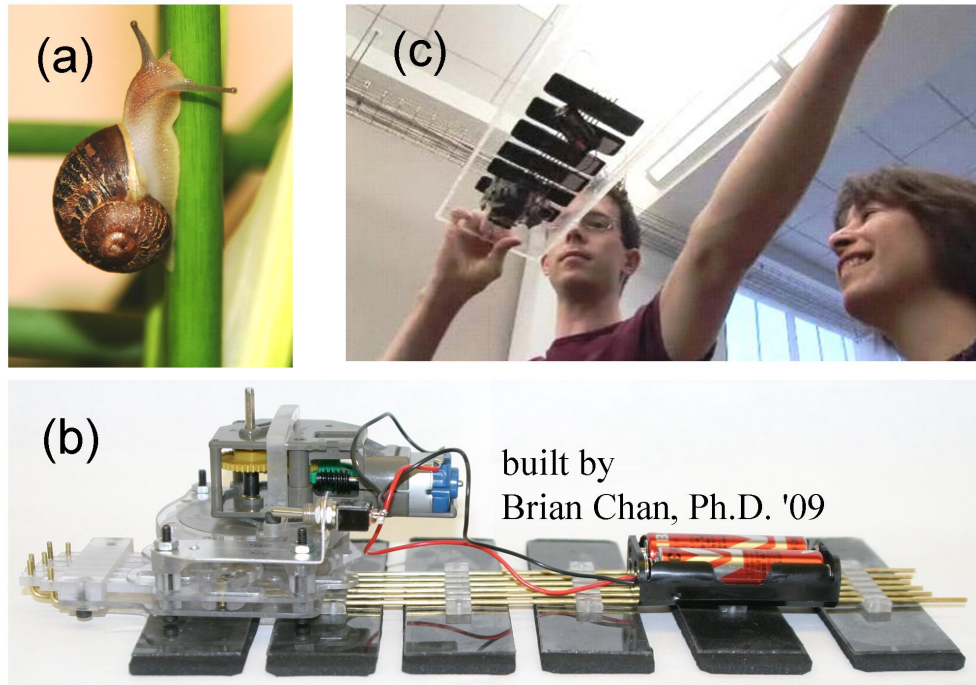


Figure 8-10: (a) The common garden snail *helix aspera* (and other terrestrial gastropods) use the nonlinear viscoelastic properties of excreted trail mucus for transitory attachment, allowing locomotion on inclined surfaces. (b) Bioinspired embodiment of a mechanical crawler that successfully uses adhesive locomotion to traverse inclined and inverted surfaces, as in (c), using appropriately designed complex fluids described in this thesis.

8.3 Demonstration of feasibility

The wall-climbing ability of terrestrial gastropods (Fig. 8-10a) has been successfully biomimicked using the fluid design rules outlined in this Chapter. It is non-trivial to duplicate biological functionality, given the constraints on conventional engineering components such as motors and actuators [128]. For example, it has been exceedingly difficult to mimic flapping wing flight with a self-contained device due to power requirements and actuator efficiency; instead we have found the best engineering success with fixed-wing flight powered by propeller or jet engines. Together with Brian Chan (Ph.D. '09)[129], we have shown that adhesive locomotion can be used as the locomotion strategy of a self-contained device. The crawler (Fig. 8-10b, designed and built by Brian Chan) has been designed to meet the requirements of appropriate

motion and geometry for adhesive locomotion. It employs on-board power (two AA batteries), is driven by a single DC motor, and relies on a unique custom-designed cam system that transfers power to discrete foot pads. From the work described in this thesis, a suitable non-Newtonian yield stress fluid has been formulated to enable the crawler of Fig. 8-10b to traverse inclined and inverted terrain (Fig. 8-10c).

The fluid used is the aqueous polymeric microgel Carbopol 940 (4 wt%) at neutral pH (c.f. Figs. 8-3,8-4). This complex fluid has sufficiently large yield stress to support the crawler, a reasonably low flow viscosity after yield, and an adequate self-healing time (the time required to restructure into a solid-like material once a load is removed), the criteria for which are outlined in this thesis Chapter. It has thus been demonstrated that the adhesive locomotory strategy can be successfully implemented with existing engineering technology. Although a synthetic fluid can be concocted to adequately mimic the nonlinear mechanical properties of pedal mucus, and demonstrate the feasibility of mimicking adhesive locomotion, native slime is still superior to the synthetic self-healing materials explored. Native pedal mucus self-heals more quickly following cessation of deformation and has a sharper yielding transition at the critical stress for flow (or “yield stress”). The superior performance of the natural mucus gel motivates a detailed understanding of the linear to nonlinear viscoelastic properties of pedal mucus, which are discussed in Section 4.2.2 of this thesis.

8.4 Conclusions

It has been known for some time that pedal mucus from terrestrial gastropods exhibits a yield stress[99], but the present work is the first examination of the progressive transition from an elastic gelled solid to a nonlinear viscoelastic fluid as the oscillatory shear stress amplitude is increased. Lissajous curves (such as Figure 8-8) can be used to graphically indicate the observed strain-stiffening behavior of native pedal mucus. The bulk rheological response of native slime was used to provide a set of benchmarks for comparing two possible complex fluids (a particulate gel and a polymeric gel) for the purpose of enabling mechanical adhesive locomotion.

A large number of structured materials were surveyed as possible slime simulants, including polymer gels, particulate gels, emulsions, wet foams, and composites (Figure 8-3). Two simulants which could be formulated to have similar yield stresses to that of native slime (Figure 8-4) were then chosen for further study. When examined in detail, in linear and nonlinear deformation, the simulants show some differences in rheological properties. Table 8.1 summarizes the results of the comparison of these simulants with native gastropod pedal mucus.

The three key parameters for a complex fluid to be useful in adhesive locomotion are a high yield stress, σ_y , to support the crawler on an inclined surface, a low post yield viscosity, η , to increase speed, and a small restructuring timescale, λ , also to increase speed. Of the two simulants analyzed in this work, the Carbopol-based polymer gel is the best candidate for use in adhesive locomotion. It provides sufficient yield stress, a moderate post-yield viscosity, and a restructuring time that is more than an order of magnitude smaller than the Laponite-based colloidal gel simulant. Native pedal mucus, however, is still better than the best simulant; it provides comparable yield stress and restructuring time, but a lower post-yield viscosity.

A more general scientific question related to this work is how to characterize soft condensed matter under relevant loading conditions. One aspect of relevant characterization is the length scale of interest. It is noteworthy that no rheological measurements have been reported for native pedal mucus at the physiologically relevant gap thickness $h = 10 - 20 \mu\text{m}$, including the results presented here. Most tests are reported with a gap height one to two orders of magnitude larger than this, and it is possible that native pedal mucus acts differently in a confined space. Effects of narrow gap polymer rheology such as gap-dependent relaxation times have been the subject of debate[130] and gap-dependent yield stress levels as well as wall slip velocities have been observed with emulsions[131] and other complex fluids[132].

The type of rheological test performed must also be relevant to the intended use of the material. Linear viscoelasticity is robust (in the linear regime), but may not fully apply to the intended use of the material. In this work, nonlinear rheological tests were used to quantify properties such as the yield stress, yield strain, and thixotropic

restructuring time, as well as to investigate the nature of the yield transition and the existence of strain-stiffening in native slime. However, this strain-stiffening could not be observed with the common measures of nonlinear viscoelasticity (G'_1 and G''_1). This is in contrast to the colloidal gels examined by Gislser et al.[42] and the semi-flexible biopolymer gels studied by Storm et al.[39] in which strain-stiffening of the networks could be detected in the first harmonic elastic modulus, G'_1 . This difference arises presumably from the differing flexibility of semi-flexible chains such as F-actin and the heavily glycosylated mucin protein studied here. In the present study, strain-stiffening can only be revealed by representing the raw data in the form of Lissajous curves. A suitable measure to quantify this local strain-stiffening behaviour has been derived for strain-controlled deformation (Chapter 2), and used to characterize the nonlinear viscoelastic response of gastropod pedal mucus (Section 4.2.2). In general, when soft condensed matter is exposed to large stresses or strains in situ, the nonlinear material properties will be significant, and one must decide which tests and measures provide the most relevant rheological fingerprint of the material.

	Native pedal mucus	Carbomer-based simulant (polymer gel)	Clay-based simulant (particulate gel)
Yield stress	100 - 240 Pa	108 Pa	90.8 Pa
Post-yield viscosity, $\eta(\dot{\gamma} = 10\text{s}^{-1})$	10.4 - 25 Pa.s	31.6 Pa.s	9.6 Pa.s
$G'(\omega = 1\text{rad.s}^{-1})$	200 Pa	540 Pa	1800 Pa
$G''(\omega = 1\text{rad.s}^{-1})$	20 Pa	30 Pa	60 Pa
Yield stress transition	Sharp	Soft	Sharp
Pre-yield stiffening	Yes	No	No
Single exponential restructuring time, λ	0.85 s (adapted from ref. [127])	0.8 s	17 s (for 3% gel)

Table 8.1: Summary of rheological properties of two simulants with similar apparent yield stresses compared with native gastropod pedal mucus. Although the concentrations and microscopic structure are different, fluids with similar yield stresses are compared since the macroscopic rheological property of a yield stress is the primary requirement for inclined adhesive locomotion, c.f. Eq. 8.1.

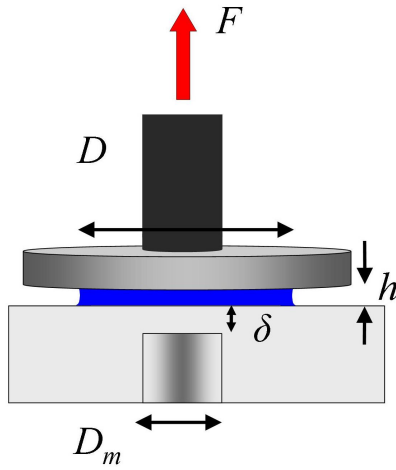
Chapter 9

Tunable and reversible adhesion using field-activated “smart” fluids

Viscous Newtonian fluids confined in sufficiently small gaps can provide strong resistance to the separation of two parallel rigid surfaces, a phenomenon known as Stefan adhesion[133]. However, the resistance to a shear load is considerably lower than for normal loads in such confined geometries. In principle, a field-responsive “smart” fluid, which exhibits a field-dependent microstructure with dramatically increased resistance to shear loading, can be used in place of a Newtonian fluid enabling externally-tunable adhesion. Adhesion to arbitrary surfaces (such as walls or windows) inhibits the option of creating a homogeneous magnetic field condition. Therefore successful adhesion in general must tolerate an inhomogeneous magnetic field. Here it is demonstrated experimentally that MR fluids can be used with inhomogeneous fields (e.g. created by a permanent magnet near the fluid) to attach to non-ferromagnetic substrates including plastic, aluminum, glass, ceramic tile, and wood.

Adhesive performance will depend on the method of separation of the two surfaces, such as normal pulling off, shearing, or peeling[134]. Experimental results are reported for both normal and shear loading of a field-responsive yield stress fluid confined between rigid surfaces as the external magnetic field and the geometry of the adhesive contact are varied. The peak adhesive force and the mode of failure are all controlled

(a) Configuration



(b) Free body diagrams

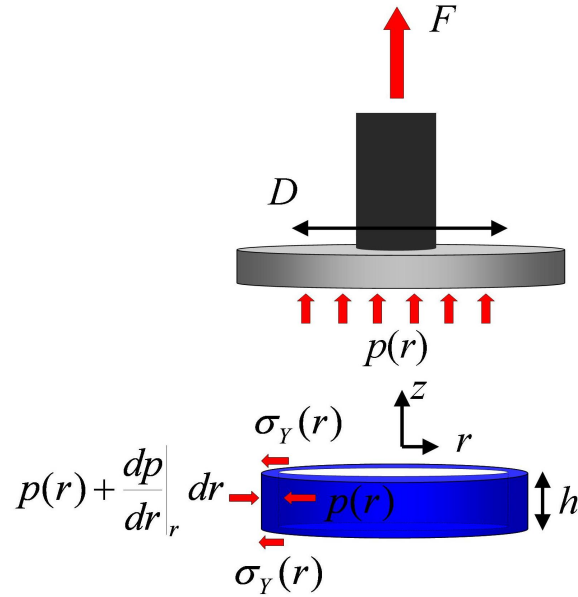


Figure 9-1: (a) Sketch of the experimental setup for adhesive pull-off tests of a field-responsive magnetorheological fluid. Instrument materials are non-magnetic. The adhesive fluid layer (diameter D , gap height h) resides between rigid surfaces. The lower plate allows for a permanent magnet (diameter D_m) to be introduced to “activate” the adhesive with an inhomogeneous field. The top of the magnet is separated from the bottom of the fluid by a distance δ . (b) Free body diagrams for yield stress fluid adhesion. For the top plate only forces in the z -direction are shown. The fluid is modeled locally as a perfect plastic with radially dependent yield stress. Small gaps are assumed ($h/D \ll 1$), so that material deformation consists primarily of shear.

by the field-responsive nature of the magnetorheological fluid forming the adhesive layer.

9.1 Experimental setup and materials

Simple shearing deformation is examined by shear rheometry, whereas normal adhesion experiments are performed on a linear force/displacement instrument with sensitive normal force resolution.

9.1.1 Instrumentation

Shear rheometry is probed using the AR-G2 rotational rheometer (TA Instruments, New Castle, DE). For the Newtonian oil, a cone-plate setup was used ($D = 40$ mm, $\theta = 2^\circ$) in which the lower surface (Peltier plate) is temperature-controlled. Carbopol samples were tested with a plate-plate geometry ($D = 40$ mm, $h = 1000\mu\text{m}$) using a solvent trap to stifle evaporation. The magnetorheological fluid was also tested with a plate-plate geometry, with gap $h = 500\mu\text{m}$. Ambient tests of the MR fluid used the standard rheometer setup and a top plate with $D = 40$ mm. To examine the magnetic field dependent rheology, a top plate with diameter $D = 20$ mm was used in concert with the MRF Rheometer Cell developed by Murat Ocalan[135]. For both the Carbopol and MR fluid, adhesive-backed waterproof sandpaper (600 grit, Eastwood Co., Pottstown, PA) was attached to the top and bottom plates to help avoid slip at the bounding surfaces.

The parallel plate geometry imposes an inhomogeneous strain field, and therefore the measured torque represents only the apparent shear stress in the material. To correct for this, the true stress can be determined from $\sigma_R = \sigma_A \frac{1}{4} (3 + d \ln \sigma_A / d \ln \dot{\gamma}_R)$ (e.g. see Macosko[94]), where σ_R is the true stress at the edge of the disk and σ_A is the apparent stress determined by $\sigma_A = 2M/\pi R^3$ where M is the measured torque and R is the disk radius. Applying this correction requires derivatives of the apparent stress data. To calculate the required derivatives, we fit a fifth order polynomial function to the raw data of $\ln \sigma_A$ vs. $\ln \dot{\gamma}_R$, since this allows calculation of the derivative of a smooth analytical function rather than differentiating discrete raw data. This was required for the both the Carbopol solution and MR fluid.

The normal “pull off” adhesion was examined using a linear load/displacement instrument, the TA.XTplus Texture Analyzer (Stable Micro Systems, UK). The fluid is confined between two rigid surfaces which are separated in the normal direction as shown in Fig. 9-1. This experiment is sometimes referred to as a “probe tack” test. The bottom plate is fabricated from transparent plastic. One plate is solid polycarbonate of thickness 0.475” ($\delta = 12.1$ mm), with a sandblasted surface to provide a

finite roughness (r.m.s. roughness $R_q = 1.84\mu\text{m}$ from 2D surface profilometry (Tencor P-11 Surface Profiler)). A second plate is made from transparent acrylic, thickness 0.325" (8.3 mm), and fabricated with with a cylindrical hole in which a magnet can be placed $\delta = 1.0$ mm from the fluid (Fig. 9-1). For the Newtonian oil and MR fluid tests, the diameter of the top plate (typically $D = 48$ mm) is always bigger than the initial fluid diameter. This avoids the uncertainties associated with contact lines pinned to the edge of the plate. For the Carbopol tests the fluid diameter and plate diameter are chosen to be the same, $D = 48$ mm, to increase experimental precision. Here the yield stress fluid is cut to size after overfilling and retains its shape, thus the shape of the fluid-air interface can be controlled for this case.

The Texture Analyzer is known to exhibit finite compliance in the loading direction which can cause experimental artifacts under certain adhesive test conditions[136]. The system stiffness was measured to be $K = 12,600$ g_f/mm (Compliance= $79\mu\text{m}/\text{kg}_f$). Additional error may come from the parallelism error of the bounding surface. To measure the parallelism error, the top surfaces were brought into contact. For finite parallelism error, the contact occurs at a single point on the edge of the top plate. A gap will persists around the rest of the plate edge, and this maximum gap is measured by sliding shim stock of known thickness into the gap, such that the maximum thickness which fits into the gap estimates the parallelism error. For the $D = 48$ mm plate, the parallelism error is approximately $d \approx 127\mu\text{m}$. The minimum apparent gap height used in these studies is $h = 500\mu\text{m}$.

9.1.2 Materials

The Newtonian oil is a PDMS Silicone Oil, "10,000 cst." The dynamic viscosity at $T = 25^\circ$ was measured here to be $\eta = 9.28$ Pa.s (see Appendix E for detailed rheological characterization). Carbopol 940 was obtained from the Noveon corporation (Cleveland, OH). The Carbopol-based solution was prepared at a concentration of 2%(w/w), where w/w refers to weight of the additive with respect to the total weight of the mixture. The polymer was obtained as a white powder, and was added to deionized water being agitated with a magnetic stirrer. Samples were mixed for a

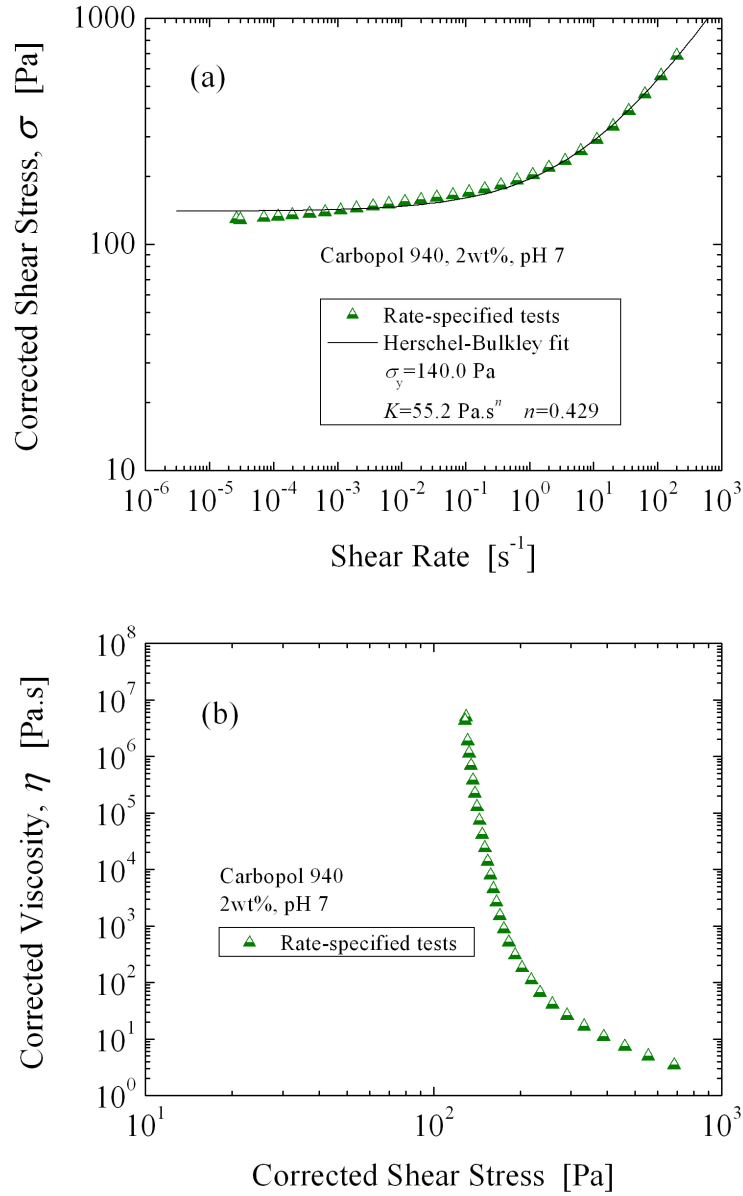


Figure 9-2: Rheological characterization of the passive yield stress fluid, Carbopol 2wt%, pH 7.

minimum of 30 minutes. The Carbopol-water mixture initially has a pH near 3, and each was neutralized with 4 M NaOH solution to achieve a pH=7, producing a clear gel at the targeted concentration. The rheology of Carbopol mixtures depends on the pH, with maximum thickening occurring within a pH range of 5-9[108].

Rheological measurements for this particular batch of Carbopol are presented in

Fig. 9-2. These tests were performed by specifying the shear-rate, in which case the instrument uses a control feedback loop to impose the appropriate torque. A rate-specified test was preferred here because the normal adhesion tests impose kinematic deformation conditions, i.e. displacement controlled tests. Furthermore, a rate-specified rheological test allows for the observation of a stress plateau across a broad range of shear-rates.

The (corrected) shear stress is shown as a function of shear-rate in Fig. 9-2a. This Carbopol solution is not a perfect plastic material for all shear-rates. However, at low shear-rates the shear stress may be approximated as a plateau. The results across the entire range of shear-rates are fit to the Herschel-Bulkley model,

$$\sigma = \sigma_y + K\dot{\gamma}^n. \quad (9.1)$$

resulting in $\sigma_y = 140.0$ Pa, $K = 55.2$ Pa.s^{*n*}, and $n = 0.429$ (shown in Fig. 9-2a). The method of fitting a Herschel-Bulkley model results in a larger estimate for yield stress than identifying the corner in a viscosity vs. stress curve, which was done in Chapter 8 for a similar material, in which the yield stress was estimated to be $\sigma_y = 108$ Pa (Table 8.1).

For the field-controllable tests a commercial magnetorheological (MR) fluid is used, purchased from the LORD Corp., designated as MRF-132DG. The MR fluid is oil-based and contains carbonyl iron particles (1-20 μ m), plus additives. The iron particles serve as magnetically-responsive constituents. An external magnetic field induces magnetic dipoles in the particles, causing them to form chains which dramatically change the mechanical properties of the solution.

The shear rheology of the MR fluid is shown in Fig. 9-3, for the ambient state (open symbols) and various magnetic field activation (closed symbols). Fig. 9-3a shows the corrected shear stress as a function of the imposed shear-rate. The ambient state exhibits a broad stress plateau across several orders of magnitude in shear-rate, which serves as an apparent yield stress. The material is not perfectly plastic, however, and the stress eventually increases as a function of shear-rate. The MR fluid becomes more

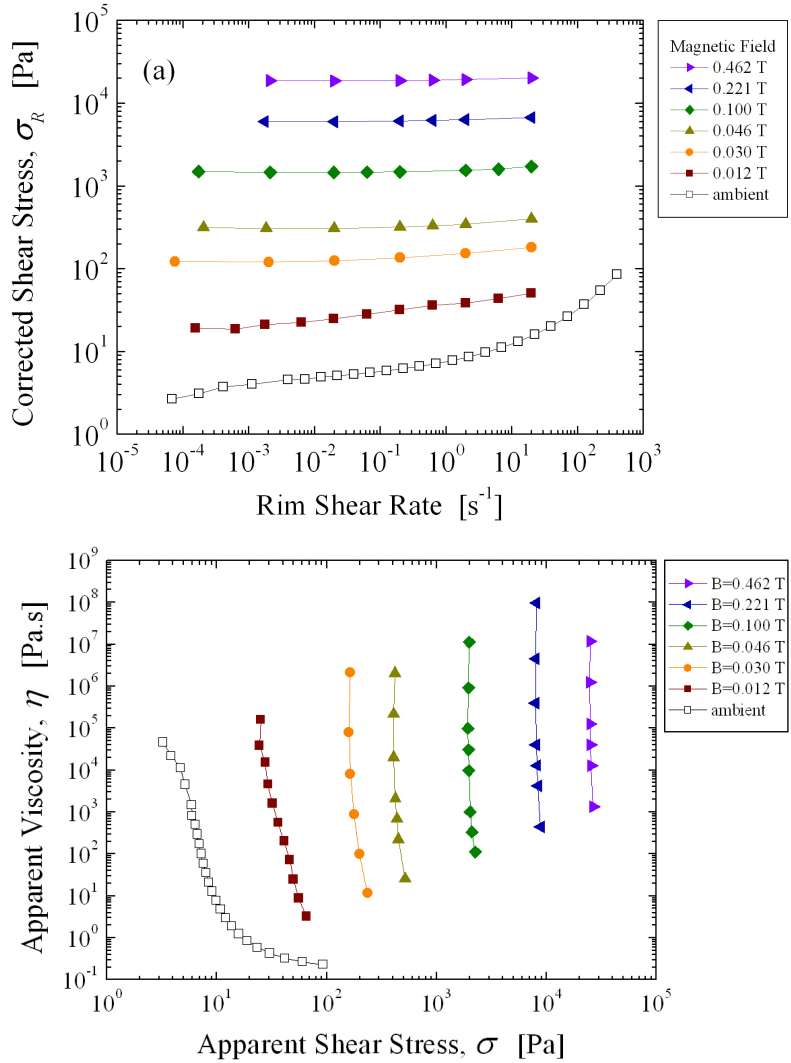


Figure 9-3: Steady flow characterization of the magnetorheological fluid, which behaves as a nearly perfect viscoplastic with constant stress as a function of shear rate (a). Another method of showing viscoplastic yield stress behavior is shown in (b), which depicts steady flow viscosity as a function of the imposed shear stress. The viscosity and stress values have been corrected for the parallel plate geometry.

of a perfect plastic material as the magnetic field strength increases, as evidenced by the flat stress profiles in Fig. 9-3a. An alternative way to visualize such yield stress fluids is to plot viscosity as a function of stress, which is shown in Fig. 9-3b. Here an apparent yield stress is indicated by the viscosity changing by several orders of magnitude over a narrow range of stress.

The apparent yield stress is extracted from the corrected flow curves of Fig. 9-3.

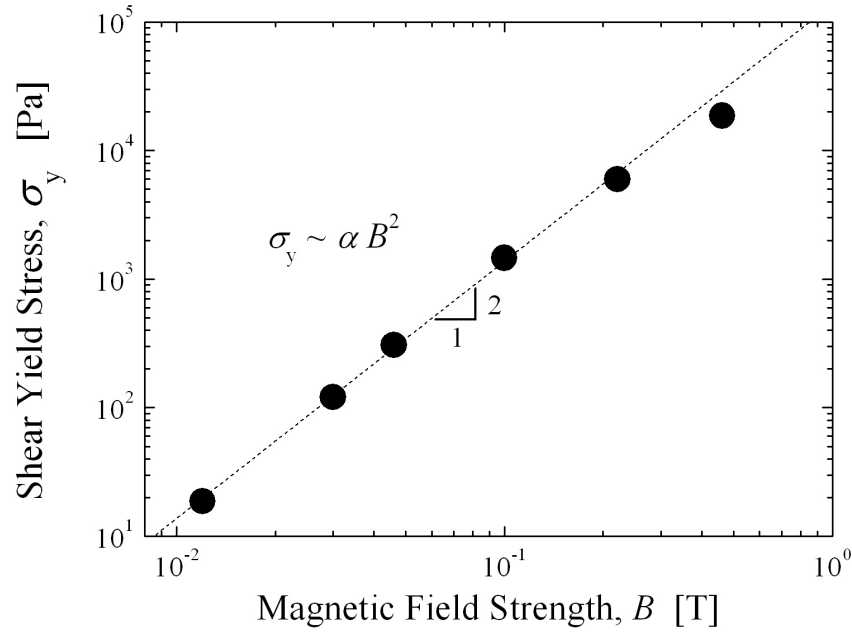


Figure 9-4: Shear yield stress for the magnetorheological fluid as a function of the external magnetic field strength (field lines perpendicular to shearing direction). Yield stress values extracted from Fig. 9-3 (circles). The dashed line is a power law fit to the data (ignoring the data point at $B = 0.462$ T), resulting in $\alpha = 137737 \text{ Pa}\cdot\text{T}^{-2}$.

For the field-activated states, the yield stress is estimated from the average stress at the lowest three shear-rate data points. For the ambient response (open symbols), the effective yield stress may depend on the characteristic shear-rate. For instance, $\sigma_{y0} \approx 6.75 \text{ Pa}$ at a characteristic shear rate $\dot{\gamma} = 2\dot{h}R_0/h_0^2 = 0.5 \text{ s}^{-1}$, which corresponds to the experimental parameters $h_0 = 0.5 \text{ mm}$, $R_0 = 6.35 \text{ mm}$, and $\dot{h} = 10 \mu\text{m}\cdot\text{s}^{-1}$.

9.1.3 Magnetic field configuration for pull-off tests

Three different permanent magnets were used to activate the MR fluid. The weakest magnet is made from Alnico8, with geometry $R_m = 6.35 \text{ mm}$ and $L_m = 6.35 \text{ mm}$. The magnetic strength was measured with a Hall effect probe (F.W. Bell, model #5180 Gauss/Tesla probe). On the face of the magnet, a magnetic field of $B = 0.068 \text{ T}$ was measured at the center. On average (near $R_m/2$) the field strength is $B = 0.077 \text{ T}$. Across the $\delta = 1.0 \text{ mm}$ acrylic surface, the measurements are $B = 0.059 \text{ T}$ at the

center and $B = 0.061$ T on average (near $R_m/2$). For modelling and analysis, $B_0 = 0.061$ T is used to represent the field across the area of the magnet.

Nedodymium magnets are used for the two strongest magnets. These are rare earth magnets comprised of neodymium, iron, and boron. The first of these has dimensions $R_m = 6.35$ mm, $L_m = 0.95$ mm. On the face of the magnet, the field measurements are $B = 0.398$ T at the center and $B = 0.389$ T on average at $R_m/2$. Across the $\delta = 1.0$ mm acrylic surface, the field strength is measured to be $B = 0.319$ T at the center and $B = 0.296$ T on average near $R_m/2$. This final value is used to describe the field strength for adhesive tests, $B_0 = 0.296$ T.

The third magnet is the largest, $R_m = 12.7$ mm and $L_m = 0.95$ mm. This magnet is not used in the cutout cylindrical hole of the bottom plate, but is instead used beneath the entire thickness of the bottom acrylic plate, $\delta = 12.1$ mm. At this distance the field measured at the center is $B = 0.051$ T, and the average field is $B = 0.046$ T. This final value is used as the field strength for MR fluid adhesive tests, $B_0 = 0.046$ T.

At sufficiently large distances, the magnet appears as a magnetic dipole. The magnetostatic problem for a magnetic dipole can be solved analytically only in the far field, in which case the magnetic field strength decays as $B \sim L^{-3}$, where L is the distance from the dipole[137]. The region of interest for this problem is close to the magnet, and therefore the analytical solution does not strictly apply. Finite element analysis (FEA) was used to determine the magnetic field using the freely available software Maxwell SV (Ansoft, LLC, Pittsburgh, PA) (see Appendix E). Results were obtained for the magnetostatic problem of a cylindrical permanent magnet with a thin, disk-shaped layer of MR fluid at a finite z -distance. For a given distance above the magnet, δ , the FEA results indicate that the magnetic field strength is approximately constant for $r \leq R_m$, but decays as a power law $B \sim r^{-3}$ for $r > R_m$.

9.2 Background: fluid adhesion

Three classes of fluid adhesion are considered here for a fluid confined between rigid parallel surfaces. The focus here is on normal adhesion with small gaps ($h/D \ll 1$). First, capillary phenomena may exert a force on the top plate of Fig. 9-1. The capillary forces, assuming an axially and vertically symmetric meniscus, are given by[138]

$$F_{\text{Capillary}} = \gamma \frac{\cos \theta_E}{h/2} \pi R^2 + \gamma \sin \theta_E 2\pi R. \quad (9.2)$$

which is the superposition of a capillary pressure drop and the line traction at $r = R$. For a wetting fluid $\theta_E < 90^\circ$ and the fluid acts to pull the plates together. The pressure profile in the fluid is constant as a function of the radius, $p(r) \sim r^0$, since no other forces exist in the radial direction.

The pressure profile is not constant during plate separation at finite velocity, due to the no-slip condition which induces radial fluid flow. The classic problem of ‘‘Stefan adhesion’’[133, 139] considers the case of an incompressible Newtonian fluid in the limit of small gaps ($h/D \ll 1$). For quasi-static loading, the momentum balance in the z -direction is determined by the free body diagram of Fig. 9-1b, resulting in

$$F = -2\pi \int_0^R p(r)rdr \quad (9.3)$$

where $p(r)$ is the pressure relative to atmospheric conditions, such that the pressure at the free surface is zero, $p(R) = 0$ (neglecting surface tension). Positive adhesive forces, $F > 0$, correspond to negative pressures in the fluid. Negative pressure will exist in order to drive fluid flow inward, and inward fluid flow is required by continuity (assuming that the fluid remains in contact with the bounding surfaces). For a Newtonian fluid at low Reynolds number with $h/D \ll 1$, the lubrication approximation is valid, and the momentum balance in the r -direction is

$$\frac{\partial p}{\partial r} = \eta \frac{\partial^2 v_r}{\partial z^2} \quad (9.4)$$

where η is the (constant) viscosity and $v_r(r, z)$ is the radial fluid velocity. Combining the momentum balance with continuity,

$$\frac{1}{r} \frac{\partial(rv_r)}{\partial r} + \frac{\partial v_z}{\partial z} = 0, \quad (9.5)$$

results in a parabolic pressure profile and a required force[139]

$$F_{\text{Newtonian}} = \frac{3}{2} \eta \frac{\dot{h}}{h} \pi R^2 \left(\frac{R}{h} \right)^2 \quad (9.6)$$

where terms have been grouped to suggest a viscous stress ($\eta\dot{h}/h$) acting across the area πR^2 , multiplied by the square of the aspect ratio $(R/h)^2$. A Newtonian fluid therefore acts as an adhesive but only in response to a dynamic situation with non-zero separation velocity \dot{h} .

A yield stress fluid can be used to support an adhesive force F under static conditions[140]. For a deforming perfect plastic material the magnitude of the shear stress is a constant, σ_y , independent of the shear-rate and therefore independent of the kinematics of deformation. For thin gaps ($h/D \ll 1$), the deformation is primarily shear. The momentum balance in the r -direction is then determined from the free body diagram of Fig. 9-1b, and is given by

$$\frac{dp}{dr} = \frac{2\sigma_y(r)}{h} \text{sgn}(\dot{h}) \quad (9.7)$$

where h is the height of the fluid and $\text{sgn}(\dot{h})$ is used to achieve the appropriate sign for either squeeze flow ($\text{sgn}(\dot{h}) = -1$) or pull-off adhesion tests ($\text{sgn}(\dot{h}) = +1$). In this chapter only “probe tack” adhesion tests are performed, in which case $\text{sgn}(\dot{h}) = +1$. The yield stress may vary as a function of the radius, $\sigma_y(r)$, for example due to an inhomogeneous magnetic field which activates the fluid (this is considered in the following section). For a passive yield stress fluid, $\sigma_y = \text{constant}$ throughout the entire fluid, and Eq. 9.7 can be integrated from R to r to reveal a linear pressure profile. This pressure field is then integrated according to the vertical force balance (Eq. 9.3), giving the pull-off adhesion force for a perfect plastic fluid with constant

Mechanism	Normal force
Capillary effects (wetable surface)	$F_{\text{Capillary}} = \gamma \frac{\cos \theta_E}{h/2} \pi R^2$
Yield stress fluid (perfect plastic)	$F_{\text{yield-stress}} = \frac{2}{3} \sigma_y \pi R^2 \left(\frac{R}{h}\right)$
Viscous effects (Newtonian fluid)	$F_{\text{Newtonian}} = \frac{3}{2} \eta \left(\frac{\dot{h}}{h}\right) \pi R^2 \left(\frac{R}{h}\right)^2$

Table 9.1: Various fluid adhesion mechanisms.

yield stress,

$$F_{\text{yield-stress}} = \frac{2}{3} \sigma_y \pi R^2 \frac{R}{h} \quad (9.8)$$

where terms have been grouped to suggest an yield stress σ_y acting over the contact area πR^2 multiplied by the aspect ratio (R/h) . This result assumes small gaps ($h/D \ll 1$) and constant fluid contact with the bounding surfaces. The material deformation is primarily shear and therefore adhesive performance depends on the shear properties of the fluid.

The results of these thin-gap fluid adhesion mechanisms (capillary, viscous(Newtonian), and perfect plastic) are summarized in Table 9.1.

9.3 Theory: magnetorheological fluid adhesion with an inhomogeneous field

Here we extend the previous results of yield stress fluid adhesion discussed in Section 9.2 to include radially dependent yield stress caused by an inhomogeneous magnetic field. The momentum balance in the z -direction (Eq. 9.3) and the r -direction (Eq. 9.7) are still valid. Additionally, we must identify the constitutive equation relating shear yield stress to magnetic field strength and the configuration of the magnetic field.

For the magnetorheological fluid used here, an apparent shear yield stress exists in the off state ($B = 0$) and the yield stress increases in response to an external magnetic

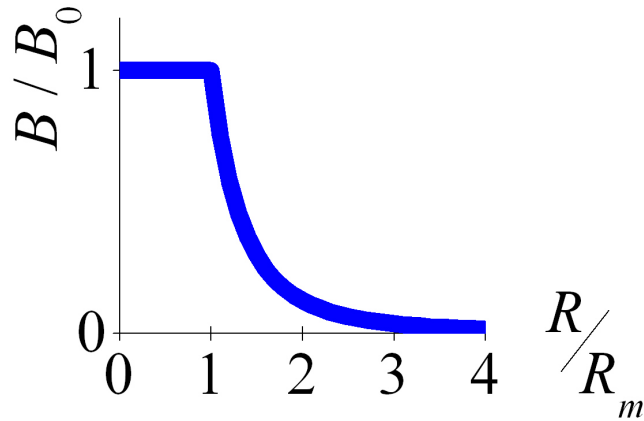


Figure 9-5: Idealization of B-field which activates the magnetorheological fluid. The field is constant above the magnet ($R/R_m < 1$), then decays by the power-law r^{-3} .

field strength B according to a power law relationship (Fig. 9-4, with field lines perpendicular to the shearing direction). Up to moderate field strengths $B \approx 0.2$ T, the constitutive equation relating shear yield stress to (perpendicular) field strength can be written as

$$\sigma_y = \sigma_{y0} + \alpha B^2 \quad (9.9)$$

where $\alpha = 137737 \text{ Pa}\cdot\text{T}^{-2}$ is the measured value for the MR fluid used here (c.f. Fig. 9-4).

The final required condition is the form of the magnetic field which activates the fluid $B(r)$. Here we consider the case of a cylindrical permanent magnet (radius R_m , length L_m) which is offset from the fluid a finite distance δ (Fig. 9-1). All other materials and structures in the setup are non-ferromagnetic, and therefore have negligible influence on the magnetic field lines. The permanent magnet creates an inhomogeneous magnetic field within the region of interest. For a given distance above the magnet, δ , the FEA results indicate that the magnetic field strength is approximately constant for $r \leq R_m$, but decays as a power law $B \sim r^{-3}$ for $r > R_m$. Field lines are not perpendicular to the shearing direction in this case. However, for

simplicity we will neglect the field orientation and consider only the magnitude of the excitation field. The field magnitude is then represented analytically as

$$B(r) = \begin{cases} B_0 & r/R_m \leq 1 \\ B_0 \left(\frac{r}{R_m}\right)^{-3} & r/R_m \geq 1 \end{cases} \quad (9.10)$$

which is shown graphically in Fig. 9-5.

Equations 9.3, 9.7, 9.9, 9.10 can be combined to determine the adhesive force F resulting from the field-activated MR fluid setup. Two cases are distinguished. Case 1 will refer to the situation of $R \leq R_m$, i.e. the fluid does not extend beyond the cross-sectional area of the magnet and is therefore activated by a constant magnetic field B_0 . Case 2 will refer to $R \geq R_m$, in which the fluid at $r > R_m$ experiences an inhomogeneous and decaying magnetic field strength.

For Case 1 ($R \leq R_m$) the yield stress is constant, $\sigma_y = \sigma_{y0} + \alpha B_0^2$ (Eq. 9.10). Integrating Eq. 9.7 from R to r and using the boundary condition $p(R) = 0$ shows that the pressure field is linear,

$$p(r) = -\frac{2(\sigma_{y0} + \alpha B_0^2)}{h}(R - r), \quad (9.11)$$

and takes the maximum negative value $p(r = 0) = -2\sigma_y(R/h) = -2(\sigma_{y0} + \alpha B_0^2)(R/h)$. This pressure field is then used in Eq. 9.3 to determine the force F acting on the top plate,

$$F = \frac{2}{3}\pi(\sigma_{y0} + \alpha B_0^2)\frac{R^3}{h}. \quad (9.12)$$

which applies only for Case 1 with $R \leq R_m$.

For Case 2 ($R \geq R_m$) the same procedure is followed, but the inhomogeneous magnetic field strength must be considered. For the region $0 \leq r \leq R_m$, the yield stress is constant, $\sigma_y = \sigma_{y0} + \alpha B_0^2$, and Eq. 9.7 is integrated from R_m to r to find

$$p(r) = p(R_m) - \frac{2(\sigma_{y0} + \alpha B_0^2)}{h}(R_m - r), \quad (\text{for } 0 \leq r \leq R_m), \quad (9.13)$$

which is similar to Eq. 9.11 but includes the matching condition $p(R_m)$. The pressure field for $R_m \leq r \leq R$ is found by integrating Eq. 9.7 from R to r , using the boundary condition $p(R) = 0$. Integration of Eq. 9.7 requires the yield stress expression (Eq. 9.9) and the field condition (Eq. 9.10), and results in the pressure field

$$p(r) = -\frac{2\sigma_{y0}}{h}(R-r) - \frac{2}{5}\alpha B_0^2 \frac{R_m}{h} \left[\left(\frac{r}{R_m}\right)^{-5} - \left(\frac{R}{R_m}\right)^{-5} \right], \quad (\text{for } R_m \leq r \leq R). \quad (9.14)$$

The decay of the field-induced pressure magnitude for $r \geq R_m$ is very strong, since $dp/dr \sim \sigma_y \sim B^2 \sim (r/R_m)^{-6}$ in this region. The pressure field expressions (Eqs. 9.13 and 9.14) are then used to determine the force F , first by using Eq. 9.14 to solve for the term $p(R_m)$, and then by substitution into and integration of Eq. 9.3. The expression for the normal force F is

$$\frac{F}{F_m} = \begin{cases} \left(1 + \frac{\sigma_{y0}}{\alpha B_0^2}\right) \left(\frac{R}{R_m}\right)^3 & R/R_m < 1 \\ \left[2 - \left(\frac{R}{R_m}\right)^{-3} + \frac{\sigma_{y0}}{\alpha B_0^2} \left(\frac{R}{R_m}\right)^3\right] & R/R_m > 1 \end{cases} \quad (9.15)$$

where $F_m = \frac{2}{3}\pi\alpha B_0^2 R_m^3/h_0$. The peak force required to initiate deformation, F_{peak} , is associated with the initial conditions $R = R_0$, $h = h_0$. The adhesive performance is determined by three non-dimensional variables, R/R_m , $\sigma_{y0}/\alpha B_0^2$, and F/F_m .

For $R_0/R_m \leq 1$ the fluid experiences a homogeneous field strength B_0 , and therefore exhibits a homogeneous yield stress. For this case the adhesive force is equivalent to the plastic yield stress fluid theory (see Eq. 9.8 and Table 9.1), such that adhesive force increases as the cubic of the fluid radius, $F \sim R^3$. For the fluid extending beyond the radius of the permanent magnet, $R_0/R_m > 1$, the activation field strength is inhomogeneous, decreasing for $r > R_m$. Adding more fluid (increasing R_0/R_m) will increase the peak adhesive force but with weaker dependency on R_0/R_m . If $\sigma_{y0}/\alpha B_0^2 = 0$, the adhesive performance will asymptotically approach a constant value as $R_0/R_m \gg 1$, $F/F_m \rightarrow 2$. However, the MR fluid used in this study exhibits a finite apparent yield stress at zero field, $\sigma_{y0} \approx 6.75$ Pa. The off-state yield stress

can dominate the response if $\sigma_{y0}/\alpha B_0^2(R/R_m)^3 \gg 2$, e.g. when the fluid extends far beyond the magnet.

The validity of these models is tested with experiment in the following sections.

9.4 Results: Passive Fluids

The experimental system is validated by probe-tack tests on a Newtonian oil and the Carbopol gel. To setup a probe tack test, an initial volume of fluid is placed on the lower plate and the upper plate is lowered to squeeze the fluid into a circular disk shape with apparent height h . For Newtonian fluids the radius is kept smaller than the upper plate radius, so that contact line pinning is avoided at the edge of the plate. For Carbopol gel tests, the fluid is deliberately overfilled so that excess material squeezes out all sides of the confinement space. Excess gel is then scraped away using a flat edge so that the initial shape and the fluid radius can be precisely controlled. Adhesive probe tack tests are performed by increasing the apparent height at a constant speed, and the resulting force curves are measured.

The adhesive force predictions summarized in Table 9.1 are for instantaneous values of fluid radius R and height h . For the experimental results presented here the fluid volume is constant, which imposes a constraint on the relationship between the instantaneous values of R and h . The constraint results in

$$R^2 = \frac{R_0^2 h_0}{h} \quad (9.16)$$

in which R_0 and h_0 are the initial values of fluid radius and height, respectively.

9.4.1 Newtonian oil viscous adhesion

Experimental results for the adhesive performance of the Newtonian oil are given in Figure 9-6, which shows measured force as a function of the apparent gap height. The theoretical results predicted by the Stefan adhesion model are shown by the dashed lines in the Figure. No fitting parameters are used here since all geometrical

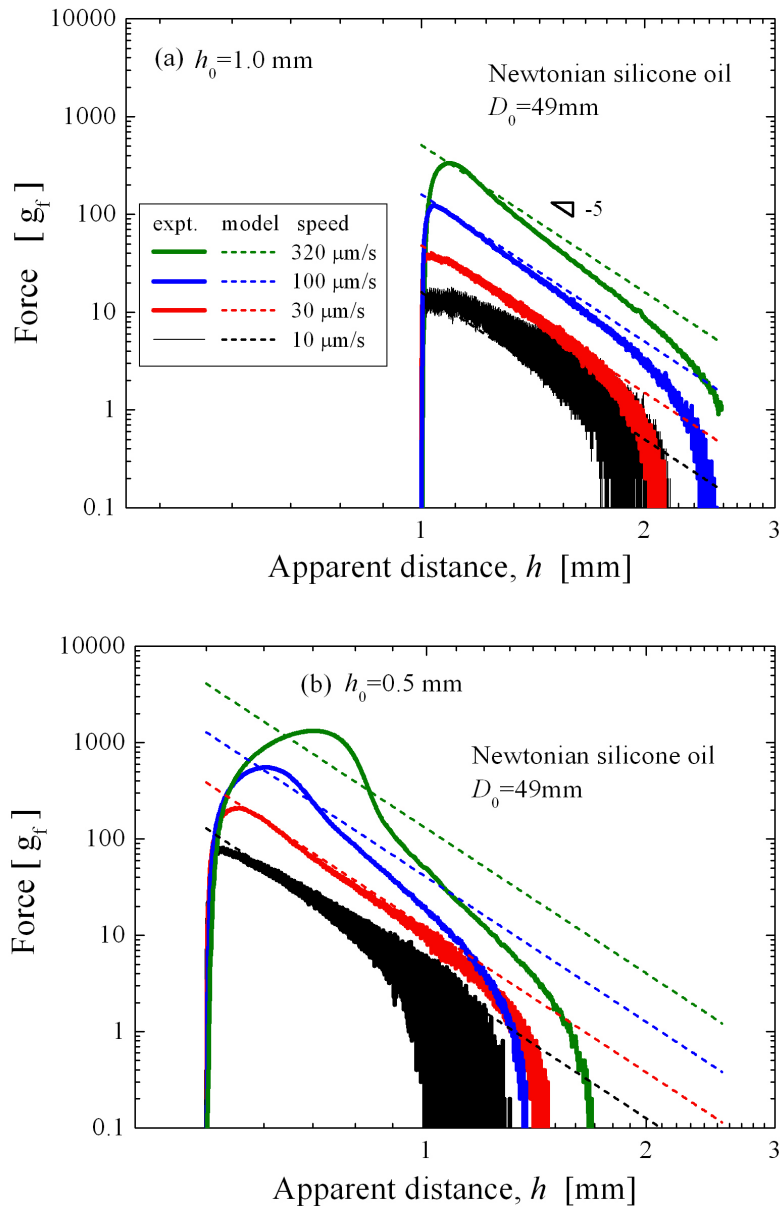


Figure 9-6: Newtonian oil adhesive performance, measured force as a function of apparent gap height. The Stefan adhesion model (dashed lines) is predictive for sufficiently small loads when system compliance is negligible, and sufficiently small values of $h(t)/R(t)$ such that the lubrication approximation holds. Here $D_0 = 49$ mm and $\eta = 9.281$ Pa.s for all tests. \dot{h} is given in the key. (a) $h_0 = 1.0$ mm, (b) $h_0 = 0.5$ mm.

parameters are known and the viscosity was measured to be $\eta = 9.281$ Pa.s. Notice the model scaling of $F \sim h^{-5}$ which results from substituting the constant volume constraint, Eq. 9.16, into Eq. 9.6. Specifically, the force can be written as a function

of the initial geometry, R_0 , h_0 , and the instantaneous thickness h , such that

$$F_{\text{Newtonian}} = \frac{3}{2}\pi\eta R_0^4 h_0^2 \dot{h} \frac{1}{h^5}. \quad (9.17)$$

The adhesive performance is quantitatively predicted by the Stefan model within a certain range of experimental parameters. First, it is applicable for sufficiently small values of $h(t)/R(t)$ such that the lubrication approximation holds, as indicated by the deviation of model and experiment at large apparent gap thickness. Second, the model is applicable for sufficiently small loads when system compliance is negligible. The system compliance has a strong effect for the Newtonian fluid adhesion because the force depends so sensitively on the true gap, h , and also depends on the instantaneous velocity \dot{h} . Figure 9-6 demonstrates the limits of the Stefan adhesion model for this system. Here h is the apparent gap height (neglecting compliance). For sufficiently small loads, the system compliance is negligible and the Stefan adhesion model accurately describes the adhesive performance of the Newtonian silicone oil.

9.4.2 Passive yield stress fluid adhesion

Adhesive probe tack tests for the passive yield stress fluid (Carbopol 940, 2wt%) are shown in Figure 9-7, in which the gap height values h have been corrected for instrument compliance. The initial force is negative for these tests because the fluid was squeezed down to a thickness h_0 , and a residual force exists after squeezing stops. The predicted initial force is shown by the line in Figure 9-7a, calculated from Eq. 9.8 using the yield stress value $\sigma = 140.0$ Pa. This yield stress value was identified from the Herschel-Bulkley model fit in Figure 9-2. The experimentally measured initial force is systematically lower in magnitude than the prediction, which may result from an overprediction of the yield stress at small rates (cf. Figure 9-2) or a small amount of stress relaxation of the material.

Once the pull off test is initiated, the initial residual force is released and thereafter the adhesive force increases. The force reaches a maximum after only a small change in gap height (likely due to elasticity in the material before yield), and then decays

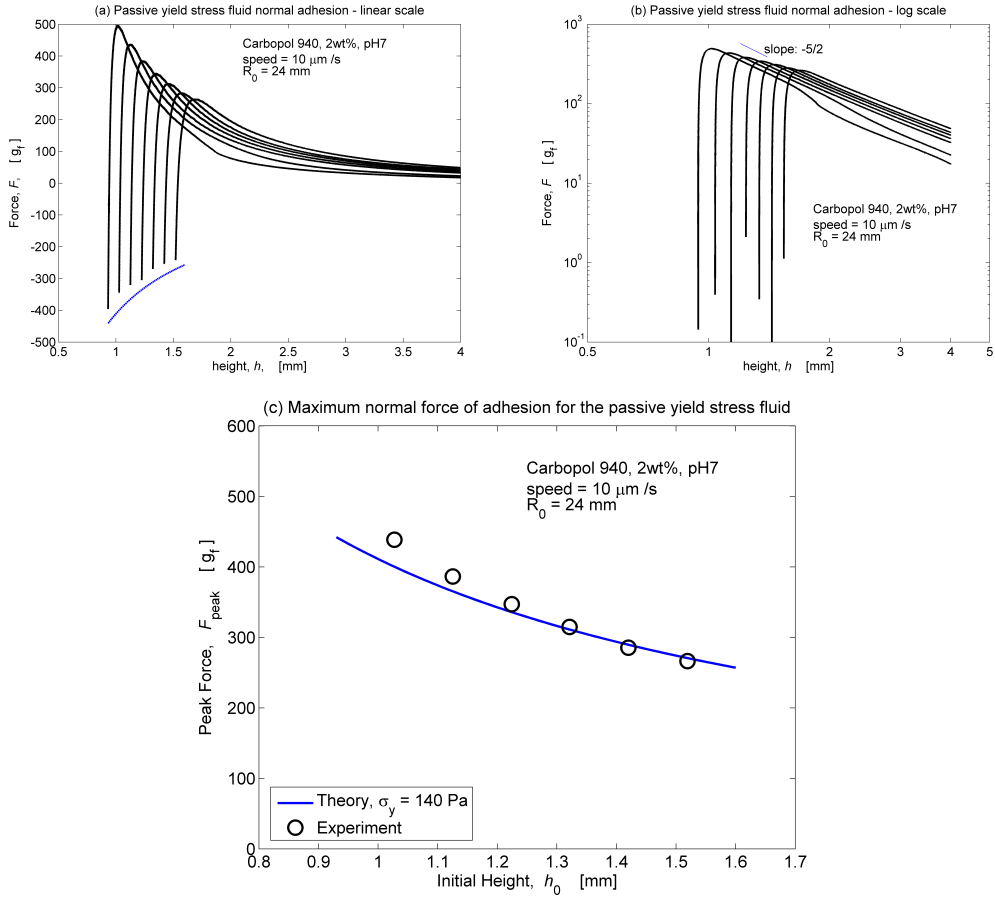


Figure 9-7: Adhesive performance of the passive yield stress fluid, Carbopol 2wt%.

as the height increases. For this constant volume adhesive failure the force can be written as a function of the initial geometry, R_0 , h_0 , and the instantaneous thickness h , by substituting the constant volume constraint, Eq. 9.16, into Eq. 9.8, resulting in

$$F_{\text{YieldStress}} = \frac{2}{3} \pi \sigma_y R_0^3 h_0^{3/2} \frac{1}{h^{5/2}}. \quad (9.18)$$

Notice here that the scaling relationship for constant volume deformation of a perfect plastic material is $F \sim h^{-5/2}$. The log-log plot of Figure 9-7b shows that this scaling relationship indeed holds for these tests. The peak adhesive force (failure force) predicted by this model can be compared with experiment, which is shown in Figure 9-7c for various initial conditions. No fitting parameters are used here, since the geometry is known and the rheology was measured (cf. Figure 9-2). The model coincides well

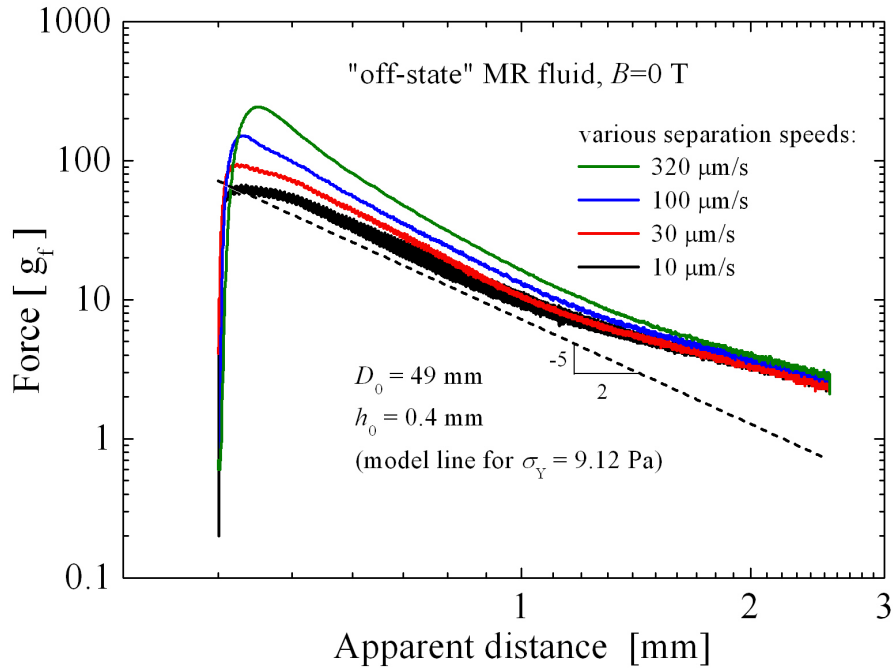


Figure 9-8: Experimentally measured adhesive performance of the “off state” MR fluid. Various separation speeds are examined for the same initial diameter $D_0 = 49$ mm and initial height $h_0 = 0.4$ mm. Here the dashed line is the prediction of the perfect plastic yield stress adhesion model with $\sigma_y = 9.12$ Pa, corresponding to the experimentally measured shear stress at the characteristic shear rate $\dot{\gamma} = 2hR_0/h_0^2 = 3.06$ s $^{-1}$. Top plate is native aluminum surface.

with experimental results, although a small systematic deviation is apparent at the smallest initial gap heights h_0 .

The correspondence between model and experiment for passive fluids provides confidence that the experimental setup can be used to explore the unique situation of field-activated magnetorheological fluid adhesion against non-magnetic substrates.

9.5 Results: Field-responsive magnetorheological fluid

Probe tack tests for the MR fluid are performed as described for the passive fluids. For field-activated tests, there is an additional step of introducing the permanent magnet after the fluid is squeezed to a thickness h_0 . Experimental results for the

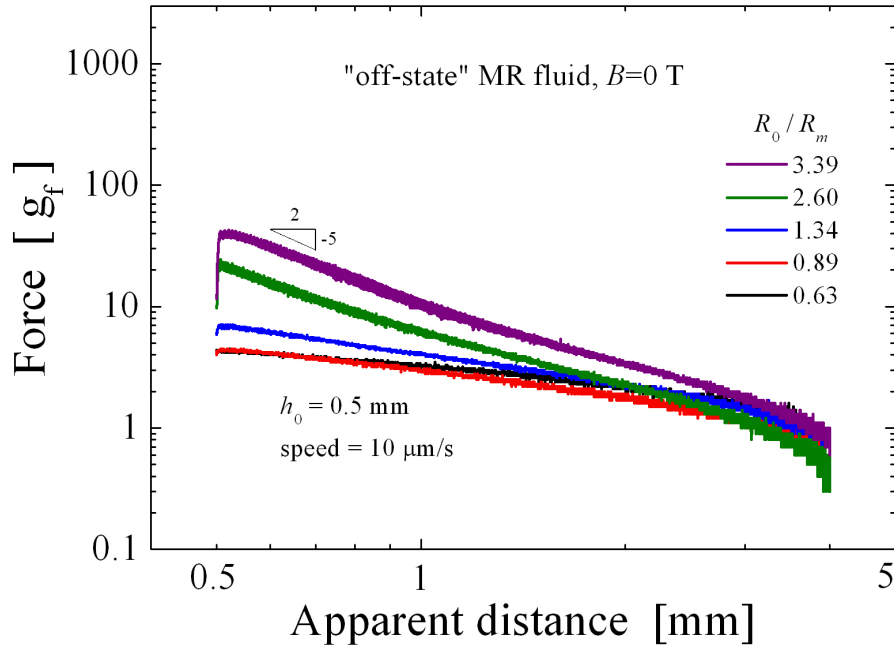


Figure 9-9: Experimentally measured adhesive performance of the “off state” MR fluid. Various initial diameters D_0 examined for the same separation speed $\dot{h} = 10\mu\text{m/s}$ and initial height $h_0 = 0.5\text{ mm}$. Top plate covered with P2000 grit sandpaper. For reference $D_m = 12.7\text{ mm}$, but no magnet was used for these ambient tests.

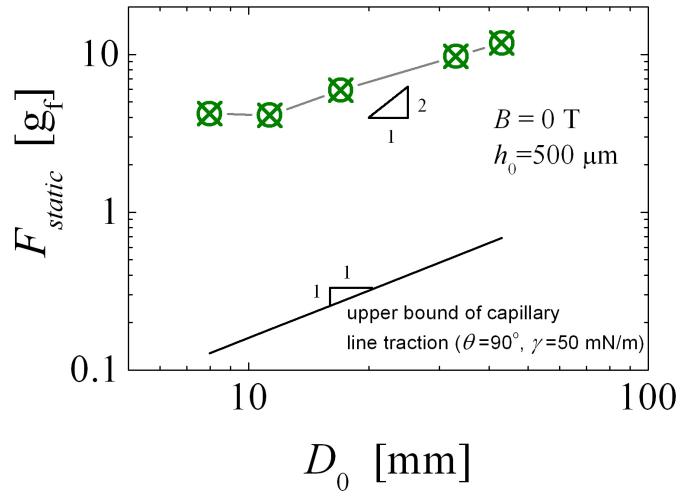


Figure 9-10: Initial static force measurement, for data set shown in Fig. 9-9. Top plate covered with P2000 grit sandpaper. For reference $D_m = 12.7\text{ mm}$, but no magnet was used for these ambient tests.

“off-state” MR fluid (no permanent magnet) are shown in Figures 9-8 – 9-10. The influence of separation speed \dot{h} is shown in Figure 9-8, indicating that the off-state MR fluid is not a perfect plastic material, since the pull-off force slightly increases as a function of pull-off speed. Although the dependence is weak, the slowest pull-off speed available ($\dot{h} = 10\mu\text{m}\cdot\text{s}^{-1}$) is used in all subsequent tests to avoid artifacts related to speed. Figure 9-8 includes a dashed line indicating the model prediction using a yield stress value $\sigma(\dot{\gamma} = 3.1\text{s}^{-1}) = 9.12\text{ Pa}$. This stress (from linear interpolation of experimental data points in Figure 9-3a) corresponds to the characteristic shear-rate for the conditions $\dot{h} = 10\mu\text{m}/\text{s}$, $R_0 = 24.5\text{ mm}$, $h_0 = 0.4\text{ mm}$. The scaling of $F \sim h^{-5/2}$ is also apparent in Figure 9-8.

The influence of initial geometry conditions is shown in Figure 9-9. Here the fluid radius varies while all other parameters are kept constant. The scaling of $F \sim h^{-5/2}$ is again seen here, since the off-state MR fluid has a static yield stress. The initial force can be observed to be non-zero for these tests, and is positive (i.e. the fluid pulls downward on the upper plate). This may result from capillary forces, but the trend does not clearly correspond with any theory (Figure 9-10). For perfectly parallel and smooth surfaces, the predicted force caused by capillary effects is

$$F_{\text{Capillary}} = \gamma \frac{\cos \theta_E}{h/2} \pi R^2 + \gamma \sin \theta_E 2\pi R. \quad (9.19)$$

The maximum line traction is shown in Fig. 9-10, which scales linearly as a function of the diameter, $F \sim D_0$. The measured force is much larger than this, and therefore the initial static force is expected to come primarily from a capillary pressure drop. We observe that the static force does not scale as expected from Eq. 9.19, which predicts $F \sim D_0^2$. This contradiction indicates that either the capillary forces are more complicated (due to contact line pinning, large gaps, or parallelism error), or that the finite yield stress of the fluid plays a role in this initial static force. For analysis of peak adhesive force, we will take $F_{\text{peak}} - F_{\text{static}}$, to eliminate the static force contribution.

The adhesive force is increased by introducing a permanent magnet to activate

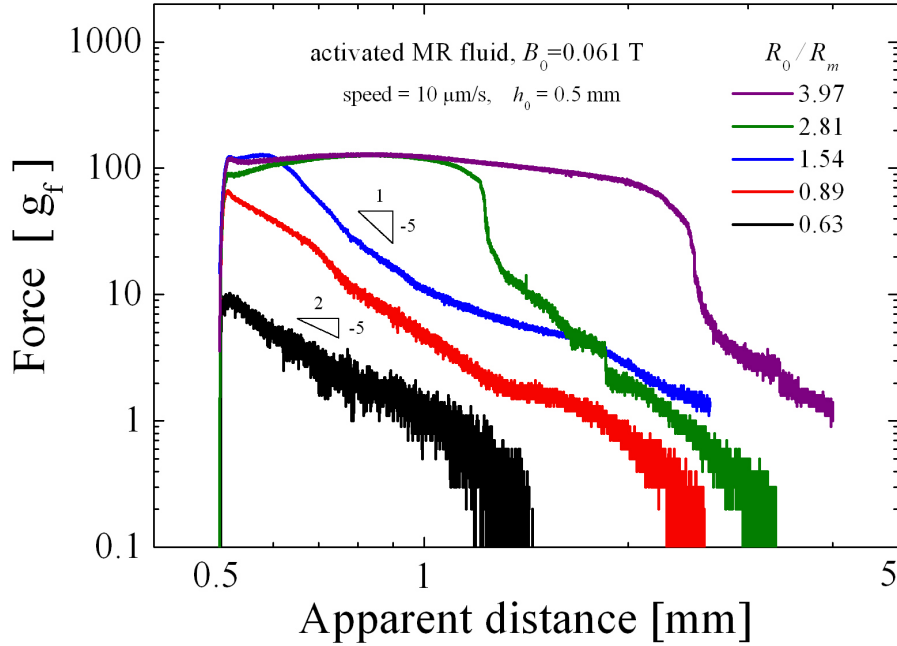


Figure 9-11: Experimentally measured adhesive performance for a moderately activated MR fluid (Alnico 8 disc magnet), $B_{face} = 0.077$ T on face of magnet, but just above bottom plastic surface $B_0 = 0.061$ T. Various initial diameters D_0 examined for the same separation speed $\dot{h} = 10 \mu\text{m/s}$ and initial height $h_0 = 0.5$ mm. The top plate is covered with P2000 grit sandpaper, $D_m = 12.7$ mm.

the magnetorheological fluid. Figure 9-11 shows force vs. displacement curves for the Alnico8 permanent magnet, with $B_0 = 0.061$ T. Each curve corresponds to different values of R_0/R_m , with all other parameters held constant. A line representing $F \sim h^{-5/2}$ is shown for reference, which would be expected to apply for the cases with $R_0/R_m \leq 1$. This is approximately the case, at least initially as the plates begin to pull apart. The maximum adhesive force occurs at the beginning of the pull-off test for these curves. Interestingly, the adhesive force peaks and is approximately constant over a range of h for the curves with $R_0/R_m \geq 1$. This behavior is distinct from the passive yield stress fluid performance, and may be related to the inhomogeneous magnetic field condition, in which a supply of ‘low-activation’ fluid is available to flow into the region with approximately constant magnetic field B_0 .

Experimental measurements with a stronger magnetic field are shown in Figure 9-12, in which $B_0 = 0.296$ T. Just as in Figure 9-11, the fluid radius R_0/R_m is varied

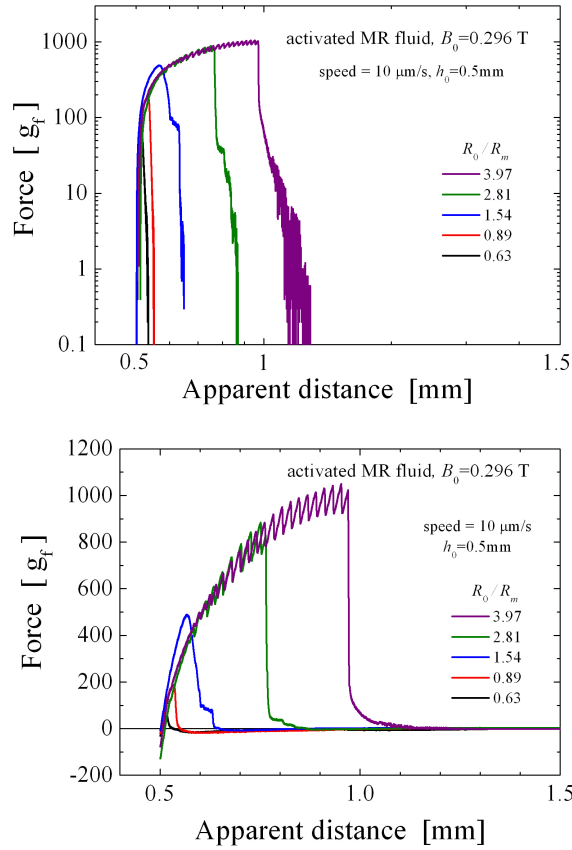


Figure 9-12: Experimentally measured adhesive performance for a strongly activated MR fluid (Neodymium disc magnet), $B_{face} = 0.389$ T on face of magnet, but just above bottom plastic surface $B_0 = 0.296$ T. Various initial diameters D_0 examined for the same separation speed $\dot{h} = 10\mu\text{m/s}$ and initial height $h_0 = 0.5$ mm. The top plate is covered with P2000 grit sandpaper, $D_m = 12.7$ mm. (a) Log-Log plot, (b) Linear-Linear plot of same data, which highlights the iterative sawtooth failure leading up to the peak force (for $R/R_m = 2.81, 3.97$).

while all other experimental parameters are held constant. The force vs. displacement curves for this case are very different than previous observations. In this case the peak stress does not occur near the initial gap height, rather the force grows to a maximum value. Furthermore, a distinct sawtooth pattern can be seen in the curves for $R_0/R_m = 2.81, 3.97$. The linear-linear plot in Figure 9-12b highlights the sawtooth behavior. This sawtooth pattern is extremely repeatable, and performing successive tests on the same sample results in curves that are almost identical, in which the saw tooth portions overlap. The spatial frequency of the sawtooth pattern has been

observed to depend on speed, such that the spatial frequency increases as \dot{h} increases, eventually leading to smooth force vs. displacement curves at a sufficient separation speed \dot{h} . The sawtooth pattern is likely associated with a stick-slip phenomenon, which is correlated with the finite compliance of the instrument. When viewed from below through the transparent bottom plate, the fluid radius R can be observed to “jump” at a frequency which seems to correspond with the sawtooth frequency. The analysis of the sawtooth pattern is kept as future work, but one motivation for such understanding is the fact that a sawtooth pattern may help to indicate the proximity to adhesive failure of a functional device.

The peak adhesive forces from experimental measurements (including other data not shown here) are compared with predictions of the model developed in Section 9.3. Figure 9-13 shows that the models are quantitatively predictive for the case of low to moderate field activation $B_0 < 0.1$ T. The peak force increases as a function of the fluid radius, levels off as $R_0/R_m > 1$, and increases again once the static yield stress becomes significant.

For magnetic activation with higher fields ($B_0 > 0.1$ T), the model of Section 9.3 overpredicts the experimental measurements, as shown in Figure 9-14. Indeed, the experimental force vs. displacement curves (Figure 9-12) show dramatically different behavior than for the low field activation. This is most pronounced by the growth of adhesive force as the gap is increased, and also the dramatic failure near the peak force. It is likely that interfacial failure is occurring with these tests, which is not currently included in the model presented here.

9.5.1 Failure modes and pattern formation with magnetorheological fluid adhesion

In the context of adhesive locomotion, one stark benefit of MR fluids is that very little fluid is left on the substrate under certain circumstances. If adhesive failure occurs while the fluid is activated, then the fluid will be attracted to the magnetic field source and therefore pull away from the underlying substrate. Thus, in contrast

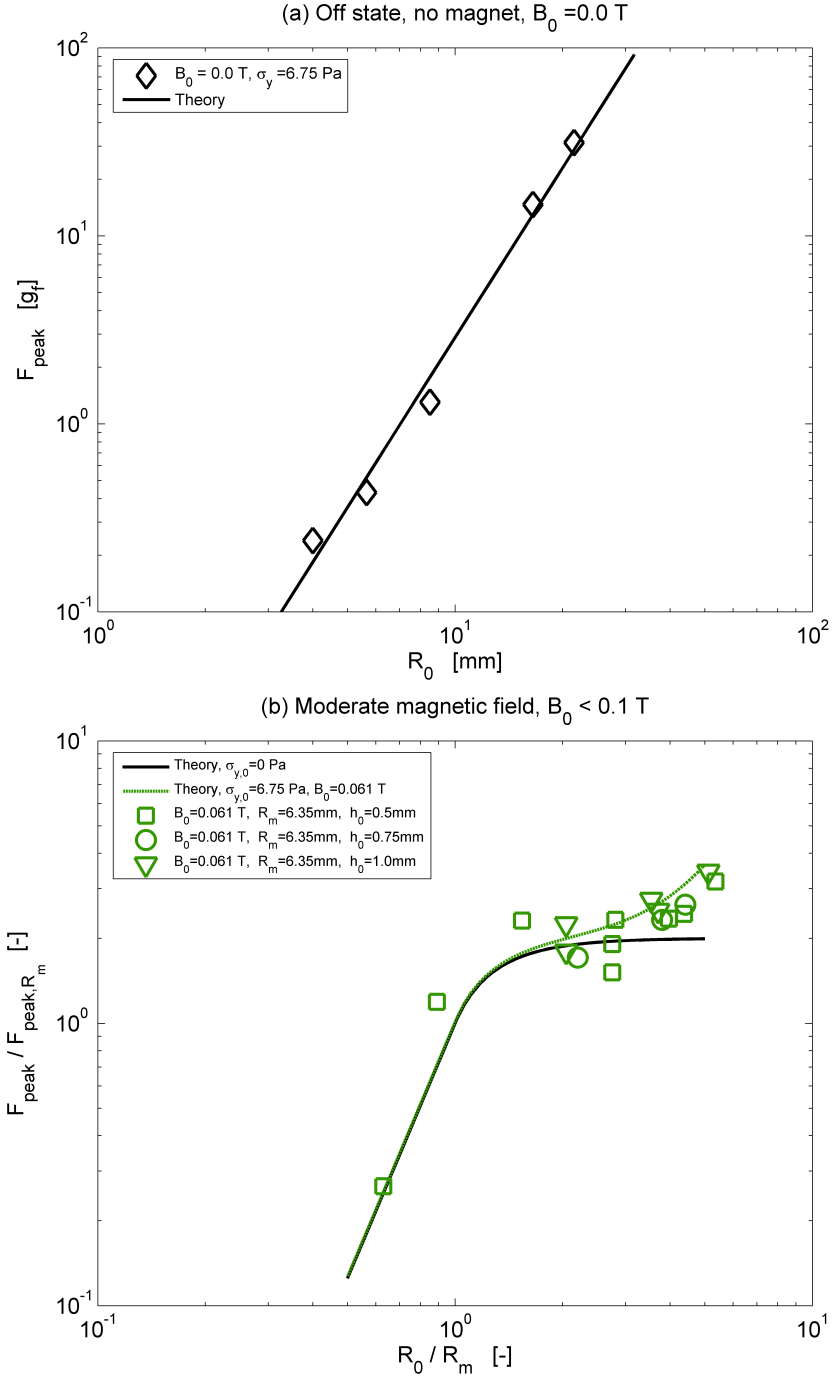


Figure 9-13: Experimentally measured peak adhesive force (open symbols) at moderate magnetic field $B_0 = 0.61$ T, for various initial geometries h_0 and (R_0/R_m) . The theoretical predictions of the current model are given by the lines (see Section 9.3). No fitting parameters are used.

to real snails and slugs, a robotic crawler using MR fluid may be able to leave no slime trail at all!

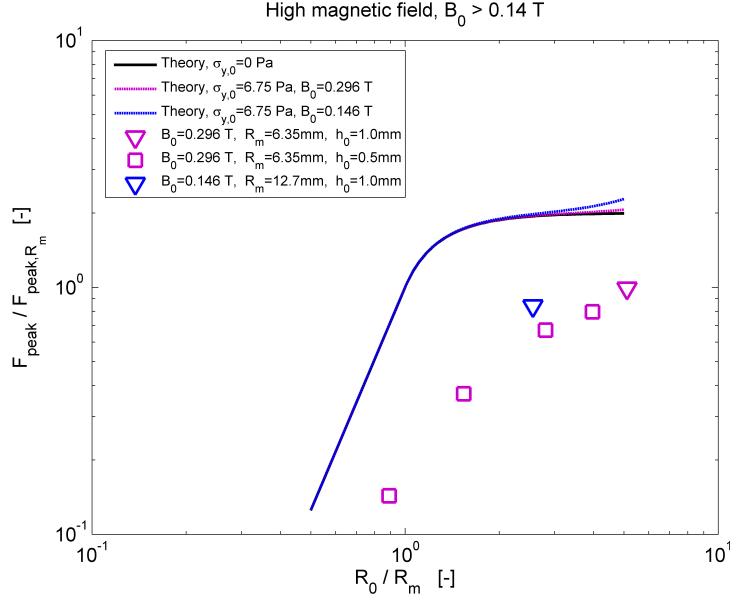


Figure 9-14: Experimentally measured peak adhesive force (open symbols) at high magnetic field $B_0 > 0.14$ T, for various initial geometries h_0 and (R_0/R_m) . The theoretical predictions of the current model are given by the lines (see Section 9.3). No fitting parameters are used. The experimentally measured adhesive strength is systematically lower than predicted by theory for these field strengths.

Furthermore, some very interesting patterns were observed in the fluid which remained on the “foot” surface containing the magnet. Figure 9-15 maps out some regimes in which cusp-like flower petals can be observed on the substrate. These initial observations are currently under investigation and will be the subject of future work.

9.6 Conclusions

In addition to the experimental investigations in this chapter, Fig. 9-16 demonstrates the feasibility of using magnetic fields for on/off adhesion to various nonmagnetic substrates, including aluminum, plastic, wood, ceramic tile, and glass. This adhesion is enabled by a field-responsive viscoplastic magnetorheological fluid. A model of MR fluid adhesion under inhomogeneous magnetic fields has been developed, and quantitatively describes the peak force performance for moderate magnetic field strengths. The reversible adhesion mechanism is fast (sub-second) and allows for “leave low

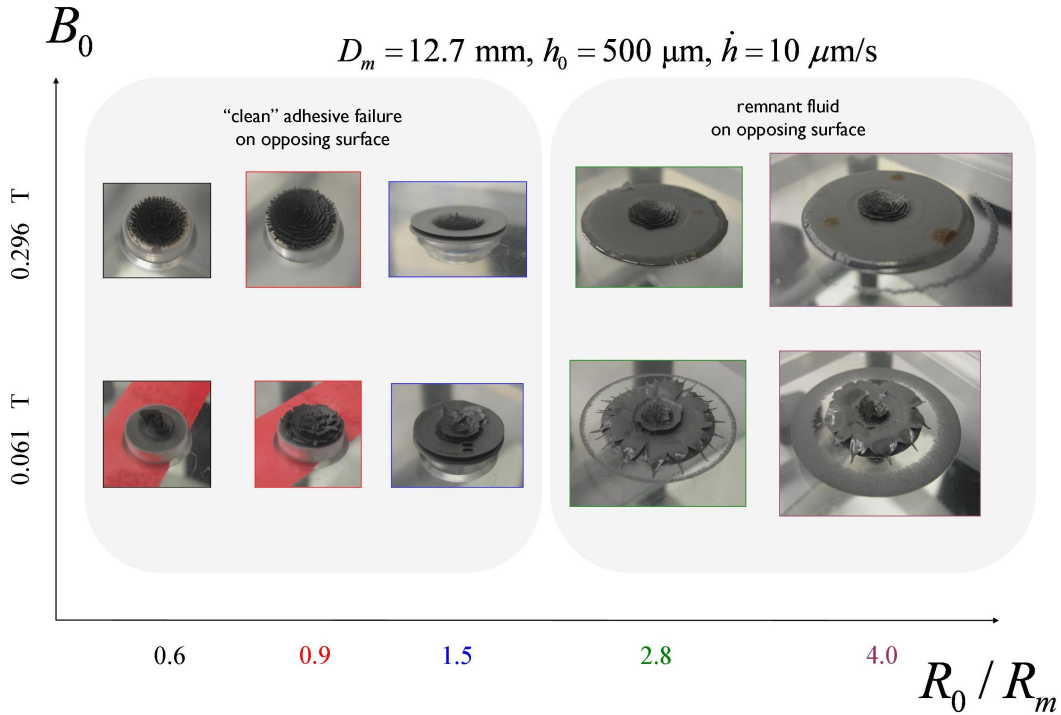


Figure 9-15: Remnant fluid patterns after adhesive failure, for various parameter values B_0 and R_0/R_m . Images shown of the surface containing the permanent magnet. Opposing top surfaces are not shown, which exhibit “clean” failure for $R_0/R_m \leq 1.5$ and remnant fluid rings for $R_0/R_m \geq 2.8$. The “flower” instability is observed for large R_0/R_m and moderate magnetic fields.

trace” adhesion since the adhesive fluid is attracted to the magnetic field source and the adhesive can remain attached to the magnetic “foot” at failure.

Many unexplored parameters still exist for the problem of field-responsive magnetorheological fluid adhesion, such as substrate material, surface roughness, fluid thickness, magnetic field orientation, and other modes of adhesive failure such as peeling. Furthermore, a number of interesting phenomena can be explored in more detail in the future, such as the stick/slip sawtooth waves observed in the force vs. displacement curves with strong magnetic fields, the over-prediction of peak forces for strong magnetic fields, and the “flower” instability which is observed at moderate magnetic field strength. The topic of field-activated MR fluid adhesion should be a rich source of both scientific and engineering development in the future.

MR fluid adhesion with a variety of substrates

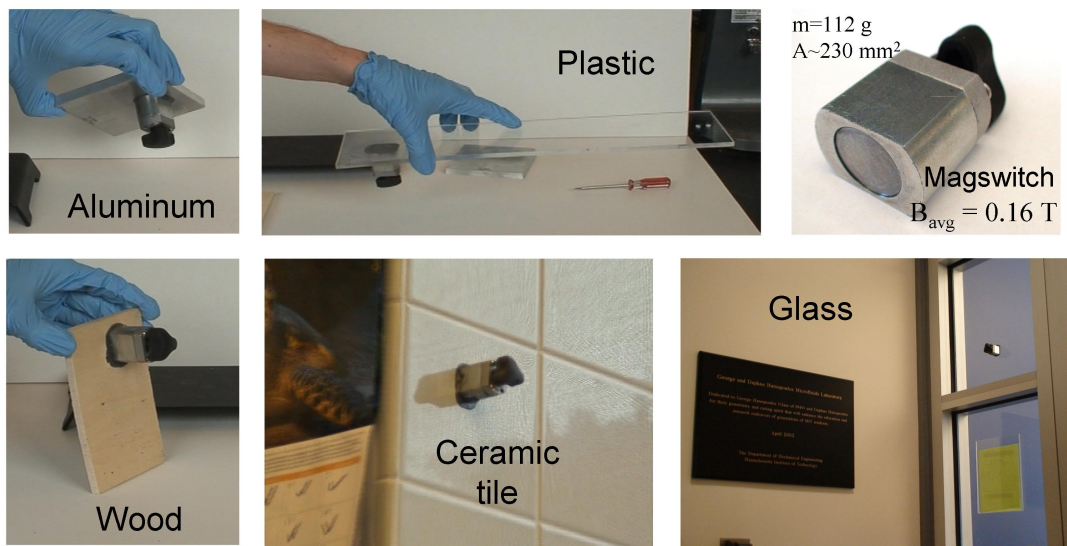


Figure 9-16: Demonstration of using magnetic fields for reversible adhesion to non-magnetic substrates, enabled by a viscoplastic magnetorheological fluid. Surfaces shown are aluminum, plastic, wood, ceramic tile, and glass. The suspended mass, $m = 112 \text{ g}$, is a switchable permanent magnet configuration which creates a magnetic field strength on the order of $B = 0.16 \text{ T}$ over an area of approximately $A \sim 230 \text{ mm}^2$. The holding stress is therefore at least $mg/A \sim 4.8 \text{ kPa}$.

Chapter 10

Conclusions and outlook

The core of this thesis is rheology, which connects multiple aspects of the work including biomechanics and bioinspiration, adhesion science, robotics, field-responsive fluids, measurement theory and techniques, and design. The contributions presented here span the spectrum from theory and modeling to experimental rheometry and demonstrated applications of complex fluids and soft solids. The two questions which have driven these contributions are: “How do we best describe nonlinear viscoelasticity?” and “How can we use nonlinear rheological properties to our advantage?”

The first question of how best to describe nonlinear rheological behavior was primarily addressed by a new theoretical framework and language (or *ontology*) for describing Large Amplitude Oscillatory Shear (LAOS) rheometry. There exists a need for self-consistent, laboratory-independent, low-dimensional descriptions of nonlinear material responses. I have proposed a descriptive language and a set of unambiguous material measures which quantify LAOS responses in such a way (Chapter 2). The scheme provides a physical interpretation of deviations from linear viscoelastic behavior, characterizing elastic and viscous nonlinearities separately, simultaneously, and more thoroughly than currently-reported measures. This is facilitated by interpreting the stress response $\sigma(t)$ as a function of the two orthogonal mechanical inputs of strain $\gamma(t)$ and strain-rate $\dot{\gamma}(t)$, i.e. $\sigma(\gamma(t), \dot{\gamma}(t))$, rather than simply a function of time as is conventionally done with Fourier transform rheology. The analysis can be applied generally to LAOS results using the raw oscillatory data of strain $\gamma(t)$ and stress $\sigma(t)$.

Such data can be analyzed with software developed during this thesis (Chapter 3), which has already been distributed to more than 25 academic and industrial users that have requested the software (contact MITlaos@mit.edu with requests).

The new LAOS framework was used for describing various constitutive models and experimental results (Chapters 4 and 7). In the future, this framework could be applied to the study of many other complex fluids and soft solids, including biopolymer networks, foods, nano-composites, and concentrated suspensions. Extensions of the framework to other large amplitude oscillatory tests were discussed in Chapter 5. This thesis has documented some initial thoughts on the issue of a stress-controlled LAOS framework, including definitions of nonlinear compliances and nonlinear fluidities. The detailed definition of the stress-controlled orthogonal polynomial decomposition remains for future work.

The new LAOS framework presented herein is broadly applicable to any material which can be tested in oscillatory shear, including complex fluids and soft solids, and serves as a complement to the familiar and successful linear viscoelastic framework embodied in the familiar material functions $G'(\omega)$ and $G''(\omega)$. The new measures presented here provide a framework for meaningful nonlinear property measurements that will provide a more rigorous test of constitutive models, and serve as a sensitive probe for comparing and understanding the true nonlinear rheological properties of different materials. This framework can support further refinements in our understanding of structure-property relationships and help researchers and engineers share knowledge about complex nonlinear viscoelastic materials in a clear, concise, and complete way. It is hoped that a better description of nonlinear rheological properties will make these complex materials easier to understand, and therefore easier to use in engineering designs.

The second theme driving this thesis is the use of nonlinear rheological properties to enable new functionalities. Several novel uses of nonlinear rheological properties have been modeled and demonstrated, including snail-like wall climbing using bioinspired yield stress fluids (Chapter 8) and tunable, fast-switching, low-residue adhesion using magnetorheological fluids (Chapter 9). These technologies depend on nonlin-

ear rheological properties to function properly. The feasibility of both concepts was modeled and demonstrated by considering the adhesive materials to be yield stress fluids. The tunable adhesion using magnetorheological fluids is a future research area which is particularly rich. The experiments, models, and feasibility presented here provide a strong foundation for future work, and a number of interesting phenomena have been documented (Chapter 9), however they are yet to be fully explored. Furthermore, it is envisioned that optimization of both applications will necessarily require an advanced understanding of the nonlinear rheological properties, e.g. with the use of the ontology developed in this thesis.

The work presented here provides the means to a better understanding of biological and engineered systems which involve nonlinear viscoelastic materials. This naturally applies to many physiological, processing, and in-use situations. Additionally, complex rheological behavior can be deliberately utilized to enable novel functionality. It is envisioned that future engineered systems will rely on such materials which defy categorization as simply fluid or solid. As such, the description, understanding, and use of nonlinear viscoelastic materials will be of critical importance.

Appendix A

Chebyshev polynomials

The Chebyshev polynomials of the first kind are orthogonal over the domain $[-1,1]$. The $n = 0 - 5$ order polynomials, along with the recursive definition are given below [46].

$$\begin{aligned} T_0(x) &= 1 & T_4(x) &= 8x^4 - 8x^2 + 1 \\ T_1(x) &= x & T_5(x) &= 16x^5 - 20x^3 + 5x \\ T_2(x) &= 2x^2 - 1 & T_{n+1}(x) &= 2xT_n(x) - T_{n-1}(x) \\ T_3(x) &= 4x^3 - 3x \end{aligned} \tag{A.1}$$

The first, third, and fifth order polynomials are shown in Figure A-1. The orthogonality relation is given by

$$\int_{-1}^1 \frac{T_m(x)T_n(x)}{(1-x^2)^{1/2}} dx = \begin{cases} \frac{1}{2}\pi & \text{for } m \neq 0, n \neq 0 \\ \pi & \text{for } m = n = 0 \end{cases} . \tag{A.2}$$

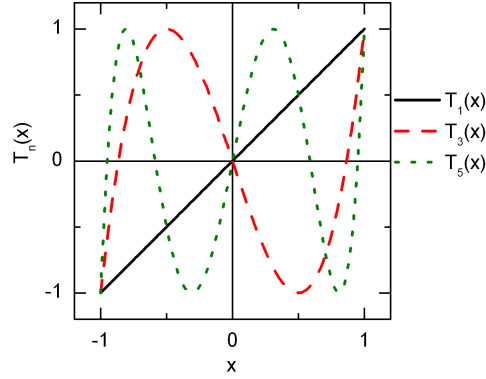


Figure A-1: Chebyshev polynomials of the first kind; plots of the first few odd polynomials.

In this use is made of the identity $T_n(\cos \theta) = \cos(n\theta)$. This can be used to derive the identity for $T_n(\sin \theta)$ by using $\sin \theta = \cos(\pi/2 - \theta)$.

$$\begin{aligned}
 T_n(\sin \theta) &= T_n\left(\cos\left(\frac{\pi}{2} - \theta\right)\right) \\
 &= \cos(n\pi/2 - n\theta) \\
 &= \cos(n\pi/2)\cos(n\theta) + \sin(n\pi/2)\sin(n\theta) \\
 &= \begin{cases} \sin(n\theta)(-1)^{(n-1)/2} & n : \text{odd} \\ \cos(n\theta)(-1)^{n/2} & n : \text{even} \end{cases}
 \end{aligned} \tag{A.3}$$

Appendix B

MATLAB source code

This Appendix includes the MATLAB source code behind the data analysis performed by MITlaos (3). The data processing of MITlaos is based on the processing presented here, however, MITlaos also includes a graphical user interface and a few features which make data analysis easier. For clarity, such additional code associated with the graphical user interface of MITlaos is *not* included here. The source code for automatic batch processing of LAOS results follows.

B.1 JoR_laos_batch_analyze_v2p0.m

The MATLAB script ‘JoR_laos_batch_analyze_v2p0.m’ performs automated batch processing for a collection of LAOS test results, each contained in an individual file. There is no graphical user interface associated with this script. It repeatedly calls ‘JoR_laos_analyze_v3p3.m’ to perform the analysis, and compiles all of the viscoelastic parameters into a single data file.

```
1 % =====
2 % Batch process LAOS analysis
3 % RHEwoldt
4 %
5 % Performs the following functions
6 % * Loads files created with appropriate naming structure
7 % * Combines data from selected files into one matrix
8 % * Writes this large matrix to a single data file
9 %
10 % =====
```

```

11
12
13 clear
14 clc
15
16
17 directory = 'C:\Research\ARES\070123.Micellar_LAOS\RawDataNewNames\ReducedPipkinSpace-NoAxes\'
18
19 %files that end in *.dat are original raw data files
20 files = dir(strcat(directory, '*.dat'))
21 savefileE = strcat(directory, '070608-CPyCL-ReduxDATA-Eparameters.txt')
22 savefileV = strcat(directory, '070608-CPyCL-ReduxDATA-Vparameters.txt')
23
24 for i=1:length(files)
25
26     %==== START Extract omega from file name
27     for k=1:length(files(i).name)-4
28         if 'omega'==files(i).name(k:k+4)
29             omeganum = k;
30         end
31     end
32     Swl0 = files(i).name(omeganum+5:omeganum+6);
33     Sw00p10 = files(i).name(omeganum+8:omeganum+9);
34
35     omega = str2num(Swl0) + str2num(Sw00p10)/100
36     %==== END Extract omega from file name
37
38     data = JoR_laos_analyze_v3p3(strcat(directory, files(i).name), omega);
39     data_all_e(i,:) = data(1,:);
40     data_all_v(i,:) = data(2,:);
41
42     if i==round(length(files)/2)
43         msgbox('5 second pause in middle of processing')
44         pause(5)
45     end
46
47 end
48
49 fid = fopen(savefileE, 'w');
50 fprintf(fid, 'omega   gam_0   G1''   GM''   GL''   e3   G3''   S');
51 fprintf(fid, '\n');
52 for m=1:length(data_all_e(:,1))
53     fprintf(fid, '%d %d %d %d %d %d %d %d \n', data_all_e(m,:));
54 end
55 fclose(fid)
56
57
58 fid = fopen(savefileV, 'w');
59 fprintf(fid, 'omega   gam_0   G1''''   EtaM''   EtaL''   v3   G3''''   T');
60 fprintf(fid, '\n');
61 for m=1:length(data_all_v(:,1))
62     fprintf(fid, '%d %d %d %d %d %d %d %d \n', data_all_v(m,:));
63 end
64 fclose(fid)
65
66
67 open(savefileE)
68 open(savefileV)

```

B.2 JoR_laos_analyze_v3p3.m

The MATLAB script 'JoR_laos_analyze_v3p3.m' performs automated data analysis on an individual LAOS test waveform.

```

1 function datasave = JoR_laos_analyze_v3p3(loadfile, omega)
2 % =====
3 % Processing of LAOS raw data (automatically, through batch process call)
4 % RHEwoldt February 2007
5 %
6 % Skeleton of script from Janmey_Analysis.m (RHE Feb 2007)
7 %
8 % Performs the following functions
9 % *Loads a single data file at a given strain amplitude and frequency
10 % *User selects window of data to analyze
11 % *FT analysis for multiple cycles of data
12 % *Calculates moduli: Gn', Gn'', M, L, S, S.2 based on FT decomposition
13 % *Plots/Prints various figures as desired
14 % *Saves data files (if desired) of filtered [gamma, tau, tau_e]
15 % and filtered [gammadot, tau, tau_v]
16 % =====
17
18 % % % % % % % clear %kept here for debugging purposes
19 % % % % % % % clc
20
21 %%%%%%%%%%%%%%%%%%%%%%%%%%%%%%%%%%%%%%%%%%%%%%%%%%%%%%%%%%%%%%%
22 % ===== START Manual Input Required =====
23 %%%%%%%%%%%%%%%%%%%%%%%%%%%%%%%%%%%%%%%%%%%%%%%%%%%%%%%%%%%%%%%
24
25 % time gamma gammadot tau_xy tau_xx-tau_yy (Dumbbell data setup)
26 timecol = 0; %Column in data file containing time [s]
27 % (set to 0 if no time available)
28 straincol = 1; %Column in data file containing strain[-]
29 stresscol = 2; %Column in data file containing stress[Pa]
30
31 % windowing percentage
32 winpctfront = 5; %set to 0 for no window, or chose percent of front/back
33 winpctback = 5; % of data range to ignore
34
35 %START Plotting & Saving On/Off Switches:
36 SaveData = 1;
37
38 POver = 0; %Overview plot, includes Lissajous, Chebyshev
39 POverPrint = 0; % unfiltered data, FT spectrum, Viscoelastic Quantifiers
40
41 PPipLiss = 1; % Lissajous plots for creating Pipkin space (NO AXES!)
42
43
44 PLeg = 0; % Legednre polynomial decomposition
45 PLegPrint = 0; %
46
47 PCheb = 0; % Chebyshev
48 PChebPrint = 0; %
49
50 PFT = 0; % Full Raw Data with FT decomposition
51 PFTPrint = 0; %
52
53 PLiss = 0; % Lissajous curves of Raw, & Recon
54 PLissPrint = 0; %
55
56 PGeo = 0; % Geo Interp Only
57 PGeoPrint = 0;
58 %END Plotting & Saving On/Off Switches
59
60
61
62
63 %%%===== FOR BATCH PROCESSING =====
64 pathname='';
65 file = loadfile;
66 % % % % % % % directory = 'C:\Research\Carreau\'; %Start directory for OPEN dialog
67 % % % % % % % [file, pathname] = uigetfile(strcat(directory,'*dat'), 'Pick a Data File')
68 %%%===== FOR BATCH PROCESSING =====

```

```

69
70
71 % Filenames of saved files
72 savefile_img_TTe_Strn = strcat(pathname,file,'.Fig.TTe-Strn.tiff');
73 savefile_img_TTv_Rate = strcat(pathname,file,'.Fig.TTv-Rate.tiff');
74 savefile_vStrain = strcat(pathname,file,'.1cycle-vStrain.txt');
75 savefile_vRate = strcat(pathname,file,'.1cycle-vRate.txt');
76 savefile_VEparameters = strcat(pathname,file,'.VEparameters.txt');
77
78 % % % % % % % % winput = inputdlg('Angular Frequency [rad/s'],'Numerical Input');
79 % % % % % % % % w = str2num(cell2mat(winput))
80 w = omega;
81
82 m=11; % Number of "Higher Harmonics" to consider
83 PPQC=100; %Points Per Quarter Cycle for FT reconstruction
84
85 contents = importdata(strcat(pathname,file));
86
87 if size(contents) == 1
88     data = contents.data;
89 else
90     data = contents;
91 end
92
93 % this code was used when manually selecting the input range
94 % % % if timecol  $\neq$  0
95 % % %     H=figure;plot(data(:,timecol),data(:,straincol)/max(data(:,straincol)),'b');
96 % % %     hold on;plot(data(:,timecol),data(:,stresscol)/max(data(:,stresscol)),'r');
97 % % %     xlabel('Time [s]');axis tight
98 % % % else
99 % % %     H=figure;plot(data(:,straincol),'b');hold on;plot(data(:,stresscol),'r');
100 % % %     xlabel('Index')
101 % % % end
102 % % % legend('Strain','Stress','Location','SouthEast');ylabel('Arbitrary');
103 % % %
104 % % % title('Click to Select TWO Bounds of Input Limits, then Press >ENTER')
105 % % %
106 % % % %Window data from Front and Back, enter percentage to discard:
107 % % % winbox = ginput;
108 % % % close(H)
109 % % %
110 % % % if length(winbox(:,1))  $\neq$  2
111 % % %     errordlg('Start Over: Please select TWO points for windowing data')
112 % % %     return
113 % % % end
114
115 %%%%%%%%%%%%%%%%%%%%%%%%%%%%%%%%%%%%%%%%%%%%%%%%%%%%%%%%%%%%%%%%%%%%%%%%%
116 % ===== END Manual Input Required =====
117 %%%%%%%%%%%%%%%%%%%%%%%%%%%%%%%%%%%%%%%%%%%%%%%%%%%%%%%%%%%%%%%%%%%%%%%%%
118
119
120 %%%%%%%%%%%%%%%%%%%%%%%%%%%%%%%%%%%%%%%%%%%%%%%%%%%%%%%%%%%%%%%%%%%%%%%%%
121 % ===== START Data Preprocessing =====
122 %%%%%%%%%%%%%%%%%%%%%%%%%%%%%%%%%%%%%%%%%%%%%%%%%%%%%%%%%%%%%%%%%%%%%%%%%
123
124 % Data Windowing
125 winstart=round(length(data(:,straincol))*winpctfront/100 + 1);
126 winstop = round(length(data(:,straincol)) - length(data(:,straincol))*winpctback/100);
127
128 % this code was used when manually selecting the input range
129 % % % % % % % if timecol  $\neq$  0
130 % % % % % % % % Find index of selected times for windowing
131 % % % % % % % % TimeWin = winbox(:,1);
132 % % % % % % % % winstart = find(min(TimeWin) < data(:,timecol),1);
133 % % % % % % % % if max(TimeWin) > max(data(:,timecol))
134 % % % % % % % %     winstop = length(data(:,timecol));
135 % % % % % % % % else
136 % % % % % % % %     winstop = find(max(TimeWin) < data(:,timecol),1);

```



```

137 % % % % % % % % end
138 % % % % % % % % else
139 % % % % % % % % %Identify selected indices for windowing
140 % % % % % % % % RowWin = round(winbox(:,1));
141 % % % % % % % % winstart = min(RowWin);
142 % % % % % % % % if winstart <1
143 % % % % % % % %     winstart = 1;
144 % % % % % % % % end
145 % % % % % % % % winstop = max(RowWin);
146 % % % % % % % % if winstop > length(data(:,straincol)) %if index exceeds dimensions
147 % % % % % % % %     winstop = length(data(:,straincol)); %set stop index to end
148 % % % % % % % % end
149 % % % % % % % % end
150
151 %Extract selected data
152 if timecol ≠0
153     time_uneven = data(winstart:winstop,timecol);
154     disp_uneven = data(winstart:winstop,straincol); %Strain data - Raw
155     torque_uneven = data(winstart:winstop,stresscol); %Stress data - Raw
156
157     %Force strain & stress data to be linearly space in time
158     time=linspace(time_uneven(1),time_uneven(end),length(time_uneven));
159     disp = interp1(time_uneven,disp_uneven,time);
160     torque = interp1(time_uneven,torque_uneven,time);
161 else
162     disp = data(winstart:winstop,straincol); %Strain data - Raw
163     torque = data(winstart:winstop,stresscol); %Stress data - Raw
164 end
165
166 clear data
167
168 % Trim data to be an integer number of cycles, starting with SINE strain
169 [gam, tau, Ncycles]= cycletrim(disp, torque);
170
171 %%%%%%%%%%%%%%%%%%%%%%%%%%%%%%%%%%%%%%%%%%%%%%%%%%%%%%%%%%%%%%%%%%%%%%%%%
172 % ===== END Data Preprocessing =====
173 %%%%%%%%%%%%%%%%%%%%%%%%%%%%%%%%%%%%%%%%%%%%%%%%%%%%%%%%%%%%%%%%%%%%%%%%%
174
175
176 %%%%%%%%%%%%%%%%%%%%%%%%%%%%%%%%%%%%%%%%%%%%%%%%%%%%%%%%%%%%%%%%%%%%%%%%%
177 % ===== START FT Decomposition and Reconstruction =====
178 %%%%%%%%%%%%%%%%%%%%%%%%%%%%%%%%%%%%%%%%%%%%%%%%%%%%%%%%%%%%%%%%%%%%%%%%%
179
180 [A0, AnS, BnS]= FTtrig(tau); %will neglect A0 in reconstruction
181 [gA0, gAnS, gBnS]= FTtrig(gam); %will neglect gA0 in reconstruction
182
183 % gam_0 = abs(gBn(Ncycles)); %identify strain amplitude
184 %acknowledge possible phase shift, but neglect h.o.t.
185 gam_0 = sqrt( gBnS(Ncycles)^2 + gAnS(Ncycles)^2 );
186 Δ = atan( gAnS(Ncycles) / gBnS(Ncycles)); %raw signal phase shift
187
188 for q=1:length(AnS) %Create NOT SHIFTED Fourier coefficients
189     An(q) = AnS(q)*cos(q*Δ/Ncycles) - BnS(q)*sin(q*Δ/Ncycles);
190     Bn(q) = BnS(q)*cos(q*Δ/Ncycles) + AnS(q)*sin(q*Δ/Ncycles);
191 end
192 % Now proceed as it was before (Introduction of UNshift in v3p3 RHE) %
193
194
195 PPC=4*PPQC; %Points Per Cycle
196 TP=6*PPQC+1; %Total Points: Points for Three Half-Cycles plus one for overlap
197
198 gam_recon=zeros(PPC,1);
199 for q=1:PPC %sum for each point in time, 1 full cycle, no overlap
200     gam_recon(q) = gam_0*sin(2*pi*(q-1)/PPC);
201 end
202 %make gam_recon 1.5 cycles with 1 point overlap
203 gam_recon = [gam_recon; gam_recon(1:2*PPQC+1)];
204

```

```

205 % w (omega) is currently a MANUAL input
206 % strain-rate is equal to omega*strain-shifted-1/4-cycle
207 gamdot_recon=w*gam_recon(PPQC+1:PPQC+PPC); %One cycle of gamdot
208 gamdot_recon=[gamdot_recon; gamdot_recon(1:2*PPQC+1)]; %make 1.5 cycles
209 % figure;plot(gamdot_recon);hold on;plot(gam_recon)
210
211 %% Obsolete, now that I'm reconstructing strain data too.
212 % T=round(length(gam)/Ncycles) %integer number of data points per cycle
213 % Tnum = length(gam)/Ncycles; %decimal number of data points per cycle
214
215 tau_recon = zeros(PPC,1); %initialize tau_recon (m harmonics included)
216 FTtau_e = zeros(PPC,1);
217 FTtau_v = zeros(PPC,1);
218
219 tau_recon1 = zeros(PPC,1); %initialize tau_recon1 (1st harmonic only)
220 tau_recon3 = zeros(PPC,1); %initialize tau_recon3 (1st & 3rd Harmonics)
221
222 for q=1:PPC %sum for each point in time for 1 full cycle, no overlap
223     for p=1:2:m %m:total number of harmonics to consider
224         %sum over ODD harmonics only
225         tau_recon(q) = tau_recon(q) + Bn(Ncycles*p)*sin(p*2*pi*(q-1)/PPC) ...
226             + An(Ncycles*p)*cos(p*2*pi*(q-1)/PPC);
227
228         FTtau_e(q) = FTtau_e(q) + Bn(Ncycles*p)*sin(p*2*pi*(q-1)/PPC);
229         FTtau_v(q) = FTtau_v(q) + An(Ncycles*p)*cos(p*2*pi*(q-1)/PPC);
230
231     end
232     for p=1:3 %Now just the first 3 harmonics
233         tau_recon3(q) = tau_recon3(q) + Bn(Ncycles*p)*sin(p*2*pi*(q)/PPC) ...
234             + An(Ncycles*p)*cos(p*2*pi*(q)/PPC);
235     end
236     for p=1 %Now just the first harmonic
237         tau_recon1(q) = tau_recon1(q) + Bn(Ncycles*p)*sin(p*2*pi*(q)/PPC) ...
238             + An(Ncycles*p)*cos(p*2*pi*(q)/PPC);
239     end
240 end
241 %make FTtau_* have one point overlap
242 FTtau_e(PPC+1,1)=FTtau_e(1);
243 FTtau_v(PPC+1,1)=FTtau_v(1);
244 %make tau_recon* 1.5 cycles with 1 point overlap
245 tau_recon = [tau_recon; tau_recon(1:2*PPQC+1)];
246 tau_recon3 = [tau_recon3; tau_recon3(1:2*PPQC+1)];
247 % figure;plot(gam_recon, tau_recon)
248
249 %%%%%%%%%%%%%%%%%%%%%%%%%%%%%%%%%%%%%%%%%%%%%%%%%%%%%%%%%%%%%%%%%%%%%%%%%
250 % ===== END FT Decomposition and Reconstruction =====
251 %%%%%%%%%%%%%%%%%%%%%%%%%%%%%%%%%%%%%%%%%%%%%%%%%%%%%%%%%%%%%%%%%%%%%%%%%
252
253 %%%%%%%%%%%%%%%%%%%%%%%%%%%%%%%%%%%%%%%%%%%%%%%%%%%%%%%%%%%%%%%%%%%%%%%%%
254 % ===== START Geo Interp Calculation =====
255 % Using FT reconstruction signals.
256 % FT_recon must be made such that
257 % strain=0 exactly after each 1/2 cycle,
258 % and strain=max exactly after each 1/2 cycle
259 %%%%%%%%%%%%%%%%%%%%%%%%%%%%%%%%%%%%%%%%%%%%%%%%%%%%%%%%%%%%%%%%%%%%%%%%%
260 tau_v = zeros(PPC,1);
261 tau_e = zeros(PPC,1);
262 for k=1:PPC
263     %viscous stress, odd wrt strain-rate
264     tau_v(k) = 0.5 * (tau_recon(k) - tau_recon(TP+1-k));
265     %elastic stress, odd wrt strain
266     tau_e(k) = 0.5 * (tau_recon(k) - tau_recon(PPC+2-k));
267 end
268 tau_v(PPC+1)=tau_v(1); % create overlap points
269 tau_e(PPC+1)=tau_e(1); %
270
271 %
272 % START Polynomial Decomposition

```

```

273 %
274 % Create domains for elastic and viscous, from [-1:+1]
275 Xe=gam.recon(3*PPQC+1:5*PPQC+1)/gam_0; %gam.recon is 1.5 cycles
276 Xv=gamdot.recon(2*PPQC+1:4*PPQC+1)/(gam_0*w); %gamdot.recon is 1.5 cycles
277 % Create corresponding input function from Geo. Interp. decomposition
278 fe=[tau_e(3*PPQC+1:4*PPQC); tau_e(1:PPQC+1)]; %tau_e is 1 cycle
279 fv=tau_v(2*PPQC+1:4*PPQC+1); %tau_v is 1 cycle
280
281 %
282 % Legendre Polynomial Decomposition
283 % Use Xe, fe
284 % and Xv, fv
285 % for inputs
286 Cn_e = legendre_decompose(fe,15,Xe);
287 Cn_v = legendre_decompose(fv,15,Xv);
288
289 % Legendre Polynomial Reconstruction
290 %
291 % Elastic
292 fe_L1 = legendre_compose(Cn_e(1),Xe);
293 fe_L3 = legendre_compose(Cn_e(1:3),Xe);
294 fe_L5 = legendre_compose(Cn_e(1:5),Xe);
295
296 % Viscous
297 fv_L1 = legendre_compose(Cn_v(1),Xv);
298 fv_L3 = legendre_compose(Cn_v(1:3),Xv);
299 fv_L5 = legendre_compose(Cn_v(1:5),Xv);
300
301
302 %
303 % Chebyshev Polynomial Decomposition
304 % Use Xe, fe
305 % and Xv, fv
306 % for inputs
307 An_e = chebyshev_decompose(fe,15,Xe);
308 An_v = chebyshev_decompose(fv,15,Xv);
309 %
310 % Chebyshev Polynomial Reconstruction
311 % NOTE: An(1) is ZEROETH order polynomial
312 % this is currently different than Cn from Legendre decomposition
313 %
314 % Elastic
315 fe_C1 = chebyshev_compose(An_e(1:2),Xe);
316 fe_C3 = chebyshev_compose(An_e(1:4),Xe);
317 fe_C5 = chebyshev_compose(An_e(1:6),Xe);
318 % Viscous
319 fv_C1 = chebyshev_compose(An_v(1:2),Xv);
320 fv_C3 = chebyshev_compose(An_v(1:4),Xv);
321 fv_C5 = chebyshev_compose(An_v(1:6),Xv);
322
323 %%%%%%%%%%%%%%%%%%%%%%%%%%%%%%%%%%%%%%%%%%%%%%%%%%%%%%%%%%%%%%%%%%%%%%%%%
324 % ===== END Geo Interp Calculation =====
325 %%%%%%%%%%%%%%%%%%%%%%%%%%%%%%%%%%%%%%%%%%%%%%%%%%%%%%%%%%%%%%%%%%%%%%%%%
326
327 %%%%%%%%%%%%%%%%%%%%%%%%%%%%%%%%%%%%%%%%%%%%%%%%%%%%%%%%%%%%%%%%%%%%%%%%%
328 % ===== START Calculate Moduli: Gn', Gn'', M, L, S, S2 =====
329 %
330 % Note: An: cosine term > Gn''
331 % Bn: sine terms > Gn'
332 % since we're looking at stress response after a SINE STRAIN INPUT
333 %%%%%%%%%%%%%%%%%%%%%%%%%%%%%%%%%%%%%%%%%%%%%%%%%%%%%%%%%%%%%%%%%%%%%%%%%
334
335 if Bn(Ncycles)>0 %ensure that G_1' is positive
336 Gp = Bn/gam_0; %G' from sine terms
337 else
338 Gp = -Bn/gam_0;
339 end
340

```

```

341 if An(Ncycles) > 0 %ensure that G_1'' is positive
342     Gpp = An/gam_0; %G'' from cosine terms
343 else
344     Gpp = -An/gam_0;
345 end
346
347 N=length(An); % number of available harmonics
348 G_complex = zeros(N,1);
349 G_compNORM = zeros(N,1);
350 for j=1:N
351     G_complex(j)=(Gp(j)^2+Gpp(j)^2)^0.5;
352 end
353 for j=1:N
354     G_compNORM(j) = G_complex(j)/G_complex(Ncycles);
355     %max intensity occurs at Ncycles frequency
356 end
357
358 M=0;
359 Lo=0;
360 EtaM = 0;
361 EtaL = 0;
362 for p=1:2:m
363     M = M + p*Gp(Ncycles*p);
364     Lo = Lo + Gp(Ncycles*p)*(-1)^( (p-1)/2);
365
366     EtaM = EtaM + (1/w)*(p)*Gpp(Ncycles*p)*(-1)^( (p-1)/2);
367     EtaL = EtaL + (1/w)*Gpp(Ncycles*p);
368 end
369 M;
370 L=Lo;
371
372 S=L/M;
373 EtaT=EtaL/EtaM;
374
375 S2=(L-M)/L;
376 %%%%%%%%%%%%%%%%%%%%%%%%%%%%%%%%%%%%%%%%%%%%%%%%%%%%%%%%%%%%%%%%%%%%%%%%%
377 % ===== END Calculate Moduli =====
378 %%%%%%%%%%%%%%%%%%%%%%%%%%%%%%%%%%%%%%%%%%%%%%%%%%%%%%%%%%%%%%%%%%%%%%%%%
379
380
381
382 %%%%%%%%%%%%%%%%%%%%%%%%%%%%%%%%%%%%%%%%%%%%%%%%%%%%%%%%%%%%%%%%%%%%%%%%%
383 % ===== START Plotting =====
384 %%%%%%%%%%%%%%%%%%%%%%%%%%%%%%%%%%%%%%%%%%%%%%%%%%%%%%%%%%%%%%%%%%%%%%%%%
385
386 % The .tiff plots of TTe_vStrn
387 % and TTV_vRate
388 % are NOT optional, because they are needed to generate the full Pipkin
389 % Space plot
390
391 if PPipLiss ==1
392
393     I=figure;
394     set(I,'PaperUnits','inches')
395     set(I,'Units','inches')
396     set(I,'Position',[10 4 1 1]);
397     set(I,'PaperSize',[1 1])
398     set(I,'PaperPosition',[0.0 0.0 1 1]);
399 %     axes('Position',[0.01 0.01 0.775 0.815],'Parent',I)
400     axes('Position',[0.01 0.01 0.85 0.85],'Parent',I)
401     H=plot(gam_0*Xe,fe,'r—',gam_recon(1:PPC),tau_recon(1:PPC),'b',[0],[0],'k+');
402     axis off; axis square; axis tight;
403     set(H,'LineWidth',1)
404     set(H,'MarkerSize',3)
405
406     Xlimits = get(gca,'XLim')
407     Ylimits = get(gca,'YLim')
408     set(gca,'XLim',Xlimits*1.05) %loosen axis limits; too tight and the trim linewidth!

```

```

409     set(gca,'YLim',Ylimits*1.05)
410     strtau0 = num2str(abs(max(tau_recon)))
411     if strtau0(1) == 0
412         %Force 3 significant figures: I expect tau is always less than 100, and larger than 0.1
413         strtau0end = 5;
414     else
415         strtau0end = 4;
416     end
417     text(0,1.2*Ylimits(2),strcat(strtau0(1:strtau0end),' Pa'),'FontSize',8)
418
419     print('-dtiff','-r600',savefile_img_TTe_Strn)
420     close(I)
421
422
423
424     I=figure;
425     set(I,'PaperUnits','inches')
426     set(I,'Units','inches')
427     set(I,'Position',[10 4 1 1]);
428     set(I,'PaperSize',[1 1])
429     set(I,'PaperPosition',[0.0 0.0 1 1]);
430     axes('Position',[0.01 0.01 0.85 0.85],'Parent',I)
431     H=plot(gam_0*w*Xv,fv,'r—',gamdot_recon(1:PPC),tau_recon(1:PPC),'b',[0],[0],'k+');
432     axis off; axis square; axis tight;
433     set(H,'LineWidth',1)
434     set(H,'MarkerSize',3)
435
436     Xlimits = get(gca,'XLim')
437     Ylimits = get(gca,'YLim')
438     set(gca,'XLim',Xlimits*1.05) %loosen axis limits; too tight and the trim linewidth!
439     set(gca,'YLim',Ylimits*1.05)
440     strtau0 = num2str(abs(max(tau_recon)))
441     text(0,1.2*Ylimits(2),strcat(strtau0(1:strtau0end),' Pa'),'FontSize',8)
442     print('-dtiff','-r600',savefile_img_TTv_Rate)
443     close(I)
444
445
446 end
447
448 % Plot Legendre polynomial decomposition of Geo. Interp. Decomposition
449 %
450 if PLeg==1
451
452     I=figure;
453     set(I,'Position',[100 100 1020 840]);
454     set(I,'PaperPosition',[0.2500 2.5000 12.0000 9.6000]);
455     subplot(2,2,1);
456     H=plot(gam_recon(1:PPC),tau_recon(1:PPC),'b');set(H,'LineWidth',2)
457     hold on;
458     H=plot(gam_0*Xe,fe,'r');set(H,'LineWidth',2)
459     title(file)
460     H=plot(gam_0*Xe,fe_L1,'k');set(H,'LineWidth',2)
461     H=plot(gam_0*Xe,fe_L3,'g');set(H,'LineWidth',2)
462     H=plot(gam_0*Xe,fe_L5,'m');set(H,'LineWidth',2)
463     axis tight
464     xlabel('Strain \gamma [-]')
465     ylabel('Elastic Stress \tau_e [Pa]')
466     legend('\tau_{total}','\tau_e Total','Legendre Recon: 1','Legendre Recon: 1+3',...
467           'Legendre Recon: 1+3+5','Location','SouthEast')
468     subplot(2,2,2); bar(Cn_e/gam_0)
469     title('Legendre Decomposition of \tau_{elastic}')
470     xlabel('Polynomial Order, n')
471     ylabel('C_n')
472     pos = get(gca,'YLim')/7;
473     text(length(Cn_e)/2,4*pos(2),strcat('G_1'==',num2str(Gp(Ncycles)),' Pa'))
474     text(length(Cn_e)/2,3*pos(2),strcat('M=',num2str(M),' Pa'))
475     text(length(Cn_e)/2,2*pos(2),strcat('L=',num2str(L),' Pa'))
476     subplot(2,2,3);

```

```

477 H=plot(gamdot_recon(1:PPC),tau_recon(1:PPC),'b');set(H,'LineWidth',2)
478 hold on;
479 H=plot(gam_0*w*Xv,fv,'r');set(H,'LineWidth',2)
480 H=plot(gam_0*w*Xv,fv_L1,'k');set(H,'LineWidth',2)
481 H=plot(gam_0*w*Xv,fv_L3,'g');set(H,'LineWidth',2)
482 H=plot(gam_0*w*Xv,fv_L5,'m');set(H,'LineWidth',2)
483 axis tight
484 xlabel('Strain-Rate [s^{-1}]')
485 ylabel('Viscous Stress \tau_v [Pa]')
486 legend('\tau_{total}','\tau_v Total','Legendre Recon: 1','Legendre Recon: 1+3',...
487 'Legendre Recon: 1+3+5','Location','SouthEast')
488 subplot(2,2,4); bar(Cn_e/(gam_0*w))
489 title('Legendre Decomposition of \tau_{viscous}')
490 xlabel('Polynomial Order, n')
491 ylabel('C_n')
492 pos = get(gca,'YLim')/7;
493 text(length(Cn_e)/2,4*pos(2),strcat('G_1=' ,num2str(Gpp(Ncycles)), ' Pa'))
494
495 if PlegPrint==1
496     print('-djpeg',strcat(pathname,file,'Fig_Legendre.jpg'))
497 end
498
499 end
500
501
502
503 % Plot Chebyshev polynomial decomposition of Geo. Interp. Decomposition
504 %
505 if PCheb == 1
506
507     I=figure;
508     set(I,'Position',[100 100 1020 840]);
509     set(I,'PaperPosition',[0.2500 2.5000 12.0000 9.6000]);
510     subplot(2,2,1);
511     H=plot(gam_recon(1:PPC),tau_recon(1:PPC),'b');set(H,'LineWidth',2)
512     hold on;
513     H=plot(gam_0*Xe,fe,'r');set(H,'LineWidth',2)
514     title(file)
515     H=plot(gam_0*Xe,fe_C1,'k');set(H,'LineWidth',2)
516     H=plot(gam_0*Xe,fe_C3,'g');set(H,'LineWidth',2)
517     H=plot(gam_0*Xe,fe_C5,'m');set(H,'LineWidth',2)
518     axis tight
519     xlabel('Strain \gamma [-]')
520     ylabel('Elastic Stress \tau_e [Pa]')
521     legend('\tau_{total}','\tau_e Total','Chebyshev Recon: 1','Chebyshev Recon: 1+3',...
522     'Chebyshev Recon: 1+3+5','Location','SouthEast')
523     subplot(2,2,2); bar([0:1:length(An_e)-1],An_e/gam_0)
524     set(gca,'XLim',[-1 length(An_e)])
525     title('Chebyshev Decomposition of \tau_{elastic}')
526     xlabel('Polynomial Order, n')
527     ylabel('C_n')
528     pos = get(gca,'YLim')/7;
529     text(length(An_e)/2,4*pos(2),strcat('G_1=' ,num2str(Gp(Ncycles)), ' Pa'))
530     text(length(An_e)/2,3*pos(2),strcat('M=' ,num2str(M), ' Pa'))
531     text(length(An_e)/2,2*pos(2),strcat('L=' ,num2str(L), ' Pa'))
532     subplot(2,2,3);
533     H=plot(gamdot_recon(1:PPC),tau_recon(1:PPC),'b');set(H,'LineWidth',2)
534     hold on;
535     H=plot(gam_0*w*Xv,fv,'r');set(H,'LineWidth',2)
536     H=plot(gam_0*w*Xv,fv_C1,'k');set(H,'LineWidth',2)
537     H=plot(gam_0*w*Xv,fv_C3,'g');set(H,'LineWidth',2)
538     H=plot(gam_0*w*Xv,fv_C5,'m');set(H,'LineWidth',2)
539     axis tight
540     xlabel('Strain-Rate [s^{-1}]')
541     ylabel('Viscous Stress \tau_v [Pa]')
542     legend('\tau_{total}','\tau_v Total','Chebyshev Recon: 1','Chebyshev Recon: 1+3',...
543     'Chebyshev Recon: 1+3+5','Location','SouthEast')
544     subplot(2,2,4); H=bar([0:1:length(An_e)-1],An_v/(gam_0));

```

```

545     set(gca,'XLim',[-1 length(An_e)])
546     title('Chebyshev Decomposition of \tau_{viscous}')
547     xlabel('Polynomial Order, n')
548     ylabel('C_n')
549     pos = get(gca,'YLim')/7;
550     text(length(An_e)/2,4*pos(2),strcat('G_1"',num2str(Gpp(Ncycles)), ' Pa'))
551
552     if PChebPrint == 1
553         print('-djpeg',strcat(pathname,file,'_Fig_Chebyshev.jpg'))
554     end
555
556 end
557
558
559 % Plot Geo. Interp. decomposition, along with Total stress & partially
560 % reconstructed stress
561 if PGeo == 1
562
563     I=figure;
564     set(I,'Position',[100 100 560 840]);
565     set(I,'PaperPosition',[0.2500 2.5000 6.0000 9.6000]);
566     subplot(2,1,1);
567     H=plot(gam_recon(1:PPC),tau_recon(1:PPC),'b');set(H,'LineWidth',2)
568     hold on;
569     H=plot(gam_recon(1:PPC),tau_recon3(1:PPC),'g');set(H,'LineWidth',2)
570     H=plot(gam_recon(1:PPC),tau_e(1:PPC),'r');set(H,'LineWidth',2)
571     title(file)
572     xlabel('Strain [-]');ylabel('(Elastic) Shear Stress');
573     axis tight
574     legend(strcat('\tau_{total} from FT-recon: ',num2str(m),' harmonics'),...
575            '\tau_{total} from FT-recon: 1&3 harmonics','\tau_{elastic} from Geo. Interp.',...
576            'Location','SouthEast')
577
578     subplot(2,1,2);
579     H=plot(gamdot_recon(1:PPC),tau_recon(1:PPC),'b');set(H,'LineWidth',2)
580     hold on;
581     H=plot(gamdot_recon(1:PPC),tau_recon3(1:PPC),'g');set(H,'LineWidth',2)
582     H=plot(gamdot_recon(1:PPC),tau_v(1:PPC),'r');set(H,'LineWidth',2)
583     title('From Fourier Transform Reconstruction using Odd Harmonics')
584     xlabel('Strain-Rate [s^{-1}]');ylabel('(Viscous) Shear Stress');
585     axis tight
586     legend('see above','see above','\tau_{viscous} from Geo. Interp.','Location','SouthEast')
587
588     if PGeoPrint == 1
589         print('-djpeg',strcat(pathname,file,'_Fig_GeoInterp.jpg'))
590     end
591
592 end
593
594
595
596 % Plot FT Decomposition
597 %
598 if PFT == 1
599
600     dw = w/Ncycles;
601     wn = [dw:dw:N*dw];
602
603
604     I=figure;
605     set(I,'Position',[100 100 560 840]);
606     set(I,'PaperPosition',[0.2500 2.5000 6.0000 9.6000]);
607
608     subplot(4,1,1); H=plot(tau);
609     title(file)
610     % set(H,'LineWidth',1)
611     xlabel('Time [arb]'); ylabel('Stress [Pa]');
612

```

```

613 subplot(4,1,2); plot(wn,G_compNORM)
614 set(gca,'YScale','log','YTick',[1e-5 1e-4 1e-3 1e-2 1e-1 1e0],'YLim',[1e-5 2])
615 xlabel('\omega [rad.s^{-1}]')
616 ylabel('|G_n*|/|G_1*|')
617 title('Full FT Spectrum')
618
619 subplot(4,1,3); bar(wn(1:Ncycles*m),Gp(1:Ncycles*m))
620 title(strcat('FT Spectrum: ',num2str(m),' cycles'))
621 xlabel('\omega [rad.s^{-1}]')
622 ylabel('G_n' [Pa])
623 subplot(4,1,4); bar(wn(1:Ncycles*m),Gpp(1:Ncycles*m))
624 xlabel('\omega [rad.s^{-1}]')
625 ylabel('G_n" [Pa]')
626
627 if PFTPrint == 1
628     print('-djpeg',strcat(pathname,file,'_Fig_FT.jpg'))
629 end
630
631 end
632
633
634
635
636 % Plot "1 cycle" of data from FT reconstruction: v. Time & Lissajous
637 %
638 if PLiss == 1
639
640     C1 = 1; %Which raw data cycle to plot
641     T=round(length(gam)/Ncycles); %integer number of data points per cycle
642     Tnum = length(gam)/Ncycles; %decimal number of data points per cycle
643     tarb_raw = [1:T]*(PPC/Tnum); %for co-plotting raw data and FT.recon data
644     ibeg = round(Tnum*(C1-1)+1); %index to start plotting raw data
645     ifin = ibeg + T -1; % " " " stop " " " " "
646
647     I=figure;
648     set(I,'Position',[100 100 560 840]);
649     set(I,'PaperPosition',[0.2500 2.5000 6.0000 9.5000]);
650
651     subplot(2,1,1); H=plot(tau_recon(1:PPC),'b'); set(H,'LineWidth',2)
652     hold on
653     H=plot(tau_recon3(1:PPC),'g');
654     set(H,'LineWidth',2)
655     H=plot(tau_recon1(1:PPC),'k'); set(H,'LineWidth',2)
656     H=plot(tarb_raw,tau(ibeg:ifin),'r'); set(H,'LineWidth',2)
657     axis tight
658     xlabel('Time [arb]'); ylabel('Shear Stress [Pa]')
659     legend(strcat('FT-recon: ',num2str(m),' harmonics'),'FT-recon: 1&3 harmonics',...
660             'FT-recon: 1st harmonic','Raw Data - One cycle')
661     title(file)
662
663
664     subplot(2,1,2);
665     % H=plot(gam(ibeg:ifin),tau_recon,'b');set(H,'LineWidth',2)
666     H=plot(gam_recon,tau_recon,'b');set(H,'LineWidth',2)
667     hold on
668     H=plot(gam_recon(1:PPC),tau_recon3(1:PPC),'g');set(H,'LineWidth',2)
669     H=plot(gam_recon(1:PPC),tau_recon1(1:PPC),'k');set(H,'LineWidth',2)
670     H=plot(gam(ibeg:ifin),tau(ibeg:ifin),'r');set(H,'LineWidth',1.5)
671     axis tight
672     xlabel('Strain [-]'); ylabel('Shear Stress [Pa]')
673     legend(strcat('FT-recon: ',num2str(m),' harmonics'),'FT-recon: 1&3 harmonics',...
674             'FT-recon: 1st harmonic','Raw Data - One cycle'...
675             ,'Location','NorthWest')
676     pos = get(gca,'YLim')/7;
677     text(0,2*pos(1),strcat('G_1'='',num2str(Gp(Ncycles)),' Pa',' ', 'G_1'='',...
678             num2str(Gpp(Ncycles)),' Pa'))
679     text(0,3*pos(1),strcat('M=',num2str(M),' Pa'))
680     text(0,4*pos(1),strcat('L=',num2str(L),' Pa'))

```



```

681     text(0,5*pos(1),strcat('S=',num2str(S)))
682     text(0,6*pos(1),strcat('S_2=',num2str(S2)))
683
684     if P_Lissajous == 1
685         print('-djpeg',strcat(pathname,file,'_Fig_Lissajous.jpg'))
686     end
687
688 end
689
690
691
692 % Overview Plot
693 %
694 if P_Over == 1
695
696     I=figure;
697     set(I,'Position',[100 100 1176 840]);
698     set(I,'PaperPosition',[0.0 0.0 14.0 10.0]);
699     subplot(2,3,1);
700     H=plot(gam_recon(1:PPC),tau_recon(1:PPC),'b');set(H,'LineWidth',2)
701     hold on;
702     H=plot(gam_0*Xe,fe,'r');set(H,'LineWidth',2)
703     H=plot(gam_0*Xe,fe_C3,'g');set(H,'LineWidth',2)
704     axis tight
705     xlabel('Strain \gamma [-]')
706     ylabel('(Elastic) Stress \tau_e [Pa]')
707     legend('\tau_{total}','\tau_e Total','Chebyshev 1+3','Location','SouthEast')
708
709     subplot(2,3,4); bar([0:1:length(An_e)-1],An_e/gam_0)
710     set(gca,'XLim',[-1 length(An_e)])
711     title('Chebyshev Coeff: \tau_{elastic}')
712     xlabel('Polynomial Order, n')
713     ylabel('e_n')
714     pos = get(gca,'YLim')/7;
715     maxpos = find(max(abs(pos))); %index of maximum YLim (1:negative, 2: positive)
716     strGlp = num2str(Gp(Ncycles));
717     strM = num2str(M); strL = num2str(L); strS = num2str(S);
718     strE3 = num2str(An_e(4)/gam_0);
719     text(length(An_e)/2.5,6*pos(maxpos),strcat('G_1'='',strGlp,' Pa'))
720     text(length(An_e)/2.5,5*pos(maxpos),strcat('G_M'='',strM,' Pa'))
721     text(length(An_e)/2.5,4*pos(maxpos),strcat('G_L'='',strL,' Pa'))
722     text(length(An_e)/2.2,3*pos(maxpos),strcat('e_3 =',strE3,' Pa'))
723     text(length(An_e)/2.2,2*pos(maxpos),strcat('S = G_M'/G_L' =',strS,' '))
724
725     subplot(2,3,2);
726     H=plot(gamdot_recon(1:PPC),tau_recon(1:PPC),'b');set(H,'LineWidth',2)
727     hold on;
728     H=plot(gam_0*w*Xv,fv,'r');set(H,'LineWidth',2)
729     H=plot(gam_0*w*Xv,fv_C3,'g');set(H,'LineWidth',2)
730     axis tight
731     xlabel('Strain-Rate [s^{-1}]')
732     ylabel('(Viscous) Stress \tau_v [Pa]')
733     title(file,'FontSize',20)
734     legend('\tau_{total}','\tau_v Total','Chebyshev 1+3','Location','SouthEast')
735
736     subplot(2,3,5); H=bar([0:1:length(An_v)-1],An_v/(gam_0));
737     set(gca,'XLim',[-1 length(An_e)])
738     title('Chebyshev Coeff: \tau_{viscous}')
739     xlabel('Polynomial Order, n')
740     ylabel('v_n')
741     pos = get(gca,'YLim')/7;
742     strEta1p = num2str(Gpp(Ncycles)/w);
743     strEtaM = num2str(EtaM); strEtaL=num2str(EtaL); strEtaT = num2str(EtaT);
744     strV3 = num2str(An_v(4)/gam_0);
745     text(length(An_e)/2.5,6*pos(2),strcat('\eta_1'='G.1"/\omega=',strEta1p,' Pa.s'))
746     text(length(An_e)/2.5,5*pos(2),strcat('\eta_M'='',strEtaM,' Pa.s'))
747     text(length(An_e)/2.5,4*pos(2),strcat('\eta_L'='',strEtaL,' Pa.s'))
748     text(length(An_e)/2,3*pos(2),strcat('v_3 =',strV3,' Pa.s'))

```

```

749     text(length(An_e)/2,2*pos(2),strcat('T = \eta_M'/'\eta_L' = ',strEtaT, ' '))
750
751     subplot(2,3,3);
752     H=plot(tau/max(tau)); set(H, 'LineWidth',2)
753     hold on;
754     H=plot(gam/gam_0*0.5, 'r—'); set(H, 'LineWidth',2)
755     set(gca, 'YLim', [-1.1 +1.1])
756     xlabel('Time [arb]'); ylabel('Scaled \tau(t) , \gamma(t) [-]');
757     legend('\tau(t)', '\gamma(t)', 'Location', 'SouthEast')
758
759     dw = w/Ncycles;
760     wn = [dw:dw:N*dw];
761
762     subplot(2,3,6); plot(wn,G_compNORM)
763     set(gca, 'YScale', 'log', 'YTick', [1e-5 1e-4 1e-3 1e-2 1e-1 1e0], 'YLim', [1e-5 2])
764     xlabel('\omega [rad.s^{-1}]')
765     ylabel('|G_n*|/|G_1*|')
766     title('Full FT Spectrum')
767
768     if POverPrint == 1
769         print('-djpeg',strcat(pathname,file, '.Fig_Overview.jpg'))
770     end
771
772 end
773
774 %%%%%%%%%%%%%%%%%%%%%%%%%%%%%%%%%%%%%%%%%%%%%%%%%%%%%%%%%%%%%%%%%%%%%%%%%
775 % =====          STOP Plotting          =====
776 %%%%%%%%%%%%%%%%%%%%%%%%%%%%%%%%%%%%%%%%%%%%%%%%%%%%%%%%%%%%%%%%%%%%%%%%%
777
778
779
780
781 %%%%%%%%%%%%%%%%%%%%%%%%%%%%%%%%%%%%%%%%%%%%%%%%%%%%%%%%%%%%%%%%%%%%%%%%%
782 % =====          START Data Save          =====
783 %%%%%%%%%%%%%%%%%%%%%%%%%%%%%%%%%%%%%%%%%%%%%%%%%%%%%%%%%%%%%%%%%%%%%%%%%
784
785 datasave = [w, gam_0, Gp(Ncycles),      M,      L, An_e(4)/gam_0, Gp(3*Ncycles) , S;
786            w, gam_0, Gpp(Ncycles), EtaM, EtaL, An_v(4)/gam_0, Gpp(3*Ncycles), EtaT ];
787
788 if SaveData ==1
789     % save the strain & stress & strain-rate waveforms for future plotting;
790     % save one cycle + 1 point to ensure overlap when plotting Lissajous curves
791
792     %% Strain/Stress/ElasticStress data file
793     dlmwrite(savefile.vStrain,[gam_recon(1:PPC+1) tau_recon(1:PPC+1) tau_e], 'delimiter', ',')
794
795     %% Strain-rate/Stress/ViscousStress data file
796     dlmwrite(savefile.vRate,[gamdot_recon(1:PPC+1) tau_recon(1:PPC+1) tau_v], 'delimiter', ',')
797
798     %     fid = fopen(savefile.VEparameters, 'w');
799     %     fprintf(fid, 'omega, gam_0, G1''(G1'''), GM''(EtaM''), GL''(EtaL''), e3(v3), G3''(G3'''), S(T)');
800     %     fprintf(fid, '\n');
801     %     fprintf(fid, '%d %d %d %d %d %d %d %d \n', w, gam_0, Gp(Ncycles),      M, ...
802     %     L, An_e(4)/gam_0, Gp(3*Ncycles) , S);
803     %     fprintf(fid, '%d %d %d %d %d %d %d %d \n', w, gam_0, Gpp(Ncycles), EtaM, ...
804     %     EtaL, An_v(4)/gam_0, Gpp(3*Ncycles), EtaT );
805     %     fclose(fid)
806     %
807
808 end
809 %%%%%%%%%%%%%%%%%%%%%%%%%%%%%%%%%%%%%%%%%%%%%%%%%%%%%%%%%%%%%%%%%%%%%%%%%
810 % =====          END Data Save          =====
811 %%%%%%%%%%%%%%%%%%%%%%%%%%%%%%%%%%%%%%%%%%%%%%%%%%%%%%%%%%%%%%%%%%%%%%%%%

```

B.3 cycletrim.m

```
1 function [istrain, istress, N]= cycletrim(gamma,tau)
2 % =====
3 % Extract integer numer of strain and stress data, starting with sine
4 % strain
5 %
6 % RHEwoldt February 2007
7 %
8 % [istrain, istress, N]= cycletrim(gamma,tau)
9 %
10 % VARIABLES
11 %   gamma      strain data input, arbitrary length
12 %   tau        stress data input, arbitrary length
13 %   istrain    (integer # of cycles, sine wave start)
14 %   istress    (aligned with strain)
15 %   N          # of cycles contained
16 %
17 % SEQUENCE
18 %   (fit sine wave to strain data) – not yet implemented
19 %   find zeros in strain signal
20 %   identify first starting point of sine wave
21 %   identify final point of sine wave
22 %   output trimmed data
23 % =====
24
25
26 % %%% Diagnostic testing initialization
27 % %
28 % clear
29 % clc
30 % directory = 'C:\Research\ARES\Janmey\';
31 % files = dir(strcat(directory,'*.txt'));
32 % data=load(strcat(directory,files(8).name));
33 % norm = data(500:end,1); %Normal force data
34 % gamma = data(500:end,2)/100; %Strain data is expected to be units of percent,
35 %                               % so force it to be unitless
36 % tau = data(500:end,3); %Stress data
37 % %
38 % %%%%%%%%%%%%%%%%%%%%%%%%%%%%%%%%%%%%%%%%%%%%%%%%%%%%%%%%%%%%%%%%%%%%%%%%%
39
40
41 N=length(gamma);
42
43 k=0; %k is a counter for the number of times gamma changes sign
44 sign_gam = sign(gamma);
45 for i=1:N-1
46     if sign_gam(i) ≠ sign_gam(i+1)
47         k=k+1;
48         d_zero(k)=i+1; %index location after sign change
49     end
50 end
51
52
53 % if the sign changed, and the previous point was NEGATIVE (or ZERO)
54 % then it's the beginning of the sine wave
55
56 if gamma(d_zero(1)-1) ≤ 0
57     istart = d_zero(1);
58     init = 1;
59 else if gamma(d_zero(2)-1) ≤ 0
60     istart = d_zero(2);
61     init = 2;
62 else
63     errordlg('Something is wrong with istart')
```

```

64 end
65 end
66
67
68 lgth = length(d.zero);
69
70 if gamma(d.zero(lgth)-1) < 0
71     istop = d.zero(lgth)-1;
72     fin = lgth;
73 else if gamma(d.zero(lgth-1)-1) < 0
74     istop = d.zero(lgth-1)-1;
75     fin = lgth-1;
76     else
77         errordlg('Something is wrong with istop')
78     end
79 end
80
81 istrain = gamma(istart:istop);
82 istress = tau(istart:istop);
83 N = (fin-init)/2;
84
85 if N==round(N)
86     %Do nothing
87 else
88     errordlg('Something is wrong with N')
89 end

```

B.4 FTtrig.m

```

1 function [A0, An, Bn]= FTtrig(f)
2 % =====
3 % Find trigonometric Fourier Series components from FFT:
4 %  $f = A_0 + \sum_n (A_n \cos(n*2*\pi*t/T) + B_n \sin(n*2*\pi*t/T))$ 
5 %
6 % RHEwoldt February 2007
7 %
8 % [A0, An, Bn]= FTtrig(f)
9 %
10 % VARIABLES
11 % f          vector to be transformed
12 % A0         essentially mean(f)
13 % An         cosine terms
14 % Bn         sine terms
15 %
16 % SEQUENCE
17 % force input to have EVEN number of data points (reqd for fft.m)
18 % take FFT > complex vector results
19 % extract trigonometric terms from complex vector
20 % =====
21
22
23 if int16(length(f)/2) == length(f)/2
24     %do nothing
25 else
26     %trim last data point to force even number of data points
27     %f MUST HAVE EVEN NUMBER OF DATA POINTS!
28     d=f; % d is placeholder
29     clear f
30     f = d(1:length(d)-1);
31     clear d
32 end
33
34 n=length(f);
35 N=n/2; %N will be the number of harmonics to consider

```

```

36
37 Fn(n)=zeros; %initialize complex transform vector
38           % this will make it a ROW vector
39           % which is necessary for combination later
40
41 sizeof = size(f);
42 if sizeof(1) == 1 %if ROW vector
43     Fn = fft(f); %let Fn be ROW vector
44 else
45     frow = f';
46     Fn = fft(frow); %compute FFT Fn=[ low > high | high < low ]
47           %force input to fft to be ROW vector
48 end
49 Fn_new = [conj(Fn(N+1))  Fn(N+2:end)  Fn(1:N+1)];
50 %rearrange values such that: Fn_new = [ high < low | low > high ]
51
52 Fn_new(:) = Fn_new(:)/n; %scale results
53
54 A0 = Fn_new(N+1);
55 An = 2*real(Fn_new(N+2:end)); %cosine terms
56 Bn = -2*imag(Fn_new(N+2:end)); %sine terms

```

B.5 legendre_decompose.m

```

1 function [Cn]= legendre_decompose(F,N,X)
2 % =====
3 % Find Legendre Polynomial components of input data vector:
4 % f = C1*P1(x) + C2*P2(x) + C3*P3(x) + ...
5 %
6 % RHEwoldt February 2007
7 %
8 % [Cn]= legendre_decompose(F,N)
9 %
10 % *Assumes F occupies the domain [-1 : +1]
11 % with an arbitrary number of data points
12 % *Uses trapz.m to calculate integrals
13 %
14 % INPUT VARIABLES
15 %     F: vector of data, in domain [-1:1]
16 %     N: degree of desired Legendre Polynomial decomposition
17 %
18 % OUTPUT VARIABLE
19 %     Cn: vector of Legendre coefficients
20 %
21
22
23 % % Following lines for diagnostic purposes only
24 % F = fe;
25 % N = 11;
26 % X = Xe;
27
28 if nargin < 3,
29     % Make X (input range) linear spaced and same length as F
30     X=linspace(-1,1,length(F));
31 end
32
33 % F must be a row vector. Change if necessary
34 if length(F(1,:))==1 %if there is only 1 column
35     d=F'; clear F
36     F=d ; clear d
37 end
38
39
40

```

```

41 Cn = zeros(N,1); %initialize vector of Legendre coefficients
42
43 for i=1:N
44
45     clear P      % These are temporary placeholders within the loop
46     clear CDv   %
47     clear Cv    %
48
49     P=legendre(i,X);
50
51     CDn = trapz(X, P(1,:).^2); %calculate denominator integral
52     Cn(i) = 1/CDn * trapz(X, P(1,:).*F);
53
54 end

```

B.6 legendre_compose.m

```

1 function [f,X]= legendre_compose(Cn,X)
2 % =====
3 % Construct Legendre Polynomial components into data vector:
4 % f = C1*P1(x) + C2*P2(x) + C3*P3(x) + ...
5 %
6 % RHEwoldt February 2007
7 %
8 % [f,X]= legendre_compose(Cn)
9 %
10 %
11 % INPUT VARIABLE
12 %     Cn: vector of Legendre coefficients
13 %     m: number of data points desired in output vector
14 %     (OPTIONAL: default is 2001)
15 %
16 % OUTPUT VARIABLE
17 %     f: reconstructed data vector (using all available Cn components)
18 %     x: corresponding input vector [-1 : +1]
19 %
20
21 if nargin < 2,
22     % Make X vector linear spaced, 2001 pts
23     X=linspace(-1,1,2001);
24 end
25
26
27 N=length(Cn); %number of components to consider
28 f=zeros(1,length(X)); %initialize output vector
29
30 for i=1:N
31
32     clear P      % This is temporary placeholders within the loop
33
34     P=legendre(i,X); %Legendre polynomial of order i
35
36     f = f + Cn(i) * P(1,:); %Add this component to the previous sum
37
38 end

```

B.7 chebyshev_decompose.m

```

1 function [An]= chebyshev_decompose(F,N,X)
2 % =====
3 % Find Chebyshev Polynomial components of input data vector:

```

```

4 % f = A0*T0(x) + A1*T1(x) + A2*T2(x) + ...
5 %
6 % RHEwoldt February 2007
7 %
8 % [An]= chebyshev_decompose(F,N,X)
9 %
10 % *Assumes F occupies the domain [-1 : +1]
11 % with an arbitrary number of data points
12 % *Uses trapz.m to calculate integrals
13 %
14 % INPUT VARIABLES
15 %     F: vector of data, in domain [-1:1]
16 %     N: degree of desired Legendre Polynomial decomposition
17 %     X: Range points associated with F
18 %
19 % OUTPUT VARIABLE
20 %     An: vector of Chebyshev coefficients
21 %     An(i) = A_{i-1}
22 %
23
24
25 % % Following lines for diagnostic purposes only
26 % % F = fe;
27 % % N = 11;
28 % % X = Xe;
29 % order=0
30 % Xlength=1000
31 % X = linspace(-1,1,Xlength);
32 % F = X.^order;
33 % N = 31;
34
35
36 if nargin < 3,
37     % Make X (input range) linear spaced and same length as F
38     X=linspace(-1,1,length(F));
39 end
40
41 % F must be a row vector. Change if necessary
42 if length(F(1,:))==1 %if there is only 1 column
43     d=F'; clear F
44     F=d ; clear d
45 end
46
47
48
49 An = zeros(N,1); %initialize vector of Chebyshev coefficients
50
51 T = gallery('chebvand',X); %Matrix of Chebyshev polynomials evaluated at X
52 %T(i,:) is (i-1)order polynomial
53
54
55 %
56 % COORDINATE TRANSFORM TECHNIQUE: NO WEIGHTING NECESSARY
57 %
58
59 THETA = asin(X);
60
61 % 0th order polynomial has different front factor
62 An(1) = 1/pi * trapz(THETA, F);
63 % Remaining coefficients use same front factor
64 for i=2:N
65     An(i) = 2/pi * trapz(THETA, T(i,:).*F);
66 end
67
68 % %
69 % % Diagnostic/Proof Figure Printing
70 % %
71 % I=figure;

```

```

72 % set(I,'Position',[100 100 700 500]);
73 % set(I,'PaperPosition',[0.2500 2.5000 7.0000 5.0000]);
74 % subplot(1,2,1);
75 % H=plot(X,F,'r');set(H,'LineWidth',2)
76 % title('Input Function (Scaled)'); xlabel('X'),ylabel('F')
77 % subplot(1,2,2);bar([0:1:N-1],An)
78 % title('Chebyshev Coefficients (Coord. Txform. & trapz.m)'); xlabel('n');ylabel('A_n')
79 % text(N/2.5,0.5, strcat('X has n=',num2str(Xlength),' points'))
80 %
81 % % subplot(2,2,3);
82 % % plot(X,T(1,:), 'k');
83 % % hold on
84 % % plot(X,T(2,:), 'b')
85 % % plot(X,T(3,:), 'r')
86 % % plot(X,T(4,:), 'g')
87 % % title('Chebyshev Polynomials: Order 0, 1, 2, 3')
88 % % axis([-1.1 1.1 -1.1 1.1 ])
89 % % subplot(2,2,4);
90 %
91 % print('-djpeg',strcat('C:\Research\ARES\Polynomial_Fits\Chebyshev_Fig',...
92 %     num2str(order),'-',num2str(Xlength),'.jpg'))
93
94
95
96
97
98
99
100
101 % %
102 % % CARTESIAN TECHNIQUE, WHICH REQUIRES WEIGHTING FUNCTION
103 % %     OBSOLETE! as of Feb 8, 2007
104 %
105 %
106 %
107 % %weighting function required for orthogonality
108 % W = sqrt(1-X.^2);
109 % L=log10(W(2))
110 %
111 % W(1) = 1*10^(L-3); %Weighting function =0 @ +/-1, so make this finite
112 % W(1) %instead, because I divide by W for integrand
113 % W(end) = 1*10^(L-3); %
114 % W(end) %
115 %
116 %
117 %
118 %
119 % I=F./W; %part of integrand used for every An calculation
120 %
121 % % 0th order polynomial has different front factor
122 % Cn(1) = 1/pi * trapz(X, I);
123 % % Remaining coefficients use same front factor
124 % for i=2:N
125 %
126 %     Cn(i) = 2/pi * trapz(X(2:end-1), T(i,2:end-1).*I(2:end-1));
127 %
128 % end

```

B.8 chebyshev_compose.m

```

1 function [f,X]= chebyshev_compose (An,X)
2 % =====
3 % Construct Chebyshev Polynomial components into data vector:
4 % f = A0*T0(x) + A1*T1(x) + A2*T2(x) + A3*T3(x) + ...

```



```

5 %
6 % RHEwoldt February 2007
7 %
8 % [f,X]= chebyshev_compose(An)
9 %
10 %
11 % INPUT VARIABLE
12 %     An: vector of Chebyshev coefficients (starting from order 0)
13 %     m: number of data points desired in output vector
14 %     (OPTIONAL: default is 2001)
15 %
16 % OUTPUT VARIABLE
17 %     f: reconstructed data vector (using all available An components)
18 %     x: corresponding input vector [-1 : +1]
19 %
20
21 if margin < 2,
22     % Make X vector linear spaced, 2001 pts
23     X=linspace(-1,1,2001);
24 end
25
26
27 N=length(An); %numer of components to consider
28 f=zeros(1,length(X)); %initialize output vector
29
30 T = gallery('chebvand',X); %Matrix of Chebyshev polynomials evaluated at X
31     %T(i,:) is (i-1)order polynomial
32
33 for i=1:N
34
35     f = f + An(i) * T(i,:); %Add this component to the previous sum
36
37 end

```


Appendix C

Yield stress LAOS - supplementary figures

This appendix is a supplement to Chapter 7, and covers three parts. First, details are given for the interpolation of discrete LAOS tests to make smooth rheological fingerprints. Second, additional plots are included for the shear-thinning xanthan gum solution. Finally, additional figures related to the elastoviscoplastic drilling fluid are presented.

The collection of experimental data occurs at discrete values within the Pipkin space of (ω, γ_0) . For example, the drilling fluid data presented in Chapter 7 was spaced at 2 points per decade in frequency ω and 4 points per decade in strain-amplitude γ_0 . The viscoelastic parameters corresponding to these discrete sampling points can be visualized by plots such as Figure C-1a. Color blocks are used for this plot, which are centered about the imposed (ω, γ_0) . The width and height of the block area is determined by the spacing of the data. On a technical note, this is a non-standard use of the MATLAB ‘pcolor’ command. The (X,Y) input to pcolor defines the vertices of the blocks, so one must take the ‘omega’ and ‘gamma’ vectors and map them to ‘Xvertices’ and ‘Yvertices’ vectors. It is also required to pad the Gp matrix with an

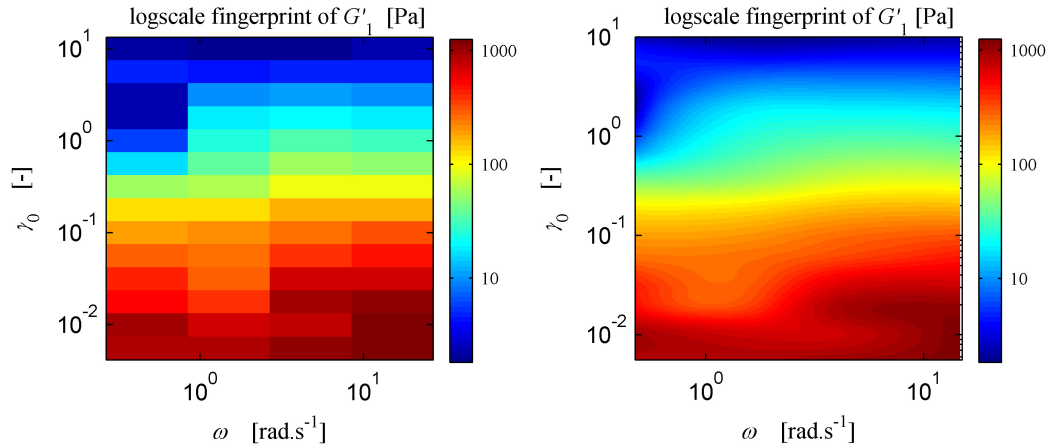


Figure C-1: Non-interpolated vs. interpolated fingerprints of viscoelastic parameters.

extra row and extra column. Note that the finite width and height of each block increases the XYlimits of the plot beyond where data was actually collected, since the blocks are centered over the corresponding (ω, γ_0) location.

To improve visualization of trends and contour lines, the data can be interpolated to produce smooth gradients of color values, as in Figure C-1b. The figures presented here have been interpolated to include 100 points per decade in both frequency ω and strain-amplitude γ_0 . As a technical note, the standard ‘flat shading’ of the ‘pcolor’ command is used for the interpolated plots. For ease of processing, the interpolated data are not precisely centered over the imposed (ω, γ_0) , since the vectors of ‘omega’ and ‘gamma’ get used to define the vertices of the blocks. Thus, the data is shifted by 0.5% in this case. This is the reason that the minor axis ticks show up on the right side of the plots.

Figures C-6 and C-7 give additional rheological fingerprints of the xanthan gum solution which were not included in Chapter 7.

Figures C-4 and C-4 show un-normalized Lissajous curves for the drilling fluid. Such plots more clearly reveal the change in peak stress as a function of the strain amplitude.

Shear-thinning xanthan gum – Elastic fingerprints

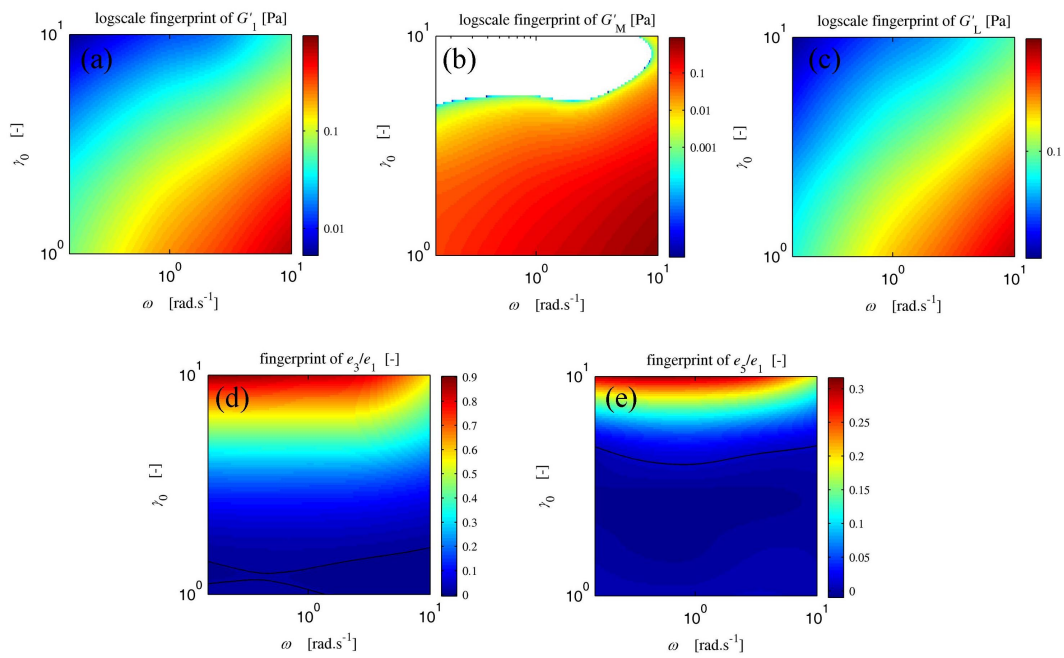


Figure C-2: Additional quantitative LAOS analysis of the xanthan gum. (a,b,c) Elastic moduli G'_1 , G'_M and G'_L respectively. (d,e) higher harmonic Chebyshev coefficients, e_3/e_1 and e_5/e_1 , respectively. Contour lines shown at ± 0.01 in (d,e).

Shear-thinning xanthan gum – Viscous fingerprints

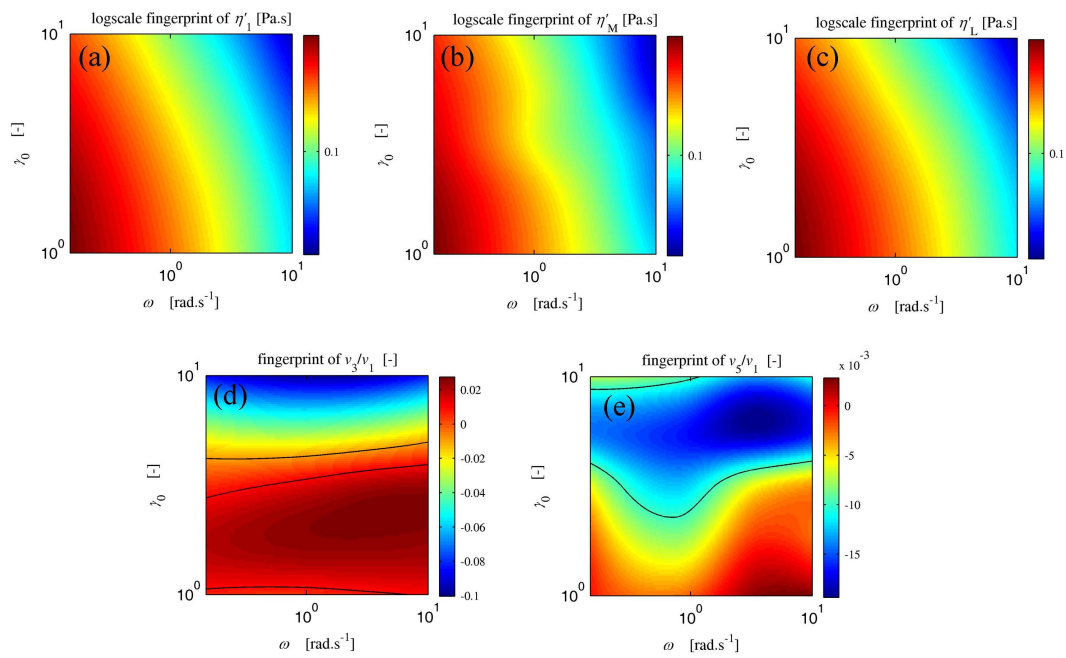


Figure C-3: Additional quantitative LAOS analysis of the xanthan gum (cf. Figures 7-7-7-8). (a,b,c) Elastic moduli η'_1 , η'_M and η'_L respectively. (d,e) higher harmonic Chebyshev coefficients, v_3/v_1 and v_5/v_1 , respectively. Contour lines shown at ± 0.01 in (d,e).

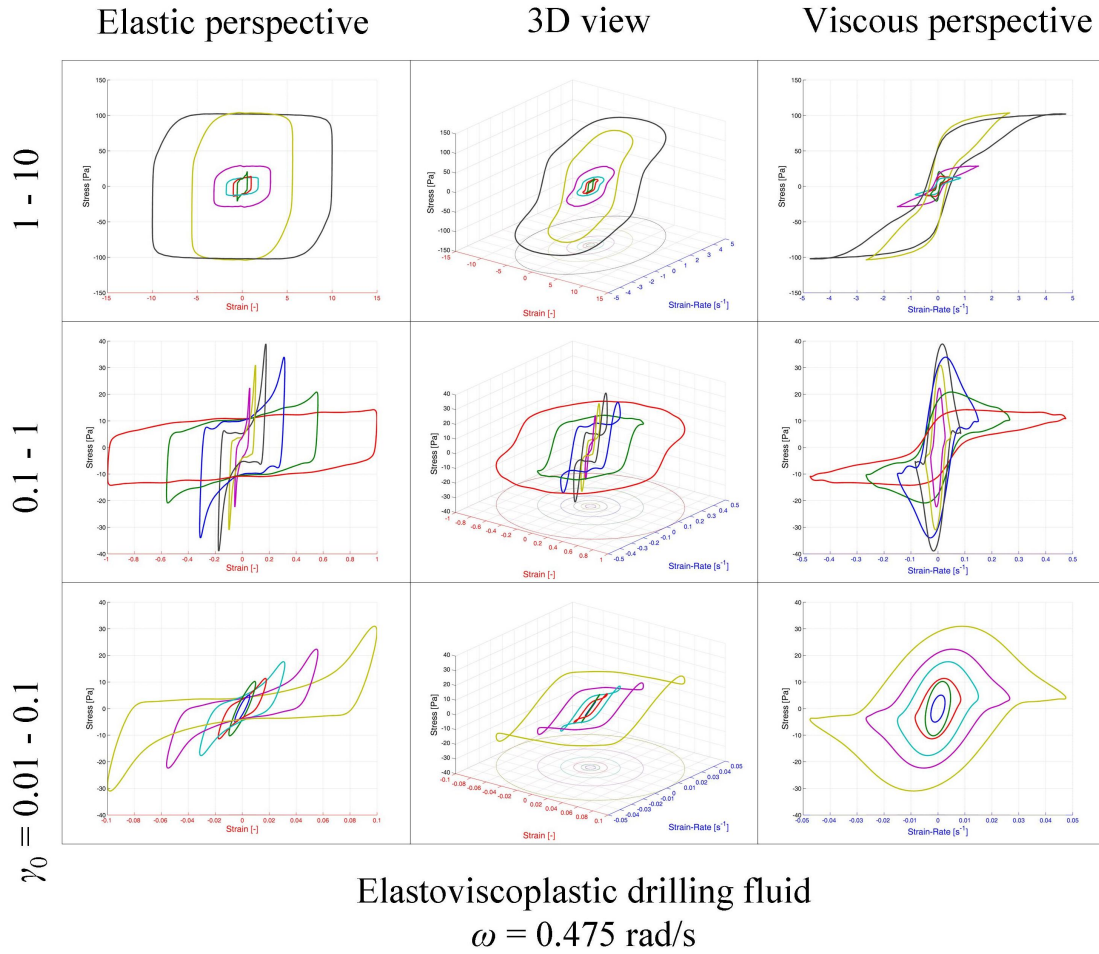
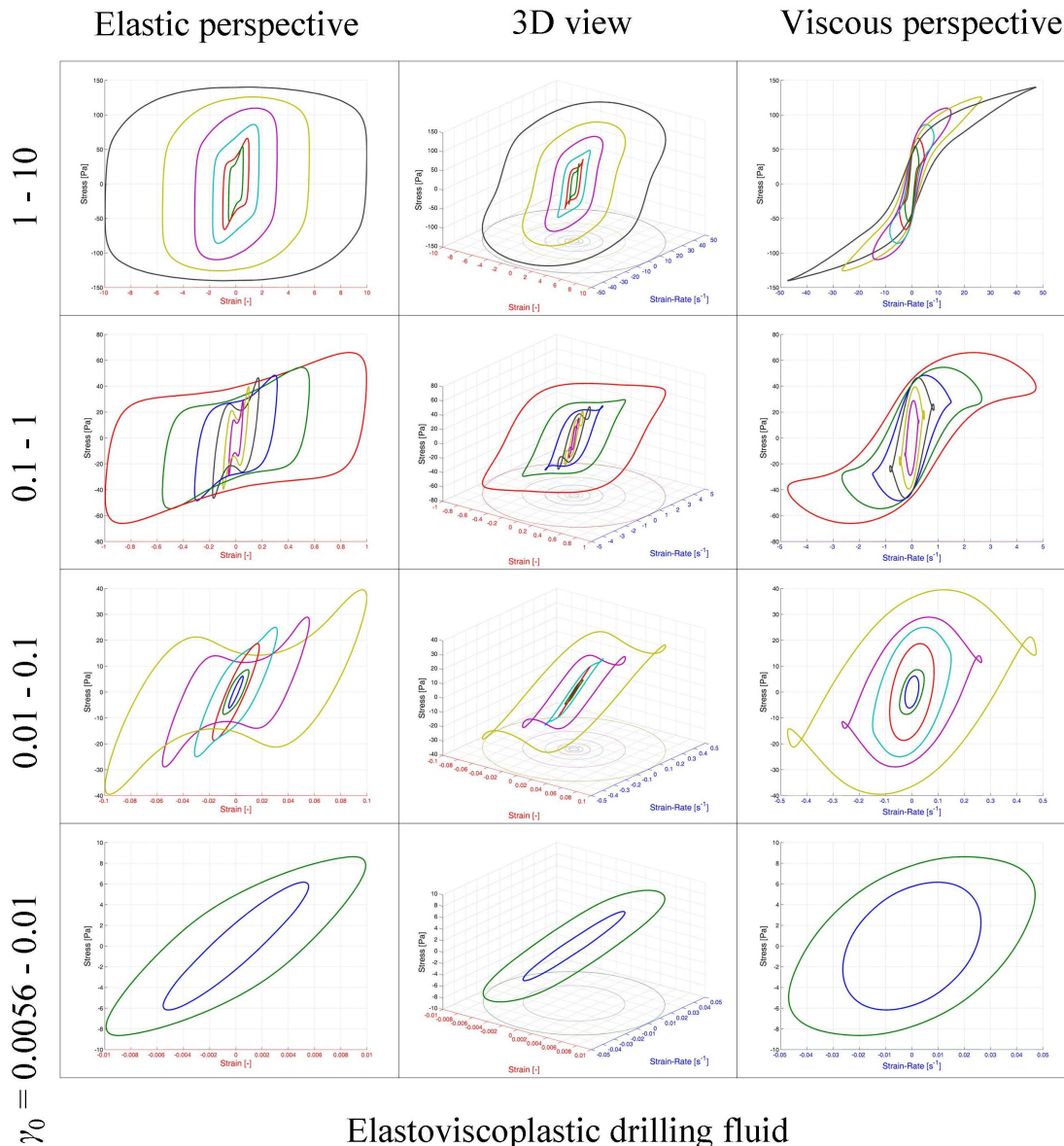


Figure C-4: Smoothed Lissajous curves for the drilling fluid. LAOS test strain-sweep at constant frequency $\omega = 0.475 \text{ rad}\cdot\text{s}^{-1}$, increasing strain amplitude γ_0 from bottom row. (left column) Elastic perspective, 2D projection onto stress vs. strain axes; (middle column) 3D view with strain, strain-rate, and stress as the coordinate system; (right column) Viscous perspective, 2D projection onto stress vs. strain-rate axes.



Elastoviscoplastic drilling fluid
 $\omega = 4.75 \text{ rad/s}$

Figure C-5: Smoothed Lissajous curves for the drilling fluid. LAOS test strain-sweep at constant frequency $\omega = 4.75 \text{ rad}\cdot\text{s}^{-1}$, increasing strain amplitude γ_0 from bottom row. (left column) Elastic perspective, 2D projection onto stress vs. strain axes; (middle column) 3D view with strain, strain-rate, and stress as the coordinate system; (right column) Viscous perspective, 2D projection onto stress vs. strain-rate axes.

Elastoviscoplastic drilling fluid – Elastic fingerprints

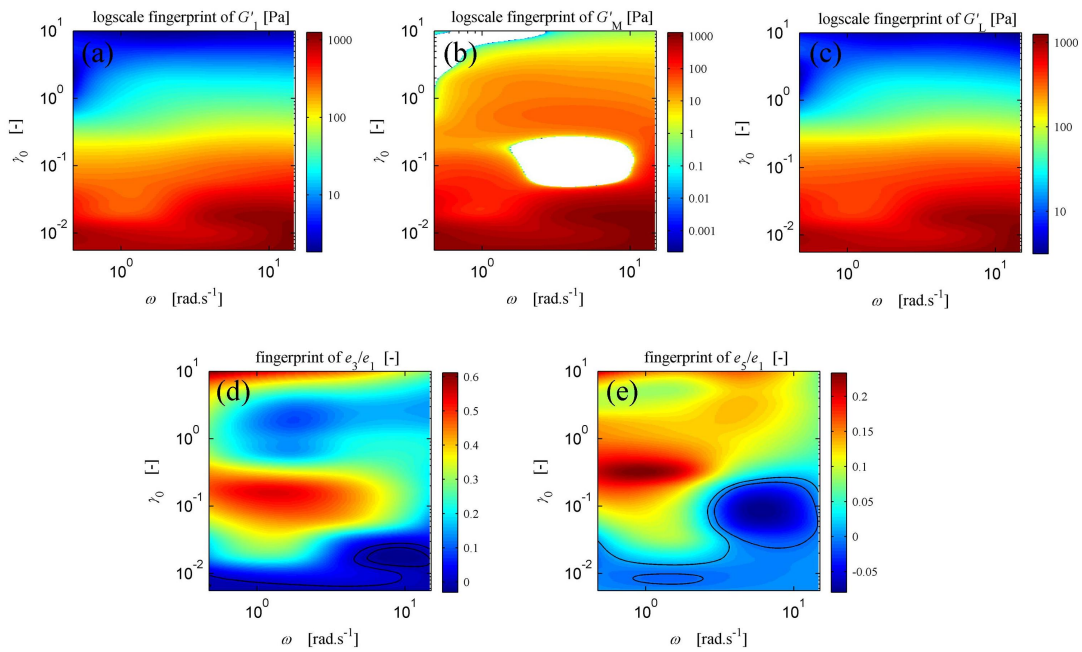


Figure C-6: Additional quantitative LAOS analysis of the drilling fluid (cf. Figures 7-9 and 7-10). (a,b,c) Elastic moduli G'_1 , G'_M and G'_L respectively. (d,e) higher harmonic Chebyshev coefficients, e_3/e_1 and e_5/e_1 , respectively. Contour lines shown at ± 0.01 in (d,e).

Elastoviscoplastic drilling fluid – Viscous fingerprints

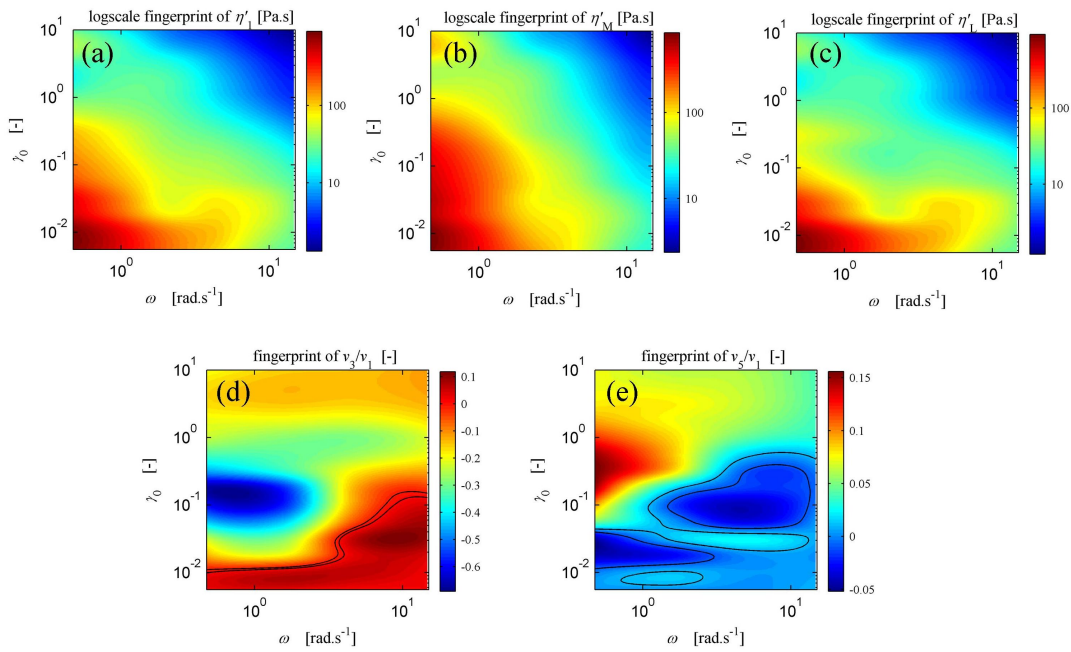


Figure C-7: Additional quantitative LAOS analysis of the drilling fluid (cf. Figures 7-9 and 7-10). (a,b,c) Elastic moduli η'_1 , η'_M and η'_L respectively. (d,e) higher harmonic Chebyshev coefficients, v_3/v_1 and v_5/v_1 , respectively.

Appendix D

Details of Slime Simulant Survey

Material details

High vacuum grease was purchased from the Dow Corning Corporation (Midland, MI). Carbopol preparation is described in the article. Aloe gel was purchased under the Banana Boat brand name, labeled as *Soothing Aloe Aftersun Gel*. The aloe gel is distributed by Sun Pharmaceuticals Corp (Delray Beach, FL). Locust bean gum was a gift from P.L. Thomas & Co., Inc. (Morristown, NJ). The collagen mixture was prepared by adding 0.25 g of microfibrillar, type I collagen isolated from bovine tendon (Integra LifeSciences, Plainsboro, NJ) to 4 ml of DI water. After mixing the solution, 1 ml of 3.0M acetic acid was injected, resulting in a mixture of 5% (w/w) collagen in 0.6M acetic acid solution. The collagen and acetic acid solution was mixed using two syringes joined with a female-female Luer-lock assembly, in which the solution was pushed from one syringe to another ten times in succession. The solution was allowed to rest for three hours in order to equilibrate. The mixture was then centrifuged for 45 minutes at 4000g to remove air bubbles. The resulting clear gel was kept at T=4C until it was needed for testing. Locust bean gum was added directly to a Ringer's solution and mixed with a magnetic stirrer. The Ringer's

Legend name	Description
Grease	Dow Corning high vacuum grease
Carbopol	Carbopol 940 in water, pH7; 0.5%, 1%, 2%, 3%, 4% (w/w)
Aloe Gel	Banana Boat, Soothing Aloe Aftersun Gel
Collagen	Type I collagen in water; 0.5%, 2%, 3.5%, 5% (w/w)
LBG	Locust bean gum in Ringer's solution; 1% (w/w)
Laponite	LaponiteRD in water, pH=10; 3%, 4%, 5%, 7% (w/w)
Cream 3	Westin's Heavenly Bath brand "hydrating cream"
Conditioner	Westin's Heavenly Bath brand conditioner
Toothpaste	Crest regular paste
Garden snail	Native pedal mucus from the common garden snail (<i>Helix aspera</i>)

Table D.1: Details of personal data from Figure 8-3

solution is DI water containing 0.86 mg/ml NaCl, 0.03 mg/ml KCl, and 0.033 mg/ml CaCl. Laponite preparation is described in the article.

The Cream 3 and Conditioner samples are made available by Westin hotels under the Heavenly Bath brand name. Toothpaste was purchased from a local store, sold by the Crest Co., labeled as *Regular paste - tartar control*. The toothpaste is opaque, and light blue in color. Pedal mucus collection is described in the article.

Legend name	Description	Reference
Banana slug	Native pedal mucus from the banana slug (<i>Ariolimax columbianus</i>); yield stress value from stress overshoot tests, extrapolated to limit of zero strain-rate	[99]
Grease in oil	Dow Corning high vacuum grease in 0.1 Pa.s silicone oil; 15wt%, 25wt%	[141]
Alginate	Alginate in water; 4.4% (w/w) with Ca cations; τ_y extrapolated from data	[142]
Carageenan	Grindsted Carageenan in water; 2%, 3%	[143]
Xanthan	Xanthan in water; 1%, 2%, 3%	[143]
Dextran	Dextran in water; 250mg/ml; 0mM CaCl ₂ , 1.9mM CaCl ₂ ;	[144]
HPG3	hydrophobically modified (hydroxypropyl) guar, called HPG3, in water; 1.5wt%; $\eta \approx 10^2$ Pa.s for $\tau < \tau_y$	[145]
Blend	Carbopol 940 : sodium alginate : guar gum in artificial tear fluid; 0.5:0.2:0.2, 0.6:0.3:0.3; unknown concentration, fit to Bingham model	[146]
Hair gel	Miss Helen blue hair gel	[147]

Table D.2: Details of polymeric gels from Figure 8-3

Legend name	Description	Reference
Bentonite	Ca-bentonite and Na-bentonite in water; 2% (w/w), τ_y extrapolated from data	[148]
Cloisite	Exfoliated montmorillonite clay (Cloisite 20A) in xylene; 1% - 10% (w/w),	[149]
Kaolin	Kaolin (plate-like particles) in water; 51% (w/w)	[150]
TiO ₂	A-HR TiO ₂ (sphere-like particles, 0.5 μ m diameter) in water, pH=2.4; 50% (w/w)	[150]

Table D.3: Details of particulate gels from Figure 8-3

Legend name	Description	Reference
Cream 1	Commercially available skin creme (brand not reported)	[132]
Cream 2	Prepared lamellar gel-structured “cream” containing emulsifiers, 2% triethanolamine, and water; 6.5% and 13% emulsifiers	[151]
PB creamy	Commercially available “smooth” peanut butter (brand not reported), data fit to Bingham model	[152]
PB 100% nuts	Commercially available “100% peanuts” peanut butter (same brand as above, but not reported), data fit to Bingham model	[152]
Mayo 1	Factory sample of mayonnaise, fit to Herschel-Bulkley model	[151]
Mayo 2a	Apparent rheology of mayonnaise prepared with various xanthan gum concentrations; 50% (w/w) oil; 0.5%, 1.0%, 1.5% (w/w) xanthan gum	[153]
Mayo 2b	Same physical sample as Mayo 2a but with data corrected for slip	[153]
Mayo 2c	Slip corrected rheology of mayonnaise prepared with various oil concentrations, no xanthan gum; 75%, 80%, 85% (w/w) oil	[153]
Foam	Commercial shaving foam (Gillette Foamy, regular), tested with rough surface, fit to Herschel-Bulkley model	[147]

Table D.4: Details of emulsions, wet foams, and composites from Figure 8-3

Appendix E

Supplemental information for normal adhesion tests

E.1 Newtonian silicone oil rheology

The silicone oil used for the adhesive tests in Chapter 9, “10,000 cst”, is Newtonian. This assertion is supported by the rheological data presented in this section. An ARG2 rotational rheometer was used with a cone-plate setup, $D = 40$ mm, cone angle $\theta = 2^\circ$. A steady flow test was performed across a large range of shear-rates, as shown in Fig. E-1a. The ordinate is shown on a *linear* scale to emphasize the Newtonian nature of the fluid. The average viscosity from this test is $\eta = 9.28$ Pa.s

Adhesion tests were performed under ambient conditions, without temperature control. The temperature sensitivity of the viscosity was examined with a temperature-sweep flow test, at $\dot{\gamma} = 2.863 \text{ s}^{-1}$. The results of the temperature sweep test are given in Fig. E-1. The viscosity of this silicone oil displays a weak sensitivity to temperature. An Arrhenius profile can be fit to the data, $\eta(T) = a \exp(b/T)$, resulting in $a = 0.09033$ Pa.s and $b = 1381.1$ K. The viscosity at $T = 25^\circ$, using the Arrhenius fit, is $\eta = 9.281$ Pa.s.

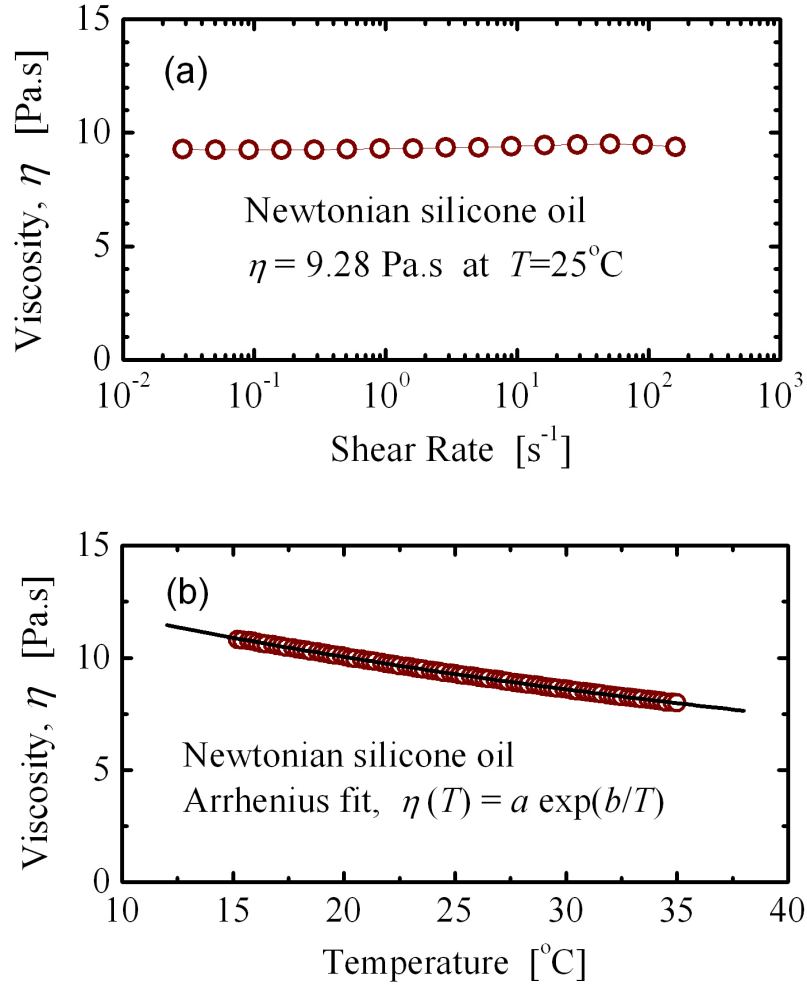


Figure E-1: Newtonian oil rheological characterization.

E.2 Magnetic field FEA

The analytical magnetostatics solution does not strictly apply for the magnetically-activated fluid adhesion, since the region of interest is close to the magnet. Finite element analysis (FEA) was used to determine the magnetic field using the freely available software Maxwell SV (Ansoft, LLC, Pittsburgh, PA). Results were obtained for the magnetostatic problem of a cylindrical permanent magnet with a thin, disk-shaped layer of MR fluid at a finite z -distance. Results are presented here for a Neodymium magnet, NdFe30, which was available as a material selection option with Maxwell SV. For this material, $\mu = 1.04457301671$, and the magnetic retentivity is

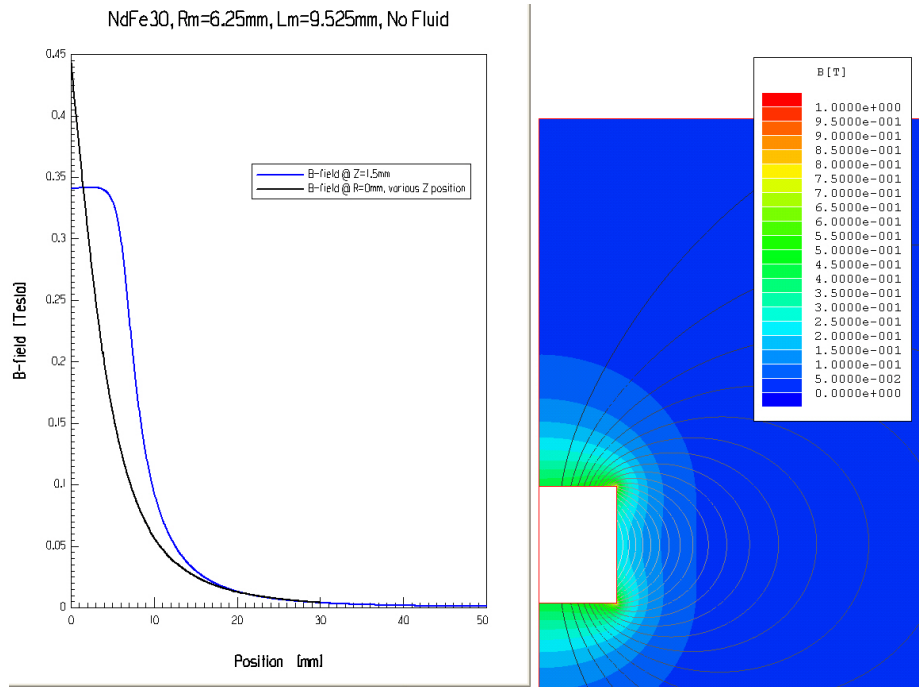


Figure E-2: Magnetic field analysis for the Neodymium magnet, $R_m = 6.35$ mm, $L_m = 9.52$ mm.

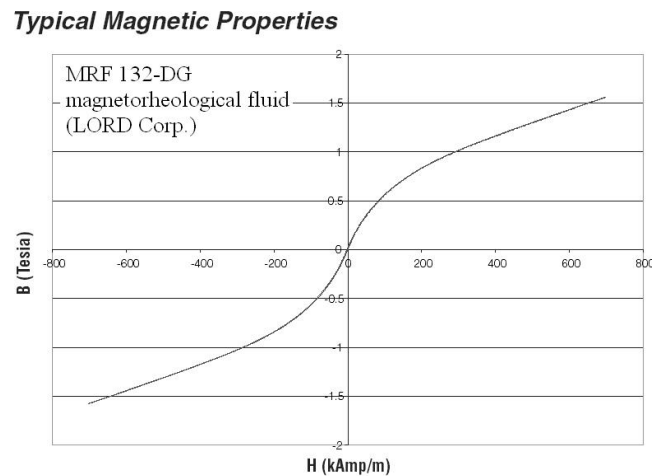


Figure E-3: Magnetic properties of the oil-based magnetorheological fluid MRF 132-DG, as given by the LORD Corporation.

$B_r = 1.1$ T. The radius of the cylindrical magnet is $R_m = 6.25$ mm, with length $L_m = 9.525$ mm. The situation is axisymmetric with a cylindrical polar coordinate system. Results are shown in z - r plane. The field configuration for the case of no fluid is shown in Fig. E-2.

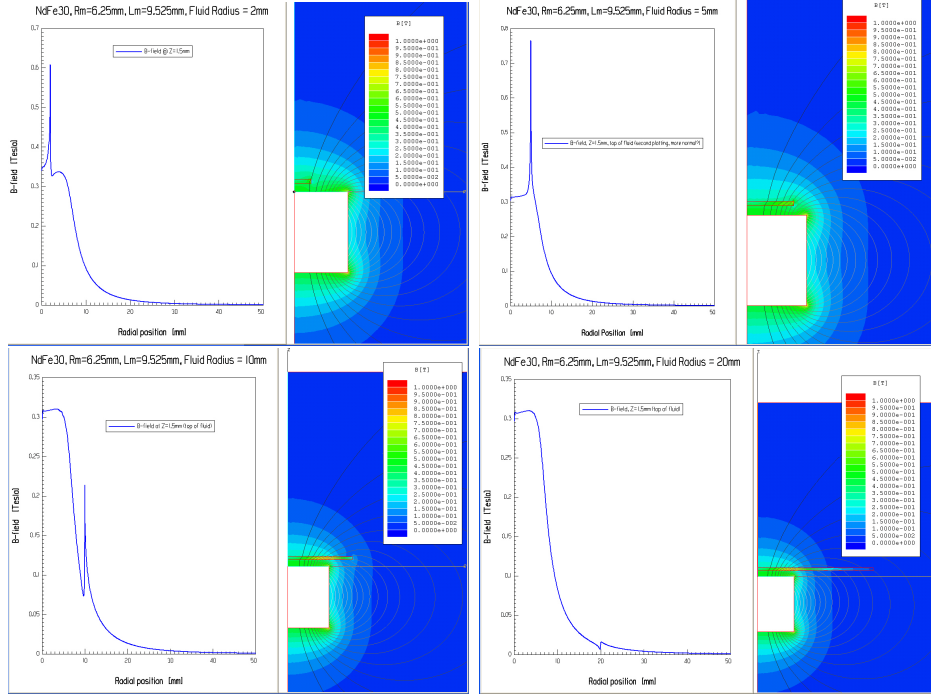


Figure E-4: Magnetic field analysis for the Neodymium magnet, $R_m = 6.35$ mm, $L_m = 9.52$ mm, including the layer of magnetorheological fluid with thickness $h = 0.5$ mm and various radii ($R = 2, 5, 10, 20$ mm).

The presence of a magnetically permeable fluid will alter the magnetic field. FEA was used to examine this effect, using a fluid/magnet separation of $\delta = 1.0$ mm, a fluid thickness $h = 0.5$ mm, and various fluid radii ($R = 2, 5, 10, 20$ mm). The plane of interest is $Z = 1.5$ mm above the surface of the magnet, which corresponds to the location at the top of fluid. The magnetic field at this surface is of interest because it is furthest from the magnet and is likely to be the weakest link in the adhesion failure problem. The fluid was modeled with a magnetic response given by the LORD Corp, as shown in Fig. E-3. The magnetic field configuration in the presence of magnetorheological fluid is given in Fig. E-4.

The results of Fig. E-4 are combined and shown in Fig. E-5. The magnetic field strength exhibits spikes near the boundary of the fluid. Aside from these localized spikes, the field configuration is approximately homogeneous above the permanent magnet ($r < R_m$). The field strength then decays away from the magnet according to

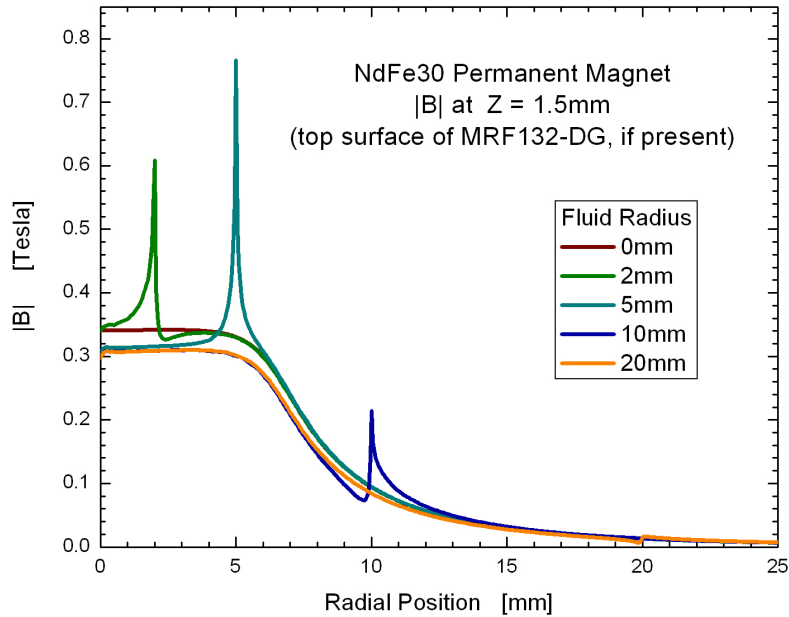
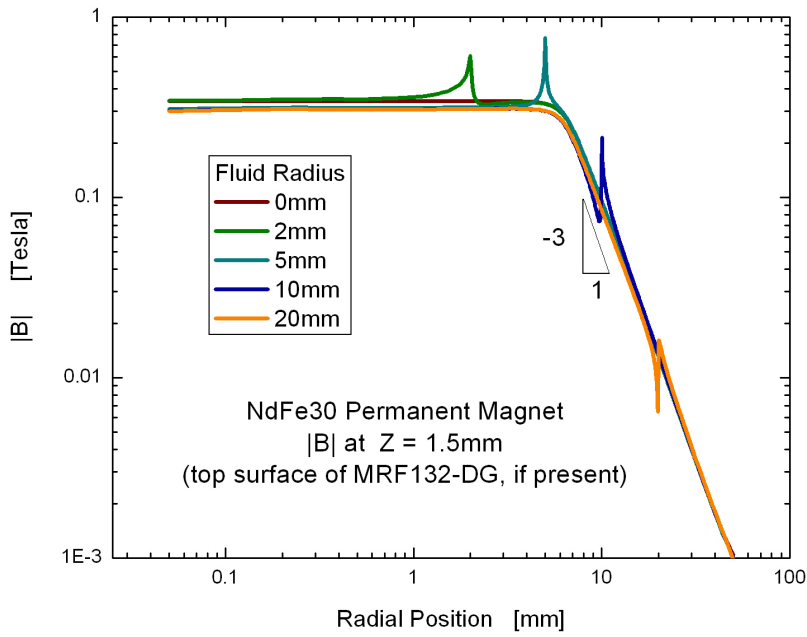


Figure E-5: Magnetic field profile for the Neodymium magnet, $R_m = 6.35$ mm, $L_m = 9.52$ mm, including the layer of magnetorheological fluid at various radii ($R = 2, 5, 10, 20$ mm). Localized spikes in the magnetic field strength occur near the edge of the fluid, but overall the profile appears flat above the magnet ($r < R_m = 6.35$ mm) and decays as a cubic power law beyond the edge of the magnet ($r > R_m$).

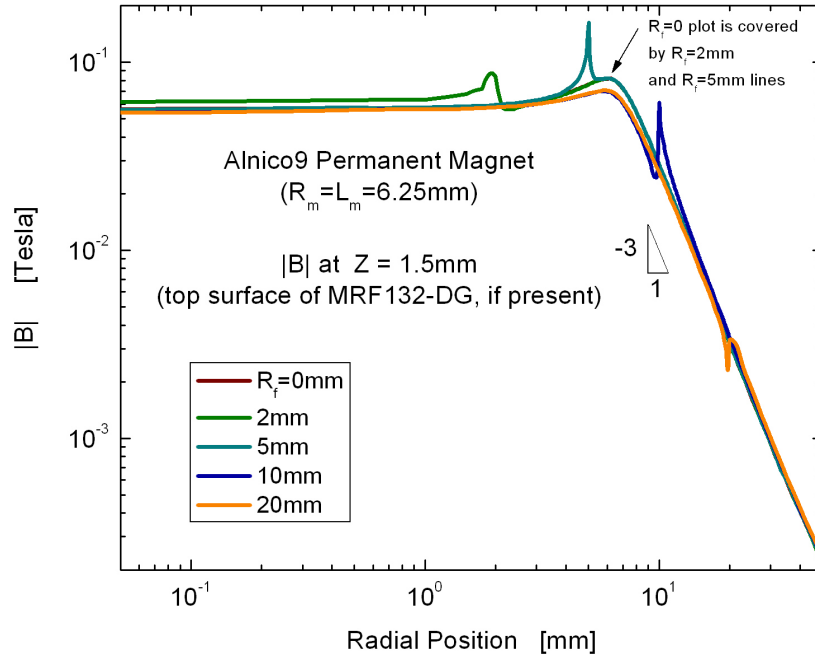


Figure E-6: Magnetic field profile for an Alnico 9 magnet, $R_m = 6.35$ mm, $L_m = 6.35$ mm, including the layer of magnetorheological fluid at various radii ($R = 2, 5, 10, 20$ mm). Localized spikes in the magnetic field strength occur near the edge of the fluid. The profile is approximately constant above the magnet ($r < R_m = 6.35$ mm), although a rise in magnetic field is observed near $r = R_m$. The field decays as a cubic power law beyond the edge of the magnet ($r > R_m$).

an inverse cubic power law, which is consistent with the analytical far field solution.

The magnetically-activated adhesion tests of Chapter 9 used both Neodymium and Alnico 8 magnets. In addition to the Neodymium results given in Figs. E-2-E-5, FEA was performed for an Alnico 9 magnet (which is similar to the Alnico 8 magnet used for experiments). The material properties of Alnico 9 were available within the material selection options of the Maxwell SV software. The Alnico 9 magnetic properties involve a nonlinear B-H curve. The effects with various fluid radii ($R = 2, 5, 10, 20$ mm) were examined.

Results for the Alnico 9 magnet in the presence of magnetorheological fluid are given in Fig. E-6. Again, the magnetic field spikes near the sharp boundaries of the fluid. Aside from these localized spikes, the field configuration is approximately

homogeneous above the permanent magnet, involving a slight rise near $r = R_m$. The field strength then decays away from the magnet according to an inverse cubic power law, which is consistent with the analytical far field solution.

Each magnet analyzed here (NdFe30 and Alnico9) suggest a similar profile for the magnetic field configuration which activates the fluid. The idealized behavior used for the modeling of MR fluid adhesion in Chapter 9 is that of a homogeneous magnetic field above the magnet ($r < R_m$), which decays by a cubic power-law for $r > R_m$.

Bibliography

- [1] A. C. Pipkin. *Lectures on viscoelasticity theory*. Applied mathematical sciences, v. 7. Springer, New York, 1972.
- [2] A. S. Yoshimura and R. K. Prudhomme. Response of an elastic bingham fluid to oscillatory shear. *Rheol. Acta*, 26(5):428–436, 1987.
- [3] M. W. Denny. The role of gastropod pedal mucus in locomotion. *Nature*, 285(5761):160–161, 1980.
- [4] R. E. Shadwick. Mechanical design in arteries. *J. Exp. Biol.*, 202(23):3305–3313, 1999.
- [5] S. K. Ng. *Linear to nonlinear rheology of bread dough and its constituents*. Ph.D. thesis, Massachusetts Institute of Technology, 2007.
- [6] M. L. Gardel, J. H. Shin, F. C. MacKintosh, L. Mahadevan, P. Matsudaira, and D. A. Weitz. Elastic behavior of cross-linked and bundled actin networks. *Science*, 304(5675):1301–1305, 2004.
- [7] R. H. Ewoldt, C. Clasen, A. E. Hosoi, and G. H. McKinley. Rheological fingerprinting of gastropod pedal mucus and synthetic complex fluids for biomimicking adhesive locomotion. *Soft Matter*, 3(5):634–643, 2007.
- [8] R. B. Bird, R. C. Armstrong, and O. Hassager. *Dynamics of Polymeric Liquids*, volume 1. John Wiley and Sons, Inc, New York, 2nd edition, 1987.

- [9] A. J. Giacomin and J. M. Dealy. Large-amplitude oscillatory shear. In A. A. Collyer, editor, *Techniques in rheological measurement*. Elsevier Applied Science, London, 1993.
- [10] J. D. Ferry. *Viscoelastic properties of polymers*. Wiley, 3d edition, 1980.
- [11] J. Harris. Response of time-dependent materials to oscillatory motion. *Nature*, 207:744, 1965.
- [12] W. Philippoff. Vibrational measurements with large amplitudes. *Trans. Soc. Rheol.*, 10(1):317–334, 1966.
- [13] S. Onogi, T. Masuda, and T. Matsumoto. Non-linear behavior of viscoelastic materials. I. disperse systems of polystyrene solution and carbon black. *J. Rheol.*, 14(2):275–294, 1970.
- [14] J. M. Dealy and K. F. Wissbrun. *Melt rheology and its role in plastics processing: theory and applications*. Van Nostrand Reinhold, New York, 1990.
- [15] M. Wilhelm. Fourier-transform rheology. *Macromol. Mater. Eng.*, 287(2):83–105, 2002.
- [16] B. Debbaut and H. Burhin. Large amplitude oscillatory shear and fourier-transform rheology for a high-density polyethylene: Experiments and numerical simulation. *J. Rheol.*, 46(5):1155–1176, 2002.
- [17] T. Dotsch, M. Pollard, and M. Wilhelm. Kinetics of isothermal crystallization in isotactic polypropylene monitored with rheology and fourier-transform rheology. *J. Phys.-Condes. Matter*, 15(11):S923–S931, 2003.
- [18] S. N. Ganeriwala and C. A. Rotz. Fourier-transform mechanical analysis for determining the nonlinear viscoelastic properties of polymers. *Polym. Eng. Sci.*, 27(2):165–178, 1987.

- [19] K. Hyun, S. H. Kim, K. H. Ahn, and S. J. Lee. Large amplitude oscillatory shear as a way to classify the complex fluids. *J. Non-Newton. Fluid Mech.*, 107(1-3):51–65, 2002.
- [20] K. Miyazaki, H. M. Wyss, D. A. Weitz, and D. R. Reichman. Nonlinear viscoelasticity of metastable complex fluids. *Europhys. Lett.*, 75(6):915–921, 2006.
- [21] H. M. Wyss, K. Miyazaki, J. Mattsson, Z. B. Hu, D. R. Reichman, and D. A. Weitz. Strain-rate frequency superposition: A rheological probe of structural relaxation in soft materials. *Phys. Rev. Lett.*, 98(23):238303, 2007.
- [22] C. Klein, H. W. Spiess, A. Calin, C. Balan, and M. Wilhelm. Separation of the nonlinear oscillatory response into a superposition of linear, strain hardening, strain softening, and wall slip response. *Macromol.*, 40(12):4250–4259, 2007.
- [23] C. Klein, P. Venema, L. Sagis, and E. van der Linden. Rheological discrimination and characterization of carrageenans and starches by Fourier transform-rheology in the non-linear viscous regime. *J. Non-Newton. Fluid Mech.*, 151(1-3):145–150, 2008.
- [24] K. Hyun, J. G. Nam, M. Wilhelm, K. H. Ahn, and S. J. Lee. Nonlinear response of complex fluids under LAOS (large amplitude oscillatory shear) flow. *Korea-Aust. Rheol. J.*, 15(2):97–105, 2003.
- [25] N. Bowditch. On the motion of a pendulum suspended from two points. *Mem. Am. Acad. Arts Sci.*, 3(2):413–436, 1815.
- [26] A. D. Crowell. Motion of the earth as viewed from the moon and the y-suspended pendulum. *Am. J. Phys.*, 49(5):452–454, 1981.
- [27] T. T. Tee and J. M. Dealy. Nonlinear viscoelasticity of polymer melts. *Trans. Soc. Rheol.*, 19(4):595–615, 1975.

- [28] K. S. Cho, K. H. Ahn, and S. J. Lee. A geometrical interpretation of large amplitude oscillatory shear response. *J. Rheol.*, 49(3):747–758, 2005.
- [29] P. A. Janmey, E. J. Amis, and J. D. Ferry. Rheology of fibrin clots .6. stress-relaxation, creep, and differential dynamic modulus of fine clots in large shearing deformations. *J. Rheol.*, 27(2):135–153, 1983.
- [30] N. Y. Yao, R. J. Larsen, and D. A. Weitz. Probing nonlinear rheology with inertio-elastic oscillations. *J. Rheol.*, (4):1013–1025, 2008.
- [31] R. H. Ewoldt and G. H. McKinley. Creep ringing in rheometry or how to deal with oft-discarded data in step stress tests. *Rheo. Bull.*, 76(1), 2007.
- [32] H Markovitz. Free vibration experiment in theory of linear viscoelasticity. *J. App. Phy.*, 34(1):21–25, 1963.
- [33] K. Walters. *Rheometry*. Wiley, New York, 1975.
- [34] L. C. E. Struik. Free damped vibrations of linear viscoelastic materials. *Rheol. Acta*, 6(2):119–129, 1967.
- [35] U. Zölzer and H. F. Eicke. Free oscillatory shear measurements - an interesting application of constant stress rheometers in the creep mode. *Rheol. Acta*, 32(1):104–107, 1993.
- [36] M. T. Arigo and G. H. McKinley. The effects of viscoelasticity on the transient motion of a sphere in a shear-thinning fluid. *J. Rheol.*, 41(1):103–128, 1997.
- [37] C. Baravian and D. Quemada. Using instrumental inertia in controlled stress rheometry. *Rheol. Acta*, 37(3):223–233, 1998.
- [38] N. W. Tschoegl. *The phenomenological theory of linear viscoelastic behavior : an introduction*. Springer-Verlag, New York, 1989.

- [39] C. Storm, J. J. Pastore, F. C. MacKintosh, T. C. Lubensky, and P. A. Janmey. Nonlinear elasticity in biological gels. *Nature*, 435(7039):191–194, 2005.
- [40] O. Chaudhuri, S. H. Parekh, and D. A. Fletcher. Reversible stress softening of actin networks. *Nature*, 445:295–298, 2007.
- [41] N. A. Spenley, M. E. Cates, and T. C. B. McLeish. Nonlinear rheology of wormlike micelles. *Phys. Rev. Lett.*, 71(6):939–942, 1993.
- [42] T. Gisler, R. Ball, and D. A. Weitz. Strain hardening of fractal colloidal gels. *Phys. Rev. Lett.*, 82(5):1064–1067, 1999.
- [43] K. Atalik and R. Keunings. On the occurrence of even harmonics in the shear stress response of viscoelastic fluids in large amplitude oscillatory shear. *J. Non-Newton. Fluid Mech.*, 122(1-3):107–116, 2004.
- [44] M. D. Graham. Wall slip and the nonlinear dynamics of large-amplitude oscillatory shear flows. *J. Rheol.*, 39(4):697–712, 1995.
- [45] L. L. Ma, J. Y. Xu, P. A. Coulombe, and D. Wirtz. Keratin filament suspensions show unique micromechanical properties. *J. Biol. Chem.*, 274(27):19145–19151, 1999.
- [46] M. Abramowitz and I. A. Stegun. *Handbook of Mathematical Functions with Formulas, Graphs, and Mathematical Tables*. Dover, New York, ninth Dover printing, tenth GPO printing edition, 1964.
- [47] M. J. Reimers and J. M. Dealy. Sliding plate rheometer studies of concentrated polystyrene solutions: Large amplitude oscillatory shear of a very high molecular weight polymer in diethyl phthalate. *J. Rheol.*, 40(1):167–186, 1996.

- [48] T. Neidhöfer. *Fourier-transform rheology on anionically synthesised polymer melts and solutions of various topology*. Ph.D. thesis, Johannes Gutenberg-Universitt Mainz, 2003.
- [49] R. H. Ewoldt, P. Winter, and G.H. McKinley. MITlaos version 2.1 beta for MATLAB, 2007.
- [50] R. H. Ewoldt, A. E. Hosoi, and G. H. McKinley. New measures for characterizing nonlinear viscoelasticity in large amplitude oscillatory shear. *J. Rheol.*, 52(6):1427–1458, 2008.
- [51] J. M. Li, W. R. Burghardt, B. Yang, and B. Khomami. Flow birefringence and computational studies of a shear thinning polymer solution in axisymmetric stagnation flow. *J. Non-Newton. Fluid Mech.*, 74(1-3):151–193, 1998.
- [52] M. W. Yao, G. H. McKinley, and B. Debbaut. Extensional deformation, stress relaxation and necking failure of viscoelastic filaments. *J. Non-Newton. Fluid Mech.*, 79(2-3):469–501, 1998.
- [53] G. B. Thurston. Shear rate dependence of the viscoelasticity of polymer-solutions. 1. theoretical-model. *J. Non-Newton. Fluid Mech.*, 9(1-2):57–68, 1981.
- [54] G. B. Thurston and G. A. Pope. Shear rate dependence of the viscoelasticity of polymer-solutions.2. xanthan gum. *J. Non-Newton. Fluid Mech.*, 9(1-2):69–78, 1981.
- [55] M. J. Reimers and J. M. Dealy. Sliding plate rheometer studies of concentrated polystyrene solutions: Nonlinear viscoelasticity and wall slip of two high molecular weight polymers in tricresyl phosphate. *J. Rheol.*, 42(3):527–548, 1998.

- [56] R. G. Larson. *Constitutive equations for polymer melts and solutions*. Butterworths series in chemical engineering;. Butterworths, Boston, 1988.
- [57] A. Bhardwaj, E. Miller, and J. P. Rothstein. Filament stretching and capillary breakup extensional rheometry measurements of viscoelastic wormlike micelle solutions. *J. Rheol.*, 51(4):693–719, 2007.
- [58] D. van Dusschoten and M. Wilhelm. Increased torque transducer sensitivity via oversampling. *Rheol. Acta*, 40(4):395–399, 2001.
- [59] H. Kim, K. Hyun, D. J. Kim, and K. S. Cho. Comparison of interpretation methods for large amplitude oscillatory shear response. *Korea-Aust. Rheol. J.*, 18(2):91–98, 2006.
- [60] M. Wilhelm, P. Reinheimer, and M. Ortseifer. High sensitivity fourier-transform rheology. *Rheol. Acta*, 38(4):349–356, 1999.
- [61] C. J. Pipe, N. Ju Kim, and G. H. McKinley. Investigating the steady and transient non-linear rheology of wormlike micellar solutions. In *78th Annual Meeting of The Society of Rheology*, Portland, ME, 2006. Paper GP7.
- [62] N. Phan-Thien. Squeezing flow of a viscoelastic solid. *J. Non-Newton. Fluid Mech.*, 95(2-3):343–362, 2000.
- [63] N. Phan-Thien, S. Nasserri, and L. E. Bilston. Oscillatory squeezing flow of a biological material. *Rheol. Acta*, 39(4):409–417, 2000.
- [64] H. K. Rasmussen, P. Laille, and K. J. Yu. Large amplitude oscillatory elongation flow. *Rheol. Acta*, 47(1):97–103, 2008.
- [65] J. G. Nam, K. Hyun, K. H. Ahn, and S. J. Lee. Prediction of normal stresses under large amplitude oscillatory shear flow. *J. Non-Newton. Fluid Mech.*, 150(1):1–10, 2008.

- [66] W. Yu, P. Wang, and C. Zhou. General stress decomposition in nonlinear oscillatory shear flow. *J. Rheol.*, 53(1):215–238, 2009.
- [67] J. M. Jørgensen, J. P. Lomholt, R. E. Weber, and H. Malte. *The biology of hagfishes*. Chapman and Hall, London ; New York, 1998.
- [68] S. W. Downing, R. H. Spitzer, E. A. Koch, and W. L. Salo. The hagfish slime gland thread cell. 1. a unique cellular-system for the study of intermediate filaments and intermediate filament-microtubule interactions. *J. Cell Biol.*, 98(2):653–669, 1984.
- [69] R. H. Spitzer, S. W. Downing, E. A. Koch, W. L. Salo, and L. J. Saidel. Hagfish slime gland thread cells. 2. isolation and characterization of intermediate filament components associated with the thread. *J. Cell Biol.*, 98(2):670–677, 1984.
- [70] R. H. Spitzer, E. A. Koch, and S. W. Downing. Maturation of hagfish gland thread cell - composition and characterization of intermediate filament polypeptides. *Cell Motil. Cytoskeleton*, 11(1):31–45, 1988.
- [71] E. A. Koch, R. H. Spitzer, R. B. Pithawalla, and D. A. D. Parry. An unusual intermediate filament subunit from the cytoskeletal biopolymer released extracellularly into seawater by the primitive hagfish (*Eptatretus stouti*). *J. Cell Sci.*, 107:3133–3144, 1994.
- [72] E. A. Koch, R. H. Spitzer, R. B. Pithawalla, and F. A. Castillos. Hagfish biopolymer - a type-I type-II homolog of epidermal keratin intermediate filaments. *Int. J. Biol. Macromol.*, 17(5):283–292, 1995.
- [73] D. S. Fudge, N. Levy, S. Chiu, and J. M. Gosline. Composition, morphology and mechanics of hagfish slime. *J. Exp. Biol.*, 208(24):4613–4625, 2005.

- [74] L. A. Sellers, A. Allen, E. R. Morris, and S. B. Rossmurphy. Mechanical characterization and properties of gastrointestinal mucus gel. *Biorheology*, 24(6):615–623, 1987.
- [75] J. K. Dutkiewicz. Superabsorbent materials from shellfish waste - a review. *J. Biomed. Mater. Res.*, 63(3):373–381, 2002.
- [76] J. Lim, D. S. Fudge, N. Levy, and J. M. Gosline. Hagfish slime ecomechanics: testing the gill-clogging hypothesis. *J. Exp. Biol.*, 209(4):702–710, 2006.
- [77] H. A. Barnes and K. Walters. The yield stress myth. *Rheol. Acta*, 24(4):323–326, 1985.
- [78] H. A. Barnes. The yield stress - a review or ‘pi alpha nu tau alpha rho epsilon iota’ - everything flows? *J. Non-Newton. Fluid Mech.*, 81(1-2):133–178, 1999.
- [79] J. Maxey. Thixotropy and yield stress behavior in drilling fluids. (AADE-07-NTCE-37), 2007.
- [80] K. Hyun and M. Wilhelm. Establishing a new mechanical nonlinear coefficient Q from FT-rheology: first investigation of entangled linear and comb polymer model systems. *Macromolecules*, 42(1):411–422, 2009.
- [81] A.P.I. Recommended practice for laboratory testing of drilling fluids. *American Petroleum Institute*, API RP 13I, 2009.
- [82] M. M. Cross. Rheology of non-Newtonian fluids: A new flow equation for pseudoplastic systems. 20(5):417–437, 1965.
- [83] T. C. Papanastasiou. Flows of materials with yield. *J. Rheol.*, 31(5):385–404, 1987.
- [84] R. B. Bird, G. C. Dai, and B. J. Yarusso. The rheology and flow of viscoplastic materials. *Rev. Chem. Eng.*, 1(1):1–70, 1983.

- [85] E. Mitsoulis. Flows of viscoplastic materials: models and computations. In D. M. Binding, N. E. Hudson, and R. Keunings, editors, *Rheology Reviews 2007*, pages 135–178. Universities Design and Print, Glasgow, 2007.
- [86] A. Mujumdar, A. N. Beris, and A. B. Metzner. Transient phenomena in thixotropic systems. *J. Non-Newton. Fluid Mech.*, 102(2):157–178, 2002.
- [87] P. Saramito. A new constitutive equation for elastoviscoplastic fluid flows. *J. Non-Newton. Fluid Mech.*, 145(1):1–14, 2007.
- [88] W. C. Macosporran and R. P. Spiers. The dynamic performance of the Weissenberg rheogoniometer. 2. large-amplitude oscillatory shearing - fundamental response. *Rheol. Acta*, 21(2):193–200, 1982.
- [89] W. C. Macosporran and R. P. Spiers. The dynamic performance of the Weissenberg rheogoniometer. 3. large-amplitude oscillatory shearing - harmonic analysis. *Rheol. Acta*, 23(1):90–97, 1984.
- [90] P. O. Brunn and H. Asoud. Analysis of shear rheometry of yield stress materials and apparent yield stress materials. *Rheol. Acta*, 41(6):524–531, 2002.
- [91] J. Harris and K. Bogie. The experimental analysis of non-linear waves in mechanical systems. *Rheol. Acta*, 6(1):3–5, 1967.
- [92] C. Fischer, C. J. G. Plummer, V. Michaud, P. E. Bourban, and J. A. E. Manson. Pre- and post-transition behavior of shear-thickening fluids in oscillating shear. *Rheol. Acta*, 46(8):1099–1108, 2007.
- [93] A. Yoshimura and R. K. Prudhomme. Wall slip corrections for couette and parallel disk viscometers. *J. Rheol.*, 32(1):53–67, 1988.
- [94] C. W. Macosko. *Rheology: principles, measurements, and applications*. Advances in interfacial engineering series;. Wiley-VCH, New York, 1994.

- [95] D. Doraiswamy, A. N. Mujumdar, I. Tsao, A. N. Beris, S. C. Danforth, and A. B. Metzner. The Cox-Merz rule extended - a rheological model for concentrated suspensions and other materials with a yield stress. *J. Rheol.*, 35(4):647–685, 1991.
- [96] Y. B. Yang, G. Chen, L. Li, and W. H. Li. On the extended Rutgers-Delaware rule for MR suspensions under magnetic fields. *Int. J. Mod. Phys. B*, 20(5):579–592, 2006.
- [97] H. A. Barnes and D. Bell. Controlled-stress rotational rheometry: An historical review. *K.-A. Rheo. J.*, 15(4):187–196, 2003.
- [98] M. W. Denny. Locomotion - the cost of gastropod crawling. *Science*, 208(4449):1288–1290, 1980.
- [99] M. W. Denny and J. M. Gosline. The physical-properties of the pedal mucus of the terrestrial slug, *ariolimax-columbianus*. *J. Exp. Biol.*, 88(OCT):375–393, 1980.
- [100] M. W. Denny. Molecular biomechanics of molluscan mucous secretions. In Peter W. Hochachka, editor, *The Molluska*, volume 1. Metabolic Biochemistry and Molecular Biomechanics. 1983.
- [101] B. Chan, N. J. Balmforth, and A. E. Hosoi. Building a better snail: Lubrication and adhesive locomotion. *Phys. Fluids*, 17(11), 2005.
- [102] J. O. Carnali and M. S. Naser. The use of dilute-solution viscometry to characterize the network properties of carbopol microgels. *Colloid Polym. Sci.*, 270(2):183–193, 1992.
- [103] N. W. Taylor and E. B. Bagley. Dispersions or solutions - mechanism for certain thickening agents. *J. Appl. Polym. Sci.*, 18(9):2747–2761, 1974.

- [104] A. Mourchid, A. Delville, J. Lambard, E. Lecolier, and P. Levitz. Phase-diagram of colloidal dispersions of anisotropic charged-particles - equilibrium properties, structure, and rheology of laponite suspensions. *Langmuir*, 11(6):1942–1950, 1995.
- [105] F. Pignon, A. Magnin, J. M. Piau, B. Cabane, P. Lindner, and O. Diat. Yield stress thixotropic clay suspension: Investigation of structure by light, neutron, and x-ray scattering. *Phys. Rev. E*, 56(3):3281–3289, 1997.
- [106] D. Bonn, H. Kellay, H. Tanaka, G. Wegdam, and J. Meunier. Laponite: What is the difference between a gel and a glass? *Langmuir*, 15(22):7534–7536, 1999.
- [107] A. M. Smith and M. C. Morin. Biochemical differences between trail mucus and adhesive mucus from marsh periwinkle snails. *Biol. Bull.*, 203(3):338–346, 2002.
- [108] Noveon Inc. Neutralizing carbopol and pemulen polymers in aqueous and hydroalcoholic systems, 1998.
- [109] A. Mourchid, E. Lecolier, H. Van Damme, and P. Levitz. On viscoelastic, birefringent, and swelling properties of laponite clay suspensions: Revisited phase diagram. *Langmuir*, 14(17):4718–4723, 1998.
- [110] R. H. Ewoldt. *Rheology of complex fluid films for biological and mechanical adhesive locomotion*. M.S. thesis, Massachusetts Institute of Technology, 2006.
- [111] E. Carretti, L. Dei, and R. G. Weiss. Soft matter and art conservation. rheoreversible gels and beyond. *Soft Matter*, 1(1):17–22, 2005.
- [112] S. B. Ross-Murphy. Structure-property relationships in food biopolymer gels and solutions. *J. Rheol.*, 39(6):1451–1463, 1995.

- [113] B. Chan. *Propulsion devices for locomotion at low-Reynolds number*. M.S. thesis, Massachusetts Institute of Technology, 2004.
- [114] H. A. Barnes. Thixotropy - a review. *J. Non-Newton. Fluid Mech.*, 70(1-2):1–33, 1997.
- [115] P. C. F. Møller, J. Mewis, and D. Bonn. Yield stress and thixotropy: on the difficulty of measuring yield stresses in practice. *Soft Matter*, 2(4):274–283, 2006.
- [116] E. Lauga and A. E. Hosoi. Tuning gastropod locomotion: Modeling the influence of mucus rheology on the cost of crawling. *Phys. Fluids*, 18(11):113102, 2006.
- [117] M. W. Denny. A quantitative model for the adhesive locomotion of the terrestrial slug, *ariolimax-columbianus*. *J. Exp. Biol.*, 91(APR):195–217, 1981.
- [118] H. A. Barnes. A review of the slip (wall depletion) of polymer-solutions, emulsions and particle suspensions in viscometers - its cause, character, and cure. *J. Non-Newton. Fluid Mech.*, 56(3):221–251, 1995.
- [119] D. M. Kalyon, P. Yaras, B. Aral, and U. Yilmazer. Rheological behavior of a concentrated suspension - a solid rocket fuel simulant. *J. Rheol.*, 37(1):35–53, 1993.
- [120] R. G. Larson. *The structure and rheology of complex fluids*. Topics in chemical engineering. Oxford University Press, New York, 1999.
- [121] S. M. Fielding, P. Sollich, and M. E. Cates. Aging and rheology in soft materials. *J. Rheol.*, 44(2):323–369, 2000.
- [122] M. Cloitre, R. Borrega, and L. Leibler. Rheological aging and rejuvenation in microgel pastes. *Phys. Rev. Lett.*, 85(22):4819–4822, 2000.

- [123] R. Lapasin, L. DeLorenzi, S. Pricl, and G. Torriano. Flow properties of hydroxypropyl guar gum and its long-chain hydrophobic derivatives. *Carbohydr. Polym.*, 28(3):195–202, 1995.
- [124] A. H. Krall and D. A. Weitz. Internal dynamics and elasticity of fractal colloidal gels. *Phys. Rev. Lett.*, 80(4):778–781, 1998.
- [125] J. R. Macdonald and J. C. Phillips. Topological derivation of shape exponents for stretched exponential relaxation. *Phys. Rev. E*, 122(7), 2005.
- [126] L. Heymann, E. Noack, L. Kaempfe, and B. Beckmann. Rheology of printing inks - some new experimental results. In A. Ait-Kadi, J.M. Dealy, D.F. James, and M.C. Williams, editors, *Proceedings of the XXIIth International Congress on Rheology*, Laval University, Quebec City (Quebec), Canada, 1996.
- [127] M. W. Denny. Mechanical-properties of pedal mucus and their consequences for gastropod structure and performance. *Am. Zool.*, 24(1):23–36, 1984.
- [128] J. D. Madden. Mobile robots: Motor challenges and materials solutions. *Science*, 318(5853):1094–1097, 2007.
- [129] B. Chan. *Bioinspired fluid locomotion*. Ph.D. thesis, Massachusetts Institute of Technology, 2009.
- [130] G. B. McKenna. Commentary on rheology of polymers in narrow gaps. *Eur. Phys. J. E*, 19(1):101–108, 2006.
- [131] C. Clasen, B. P. Gearing, and G. H. McKinley. The flexure-based microgap rheometer (FMR). *J. Rheol.*, 50(6):883–905, 2006.
- [132] C. Clasen and G. H. McKinley. Gap-dependent microrheometry of complex liquids. *J. Non-Newton. Fluid Mech.*, 124(1-3):1–10, 2004.

- [133] Stefan. Versuche ber die scheinbare adhsion. *Sitzungsber. Kais. Akad. Wiss. Math. Naturwiss.*, 69:713–735, 1874.
- [134] C. Gay and L. Leibler. On stickiness. *Phys. Today*, 52(11):48–52, 1999.
- [135] M. Ocalan. Ph.D. thesis, Massachusetts Institute of Technology, in progress.
- [136] M. Tirumkudulu, W. B. Russel, and T. J. Huang. On the measurement of “tack” for adhesives. *Phys. Fluids*, 15(6):1588–1605, 2003.
- [137] R. P. Feynman, R. B. Leighton, and M. L. Sands. *The Feynman lectures on physics*, volume 2. Pearson/Addison-Wesley, San Francisco, definitive edition, 2006.
- [138] M. A. Fortes. Axisymmetric liquid bridges between parallel plates. *J. Colloid Interface Sci.*, 88(2):338–352, 1982.
- [139] L. D. Landau and E. M. Lifshits. *Fluid mechanics*, volume 6 of *Course of theoretical physics*. Pergamon Press, New York, 2nd edition, 1987.
- [140] D. Derks, A. Lindner, C. Creton, and D. Bonn. Cohesive failure of thin layers of soft model adhesives under tension. *J. Appl. Phys.*, 93(3):1557–1566, 2003.
- [141] S. S. Deshmukh. *Field-responsive (‘Smart’) fluids for advanced automotive applications*. S.M. thesis, Massachusetts Institute of Technology, 2003.
- [142] Z. Y. Wang, Q. Z. Zhang, M. Konno, and S. Saito. Sol-gel transition of alginate solution by the addition of various divalent-cations - a rheological study. *Biopolymers*, 34(6):737–746, 1994.
- [143] M. Marcotte, A. R. T. Hoshahili, and H. S. Ramaswamy. Rheological properties of selected hydrocolloids as a function of concentration and temperature. *Food Res. Int.*, 34(8):695–703, 2001.

- [144] P. A. Padmanabhan, D. S. Kim, D. Pak, and S. J. Sim. Rheology and gelation of water-insoluble dextran from *Leuconostoc mesenteroides* NRRL B-523. *Carbohydr. Polym.*, 53(4):459–468, 2003.
- [145] T. Aubry and M. Moan. Rheological behavior of a hydrophobically associating water-soluble polymer. *J. Rheol.*, 38(6):1681–1692, 1994.
- [146] T. M. Aminabhavi, S. A. Agnihotri, and B. V. K. Naidu. Rheological properties and drug release characteristics of pH-responsive hydrogels. *J. Appl. Polym. Sci.*, 94(5):2057–2064, 2004.
- [147] A. Lindner, P. Coussot, and D. Bonn. Viscous fingering in a yield stress fluid. *Phys. Rev. Lett.*, 85(2):314–317, 2000.
- [148] S. Isci, E. Gunister, O. I. Ece, and N. Gungor. The modification of rheologic properties of clays with PVA effect. *Mater. Lett.*, 58(12-13):1975–1978, 2004.
- [149] Y. Zhong and S. Q. Wang. Exfoliation and yield behavior in nanodispersions of organically modified montmorillonite clay. *J. Rheol.*, 47(2):483–495, 2003.
- [150] P. H. T. Uhlherr, J. Guo, C. Tiu, X. M. Zhang, J. Z. Q. Zhou, and T. N. Fang. The shear-induced solid-liquid transition in yield stress materials with chemically different structures. *J. Non-Newton. Fluid Mech.*, 125(2-3):101–119, 2005.
- [151] J. R. Stokes and J. H. Telford. Measuring the yield behaviour of structured fluids. *J. Non-Newton. Fluid Mech.*, 124(1-3):137–146, 2004.
- [152] G. P. Citerne, P. J. Carreau, and M. Moan. Rheological properties of peanut butter. *Rheol. Acta*, 40(1):86–96, 2001.

- [153] L. Ma and G. V. Barbosacanvas. Rheological characterization of mayonnaise .2. flow and viscoelastic properties at different oil and xanthan gum concentrations. *J. Food Eng.*, 25(3):409–425, 1995.